Investigating the Control Mechanisms of Extracellular Electron Transfer in Gram-negative Bacteria

Alejandro Morales Flórez

PhD Thesis

University of East Anglia

School of Biological Sciences

Norwich

United Kingdom

October 2024

Abstract

Dissimilatory metal-reducing bacteria are capable of surviving in anoxic environments by transferring metabolic electrons to extracellular electron acceptors (EEA). One of these metal-reducing bacteria is *Shewanella oneidensis,* a Gram-negative facultative anaerobe, studied extensively as a model organism for extracellular electron transfer (EET). *S. oneidensis* uses the MtrCAB complex, a porin-cytochrome complex, to perform EET. Electrons pass from the periplasm through MtrA into MtrC, which is surface-exposed and facilitates electron transfer to EEA such as ferric oxides, flavins, and electrodes. However, the precise control mechanisms for EET in *S. oneidensis* remain largely unknown. In particular, the conserved domain arrangement of MtrC, where the 10 hemes are arranged into two domains separated by a β-barrel domain, is unusual and hypothesised to be involved in regulation of electron transfer. This thesis explores the control mechanisms by modifying the interactions between the domains of MtrC as well as the axial heme ligation of MtrA. Any consequent effects on electron transfer were investigated by biophysical characterisation and functional activity assays of MtrC/MtrA variants. The structures of the variant cytochromes were analysed to confirm that the changed amino acids were incorporated into the tertiary protein structure. The functional assays were performed to assess any impacts on EET rates. The results suggest that increasing the distance between the domains of MtrC resulted in minor differences to the EET rates. The increase in distance between domains I, II and domains III, IV was confirmed by SAXS. There was only a minimal difference in the UV-Vis spectra of the variants with increased inter-domain distance when compared to WT MtrC. Furthermore, there were no differences in reduction of extracellular FMN. However, removing domains III and IV of MtrC resulted in a significant decrease to the EET rates, depending directly on the electron acceptor. A structure for the MtrC variant comprised solely of domains I and II was obtained by X-ray crystallography. Finally, changing three heme distal histidines to methionines in MtrA also resulted in lowered EET rates. However, there were no major differences in the UV-Vis spectra of three single MtrA His/Met variants or a triple His/Met variant when compared to WT MtrA.These results highlight the essential role that the domains of MtrC play on the capacity of *S. oneidensis* to reduce extracellular substrates. They also show that replacing certain

distal histidines for methionines in the hemes of MtrA is possible. These results have further characterised two decaheme *c*-type cytochromes of *S. oneidensis*, MtrA and MtrC, and could help improve existing biotechnological applications like microbial fuel cells and bioremediation that exploit the electrogenic properties of *S. oneidensis*.

Acknowledgements

First, I would like to thank my supervisor Professor Tom Clarke. His tutelage has been invaluable throughout my PhD. Not only has he been friendly and patient, but also knowledgeable and understanding. I consider myself lucky to have worked alongside such a great supervisor.

I also want to thank my secondary supervisor, Professor Julea Butt, who consistently provided great insight and discussion. Her guidance and wisdom have helped shape my PhD into what it is today.

I am also grateful to Dr Marcus Edwards, who has provided vital support over the past four years. His expertise has been essential for my project. I would like to thank Drs Jessica van Wonderen, Colin Lockwood, and Simone Payne. They provided training for almost all of the techniques I have used in my project, and I have great admiration and respect for their work and who they are.

Next, I would like to thank Michael Connolly. He has greatly supported me during these past few years, listening to my long-winded stories about my experiments and why they weren't working. On days when things did not go to plan, he was always there to encourage me to keep going, and I admire his resilience and compassion to others.

Finalmente, quisiera agradecer a mi familia por todo el cariño y apoyo que han tenido. Gracias a Salomón y Juan Pablo por ser excelentes hermanos y por haberme ayudado durante estos últimos años. A Jairo y Patricia, les quisiera agradecer infinitamente por una vida entera de amor y felicidad, y por ser los mejores padres del mundo. Sin todos ustedes no estaría donde estoy hoy, y por eso los quiero mucho.

Table of Contents

Abbreviations and symbols

%	percentage
% (v/v)	percentage by volume per volume
% (w/v)	percentage by weight per volume
% (w/w)	percentage by weight per weight
~	approximately
°C	degrees Celsius
µg	microgram
µL	microlitre
µM	micromolar
µmol	micromole
Å	Angstrom
A.U.	arbitrary units
ATP	adenosine triphosphate
AUC	analytical ultracentrifugation
A_{xyz}	absorbance at xyz nanometre wavelength
bp	DNA base pairs
cm	centimetre
CV	cyclic voltammetry
cys	cysteine
Da	Dalton
DEAE	diethylaminoethanol
DNA	deoxyribonucleic acid
DT	dithionite
e^-	electron
E. coli	*Escherichia coli*
E˚	reduction potential
EDTA	ethylenediaminetetraacetic acid
EET	extracellular electron transfer
ETC	electron transport chain
f	frictional coefficient
ferrozine	3-(2-Pyridyl)-5,6-diphenyl-1,2,4-triazine-4',4''-disulfonic acid sodium salt

FAD	flavin adenine dinucleotide
FMN	flavin mononucleotide
FTO	fluoride-doped tin oxide
g	Earth's gravitational force
g	gram
GOI	gene of interest
HEPES	4-(2-hydroxyethyl)-1-piperazineethanesulfonic acid
his	histidine
ITO	indium tin oxide
K	Kelvin
kan	kanamycin
K_d	dissociation constant
kDa	kilodalton
kg	kilogram
L	litre
LB	lysogeny broth
LB_{kan}	lysogeny broth with kanamycin
LC-MS	liquid chromatography-mass spectrometry
LDAO	lauryldimethylamine oxide
M	molar
m	metre
MB water	molecular biology-grade water
met	methionine
mg	milligram
mL	millilitre
mM	millimolar
MO	methyl orange
MOPS	3-(*N*-morpholino)propanesulfonic acid
MR-1	*S. oneidensis* MR-1
mV	millivolt
MWCO	molecular weight cut-off
NADH	nicotinamide adenine dinucleotide
NADPH	nicotinamide adenine dinucleotide phosphate

ng	nanogram
nm	nanometre
nM	nanomolar
nmol	nanomole
OD_{xyz}	optical density at xyz nanometre wavelength
P	Poise, unit of dynamic viscosity
PCR	polymerase chain reaction
pDNA	plasmid DNA
PEG	polyethylene glycol
PFE	protein film electrochemistry
PITOD	polystyrene-indium tin oxide dispersion
ppm	parts per million
psi	pounds per square inch
r	radius
RB5	reactive black 5
R_g	radius of gyration
RMSD	root mean square distance
RO water	reverse osmosis water
RPM	revolutions per minute
RT	room temperature, ≈ 21°C
s	sedimentation coefficient
SAXS	small-angle X-ray scattering
SBM	Shewanella basal medium
SDS-PAGE	sodium dodecyl sulfate-polyacrylamide gel electrophoresis
SHE	standard hydrogen electrode
SMM	Shewanella minimal medium
TAE	Tris-acetic acid
TMBD	3,3',5,5'-Tetramethylbenzidine dihydrochloride hydrate
UV	ultraviolet light
UV-Vis	ultraviolet-visible
V	volt
WT	wild-type
ε	molar absorption coefficient (usually, M^{-1} cm^{-1})

ε_{XYZ}	molar absorption coefficient at XYZ nm wavelength
λ	wavelength
ρ	density

Chapter 1

Introduction

1. Introduction

1.1 The three categories of life

The classification of cellular life into different categories has changed repeatedly over the last couple of centuries. One of the earliest attempts at this taxonomic classification was the two-kingdom system proposed by Linnaeus in 1758 which divided life into the Plantae and Animalia kingdoms[1]. By 1990, however, Woese, Kandler and Wheelis proposed a system comprised of three distinct domains: the Eubacteria (now Bacteria), Archaebacteria (now Archaea), and Eukarya. The Bacteria and Archaea domains contain only one kingdom (Bacteria and Archaea, respectively), while the Eukarya domain is made up by the Protista, Fungi, Plantae, and Animalia[1,2]. Woese stipulated that based on 16S rRNA genetic data, archaea, bacteria, and eukaryotes share a Last Universal Common Ancestor (LUCA) (Figure 1.1)[3]. Metal reduction and oxidation can be seen across the three domains, ranging from bacteria like *Shewanella oneidensis*, to archaea like *Pyrococcus furiosus*, to eukaryotes like *Saccharomyces cerevisiae*[4,5].

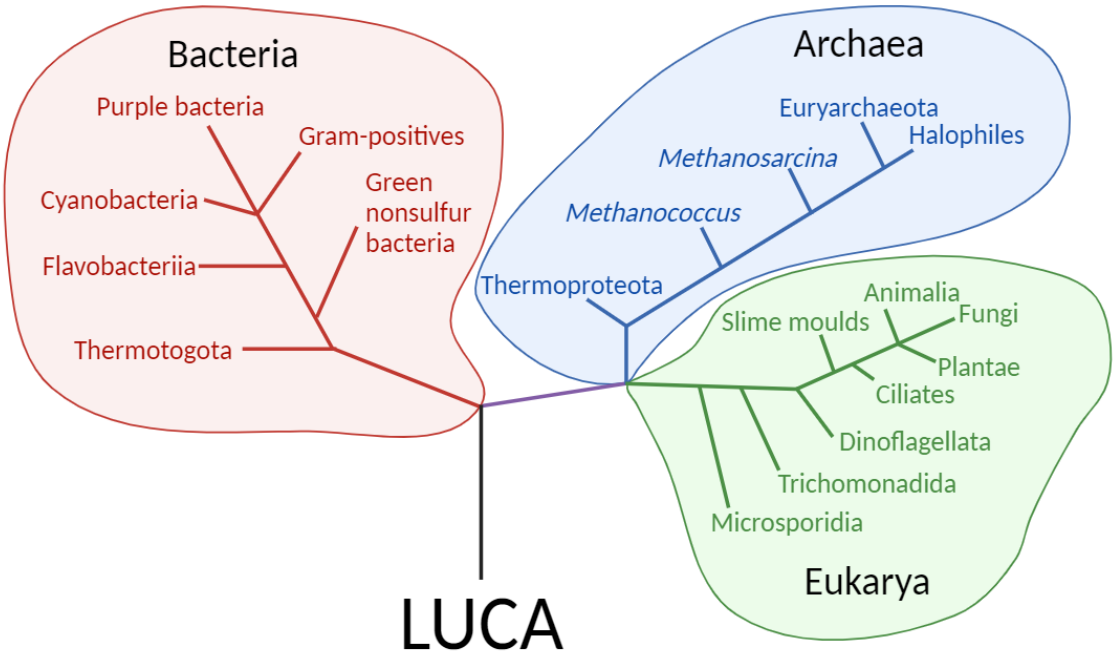

Figure 1.1. Phylogenetic tree showing the three domains of life Bacteria, Archaea, and Eukarya, with the LUCA at the bottom. Created using BioRender.com and adapted from previous work[3].

1.1.1 The Archaea

Archaea are unicellular microorganisms that were initially classified as archaebacteria (in the Archaebacteria kingdom) but have since been classified as a separate domain[2,6]. They do not contain cellular nuclei and tend to be morphologically similar to bacteria. However, archaea possess certain metabolic enzymes that are more closely related to ones found in eukaryotes, such as enzymes involved in DNA and RNA transcription and translation[7]. The Archaeal cell membranes are largely comprised of ether lipids and archaeols, something that differentiates them from bacteria and eukaryotes. Archaea derive energy from a variety of sources, ranging from hydrogen gas and metal ions to organic compounds (like sugars) and inorganic compounds (like ammonia)[3,6]. Members of the Haloarchaea class are salt-tolerant and can use sunlight as an energy source (phototrophs), while other species are capable of fixing carbon (autotrophs)[6,7]. Many members of the Archaea are extremophiles, being able to live in a variety of environments that most eukaryotes and bacteria cannot. These environments include: high pH (alkaliphiles), low pH (acidophiles), high salt concentration (halophiles), high hydrostatic pressure (barophiles), low temperature (psychrophiles), low available water (xerophiles), high temperature (thermophiles), very high temperatures (hyperthermophiles), and low/no oxygen (anaerobes)[6]. For anaerobic archaea to survive, they carry out metal reduction/oxidation. Archaea are found in the microbiota of many organisms. In the human microbiome, for example, they are prevalent on the skin, in the gut, and in the mouth[8]. However, our understanding of their role and significance is limited as they are not as well understood as bacteria and eukaryotes. Due to their global prevalence and metabolic capabilities, they play significant roles in several ecological processes like the nitrogen cycle, carbon fixation, turnover of organic compounds, and conservation of microbial symbiotic communities[6,7,9].

1.1.2 The Eukarya

Eukaryotes are organisms that are generally much larger than both bacteria and archaea. There are several kingdoms of eukaryotes that range include organisms ranging from fungi and plants to animals and other unicellular organisms[2,6]. Eukaryotes contain cells with membrane-bound nuclei, Golgi apparatus, and endoplasmic reticulum. They also contain proteins that have little to no homology

with proteins of the other domains of life, including cytoskeletal proteins, proteins related with transcription, and proteins involved in sorting of membranes[10]. Structurally speaking, eukaryotic cells are far more complex than bacterial and archaeal ones. Animal and plants cells have been studied extensively, and their internal composition is well understood. A plasma membrane surrounds these cells. In fungal, plant, and algal cells, a cell wall surrounds the plasma membrane, providing extra support and protection. Plant cell walls are composed of cellulose, hemicellulose, and pectin (polysaccharides). Other organelles that distinguish most eukaryotes from other domains of life are: cytoskeletal structures, mitochondria, plastids, and the fact that reproduction usually occurs sexually[2,6,10,11].

1.1.3 The Bacteria

Bacteria are a group of unicellular microorganisms that can live in diverse environments, ranging from human gastrointestinal tracts to deep-sea vents. These microorganisms can use organic and inorganic compounds to live, survive, and reproduce as they possess varied metabolic systems that are adapted to diverse sources of carbon and energy[12]. Unlike eukaryotic cells, bacteria contain bacterial microcompartments (BMC) which are analogous to membrane-bound organelles. Examples of these BMCs include carboxysomes (filled with RuBisCO and involved in carbon fixation) and metabolosomes (involved in aldehyde oxidation), amongst others[13]. They can be categorised by their shape: rodlike (bacillus), spherical (coccus), or curved (spirillum, vibrio, spirochete). Additionally, they can be further classified depending on their cell envelope structure. In 1884, Christian Gram designed a staining technique that allowed for the classification of most bacteria into two large groups[14]. One group would retain Gram's stain (Gram-positive) whilst the other would not (Gram-negative). Gram-negative bacterial cell envelopes are composed of an inner membrane (IM), a peptidoglycan cell wall, and an outer membrane (OM). The aqueous compartment delimited by the OM and IM was termed the periplasm in 1961[15].

Gram-positive cell envelopes do not contain an OM. Instead, the surrounding peptidoglycan layers are thicker than in Gram-negative organisms (Figure 1.2) to help combat turgor pressure exerted on the membrane. In Gram-positive microorganisms extracellular proteins contain elements that hold them in or near

the membrane. Some proteins are linked to lipid anchors in the membrane, some have transmembrane helices, and some are covalently attached or tightly associated with the peptidoglycan layer[16]. Both Gram-positive and Gram-negative

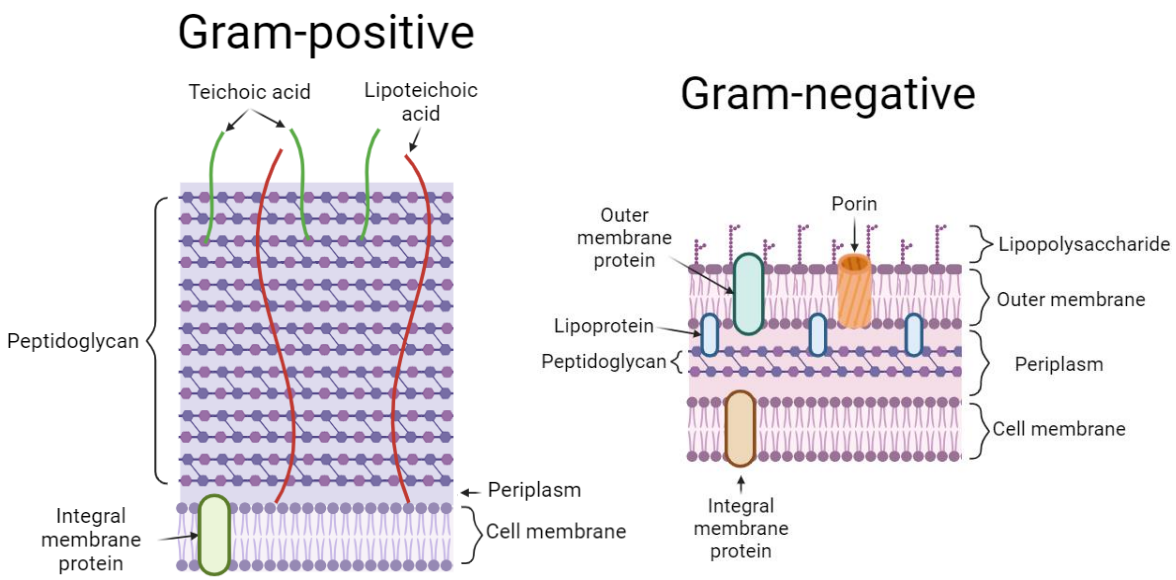

Figure 1.2. Gram-positive (**left**) and Gram-negative (**right**) cell envelope representation. Created using BioRender.com and adapted from previous work[15].

bacteria (and archaea) also contain a two-dimensional layer of (glyco)proteins that envelop the cell, known as the S-layer. These proteins are self-assembled, creating a regularly-spaced array on the cellular surface. The S-layer plays various roles in bacteria ranging from protection and adhesion to biofilm formation and maintenance of cellular integrity[17,18].

1.2 Bacterial metabolism

Metabolism encompasses all biochemical reactions that may occur within a cell. The dissimilation reactions and substrate oxidation reactions usually have the purpose of generating energy within bacteria. Furthermore, the utilisation and uptake of both inorganic and organic compounds for growth and homeostasis are also included in the scope of bacterial metabolism. These reactions can be endergonic (requiring energy) or exergonic (producing energy) and are catalysed within the cells via integrated enzyme systems with the goal of cellular replication[14].

The bacterial cell functions as a specialized energy converter, harnessing chemical energy from substrate oxidations to produce compounds with high potential energy in their chemical bonds like nicotinamide adenine dinucleotide (NADH), adenosine triphosphate (ATP), and thioester-bond-containing compounds such as acetyl-CoA

and succinyl-CoA. These compounds, contain phosphate bonds with high free energy of hydrolysis which have several important biological functions. They serve as vital energy sources for synthesizing complex organic molecules essential for cellular functions, provide energy for cellular respiration, and are useful for storing free energy[19]. Maintenance of steady-state biochemical reactions is imperative across all living cells to facilitate the formation and utilization of such high-energy compounds[14]. Kluyver and Donker (1924-1926) realised that bacterial cells were very similar to other living cells, chemically[14]. It was Peter Mitchell, however, that recognised that hydrogen transfer is a fundamental and widespread feature of almost all metabolic processes, as it leads to proton motive force (PMF)[20]. PMF is used by all organisms for differing purposes, one of the most important being driving ATP synthesis through ATP synthases[21]. Bacteria can use the phosphate bond with high free energy of hydrolysis found in ATP as their primary energy source, for flagellar movement, and for solute transport[22]. All the possible nutritional subdivisions of organisms are shown in Table 1.1.

1.2.1 Metabolic mechanisms

Table 1.1. Overview of the nutritional classification system[216–221]. Names are colour coded with their respective energy source, proton/electron donor, and carbon source.

Energy source	H^+/e^- donor	Carbon source	Name	Example
Photo- (sun light)	-organo- (organic)	-auto (CO_2)	Photoorganoautotroph	Halobacteria
		-hetero (organic)	Photoorganoheterotroph	Heliobacteria
	-litho- (inorganic)	-auto (CO_2)	Photolithoautotroph	Cyanobacteria
		-hetero (organic)	Photolithoheterotroph	Purple non-sulfur bacteria
Chemo- (chemical compounds)	-organo- (organic)	-auto (CO_2)	Chemoorganoautotroph	Anaerobic methanotrophic archaea (ANME-1)
		-hetero (organic)	Chemoorganoheterotroph	*Shewanella oneidensis*
	-litho- (inorganic)	-auto (CO_2)	Chemolithoautotroph	*Acidithiobacillus ferrooxidans*
		-hetero (organic)	Chemolithoheterotroph	*Oceanithermus profundus*

Microorganisms can be categorised into different nutritional groups (Table 1.1), depending on which mechanisms are used for growth. Usually, they are divided into two groups: heterotrophs, organisms that use organic compounds as a carbon source for biosynthetic metabolism; and autotrophs, organisms that use inorganic carbon sources such as CO_2 for biosynthetic metabolism. Within both groups, organisms can be further divided into phototrophs, where electromagnetic energy

(from the visible light spectrum) is converted into chemical energy; or chemotrophs, where chemical compounds are oxidised, producing chemical energy. Furthermore, organisms can be divided into organotrophs, which use organic compounds as hydrogen/electron donors; and lithotrophs, which use inorganic compounds as hydrogen/electron donors[23]. There are organisms that can use more than one nutritional mechanism simultaneously such as *Thiobacillus ferrooxidans* and *Rhodopseudomonas palustris*; these are known as mixotrophs[23–26].

1.3 Role of electron transfer in cellular metabolism

Heterotrophic bacteria (which includes most pathogens) acquire their energy from the oxidation of organic compounds, like amino acids. Oxidation of these organic compounds leads to ATP synthesis. This process also enables the generation of less complex organic precursor molecules used in other assimilatory or biosynthetic reactions. The intermediary compounds of the Krebs cycle function as precursors for the energy-dependent synthesis of complex organic molecules in bacterial organisms. Amphibolic pathways encompass degradation processes yielding energy and precursor molecules essential for cellular biosynthesis. Heterotrophic bacteria require exogenous organic substrates, rich in carbon and nitrogen. These serve as growth substrates, metabolised aerobically or anaerobically to produce reducing equivalents, such as NADH. These molecules serve as vital energy sources for biological oxidative and fermentative pathways[14]. Regardless of the organism, electron transfer occurs via higher energy electron donors providing electrons that are ultimately taken by the lower energy electron acceptors. NADH is one of the most common reducing equivalents that can donate electrons to other compounds of the electron transport chain (ETC). This electron transfer across a membrane is usually coupled with trans-membrane proton translocation. In both aerobic and anaerobic respiration, this generated PMF enables ATP synthesis through ATP synthase. If this PMF cannot be created, fermentation occurs instead. Fermentation occurs when there is no oxygen available and utilises substrate-level phosphorylation for ATP synthesis. Furthermore, during fermentation reduced NADH is regenerated back to NAD^+ enabling the cells to maintain their internal metabolism.

1.3.1 Electron transport chain

In microbial ETCs, electrons move from an electron donor with low redox potential to a more positive redox potential acceptor. Usually, membrane-bound enzymes catalyse these reactions by generating a transmembrane ion gradient, which subsequently drives ATP synthesis[27,28]. This way, bacteria successfully convert electrical potential differences into chemical energy[29,30]. As bacteria can be found in myriad environments, they have developed a variety of ETCs (Figure 1.3). Other players in the microbial ETC include electron-carrying co-factors such as heme, iron-sulfur (Fe-S) clusters, flavins and quinones. Some of these molecules are protein-bound catalytic co-factors (e.g., heme groups in cytochromes), whilst others (e.g., quinones) are soluble and lipophilic, and take part in the electron shuttle between large enzymatic complexes[30,31].

One of the byproducts of these ETCs is the generation of an increased proton concentration on one side of the membranes. The protons can then be transferred back through the membrane, a process that is catalysed by proteins. This leads to a concentration gradient being formed. Subsequently, a transmembrane motive force is established, which can drive ATP synthesis[30]. The difference in redox potential (ΔE) of reactions between terminal electron acceptor and donor determines the total energy gain (Gibbs free energy; ΔG) of each electron transport chain. Some bacteria can incorporate multiple ETCs and can even use them simultaneously as a response to different environmental electron donors and acceptors[29,30].

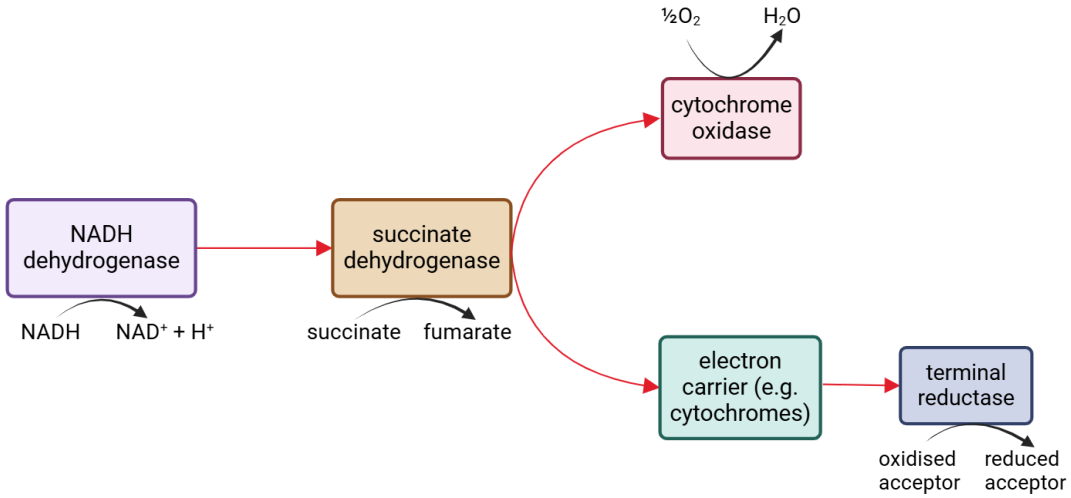

Figure 1.3. Overview of bacterial electron transport chain. In aerobic respiration, oxygen is the preferred terminal electron acceptor. During anaerobic respiration or fermentation, a variety of organic and inorganic compounds are used as the terminal electron acceptor. Red arrows indicate electron transfer.

The aforementioned respiratory overview occurs in eukaryotes (mitochondria) as well as bacteria and archaea. However, in bacteria and archaea, a wide range of (in)organic substrates can be used as electron acceptors or donors at several electrochemical potentials, driving the (an)aerobic respiratory ETCs of these microorganisms[32,33].

In most bacterial and mitochondrial ETCs, the connection between enzymatic electron donors and acceptors is via the quinone pool. Quinones are lipophilic, freely diffusible, small, membrane-bound organic molecules that can carry two protons and two electrons when fully reduced (quinol state). Varying electrochemical potentials can be seen in several types of quinones, and many bacteria are capable of synthesising more than one quinone type. Generally, when an organism can produce two quinone types, menaquinone [E'_0 (MK/MKH_2) ~ - 74 mV] is predominant under more reduced, anaerobic conditions, and ubiquinone [E'_0 (UQ/UQH_2) ~ + 110 mV] is predominant under aerobic conditions[34,35]. When speaking evolutionarily, menaquinones are considered to be more ancestral, with ubiquinones arising after with the increase in the oxygen concentration of Earth. This would explain why in *E. coli* ubiquinones (with a high redox potential) are expressed more in aerobiotic conditions where oxygen (with a redox potential of ~ + 810 mV) is the terminal acceptor so there is no need to have a quinone with a lower reduction potential. However, menaquinones (with a low redox potential) are expressed more in anaerobic respiratory chains where the quinone must have a

lower potential than the acceptor for the reaction to be thermodynamically viable[36,37].

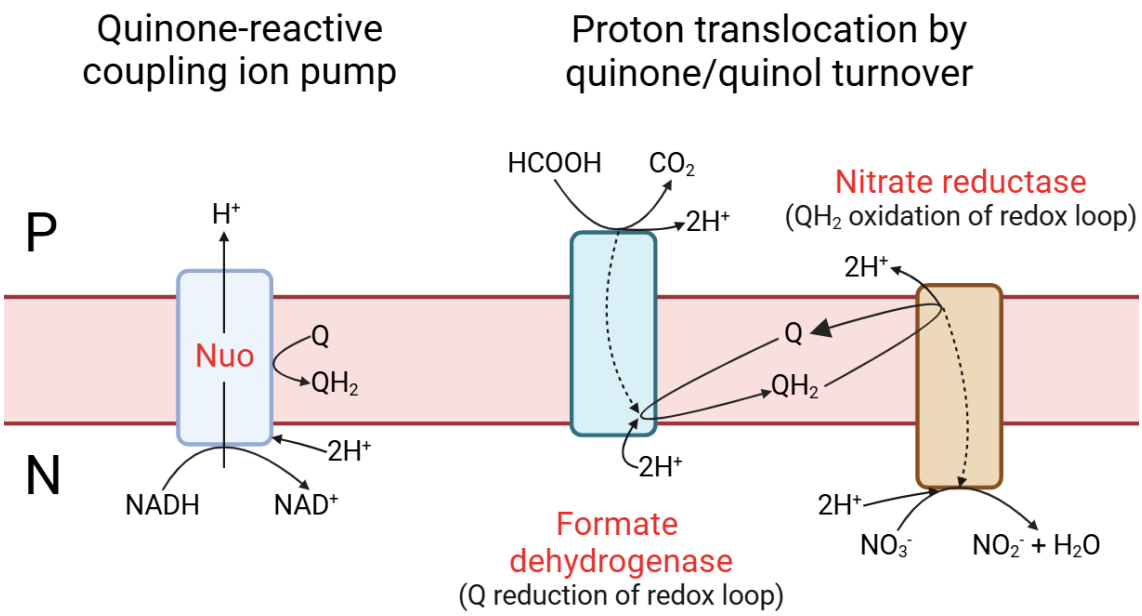

Figure 1.4. Proton motive force generation mechanism via intra/interenzymatic electron transport in *E. coli*. **Left.** Coupled ion pumping. **Right.** Quinone redox reactions coupled with proton translocation. Boxes represent the membrane-bound electron transfer enzyme complexes or enzymes, with their names shown in red text. (Nuo, NADH dehydrogenase). N and P represent the negatively and positively charged sides of the membrane, respectively. Black dashed arrows indicate electron transport. Created in BioRender.com and adapted from previous work[33,39].

The active sites of respiratory enzymes can be located at the P (positive) or N (negative) sides of the membrane across which PMF generation occurs (Figure 1.4). This also applies to the active sites of quinone/quinol turnover. These differing active site locations introduce particular considerations for mechanisms involved in the coupling of electron transfer (from donor to acceptor) to PMF generation. These considerations are addressed by the concept of redox loops, originally coined by Peter Mitchell's chemiosmotic hypothesis in 1961[33]. The principal feature of redox loops is the separation of negative and positive charges across an energy-conserving membrane. Involved proteins do not need to function as proton pumps in these charge separations . Rather, they function as components of the redox loops that enable the transmembrane electron flow from the P to the N side, ultimately contributing to the membrane potential section of the PMF via an electrogenic redox loop (Figure 1.4, right). The periplasm plays a key role for the location of many of these reactions. These redox loops are usually comprised of a quinone species functioning as a redox mediator between two quinone-reactive enzymes[33,38,39].

1.4 Respiratory mechanisms

1.4.1 Glycolytic pathways

The oxidation of glucose to pyruvate is a process that is independent of the availability of oxygen. Both aerobic and anaerobic organisms can metabolise the glucose by two different ways, the Embden-Meyerhof-Parnas (EMP) pathway, more commonly known as glycolysis, or the Entner-Doudoroff (ED) pathway. The ED pathway is also technically glycolysis, but the EMP pathway is usually referred to as glycolysis. Most eukaryotes use the EMP pathway to metabolise glucose, and even though some prokaryotes can use the EMP pathway, there is a higher diversity in prokaryotic glucose metabolism[40].

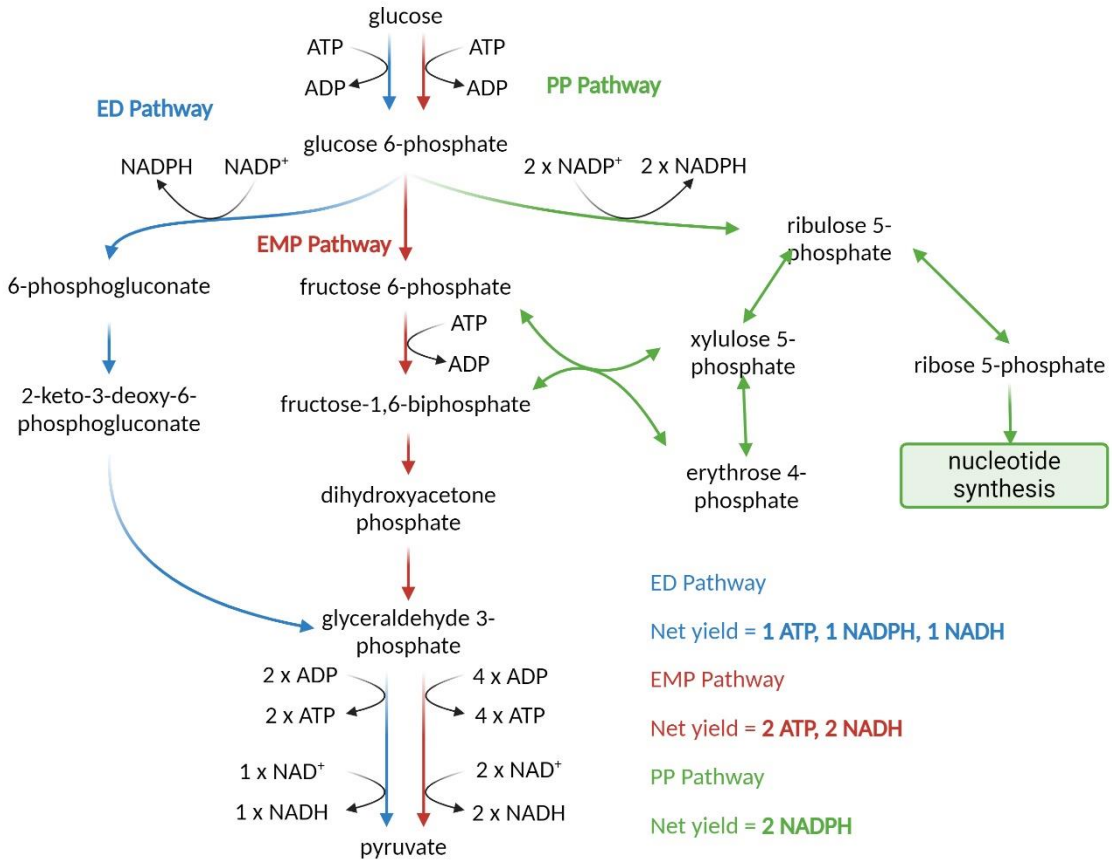

Figure 1.5. Diagram of the PPP, EMP and ED pathways, assuming that hexokinase phosphorylates glucose intracellularly and pyruvate is the final product. Created in BioRender.com and adapted from previous work[40,41]

A simplified overview of both pathways as well as the pentose phosphate (PP) pathway is shown in Figure 1.5. Some of the main roles that the PP pathway serves is to convert glucose 6-phosphate into ribose 5-phosphate while generating two NADPH molecules as well as interconverting the ribose 5-phosphate into other

glycolytic intermediates. The ribose 5-phosphate is an essential component of nucleotide synthesis, and the NADPH is an important player in the biosynthesis of important molecules like fatty acids, proline, and cholesterol[41].

The general steps in both EMP and ED pathways include phosphorylating glucose and then cleaving it into two 3-carbon molecules (pyruvate or lactate). These are then metabolised further to generate ATP. In the ED pathway, glucose is phosphorylated once and is oxidised to 2-keto-3-deoxy-6-phosphogluconate (KDPG) which is then cleaved resulting in one pyruvate and one glyceraldehyde 3-phosphate (G3P). In the EMP pathway, glucose can be phosphorylated twice and cleaved into G3P and dihydroxyacetone phosphate (DHAP). The DHAP is then quickly interconverted to G3P, resulting in 2 G3P molecules per glucose. In both pathways, the G3P can then be metabolised to pyruvate (or further to lactate) yielding 2 ATP molecules per G3P molecule. As the EMP pathway produced 2 G3P per glucose, the ATP yield is doubled to 4 ATP per glucose, as opposed to 2 ATP per glucose in the ED pathway. However, ATP is consumed during the initial oxidation of glucose to G3P. In the EMP pathway 2 ATP molecules are consumed as opposed to 1 ATP molecule in the ED pathway. Consequently, the EMP pathway has a net yield of 2 ATP per glucose, whilst the ED pathway has a net yield of 1 ATP per glucose[40,42].

Even though the EMP pathway yields twice the ATP as the ED pathway, the ED pathway is still common amongst prokaryotes. It is believed that its main goal is not to metabolise glucose but instead metabolise molecules like gluconate that cannot be metabolised by the EMP pathway. However, it is also believed that the ED pathway requires much less enzymatic protein than the EMP pathway to metabolise equal amounts of glucose per second[40]. The PP, ED, and EMP pathways all generate NAD(P)H which must be recycled back to $NAD(P)^+$ for the cell to reuse.

1.4.2 Aerobic respiration

Heterotrophic metabolism usually involves complete glucose oxidation by the following reaction: $C_6H_{12}O_6 + 6O_2 \longrightarrow 6CO_2 + 6H_2O + \text{energy}$. This process is also known as aerobic respiration. Respiration occurs through the complete oxidation of organic compounds, typically carbohydrates, resulting in the production of CO_2 and H_2O[12,24]. Primary dehydrogenases are important catalysts of these redox reactions,

which provide high-energy electrons from low reduction potential donors like NADH (~ -0.32 V vs SHE[43]).

These dehydrogenases normally couple Na^+ or H^+ transmembrane transport to electron transfer. Furthermore, membrane-localised (multi)protein complexes such as terminal oxidases (reductases) and cytochromes are also involved in ion transport across membranes. These protein complexes transfer electrons to terminal electron acceptors with a higher reduction potential such as fumarate (~ + 0.03 V vs SHE), nitrate (~ + 0.42 V vs SHE), or oxygen (~ + 0.82 V vs SHE)[30,43–45].

Bacterial oxidases catalyse redox reactions involved in electron transport chains. They can be classified into several groups by their electron acceptors and function. First, there are cytochrome *c* oxidases which are found in aerobic bacteria and play an integral role in the ETC and oxidative phosphorylation by catalysing the reduction of O_2 to H_2O while using cytochrome *c* as an electron donor. Next, there are quinol oxidases which are common in facultative anaerobes and bacteria that live in low oxygen conditions. These quinol oxidases use menaquinol or ubiquinol as electron donors instead of cytochrome *c*. Lastly, there are cytochrome bd oxidases, which have high affinity for oxygen, which enabling bacteria to grow in microaerophilic environments. These oxidases use quinol as the electron donor and are less efficient than other oxidases but play a critical role in low oxygen conditions[46].

1.4.3 Anaerobic respiration

The principial difference between aerobic and anaerobic respiration is that the latter uses electron acceptors that are not O_2. Even though oxygen is not the terminal electron acceptor, anaerobic respiration still employs the electron transport chain (unlike fermentation). Compounds used instead of oxygen by reductases from anaerobic microorganisms include, sulfate, fumarate, and nitrate amongst others[14,47]. Other groups of anaerobes include sulfate reducers and methanogens[48–50]. Examples of these are shown in Table 1.2[51]. Reduced NADH and $FADH_2$ (produced during glycolysis and the Krebs cycle) are still oxidised to produce an electrochemical proton gradient across a membrane. The reduced NADH and $FADH_2$ are oxidised by the membrane proteins with increasing reduction potentials until the electrons are donated to the terminal acceptor. Similarly to aerobic respiration, the protons can then pass through ATP synthase, resulting in the production of ATP[14,50,52]. While most organisms can use soluble electron acceptors

to remove the electrons from the ETC, some cannot and therefore need to transport these electrons outside of the cell. This is done by extracellular electron transfer.

Table 2.2. Features of characterised anaerobic respiratory systems. Adapted from previous work[47,51].

e^- acceptor	Enzyme involved	Organism	Respiratory process
NO_3^-	Nitrate reductase	*E. coli*	Nitrate reduction
NO_2^-	Nitrite reductase	*Thiobacillus denitrificans*	Denitrification
N_2O	Nitrous oxide reductase	*Paracoccus denitrificans*	Denitrification
SO_4^{2-}	APS reductase	*Desulfovibrio vulgaris*	Sulfate reduction
Fumarate	Fumarate reductase	*Proteus rettgeri*	Fumarate reduction
DMSO	DMSO reductase	*E. coli*	DMSO reduction
AsO_4^{3-}	Arsenate reductase	*Shewanella* sp. ANA-3	Arsenate reduction
SeO_4^{2-}	Selenate reductase	*Thauera selenatis*	Selenate reduction
ClO_3^-/ClO_4^-	(per)chlorate reductase	*Dechloromonas*	(per)chlorate reduction
Fe(III)	Multiheme cytochrome	*Shewanella oneidensis*	Fe(III) reduction
Mn(IV)	Multiheme cytochrome	*Shewanella oneidensis*	Mn(IV) reduction
CO_2	Coenzyme-bound C_1 intermediates	*Clostridium aceticum*	Acetone metabolism

1.4.4 Fermentation

In fermentation, an organic compound is required as a terminal electron (or hydrogen) acceptor. For fermentation to occur, anaerobic dissimilation of glucose (and other compounds) leads to the generation of simple organic products. The produced energy (ATP) is generated from the dehydrogenation reactions that happen during the enzymatic breakdown of glucose. This incomplete biological oxidation produces simple organic end products which serve as the terminal electron/hydrogen acceptors. Upon reduction, these products are secreted into the media as waste metabolites (usually acids or alcohols). Even though the organic substrates are not fully oxidised by the bacteria, they produce enough energy for bacterial growth. Many microbial fermentations (especially the ones used in biotechnological processes) involve glucose breakdown through the glycolytic pathway. The most common compound generated is pyruvate (or derivatives such as lactyl-CoA, acetyl-CoA, acetaldehyde, or α-acetolactate) in most organisms, or ethanol in yeast[14,15,32]. Fermentation is also important as it allows for the regeneration of NAD^+ from NADH. If this process did not occur, then the intracellular NADH concentration would rise to lethal levels.

Bacteria that rely solely on fermentation cannot produce as much energy as anaerobically-respiring cells. In aerobic respiration, 30-32 ATP molecules can be generated from 1 molecule of glucose. In fermentation, however, only 2 ATP molecules are produced by these ethanolic and lactate fermentations. Yet this is enough energy to enable anaerobic growth of ethanolic fermenting yeast such as *Saccharomyces cerevisiae*, and lactic acid bacteria such as *Lactobacillus casei*. In contrast with respiration, fermentative ATP generation relies solely on substrate-level phosphorylation, which are catalysed by pyruvic kinases and phosphoglycerokinases[14].

1.5 Respiration using extracellular electron transfer

Electrogenic organisms can transfer electrons to or from electrodes, producing an electric current. The direction of electron flow can vary, allowing these organisms to release/accept electrons into/from their environment, providing electrogenic bacteria the capacity to live in a variety of environments. These organisms are not defined by their physiological, taxonomical, or other biological characteristics, and are considered a highly heterogenous group of organisms. However, with more characterisation of new electrogenic organisms and systems, the line between electrogenic and non-electrogenic organisms becomes less concrete. Bacteria from the *Shewanella* and *Geobacter* genera were some of the original organisms that were investigated for their EET capabilities. Now, many others have been identified. There is growing interest in electrogenic organisms as they show promise for their role in microbial fuel cell (MFC) generators[53].

Bacteria use the extracellular electron transfer (EET) process to shuttle electrons to/from extracellular solid materials (such as electrodes or minerals). These bacteria can be classified as metal-reducing or metal-oxidising bacteria. EET utilises redox potential differences of chemical compounds and converts them into bioavailable energy, usually as ATP. Electrogenic organisms use more than just organic compounds and oxygen as electron donors and acceptors, respectively. Some microorganisms can use oxidised inorganic compounds (CO_2, sulfates, nitrates) as electron acceptors, and reduced inorganic compounds (H_2, ammonia, sulfides) and donors[54]. Others, use solid materials, such as electrodes and minerals [e.g. Fe(III) and Mn(IV)] as respiratory substrates.

However, microorganisms cannot take in these solid substrates, therefore, several extracellular molecular mechanisms are essential for EET. These mechanisms can be divided into indirect and direct EET. In indirect EET, electron mediators (low-molecular, redox-active compounds) serve as electron shuttles between the extracellular solid material and the microbial cells. Electron mediators that are reduced by the microorganisms can diffuse and donate electrons to the solid substrates. The newly oxidised mediators can then be re-reduced by the cell, cycling as respiratory substrates[54,55]. Some of the most common electron mediators include flavin derivatives and phenazine compounds, which contribute to indirect EET. The flavin derivatives are recycled and reused on the outside of the cell[56], while the phenazine compounds are taken up by the bacterial cells[57].

In direct EET, microorganisms can attach to the solid surfaces and exchange electrons directly with the solid substrate. Direct EET mechanisms have been extensively researched in model organisms such as the iron-reducing bacteria *Geobacter sulfurreducens* and *Shewanella oneidensis*[58], and iron-oxidising bacterium *Acidithiobacillus ferrooxidans*[59].

Another key component of direct and indirect EET in many microorganisms is the redox-active *c*-type cytochrome (*c*-Cyt). These periplasmic cytochromes link the IM and OM, and facilitate electron hopping through them, connecting external surfaces to the respiratory chain[54]. Moreover, *S. oneidensis*[60] can use extracellularly secreted flavin compounds associated with their OM *c*-Cyts to accelerate direct EET to solid substrates[54]. Furthermore, *Shewanella* spp. and *Geobacter* spp. can also produce extracellular bacterial biowires (structures that could be categorised as both direct and indirect mechanisms, or perhaps form part of a novel third category)[61].

1.6 Mineral respiration using EET

There are many microorganisms that can transfer electrons to/from extracellular minerals (such as iron and manganese) through the EET via various structural and redox proteins. In the Shewanella genus, these multiheme proteins are well characterised. These proteins are responsible for the connection between the extracellular redox reactions and regular intracellular metabolic processes[62]. Several of these electron-transferring proteins lie within the outer membranes. Consequently, they must be well insulated (inside porin complexes) to minimise the chance of electrons being donated to the wrong acceptor. However, as the components of these EET pathways can be phylogenetically diverse, the genomic data does not always allow for the identification of these components[58]. Figure 1.6 shows a schematic for the electron pathways in mineral respiration using EET (left) and aerobic respiration using EET (right) bacteria.

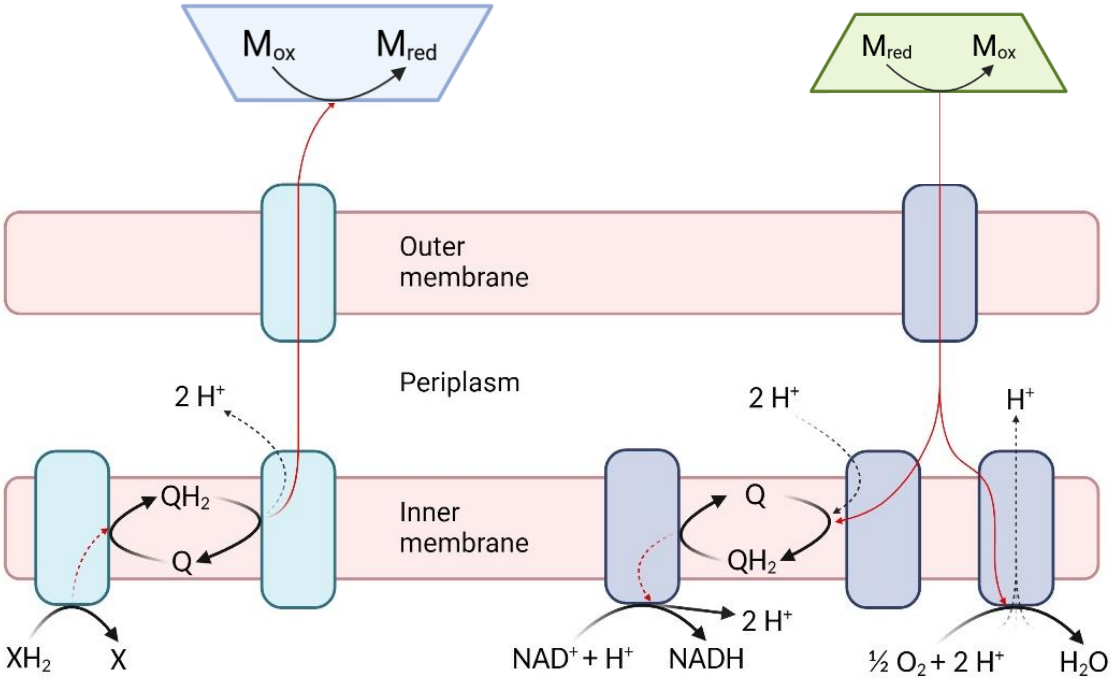

Figure 1.6. Representation of electron transport bacteria that use EET in respiration. **Left.** Mineral respiration using EET. Bacteria use quinone reductase in the IM to transfer electrons into the quinol pool. Periplasmic quinol dehydrogenases oxidise quinol, and electrons pass through the periplasm and across the OM to extracellular terminal electron acceptors (M_{ox}). **Right.** Aerobic respiration using EET. Bacteria oxidise iron, and electrons are transferred via two separate pathways: into the quinol pool for NADH synthesis, or into oxidases to produce proton motive force. Red lines indicate electron transfer, black dashed lines represent proton movement, and red dashed lines indicate electron and proton transfer. Adapted from previous work[27].

1.6.1 Electrosynthesis in microorganisms

In microbial electrosynthesis, microorganisms convert electrical energy into chemical fuel via CO_2 fixation. It is suggested the synthesis of multi-carbon compounds via microbial CO_2 fixation requires fewer steps than inorganic-based methods. These multi-carbon compounds can then be used to produce chemicals or transportation fuels[63]. Some of the principal candidates for microbial electrosynthesis are acetogenic bacteria, which are proposed to act as catalysts in chemical fuel production from CO_2. Acetogenic bacteria such as *Sporomusa* spp., *Clostridium* spp., and *Moorella thermoacetica* have shown the ability to produce multi-carbon chemicals (like 2-oxobutyrate and acetate) by using electrical energy. Usually, these bacteria use the energy released from acetate production from CO_2 to produce these multi-carbon compounds, but these bacteria have been shown to use poised electrodes as sole electron donors[63]. By genetically engineering the metabolism of these acetogenic bacteria[64], and improving the materials and production of cathodes[65], microbial electrosynthesis systems show promise as alternatives to inorganic-based multi-carbon production[54].

1.6.2 Gram-positive bacteria

As Gram-positive bacteria have a thick layer of peptidoglycan in their cell wall (Figure 1.2), it had been proposed that they would not be able to carry out extracellular electron transfer[66]. However, the ability to carry out ETC was confirmed with the successful isolation of *Thermincola potens* JR from a current-producing MFC that was functioning at high temperatures[67]. Furthermore, *T. ferriacetica*, a species with 99% similarity to *T. potens*, also displayed the ability to transfer electrons from acetate to an MFC anode, ultimately generating an electric current[68]. Similarly to most electrogenic microorganisms, *T. potens* contains various genes in its genome that code for multiheme *c*-type cytochromes (MHCs)[69]. Several of these genes have been proposed to be involved in in extracellular electron transfer[70].

The putative ETC pathway for *T. potens* and *T. ferriacetica* was hypothesised to be comprised of four proteins (named Tfer_ in *T. ferriacetica* and TherJR_ in *T. potens*): an IM-anchored decaheme cytochrome (Tfer_0070 and TherJR_1117), suggested to accept electrons from the menaquinone pool; a decaheme cytochrome found in the periplasm (Tfer_1887 and TherJR_0333), suggested to transport electrons

through the periplasm of the *Thermincola* species; a peptidoglycan-embedded hexaheme cytochrome (Tfer_0075 and TherJR_1122); and a cell surface-localised nonaheme cytochrome (Tfer_3197 and TherJR_2595), suggested to act as the terminal reductase[71]. However, only the cell surface MHC was characterised, and was then named OcwA, the outer cell-wall cytochrome A[71,72].

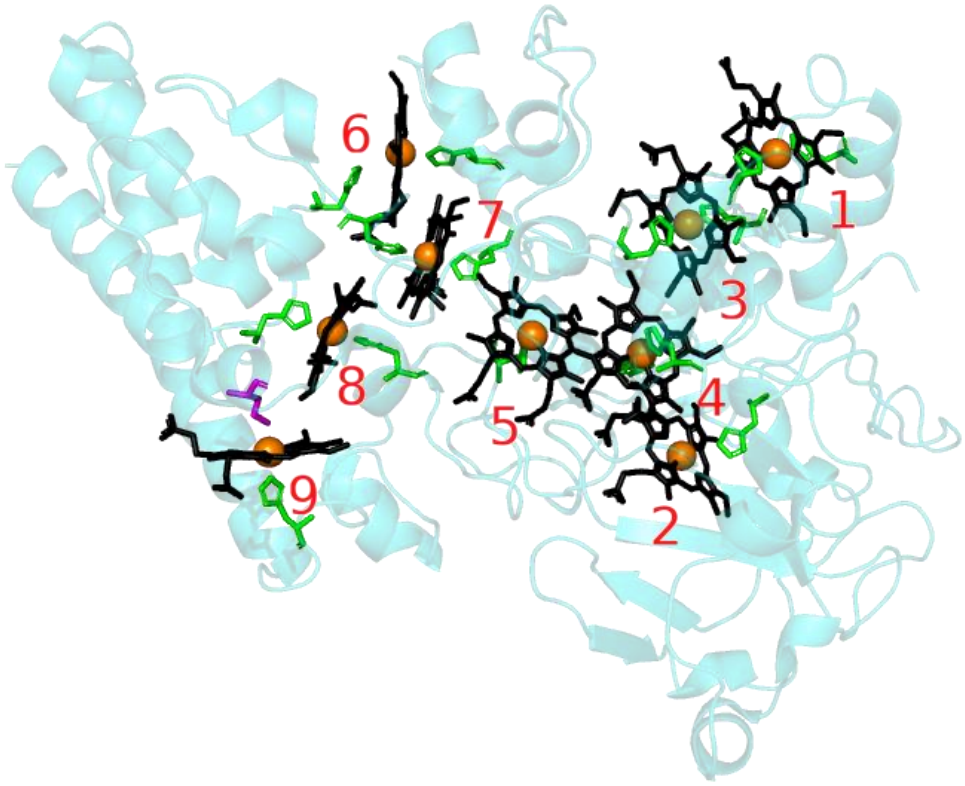

Figure 1.7. Heme arrangement of OcwA from *Thermincola potens* JR. The protein is represented as a cartoon in cyan. Hemes are numbered in red according to the CXXCH binding motif order in the amino acid sequence. The hemes are shown in black, with the iron cores shown as orange spheres. Methionine is shown in purple, and histidines in green. Image produced in PyMOL using the hemes of MtrC (PDB: LI5B) as a template.

Unlike other known insoluble compound terminal reductases, OcwA is comprised of hemes with differing axial ligand coordination: hemes 1, 3, 4, 6, 7, and 8 have the characteristic His/His axial coordination; heme 9 has a His/Met coordination; and hemes 2 and 5 contain histidine as their proximal ligand, but at the distal ligand position contain an open coordination side (Figure 1.7). Hemes 2 and 5 are positioned at opposite ends of the heme chain and have been shown to be high-spin hemes, with many unpaired electrons. Furthermore, these two hemes are proposed to act as putative substrate-binding active sites, a novel feature within the MHC family[71,72].

Heme organisation in OcwA somewhat resembles the “staggered cross” found in the OM cytochromes of the four main clades of *Shewanella*. However, it is apparent that the design is different to the “staggered cross” and is actually similar to the pentaheme NrfA (*c*-Cyt nitrite reductase) family of proteins[71]. Hemes 1-4 align with the hemes from the *Nitrosomonas europaea* tetraheme cytochrome c_{554}, while heme 2 acts as the active site. However, hemes 5-9 can be superimposed to the heme core from NrfA, with OcwA heme 5 functioning as the active site. Moreover, hemes 1-4 and 6-9 can be aligned to the MccA (sulfite reductase) heme core structure, with heme 2 functioning as the active site. Furthermore, OcwA has also been shown to reduce hydroxylamine and nitrite (as well as iron oxides), emphasising the suggested versatile role the protein plays in the ETC and respiratory processes of *Thermincola* spp[71,72]. Ultimately, OcwA grants these Gram-positive bacteria the ability to inhabit environments with differing terminal electron acceptors, providing a competitive evolutionary advantage.

1.6.3 Gram-negative bacteria

1.6.3.1 Porin cytochrome complexes

For Gram negative bacteria to use extracellular substrates as their terminal electron acceptors, the electrons need to be transferred across the OM. Usually, a porin (transmembrane β-barrel protein) or porin-like protein is involved in this transfer, insulating the characteristic *c*-Cyt protein through which the electrons travel to/from the terminal electron acceptor/donor, respectively (Figure 1.8)[73,74]. These

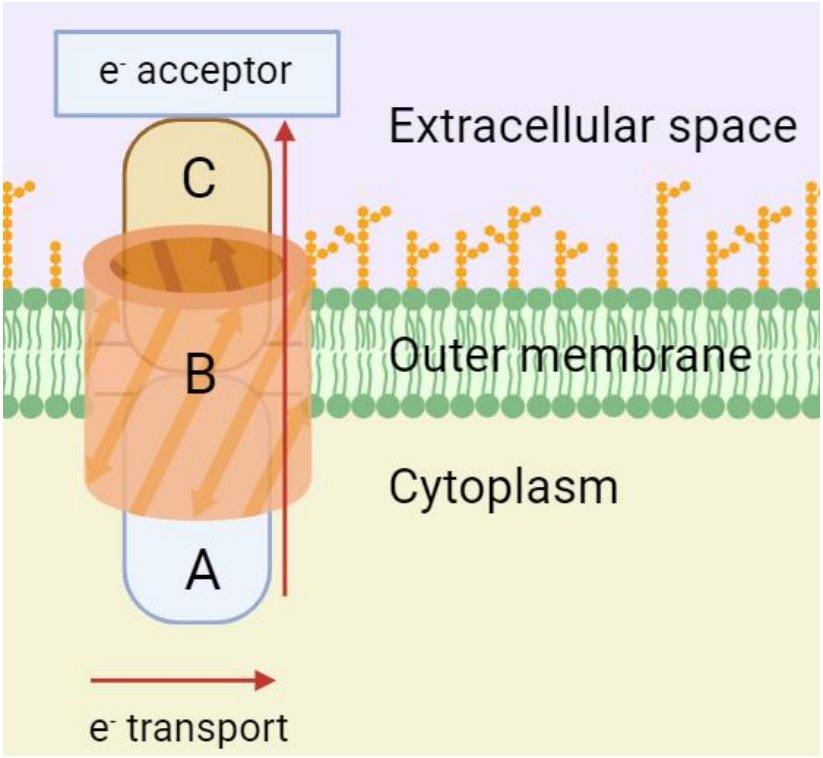

Figure 1.8. Suggested Pcc model of dissimilatory metal-reducing bacteria comprised of an outer-membrane heterotrimer. Protein A and C represent multiheme cytochromes, with one of them usually embedded in protein B, a porin. Figure created in BioRender.com and adapted from previous work[75].

complexes are known as porin cytochrome *c* (Pcc) protein complexes and are usually trans-OM complexes which link the IM quinone/quinol pool, across the periplasm and OM, to the extracellular substrates. Even though each metal-respiring/oxidising bacteria has its own Pcc gene cluster, the most researched organisms show some homology across their Pcc gene clusters[74]. Model Pcc proteins include MtrCAB from *S. oneidensis*, OmaB/OmbB/OmcB from *G. sulfurreducens*, and PioAB from *R. palustris*.

However, the *Shewanella* and *Geobacter* Pcc protein complexes are phylogenetically distant even though they carry out almost identical functions,

suggesting that Mtr and Pcc proteins might have evolved convergently[75]. This independent evolution of the Pcc and Mtr complexes (with observed organisational and functional identities) establishes the prevalence of Pcc mechanisms used in EET in Gram-negative bacteria. Furthermore, *pcc* gene clusters exist in microorganisms that are incapable of Mn(IV) and Fe(III) solid-phase reductions, such as *Desulfurivibrio alkaliphilus* AHT2 and *Ignavibacterium album* JCM 16511. This suggests that these *pcc* genes could play a role in EET reactions that use substrates other than Mn(IV) and Fe(III) oxides[74,75].

1.6.3.2 Metal oxidation in *Sideroxydans lithotrophicus*

S. lithotrophicus is a well-characterised organism that is used as a model for autotrophic growth on metals. At a circumneutral pH (~7), *S. lithotrophicus* ES-1 can oxidise Fe(II) to produce energy for autotrophic growth (Table 1.1)[76]. Genetic analyses show that *S. lithotrophicus* contains an *mto* gene cluster in its genome. This cluster contains *mtoD* (monoheme *c*-Cyt-coding gene), *mtoB* (homologue of *mtrB*), *mtoA* (homologue of *mtrA*), and *cymA*[77,78]. In MtoA, the distal ligands for all ten hemes are His, like in MtrA[79]. MtoA can directly oxidise Fe(II) or Fe(II)-containing minerals in the extracellular environment. Next, MtoD (a periplasmic *c*-Cyt) is proposed to be involved in the transfer of electrons from MtoA, in the OM, to CymA, in the IM[80,81]. Therefore, it is proposed that CymA, MtoD, MtoB, and MtoA produce a pathway that connects the oxidation of extracellular Fe(II) and Fe(II)-containing minerals to the reduction/oxidation of quinone/quinol, respectively, in the IM of *S. lithotrophicus* ES-1[62,81]. Transcriptomic analyses[82] have suggested that the genome of *S. lithotrophicus* ES-1 contains another putative Fe(II) oxidase, Cyc2. Cyc2 is a homolog of the Fe(II) oxidase identified in *Mariprofundus ferrooxydans* and *Acidithiobacillus ferrooxydans* and is present in a wide variety of microaerophilic iron oxidising bacteria. Their results state that *cyc2* expression levels were greater than *mtroA* when grown in the presence of Fe(II). Particularly, the *cyc2_1* gene was one of the most expressed genes (in the top 99th percentile). These results highlight the importance that Cyc2 plays in ferrous iron oxidation in *S. lithotrophicus* ES-1. Similarly, another investigation[83] was done to compare the relative expression of *mtoA* and *cyc2* when the *S. lithotrophicus* ES-1 were grown in the presence of Fe(II)-smectite. Similarly, their results indicate a significant expression of Cyc2 and MtoAB when grown with the smectite. These results corroborate the importance

that MtoAB in iron oxidation in *S. lithotrophicus* ES-1, but also the probable role that Cyc2 plays as well. Alongside MtoAB and Cyc2 the genome of *S. lithotrophicus* ES-1 contains other multiheme cytochrome genes. This variety of multiheme proteins allow the bacteria to successfully oxidise a variety of iron-containing substrates[82,83].

1.6.3.3 Metal oxidation in *Rhodopseudomonas palustris*

R. palustris TIE-1 is a bacterium capable of phototrophic Fe(II)-oxidation. Phototrophs use solar electromagnetic radiation (in the visible light spectrum) to synthesise organic compounds. *R. palustris* TIE-1 uses sunlight as an energy source and Fe(II) as an electron donor when fixing CO_2[84].

A *pio* gene cluster is present in the genome of *R. palustris* TIE-1 (Figure 1.9). This gene cluster is homologous to the *mtr* cluster from *S. oneidensis* and is comprised of *pioC* (coding for a high potential iron-sulfur protein), *pioB* (homologue of *mtrB*), and *pioA* (homologue of *mtrA*). The *pioB* gene product is predicted to be comprised of ~ 800 amino acids, whereas the *pioA* gene product is predicted to be larger than MtrA (300 residues) as it comprised of ~ 540 amino acids. However, the PioA N terminus undergoes post-secretory proteolysis, resulting in a mature functional *c*-Cyt with a comparable size to MtrA[85,86].

Mutants with deleted *pioC, pioB, pioA,* as well as those without the whole *pio* gene cluster, experimentally displayed a decreased capability to oxidise and/or grow on Fe(II). All these mutants also had reduced capacities when accepting electrons from extracellular electrodes[85,87]. It is suggested that PioB and PioA oxidise extracellular Fe(II), and that the released electrons are then transported across the OM to PioC, which is proposed to be located in the periplasm (Figure 1.9). Next, PioC is believed to transfer the incoming electrons in a light-dependent way to a

photoreaction centre in the IM. Then, these electrons are proposed to be involved in carbon fixation from CO_2 to fixed carbon[62,73].

Even though PioA is a homologue of MtrA, the two proteins have evolved differently to allow for electrons to be transported into the cell or out of the cell, respectively.

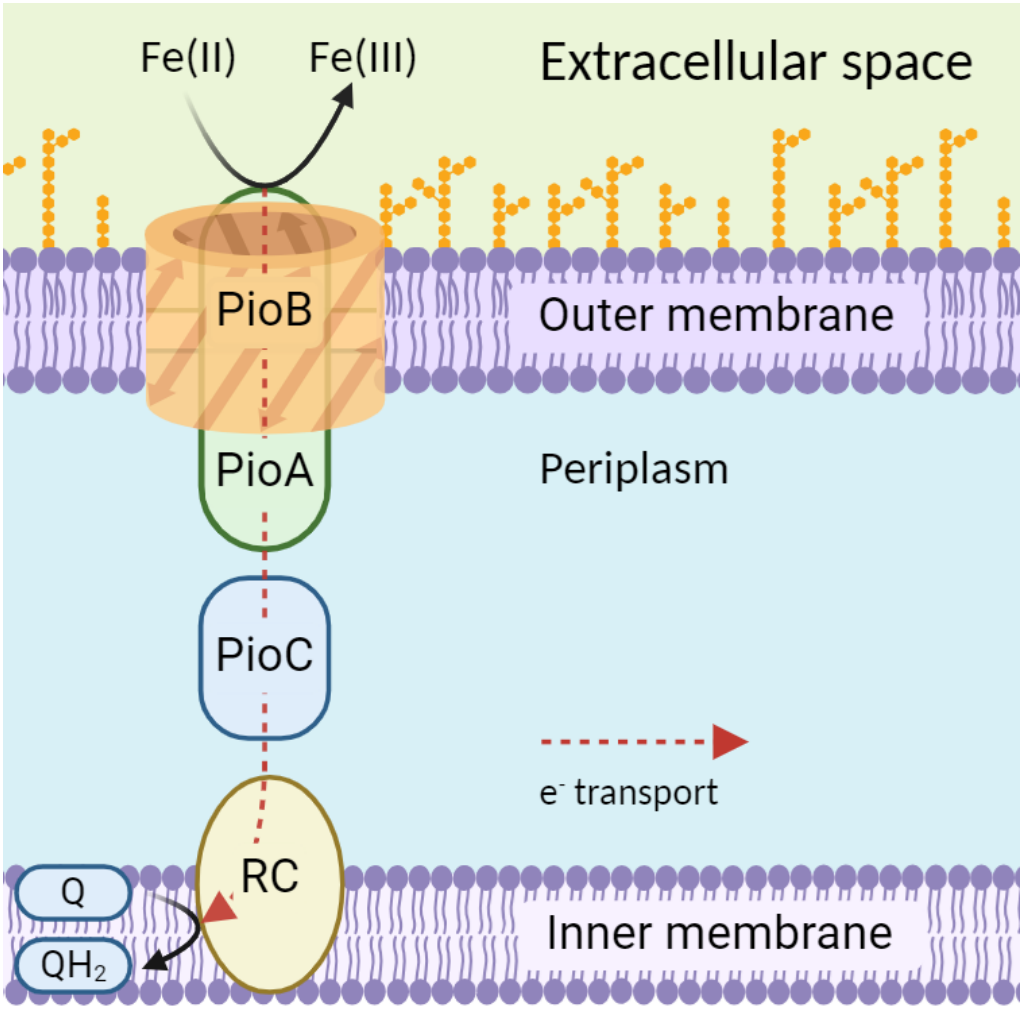

Figure 1.9. Proposed EET pathway in the Pio complex of *Rhodopseudomonas palustris* TIE-1. A schematic representation of electron transport from extracellular Fe(II) oxidation to photoreaction centre (RC) is shown. Red dashed arrows indicate electron transport. Q (reduced quinone), QH_2 (oxidised quinone). Created in BioRender.com and adapted from previous work[62].

Furthermore, there are other properties that differentiate PioA and MtrA, such as the heme axial ligand coordination. MtrA, MtrC, STC, and OmcA from *Shewanella* spp. have been shown to have His/His ligation throughout their hemes[88]. Conversely, recent studies have found that PioA in *R. palustris* has His/H_2O and His/Met ligated hemes, as opposed to His/His ligated hemes[79]. As homologues, PioA and MtrA display high sequence similarity between themselves, and also show identical distribution of the ten CXXCH *c*-heme binding motifs throughout the polypeptide. The model facilitates molecular-level insight into PioA and has revealed that adjacent PioA hemes are located close to each other and that they

have oscillating configurations of parallel and perpendicular porphyrin ring planes[79].

MtrA from *S. oneidensis* and MtoA (homologue of MtrA) from *Sideroxydans lithotrophicus* both display His/His ligation in all ten hemes in the polypeptide chain. However, the natural electron flow direction is opposite in MtoA. In PioA, the electron flow direction is the same as MtoA, regardless of having three His/Met ligated hemes. These findings suggest that the direction of electron flow in decaheme *c*-Cyts is not entirely determined by the distal ligands ligated to the hemes[79,86]. Nonetheless, His/Met ligation plays a vital role in the redox activity of PioA, allowing it to function at more positive potentials than MtrA and MtoA[79]. Li *et al.*[79] have hypothesised that the PioA hemes with His/Met ligation could possibly store the Fe(II) oxidation electrons temporarily before passing them onto PioC, which is suggested to be the immediate donor to the IM reaction centre[79,89].

1.6.3.4 Metal reduction in *Geobacter sulfurreducens*

G. sulfurreducens is a model organism used to study dissimilatory metal reduction. In *G. sulfurreducens* PCA and *G. sulfurreducens* DL-1, MHCs are also involved in transmembrane electron transport during reduction of extracellular Fe(III)-containing minerals. However, as there are many different cytochromes involved, the precise mechanism for electron transfer to solid surfaces is not fully understood. This is partly because these varied cytochromes have overlapping functions, which are proposed to enable *Geobacter* to react more proficiently to differing redox potentials[90]. The Pcc complex in *G. sulfurreducens* is comprised of a dodecaheme *c*-Cyt (OmcB/OmcC), an octaheme *c*-Cyt (OmaB/OmaC), and a porin-like protein (OmbB/OmbC). Identified MHCs can be classified by their cellular localisation: OmcB, OmcC, OmaB, and OmaC in the OM (similarly to *S. oneidensis* MR-1); PpcA and PpcD in the periplasm; and ImcH and CbcL (quinol dehydrogenases) in the IM[62,72,91,92]. OmaB/OmaC can also be considered periplasmic, as they connect the OM to the periplasm[93]. Both ImcH and CbcL are constitutively expressed and are involved in anaerobic respiration. ImcH is necessary for extracellular respiration of substrates with a potential greater than -100 mV vs SHE, whilst CbcL interacts with extracellular substrates with lower potentials[92].

Alongside OmbB and OmbC, the aforementioned OM MHCs form a trans-OM Pcc complex. This Pcc complex and MHCs are believed to mediate electron transport from the quinol/quinone pool in the IM, through the periplasmic space, and across the OM to the bacterial surface where they can interact with extracellular terminal electron acceptors. However, there are over five other gene clusters that encode for distinct Pcc complexes in *G. sulfurreducens* PCA. One of these other complexes has demonstrated the capacity to transport electrons across a lipid bilayer *in vitro*, while two others have been demonstrated to be functionally active[93]. *Geobacter* does not appear to contain any tetraheme electron shuttles like STC in *S. oneidensis* nor any flavoproteins like FccA (fumarate reductase). However, *Geobacter* instead has five tri-heme c_7 type cytochromes that are highly homologous between themselves: PpcA, PpcB, PpcC, PpcD, and PpcE. These Ppc cytochromes all cover similar redox potential ranges and contain highly conserved structures but display minor redox potential differences amongst their individual hemes. It is suggested that these redox potential differences in the hemes allow *Geobacter* spp. to vary the periplasmic electron flow depending on which extracellular electron acceptor is present[72,94]. Additionally, *G. sulfurreducens* PCA and DL-1 both contain two more transmembrane Pcc complexes as well as three other periplasmic PpcA and PpcD homologues. Therefore, these two strains contain several electron transfer pathways that can operate in parallel, and that are essential for the extracellular reduction of Fe(III)-containing minerals[62,91–93,95].

Furthermore, Pcc homologues have been discovered in all the sequenced *Geobacter* species as well as in bacteria from different phyla, including *Thermovibrio ammonificans* HB-1, *Desulfurispirillum indicum* S5, and *Ignavibacterium album* JCM16511 amongst others. These findings suggest that Pcc-like proteins and protein complexes in all these bacteria play a key role in the reduction of extracellular substrates, namely Fe(III)- and Se(IV/VI)-containing minerals, contributing considerably to the evolutionary fitness of the bacteria[62,74,75].

1.7 Shewanella oneidensis as a model for EET

Previously known as *Alteromonas putrefaciens* MR-1, *Shewanella oneidensis* MR-1 is a facultative, non-fermentative anaerobe which can respire many substrates as terminal electron acceptors. These include soluble metals, oxygen, organic compounds, inorganic compounds, and electrodes[96]. *S. oneidensis* MR-1 was one of the first bacteria to be identified that could use Mn(III)-, Mn(IV)-, and Fe(III)-containing minerals as its terminal electron acceptors[97]. Analyses on central metabolism and metabolic end products of *S. oneidensis* has revealed that the principial product under anaerobic conditions is acetate[96] and under aerobic conditions is CO_2. For both aerobic and anaerobic conditions, the starting substrates can be either D-lactate or *N*-Acetylglucosamine (NAG). *S. oneidensis* can produce pyruvate by oxidising lactate, yielding either NADH (if catalysed by lactate dehydrogenase A) or a reduced quinone (if catalysed by D-lactate dehydrogenase)[98–101] As lactate can be directly oxidised to pyruvate, it is used in experiments with *S. oneidensis* cells. NAG oxidation to pyruvate requires more intermediate steps as well as costing one ATP molecule[102].

1.7.1 Metabolic mechanisms

Under aerobic conditions (Figure 1.10, bottom), the pyruvate is converted into Acetyl-CoA (catalysed by pyruvate dehydrogenase), yielding CO_2 and NADH. The Acetyl-CoA then enters the tricarboxylic acid (TCA) or Krebs cycle where it is completely oxidised to CO_2, also yielding 3 NADH, 2 CO_2, 1 $FADH_2$, and 1 ATP molecules[96,100,103]. The electrons generated during these steps are transferred to the terminal oxidases in the ETC to generate PMF, driving oxidative phosphorylation and ATP synthesis.

S. oneidensis MR-1 expresses several oxidases: a *bd*-type quinol oxidase, two cytochrome *c* oxidases (aa_3- and cbb_3-type) as well as an intermediate bc_1 complex (ubiquinol:cytochrome *c* oxidoreductase)[104]. During aerobic respiration, it is proposed that the bc_1 complex transfers electrons to both aa_3- (aerobic conditions) and cbb_3-type (microaerobic conditions) terminal oxidases from the quinone pool. It is also proposed that when the oxygen concentration is low, the *bd*-type quinol oxidase can directly oxidise quinol and reduce oxygen. Regardless of the oxidase used to reduce oxygen, PMF is generated via charge separation across the membrane[104–106].

Mutants lacking the *cbb*$_3$-type cytochrome oxidase had a slower growth when compared to the WT, while mutants deficient in *bd* quinol oxidase had no significant change in their growth, suggesting the *cbb*$_3$-type enzyme plays a larger role as the terminal oxidase under aerobic conditions[107–110]. Furthermore, during aerobic growth ATP production is suggested to be largely done via ATP synthase and using PMF. When mutants lacking the ATP synthase operon were grown aerobically, their growth was severely impaired when compared to the WT cells. When these mutants were complemented with the WT operon again, the growth under aerobic conditions was restored[96], indicating that oxidative phosphorylation via ATP synthase was the principal mechanism for aerobic growth.

Under anaerobic conditions (Figure 1.10, left) the pyruvate can be converted into Acetyl-CoA (catalysed by pyruvate formate lyase) also yielding formate as a product. Next, the Acetyl-CoA is converted into acetylphosphate (catalysed by phosphate acetyltransferase) before being converted into acetate (catalysed by acetate kinase) which yields 1 ATP molecule. The formate produced earlier during the conversion of pyruvate to Acetyl-CoA traverses the inner membrane through FocA, a bidirectional formate transporter, into the periplasm. The formate is oxidised to produce CO_2 and H^+ (catalysed by formate dehydrogenase), and the electrons yielded from this reaction enter the menaquinone pool. These electrons can enter the menaquinone pool directly or indirectly depending on which lactate dehydrogenase is used as D- and L- lactate are metabolised via different systems by *S. oneidensis*[96]. The electrons are then transferred onto the tetraheme cytochrome, CymA, before being passed on to fumarate reductase, FccA. Here fumarate + 2 H^+ are reduced to succinate. Therefore, the oxidation of lactate or pyruvate (as the sole energy and carbon source) is considered to be coupled to the reduction of fumarate[96,99,101,103,111]. These electrons can then be transferred from FccA to extracellular electron acceptors via the Mtr pathway.

ATP synthesis during anaerobic growth is done primarily by substrate-level phosphorylation. Mutants that lacked the ATP synthase operon displayed only a minor growth deficiency when compared to the WT, and successfully oxidised either lactate or NAG to acetate as well as reducing fumarate to succinate[96]. Moreover, mutants that lacked phosphotransacetylase and acetate kinase (both required for substrate-level phosphorylation) showed a decrease in growth and

electrode current production[112], again establishing the significant role that substrate-level phosphorylation plays under anaerobic conditions.

The Mtr pathway of *S. oneidensis* is one of the most understood and characterised microbial EET pathways. Homologues of Mtr have been identified in all sequenced *Shewanella* spp. and have also been found in Fe(II)-oxidising and other metal-reducing bacteria, such as *Sideroxydans lithotrophicus*, *Rhodopseudomonas palustris* TIE-1, and *Rhodoferax ferrireducens*[62,77,85].

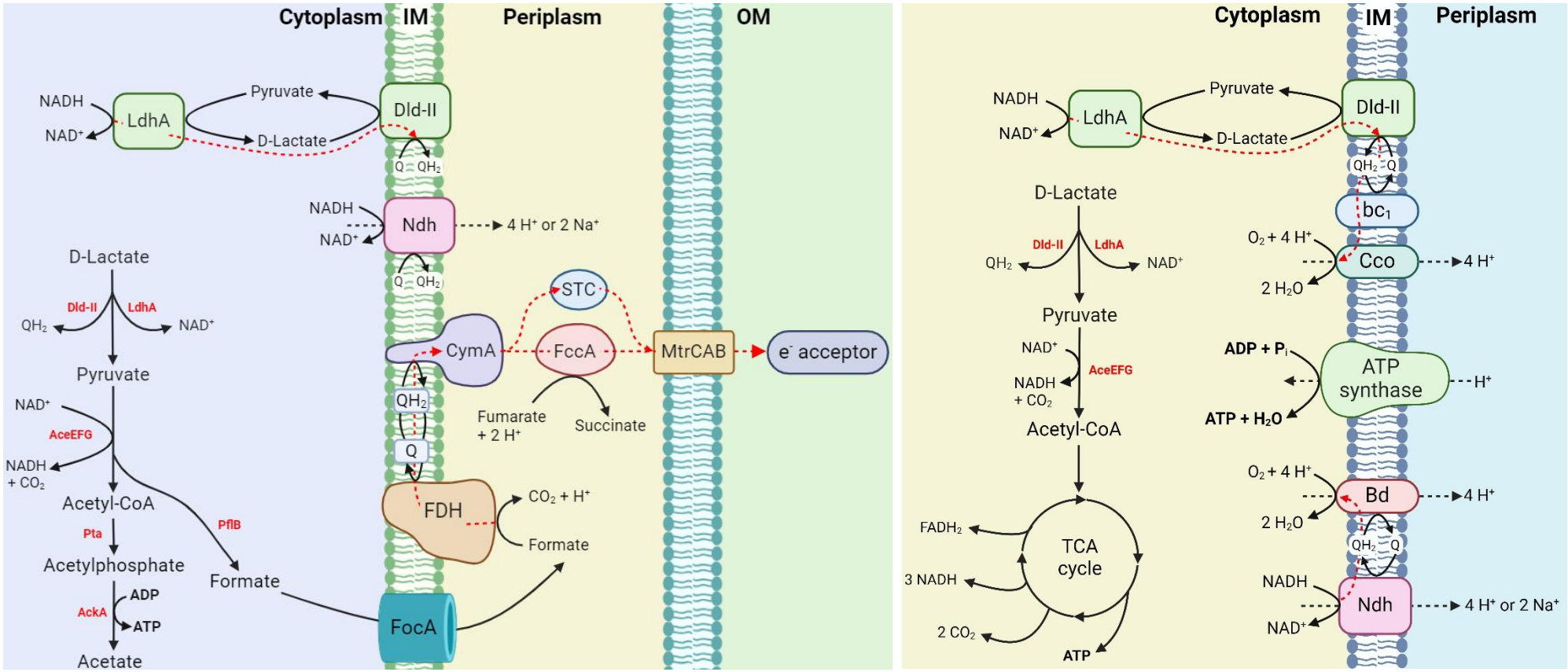

Figure 1.10. Simplified representation of the central metabolism *of S. oneidensis* MR-1, under anaerobic (**left**) and aerobic (**right**) conditions. In an anaerobic environment (**left**), pyruvate is oxidised to acetyl-CoA (producing formate as a byproduct) before being converted into acetate. The oxidation of formate is coupled to the reduction of fumarate in the periplasm. In an aerobic environment (**right**), NAD^+ is reduced to NADH, as pyruvate is fully oxidised to CO_2 in the TCA cycle. Red text depicts enzymes: LdhA, lactate dehydrogenase A; Dld-II, D-lactate dehydrogenase; PflB, pyruvate formate lyase; Pta, phosphate acetyltransferase; AckA, acetate kinase; AceEFG, pyruvate dehydrogenase (PDH) complex; FDH, formate dehydrogenase; Ndh, NADH dehydrogenase; Cco, cytochrome *c* oxidase; Bd, quinol oxidase; FccA, fumarate reductase; STC, small tetraheme cytochrome. IM, inner membrane; FocA, formate channel A; CymA, tetraheme cytochrome; QH_2, reduced quinone; Q, oxidised quinone. Electron flow is indicated with red dashed arrows. Model created using BioRender.com from several references[39,96,99–112,125].

Genetic analyses showed the direct contribution of six multiheme *c*-Cyts (MHC) in extracellular reduction of Fe(III)-containing minerals: MtrA, a decaheme *c*-Cyt; MtrC, a cell surface-localised decaheme *c*-Cyt; CymA, a tetraheme quinol dehydrogenase; fumarate reductase (Fcc_3 or FccA); small tetraheme cytochrome (STC); and OmcA. Additionally, MtrB, a 26 β-strand OM porin is also directly involved in extracellular mineral reduction[62,88,113]. It has been confirmed via functional characterisation that oxidation of quinol by CymA occurs at the cytoplasmic membrane. Next, the released electrons are transferred to periplasmic STC and FccA, which act as electron shuttles[62,113,114]. Therefore, it is suggested that STC and FccA transfer electrons from CymA to MtrA (Figure 1.11), as a mutant lacking STC or FccA was shown to have a decreased capacity to reduce Fe(III) oxides or oxyhydroxides[62,114,115].

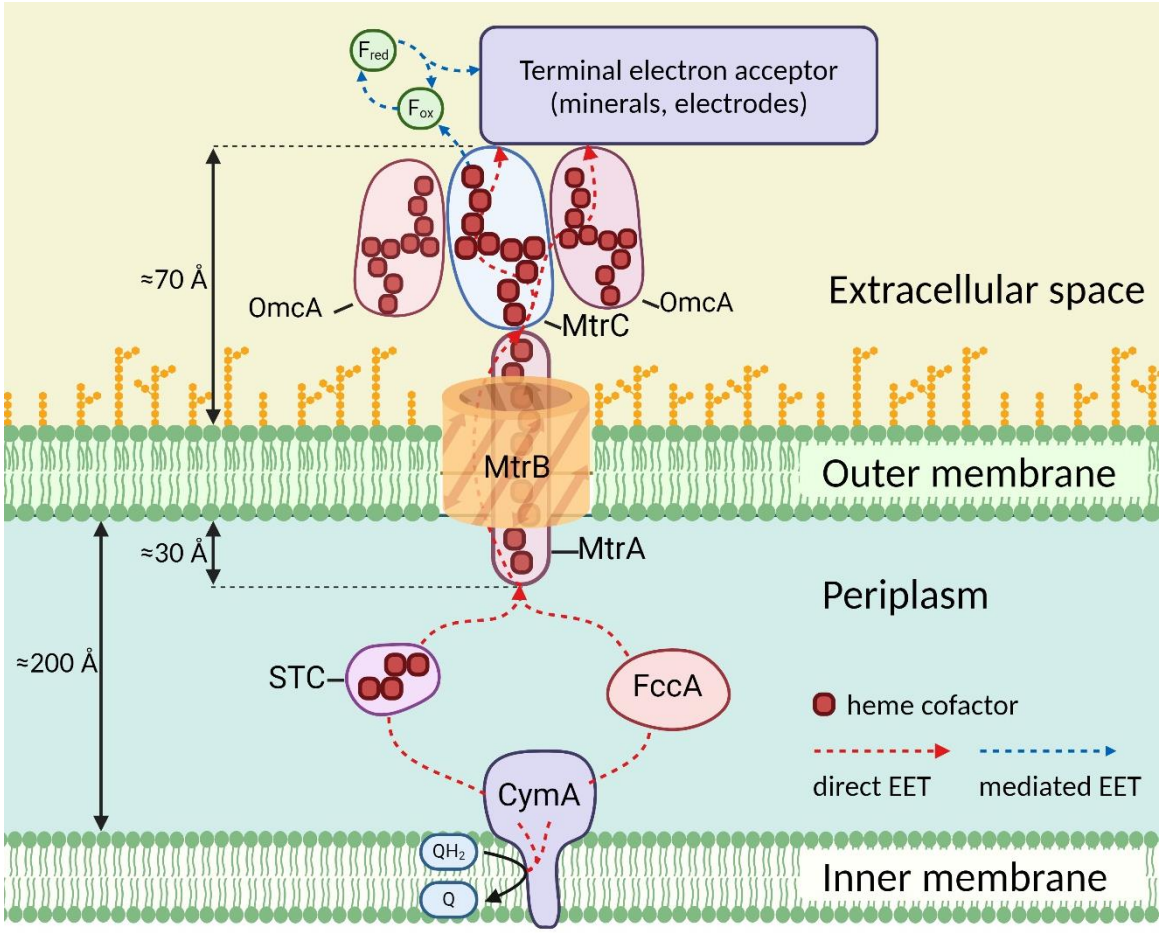

Figure 1.11. Proposed EET pathway in the Mtr complex of *Shewanella* spp. Dashed arrows indicate direct (red) and mediated (blue) electron transport. In mediated EET, flavins act as accessory electron carriers that increase extracellular reduction capacities. MQH_2, reduced menaquinone; MQ, oxidised menaquinone; STC, small tetraheme cytochrome; FccA, fumarate reductase; CymA ,tetraheme cytochrome; F_{red}, reduced flavin; F_{ox}, oxidised flavin. Created using BioRender.com and adapted from previous work[62,121].

1.7.2 The MtrCAB complex

MtrC, MtrB, and MtrA form a trans-OM protein complex, MtrCAB, that transports electrons from periplasmic proteins to the bacterial surface (Figure 1.11). The MtrCAB complex is a model and one of the most studied complexes for the mechanism of EET in metal-reducing bacteria. It is proposed that MtrA is embedded inside MtrB, forming a decaheme wire linking the extracellular environment and the periplasm[116]. The electrons are transferred between the final heme in MtrA and the first heme in MtrC. This icosaheme chain traverses the lipid bilayer and allows for Fe(II)/Fe(III) transitions of adjacent heme sites to transport electrons to the extracellular environment from the periplasm (Figure 1.11). From the X-ray crystal structure (Figure 1.12) it can be seen that all hemes in MtrA and MtrC are bis-histidine ligated and are covalently bound to CXXCH amino acid *c*-heme binding motifs throughout the protein[79].

It has been demonstrated that under specific conditions in gene knockout experiments, the MtrAB complex can directly transfer electrons to soluble electron acceptors, such as Fe(III) citrate, near the cell surface[113]. However, it cannot transfer electrons to solid-phase minerals like hematite (Fe_2O_3), amongst other insoluble iron oxides. Consequently, the MtrAB Pcc complex is proposed to be the minimal complex necessary for trans-OM electron transfer. MtrC, the cell surface-localised decaheme, is necessary for electron transport between MtrAB and solid-phase minerals[72,113]. MtrC, and other cell surface cytochromes (MtrF, OmcA, UndA), are transported to the cell surface via the type II secretion system. At the cell surface, the cytochromes are tethered to the OM by a lipid anchor. This anchor is connected to an acylated cysteine at the N-terminal of the protein backbone, which forms part of the lipobox recognition sequence[117,118]. Small angle neutron scattering (SABS) has shown that MtrC protrudes ~70 Å above the OM, and that MtrA traverses MtrB and protrudes ~30 Å into the periplasm (Figure 1.11).

These results support the theory that MtrA does not span the periplasm entirely (~ 200 Å), but rather that periplasmic *c*-Cyts (such as FccA and STC) act as electron shuttles between CymA and MtrA[119]. Likely, electrons are transferred from MtrC to OmcA before they are donated to the terminal electron acceptors. However, transfer from MtrC to the acceptors without OmcA is also possible[113,115,120,121].

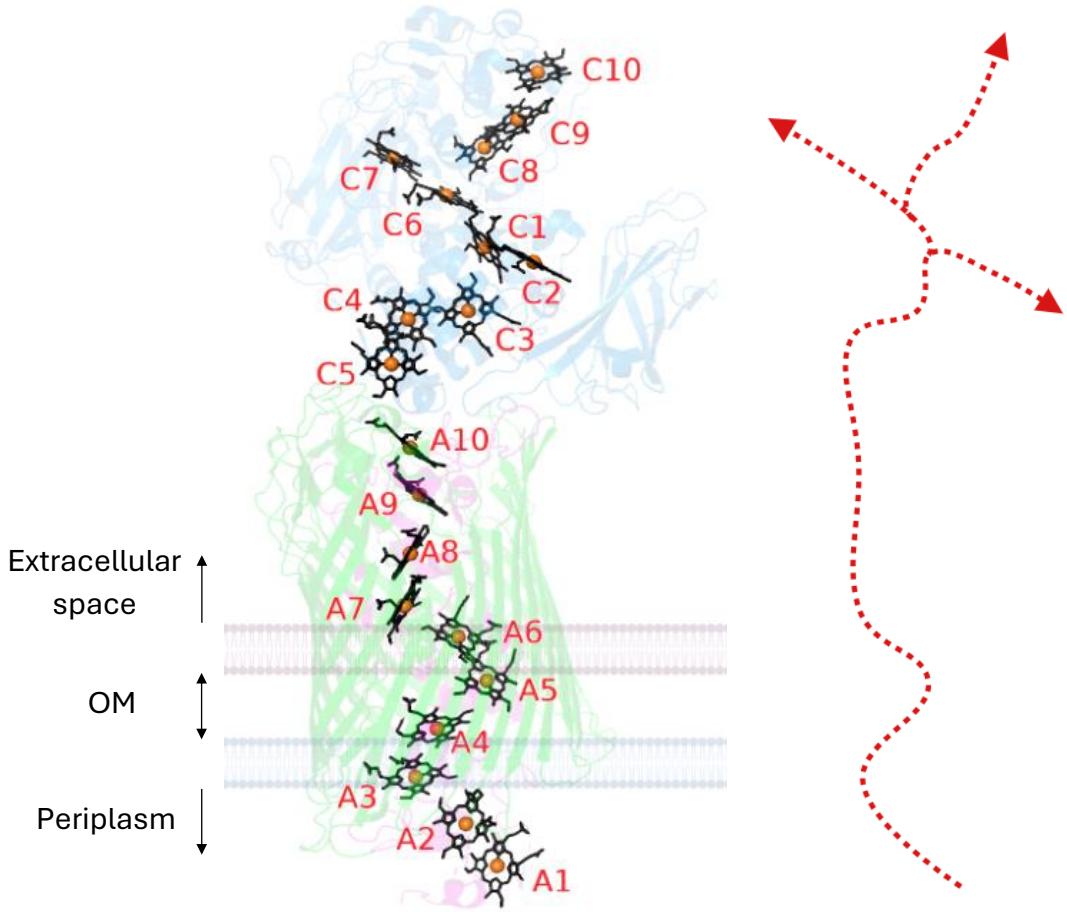

Figure 1.12. Left. X-ray crystal structure of MtrCAB complex from *S. baltica* OS185 (PDB:6R2Q). The MtrCAB complex is represented as a cartoon. MtrA (purple) is embedded inside transmembrane porin MtrB (green), with the N terminus extending into the periplasmic space. Extracellular MtrC (blue) associates with the surface of MtrB. The predicted positioning of the MtrCAB complex within the outer-membrane lipid bilayer is also shown. **Right.** Direction of electron transfer through MtrCAB (red dashed arrow). An electron is accepted by heme A1 and traverses MtrA from hemes A1 to A10, sequentially. The electron is then transferred from heme A10 of MtrA to heme C5 of MtrC, where it can be transferred from C2, C7, or C10 to the terminal electron acceptor. Image produced in PyMOL and BioRender.com and adapted from previous work[88,122,138].

Additionally, interactions between MtrA and MtrB in the MtrAB complex vary across the proteins. Approximately 80% of the MtrA polypeptide chain is comprised of flexible loops, while the remaining 20% forms helices. Temperature factors in the MtrA backbone increase from the OM-facing C terminus to the periplasmic N terminus. This demonstrates the varying mobility of MtrA, as higher temperature factor values correspond to an increased chain flexibility. There are few interactions between MtrB and the N terminus of MtrA, resulting in an increased mobility of the periplasmic section of MtrA. On the other hand, charged side chains located on the inside of MtrB form many hydrogen bonds with the loops in the C terminus of MtrA,

leading to restricted mobility. Subsequently, it is believed that the periplasmic N terminus of MtrA is the most flexible and mobile region of the polypeptide chain, facilitating interactions between MtrA and electron-donating periplasmic proteins like FccA and STC[88,115,119,122].

The MtrCAB complex has the capacity to transport electrons into & from liposomes across the lipid bilayer, emphasising the potentially bidirectional nature of the complex and its homologues[123]. Moreover, the Mtr pathway of *S. oneidensis* which usually transports electrons from CymA to extracellular minerals, can also transport them in the reverse direction, from an extracellular environment to CymA[123–125]. The versatility of electron transfer in the MtrCAB complex highlights the future potential in the biotechnological sector.

1.7.3 EET and outer-membrane cytochromes

OmcA and MtrC can also form part of extracellular bacterial 'nanowires', allowing *S. oneidensis t*o physically connect with adjacent cells. These nanowires have been demonstrated to be OmcA- and MtrC-containing protrusions of the OM and periplasm, and are proposed to facilitate electron transfer to other *S. oneidensis* MR-1 cells and extracellular minerals through an electron 'multistep hopping' system[61,126].

S. oneidensis MR-1 can also secrete extracellular flavins (riboflavin and flavin mononucleotide, FMN) which play a role in mediated EET to electrodes and minerals. The FMN exist in three redox states: reduced (with two electrons), semiquinone (with one electron), and oxidised (with no electrons). If the flavins are reduced chemically, they can directly transport electrons to Fe(III)-containing minerals[62,127]. *S. oneidensis* MR-1 *bfe* (a regulatory gene involved in extracellular flavin secretion) mutants show a significantly decreased capacity to reduce ferrihydrite[127]. Therefore, it is suggested that secreted flavins function as electron shuttles, further mediating electron transfer between MtrC/OmcA and the surfaces of extracellular minerals[128]. Additionally, it is proposed that OmcA and MtrC may have the capacity to behave as cofactors when bound to flavins. These proteins (and other similar *c*-Cyts) contain solvent-exposed hemes, allowing them to directly interact with mineral surfaces[129,130]. In anoxic environments, OmcA and MtrC bind flavins, resulting in a *c*-Cyt-flavin complex on the cell surface. This complex exists in the semiquinone state with a more positive redox potential, likely increasing

electron transfer rates[131]. However, the reduction rates of Fe(III)-containing minerals by the MtrCAB complex and the MtrCAB-flavin complex are much faster than by flavins alone[62,132,133]. *In vitro* studies of oxidised OmcA and MtrC demonstrated the interaction between the cytochromes and FMN or riboflavin. However, the dissociation constants produced during these experiments suggested the interactions between the flavins and the cytochromes were dependent on local environment [134]. Under aerobic conditions, a disulfide bridge forms between two of the MtrC cysteines, lowering the affinity for FMN, disrupting the MtrC-FMN complex[131].

S. oneidensis can use a variety of outer-membrane cytochromes to facilitate electron transfer onto the terminal acceptors. MtrC from the MtrCAB complex is one of the most studied, but there are others including OmcA (decaheme), UndA (undecaheme) and MtrF (MtrC homologue). The heme arrangement in all four of these cytochromes is similar, with the protein structure being comprised of four distinct domains[135]. Domains I and III form β-barrel structures, while domains II and IV contain hemes.

For both OmcA and MtrF, hemes 5-3, 1, 6, and 8-10 form an octaheme wire that traverses across domains II and IV[88,135]. Hemes 7 and 2 are located on either side of

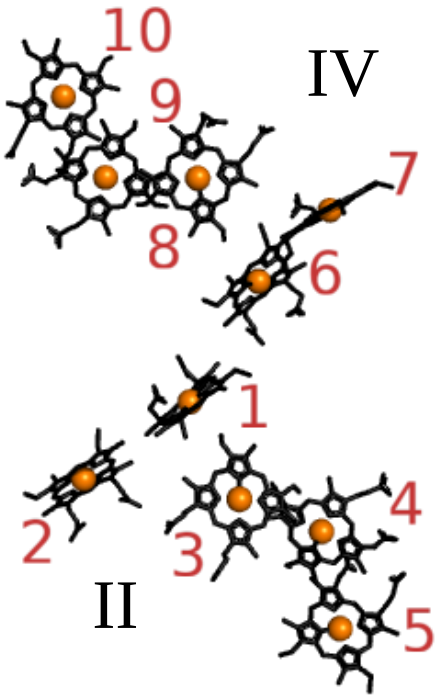

Figure 1.13. Heme arrangement in outer-membrane cytochromes of *S. oneidensis*. The hemes form the characteristic "staggered cross" arrangement, with hemes 1-5 being in domain II and hemes 6-10 in domain IV. Image produced in PyMOL using the hemes of MtrC (PDB: 4LM8)as a template.

the wire, positioned towards domains III and I, respectively (Figure 1.13). In UndA, the eleventh heme is located next to heme 7 of OmcA/MtrF/MtrC[135]. One of the most important and well-studied of these OM multiheme cytochromes is MtrC. One of the most important terminal reductases of *S, oneidensis*, MtrC takes the electrons from MtrA and transfers them to the terminal electron acceptor. This can happen in three ways, either by direct contact with the acceptor, by passing the electrons onto OmcA before the acceptor, or via electron shuttles that mediate the transfer.

1.7.4 MtrC

The cell surface-localised MtrC of *S. oneidensis* is comprised of four domains: domain I, a β-barrel domain located at the N-terminal; domain II, an α-helical domain containing five hemes; domain III, a second β-barrel domain; and domain

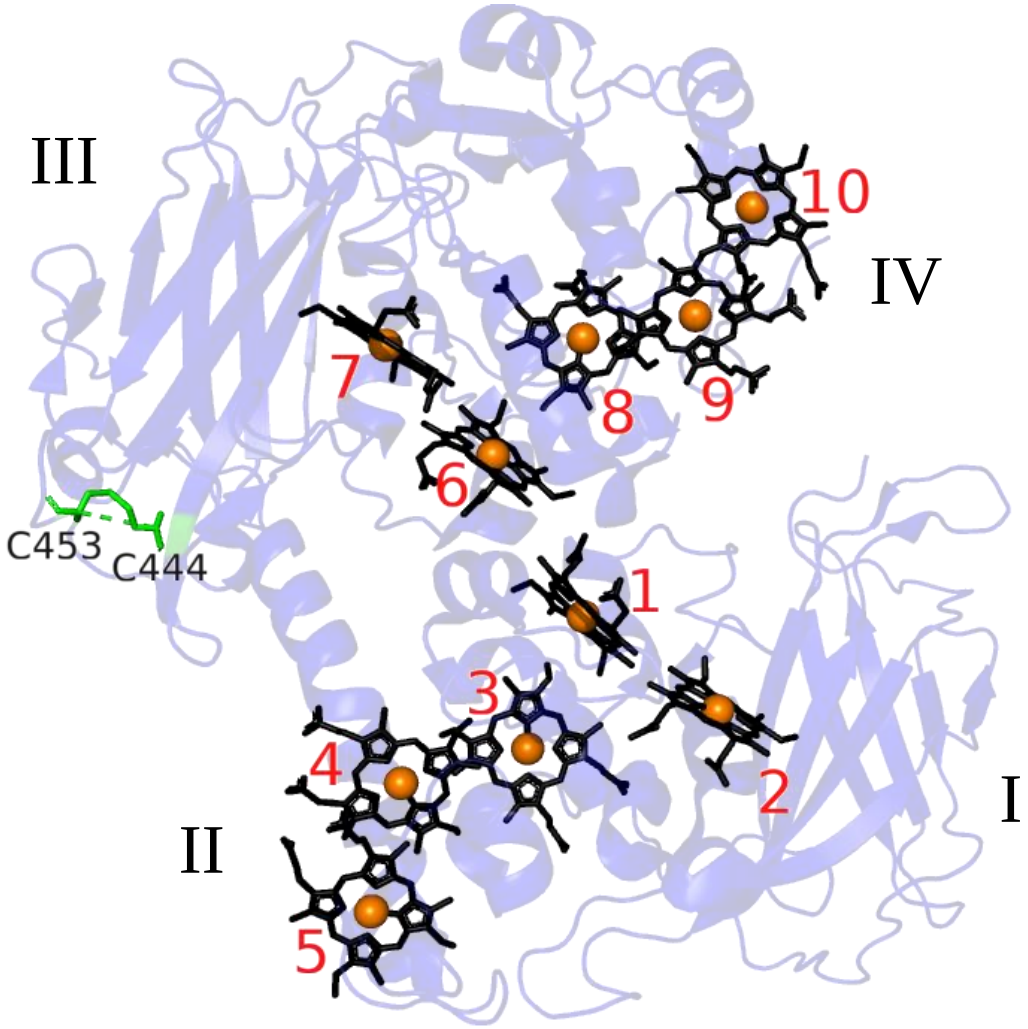

Figure 1.14. Heme arrangement in MtrC of S. oneidensis MR-1. The hemes are shown in black with the iron core shown as an orange sphere. The disulfide bridge between cysteine residues C444 and C453 is shown in green. The protein is represented as a cartoon in blue. Heme numbering corresponds with the position of heme attachment motifs (CXXCH) in the amino acid sequence. Domains are numbered with roman numerals. Image produced in PyMOL using the hemes of MtrC (PDB: 4LM8)as a template.

IV, another α-helical domain containing five hemes and located at the C-terminal (Figure 1.14)[134].

All four domains provide a scaffold for the ten bis-his coordinated hemes that are arranged in a "staggered cross". Within the MtrCAB complex, MtrC is angled in a way that the more insulated side is facing the membrane side. The negatively-charged propionates on the hemes, however, face towards the extracellular environment, providing an appropriate surface for direct electron transfer to the positively-charged extracellular electron acceptors[88]. Heme 10 in MtrC sits at the end of the MtrC heme chain at ~ 90 Å from the lipid bilayer core and lies near the PTPTD amino acid residue sequence which has been considered[136] to be a possible hydroxylated hematite (Fe_2O_3) binding motif. Consequently, this could be considered to be the principal route for direct EET to insoluble substrates.

Electronic microenvironment modelling has suggested that there is a net driving force between heme 5 of MtrC (the closest to MtrA) and heme 10 of MtrC. However, this driving force is small, which enables bidirectional electron transfer through the ten hemes of MtrC[88,137]. The redox potentials of hemes 2 and 7 of MtrC (the two "corners" of the staggered cross) are higher than those of the other hemes, which might suggest the possibility that these two hemes function as junctions and capacitors (or electron sinks) within the MtrCAB electrical network[138]. The orientation and arrangement of MtrC on the surface of *S. oneidensis* permits electrons to flow from MtrA into MtrC via a single heme (heme 5), and then be spread across the MtrC surface. This allows multiple hemes to act as potential sites for electron exchange, enabling electron transfer to both soluble and insoluble terminal electron acceptors. Consequently, this staggered cross arrangement with multiple electron exchange sites, would suggest that the rate-limiting step during EET is not the electron transfer through the outer membrane, but instead at a step before arriving to MtrA[88].

The redox state of the disulfide bridges in the MtrC cysteines seems to be important in determining electron transfer to specific electron acceptors; especially during indirect, mediated transfer through molecules like flavins. Within domain III of MtrC, the conserved 444 and 453 cysteines of the CX_8C motif create a single disulfide bond[131]. The disulfide is produced within an 8 amino acid loop that contains a solvent exposed valine and phenylalanine. At the C-terminal of the

disulfide there is a second loop of ~ 15 amino acid residues after which the β-strand of a β-barrel is formed. The majority of the amino acid residues within the surface of domain I are hydrophilic, while most of the side chains inside the β-barrels from domains I and III are hydrophobic[88,131]. There is, however, a hydrophobic cleft that contains three phenylalanines near heme 7 within domain III. MtrC-flavin complexes have been isolated after the disulfide within MtrC was reduced. However, the flavin cofactor is quickly released from the MtrC flavocytochrome upon oxygen exposure (which causes the reformation of the disulfide bond). As the nearest heme to the disulfide in MtrC is heme 7, association between FMN and MtrC is suggested to occur in the vicinity of heme 7, within domain III[131,139,140]. The edge-to-edge distance between the flavin cofactor of FccA (fumarate reductase) of *S. oneidensis* MR-1 and the nearest heme is ~ 7.5 Å, which would suggest the flavin binding site within MtrC would lie about halfway between the disulfide bond and heme 7[131,141].

The flavocytochrome complex can only form under anoxic, reducing conditions. Binding of the flavins to MtrC would not be possible in the periplasm, as many oxidation reactions occur here. Consequently, the reduced disulfide might become reoxidised leading to the reformation of the disulfide bridge which would prevent flavin binding. To overcome this, *S. oneidensis* is suggested to have generated an independent flavin export system that would allow for the transport of flavins to the extracellular environment separately from MtrC transport (which occurs through the Sec pathway). Once the flavins are transported to the extracellular space, they can form stable flavocytochrome complexes under anaerobic environments[127,131,132]. Furthermore, it has been proposed that when FMN binds to MtrC, the flavocytochrome complex may facilitate the two-electron reduction of a secondary, non-bound FMN molecule [131]. There are other systems such as the cytochrome bc_1 complex and photosystem II, that also use a tightly bound organic cofactor to enable two electron transfer to a separate organic, loosely bound electron shuttle. Consequently, it is hypothesised that in sub-oxic or anoxic environments, *S. oneidensis* can form these cell surface-localised flavocytochromes to increase the electron transfer rates to soluble molecules such as flavins or insoluble metal oxides. However, in oxic environments, rapid flavocytochrome dissociation occurs to reduce any potentially lethal oxidative damage that may happen due to non-specific reduction[131].

1.8 Applications in biotechnology

MHCs have adapted and evolved to allow microorganisms to thrive in environments that are challenging for growth. These MHCs transfer electrons across cell membranes and extracellular structures and have evolved the capacity to do so across distances of over several micrometres[142]. These characteristics have been applied in varying biotechnological applications, ranging from electricity production by MFCs to generating value-added chemicals through microbial electrosynthesis[30,143]. Furthermore, interest in purified MHCs and exploiting their electrical properties is rising, as they can now emulate organic semiconductors in terms of their conductance. Moreover, these MHCs can produce flexible, renewable, and easy-to-engineer materials that electronically combine synthetic resources to live cells[79,142,144]. The chief microbial ETC applications in biotechnology can be divided into several categories:

1.8.1 Toxic metal bioremediation

Bioremediation consists in using live organisms to detoxify, degrade, or eliminate toxic pollutants from contaminated ecosystems. Bioremediation targets can include halogenated compounds, petroleum hydrocarbons, as well as toxic metals and metalloids[145]. Noticeably, microbial technologies focusing on extracellular oxidation and reduction of metallic compounds have garnered interest as they can be used in microbiological toxic metal remediation[146]. These microbial reduction/oxidation bioremediation techniques have been used with several toxic metals and metalloids. Some reported examples include: the biomineralisation of elemental selenium (Se^0) through the reduction of selenite (SeO_3^{2-}) and selenate (SeO_4^{2-})[147]; the reduction of arsenate (AsO_4^{3-}) to arsenite (AsO_3^{3-}) leading to decreased adsorption in arsenic compounds[148]; chromium detoxification via reduction of Cr(VI) to Cr(III)[149]; and uranium insolubilisation via reduction of U(VI) to U(III)[54,150].

1.8.2 High-value metal recovery

Microbial reduction and oxidation have also been useful in the recovery of high-value metals. For example, bioleaching allows useful metals such as copper to be recovered from solid minerals like chalcopyrite ($CuFeS_2$), a copper iron sulfide mineral. In bioleaching, microbial processes help refine metals by eluting them from solid minerals[151]. Furthermore, high-value metal recovery via microbial

reduction has also been explored. Microorganisms that can perform EET, like *Geobacter* spp. and *Shewanella* spp. have shown to reduce precious metals including Au(III), Ag(I), Rd(III), Pd(II) and Pt(IV). These reductions occurred using redox potentials similar to Mn(IV) and Fe(III)[152]. These precious metals were reduced by the bacteria to their respective elemental metals, and metal nanoparticle accumulation was seen in their periplasm and cellular surfaces. Consequently, recovery of these precious metals was made easier. Therefore, it is suggested that microbial EET could play a role in the synthesis of nanomaterials as well as recovery of high-value metals[54,153].

1.8.3 Microbial fuel cells

Certain microorganisms, like *Shewanella* spp. and *Geobacter* spp., have the capacity to use conductive materials (like graphite electrodes) as electron acceptors/donors for respiration[154]. This ability to transfer electrons to/from electrodes can be exploited in bioelectrochemical systems such as MFCs. In MFCs, the chemical energy from substrates (like waste organics) is transformed into electrical energy via microbial metabolism and EET[155]. MFCs show promise over traditional electrochemical systems for a variety of reasons: the microorganisms acting as electrode catalysts are self-replicating and relatively cheap; the thermostability of MFCs allows them to function stably, even at room temperature; and the ability to use a variety of compounds, including waste matter, as fuel[156]. However, even with enhancements to electrode materials, cathode catalysts, and (bio)reactor configuration, the electrical output of MFCs does not compare to that of standard chemical fuel cells[54,157]. Subsequently, MFC research is focused on wastewater treatment, with particular interest in intensive, low-energy systems. However, MFC-based treatment technologies for wastewater systems have not been commercialised yet, as there are several issues that need to be addressed. The cost of electrode materials and components remains too high, the durability of MFC-based systems needs to be improved, and the scale of (bio)reactors needs to be increased in a cost-effective manner[54,156,158]. Additionally, MFC-based applications have also been investigated in plant rhizosphere electricity production in rice paddy fields[159], portable batteries[160], and marine & lake sediment remote batteries[161].

1.9 Thesis aims

This thesis aims to improve the current understanding of the two decaheme cytochromes, MtrA and MtrC, which form part of the MtrCAB complex in *Shewanella oneidensis*. This complex plays a key role in extracellular electron transfer in *S. oneidensis* when respiring in anaerobic conditions. Electrons from the internal metabolism are transferred across the periplasm, through MtrCAB, and donated to the terminal electron acceptor.

First, Chapter 3 explores the creation, expression, and purification of an MtrC variant that has an increased distance between domains I, II and domains III, IV. We hypothesised that by increasing the inter-domain distance within MtrC, the rate of electron transfer would be decreased. This was achieved by inserting two mutations resulting in increased repulsion between the two sets of domains in MtrC, resulting in MtrC double mutant ($MtrC_{DM}$). The biophysical properties of a soluble $MtrC_{DM}$ were largely assessed using UV-Visible spectroscopy and small angle X-ray scattering (SAXS). The effects of this double mutation on extracellular electron transfer in *S. oneidensis* expressing $MtrC_{DM}$ were characterised via a flavin mononucleotide (FMN) reduction assay.

Next, Chapter 4 investigates the role that domains III and IV play in electron transfer in MtrC. The hypothesis was that by removing domains III and IV, electron transfer to certain acceptors (like FMN) would be disrupted entirely. To do so, a variant was generated with a premature stop codon that resulted in the production of a truncated MtrC variant that was comprised exclusively of domains I and II ($MtrC_{DI,II}$). Biophysical characterisation was done by UV-Visible spectroscopy, X-ray crystallography, and protein film electrochemistry. To test the functional effects of removing domains III and IV on extracellular electron transfer, a variety of reduction assays were performed on cells expressing $MtrC_{DI,II}$. These assays used physiological electron acceptors such as FMN, OmcA, Fe(III) citrate and Fe(III) EDTA, as well as non-physiological acceptors like three azo dyes.

Finally, Chapter 5 examines the properties of the distal axial ligands of hemes in MtrA. We hypothesised that due to the more positive redox potential of methionine, the rate of electron transfer through MtrA would be slowed down. Consequently, the histidines of three of the hemes were consecutively mutated to methionines, resulting in three single His/Met mutants and a triple His/Met mutant. Biophysical

characterisation was done by UV-vis spectroscopy and an ascorbate reduction assay. To test the effects of having three methionines as distal ligands on electron transfer, a FMN reduction assay was carried out on *S. oneidensis* cells expressing the triple His/Met mutants.

Chapter 2

Experimental procedures

2. Materials and methods

2.1 General techniques

2.1.1 Media preparation

Growth media used for all experiments can be divided into the following:

I. Lysogeny broth (LB): 25 g L^{-1} of LB medium (tryptone 10 g L^{-1}, yeast extract 5 g L^{-1}, NaCl 10 g L^{-1}) in reverse osmosis (RO) water, autoclave. LB agar plates were prepared in the same way, with the addition of 15 g L^{-1} agar before autoclaving.

II. M72 medium: casein peptone 15 g L^{-1}, soybean peptone 5 g L^{-1}, and NaCl 5 g L^{-1}. Growth in M72 medium was supplemented with 20 mM sodium DL-lactate, 20 mM sodium fumarate, 20 mM HEPES ((4-(2-hydroxyethyl)-1-piperazineethanesulfonic acid), pH 8.0 (prepared as a 20x stock), at the time of inoculation. The media and supplements were prepared with RO water, and autoclaved.

III. Shewanella Basal Medium[162] (SBM): NH_4Cl 0.46 g L^{-1}, K_2HPO_4 0.225 g L^{-1}, KH_2PO_4 0.225 g L^{-1}, $MgSO_4 \cdot 7\ H_2O$ 0.117 g L^{-1}, $(NH_4)_2SO_4$ 0.225 g L^{-1}, 100 mM HEPES, pH 7.2.

IV. Shewanella Minimal Medium (SMM): SBM, vitamin mix (biotin 0.002 g L^{-1}, folic acid 0.002 g L^{-1}, pyridoxine hydrochloride 0.02 g L^{-1}, thiamine 0.005 g L^{-1}, nicotinic acid 0.005 g L^{-1}, pantothenic acid 0.005 g L^{-1}, cyanocobalamin 0.1 mg L^{-1}, *p*-aminobenzoic acid 0.005 g L^{-1}, and α-lipoic acid 0.005 g L^{-1}) 2.5 mL L^{-1}, mineral mix (nitrilotriacetic acid 1.5 g L^{-1}, $MnCl_2 \cdot 4\ H_2O$ 0.1 g L^{-1}, $FeSO_4 \cdot 7\ H_2O$ 0.3 g L^{-1}, $CoCl_2 \cdot 6\ H_2O$ 0.17 g L^{-1}, $ZnCl_2$ 1 g L^{-1}, $CuSO_4 \cdot 5\ H_2O$ 0.04 g L^{-1}, $AlK(SO_4)_2 \cdot 12\ H_2O$ 0.005 g L^{-1}, H_3BO_3 0.005 g L^{-1}, Na_2MoO_4 0.09 g L^{-1}, $NiCl_2$ 0.12 g L^{-1}, $NaWO_4 \cdot 2\ H_2O$ 0.02 g L^{-1}, Na_2SeO_4 0.1 g L^{-1}) 2.5 mL L^{-1}, pH 7.2. SBM was prepared and autoclaved first. Then, the vitamin and mineral mixes were filter-sterilised (0.4 µm filter) before addition. Finally, the pH was corrected to 7.2.

Throughout this thesis, any media/solution containing “water” refer to RO water, unless otherwise stated. All pH adjustments in this thesis were done with concentrated NaOH and HCl.

2.1.2 Kanamycin

For this entire thesis, any cultured cells that contained any form of the pBAD plasmid (with the *kanR* gene) had a final concentration of 30 μg L^{-1} kanamycin in the solid or liquid media. This was done by adding 0.1% (v/v) of a filter-sterilised (0.2 μm filter) 30 mg L^{-1} kanamycin stock to the solid or liquid media. All bacterial strains and plasmids were obtained from the Clarke group at the University of East Anglia, Norwich, and are listed in Table 2.3. All strains were stored by mixing 1 mL of overnight culture (180 RPM, 30°C) with 50% glycerol, flash with liquid nitrogen, and storing at -80°C. [163]

2.2 Modifications to plasmid DNA

Most of the mutants produced for this thesis were generated by replacing the existing amino acid codon in the gene for another. The only exceptions were when a Strep (II) tag was introduced to the C terminus of a gene. These site-directed mutageneses happened on plasmid-based copies of the genes within the pBAD plasmid (see Table 2.3). The pBAD feature map is shown in Figure 2.1.

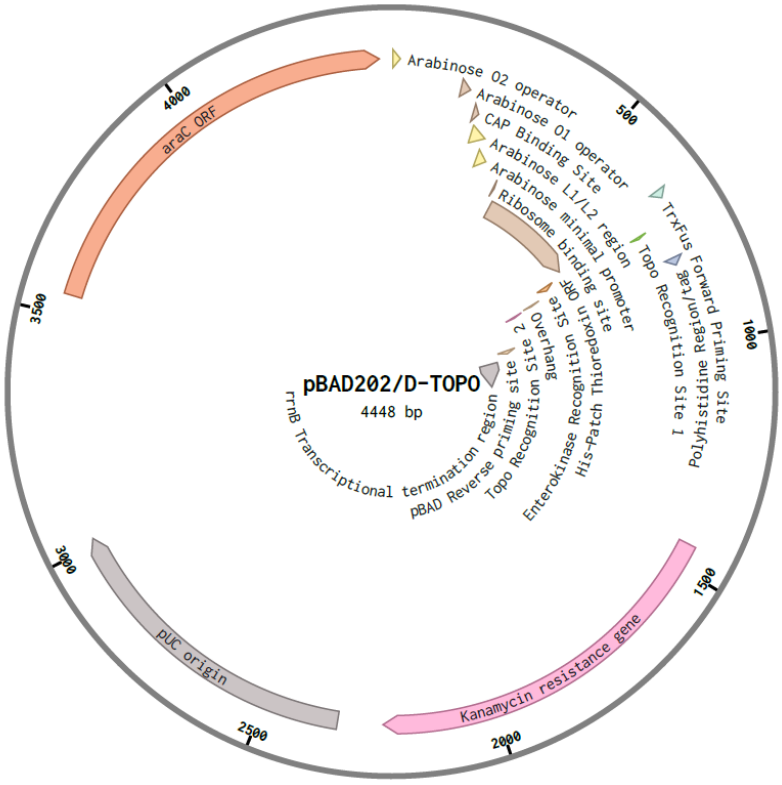

Figure 2.1. Feature map for the pBAD202/D-TOPO® plasmid. Some of the most relevant features are: *araC* ORF, allows for tight regulation of P_{BAD} promoter; pUC origin, allows replication and growth in *E.coli*; kanamycin resistance gene, allows selection of plasmid; TOPO® recognition site 1 and 2, location where the gene of interest is inserted. Plasmid was visualised on Benchling.

2.2.1 Plasmid extraction and quantification

To begin the mutations, a high yield of pure plasmid DNA (pDNA) was required. This was prepared by growing *S. oneidensis* cells containing the plasmid-based copy of the gene of interest (GOI) overnight (180 RPM, 30°C) in LB_{kan} with added kanamycin. The following day, the pDNA was extracted using a GenElute™ Plasmid Miniprep Kit (MERCK). However, pDNA was eluted in 50-75 µL molecular biology-grade water (MB water). The purity and yield of the extracted pDNA were determined using a NanoDrop™ One Microvolume UV-Vis Spectrophotometer (ThermoFisher Scientific). The yield was determined in ng uL^{-1}, and any nucleic acid or protein impurities were determined by the $\frac{A_{260}}{A_{230}}$ and $\frac{A_{260}}{A_{280}}$ ratios, respectively.

2.2.2 Primer design

The site directed mutageneses were carried out by using polymerase chain reaction (PCR) to replace and/or introduce new codons into the genes. To do so, primers containing the new DNA were designed. To improve the efficiency of the

Table 2.1. List of primers used in this thesis, with their direction (forward or reverse), sequence (5'-3'), and the purpose they served. Mutagenesis primers that were designed using the non-overlapping and overlapping protocol established by Liu and Naismith[164] are show in **bold**, while QuickChange™ primers are shown in *italic*. Sequencing primers do not fall under either category as they sit either upstream or downstream of the sequenced region.

Primer		Sequence (5'-3')	Purpose
MtrA Strep (II) tag	forward	CAATTTGAAAAATAAGTTTAAACGGT CTCCAGCTTGGCTG	Introduce Strep (II) tag to replace V5 epitope and hexa hist tags
	reverse	TGGATGGCTCCAGGCGCTGCGCT GTAATAGCTTGCCAGATGG	
MtrA H58M (heme 3)	**forward**	**TGTCATGGGTGCGATTGACTC CTCTAAGAGT**	**Change heme 3 distal histidine to methionine at residue position 58 in MtrA**
	reverse	**CGCACCCATGACACCTTTGAAAA GGTCCATG**	
MtrA H167M (heme 2)	**forward**	**AAGTAATGGTCGCAAAAGATCCTG TGTTATCTAAAAA**	**Change heme 2 distal histidine to methionine at residue position 167 in MtrA**
	reverse	**TTGCGACCATTACTTGGTGACAAG AAGCACAA**	
MtrA H200M (heme 7)	**forward**	**AAGTATGCCACTCAAATGGGCAC AAATGACCT**	**Change heme 7 distal histidine to methionine at residue position 200 in MtrA**
	reverse	**TTGAGTGGCATACTTGAGCGTTTAT TCATATCC**	
MtrC S188V	**forward**	**GTGCTGTGTGCCACGTAGAAGGT GAAAAGAT**	**Change serine to valine at residue position 188 in MtrC**
	reverse	**TGGCACACAGCACATACTTCGTG GCTAACGA**	
MtrC N251D	**forward**	**CACAAGACATTGTCCAAGATAATT GCCAAGTTTGT**	**Change asparagine to aspartic acid at residue position 251 in MtrC**
	reverse	**GGACAATGTCTTGTGCAACTGTAG GGATTTTATTG**	
MtrC E344Amber	*forward*	*CAATTAATACCTAGACTAAAGCAG*	*Change glutamic acid to premature amber stop codon at position 344 in MtrC*
	reverse	*CTGCTTTAGTCTAGGTATTAATTG*	
pBAD seq	forward	TCACTTGCCACAATCCTCAC	Used for sequencing pBAD plasmid
	reverse	AGTTCCCTACTCTCGCATGG	
MtrC seq	forward	ACACGTTGAAGATGCCTACG	Used for sequencing pBAD plasmid with *mtrC*

mutagenesis, primers were designed following the protocol from Liu and Naismith[164]. These primer pairs differ from traditional QuickChange™ primers as they contain non-overlapping bases on either side of an overlapping central region, allowing for higher yields of PCR products with fewer amplification cycles and less starting DNA template. Table 2.1 shows the primers used to introduce a Strep (II) tag to the C-terminus of the GOI (when necessary), to substitute single amino acid residues in the genes of interest, and for sequencing.

2.2.3 Polymerase chain reaction site-directed mutagenesis

For the insertion of the Strep (II) tag and any site-directed mutageneses, polymerase chain reaction (PCR) was used. All mutagenesis primers were diluted to 25 µM before use. The PCR components are as follows:

- 25 µL 2x Phusion Flash High-Fidelity PCR Master Mix (ThermoFisher Scientific)
- 22 µL MB water
- 1 µL forward primer (25 µM)
- 1 µL reverse primer (25 µM)
- 1 µL template DNA (≥50 ng μL^{-1})

Table 2.2. PCR conditions used during Strep (II) tag insertion and mutageneses. [A]This temperature was used for the Liu & Naismith[164] primers. [B]This temperature was used for QuickChange™ primers. [C]This temperature was used for addition of Strep (II) tag. [D]This step was only added when using Liu & Naismith[164] primers. [†]The annealing temperatures shown were at the centre of a temperature gradient of ± 5°C.

Step	Temperature (°C)	Duration (seconds)	Cycles
Initial denaturation	98	60	1
Denaturation	98	30	30
Annealing[†]	50[A]/56[B]/60[C]	30	
Extension	72	120	
(Liu & Naismith[2] extension)[D]	40-45	180	1
Final extension	72	300	
Hold	18	∞	

The PCR were done in a C1000 Touch Thermal Cycler (Bio-Rad) following the conditions set in Table 2.2. The only changes across the mutageneses were the annealing temperature and extension times (see Table 2.2).

2.2.4 Agarose gel electrophoresis

DNA was separated by size via electrophoresis on 0.8% agarose gels. These were prepared by mixing agarose with 1x Tris-acetic acid (TAE) buffer (40 mM Tris, 20 mM

acetic acid, 1 mM EDTA (ethylenediaminetetraacetic acid), pH 7.6) and heating the mixture until fully dissolved. The mixture was poured into a DNA gel tray and allowed to cool down, before placing in a DNA gel tank filled with 1x TAE buffer. Samples were prepared by mixing 1:1 with 2x Gel Red loading dye (100 µL Gel Red 100x [made by 1 in 100 dilution of GelRed® Nucleic Acid Stain 10,000x], 200 µL 6x loading dye [sucrose 240 g L^{-1}, Orange G 1.2 g L^{-1}, in water], 200 µL water). The DNA ladder (GeneRuler 1 kb Plus DNA Ladder) was also mixed 1:1 with the 2x Gel Red loading dye before loading on the agarose gel. When running the gels, they were limited by voltage at 120 V, until adequate separation of DNA bands by size was achieved (until the dye reached the end of the gel). The gels were imaged with UV light in a UV transilluminator, and the DNA ladder was used to determine the size in kilobases of the DNA bands.

2.2.5 DpnI digestion and PCR clean-up

After the PCR, a 0.8% agarose gel (See 2.1.3 Agarose gel electrophoresis) was run to confirm correct amplification of the pDNA. Once this was confirmed, a DpnI digestion was carried out. DpnI is an enzyme that digests the methylated template DNA (but not the non-methylated PCR product) This prevents template DNA from being transformed into the target host. 10x rCutSmart™ Buffer (New England Biolabs) was added to the successful PCR products in a 9:1 buffer:PCR products. DpnI (R0176S, New England Biolabs) was added to the mixture (1 µL 125 μL^{-1} PCR product and buffer mixture), inverted gently, and incubated for 2 hours at 37°C, 0 RPM. After the DpnI digestion, a PCR clean-up (GenElute™ PCR Clean-Up Kit, MERCK) was done to remove the DpnI and any other contaminants. The pDNA was eluted in MB water and the yield and impurities were recorded (see 2.2.1 Plasmid extraction and quantification). The pDNA from the mutated plasmids was then ready to use.

2.2.6 Gel extraction

For the plasmids that had a Strep (II) tag added to the C-terminus, further steps were required before they could be used. After running a 0.8% agarose gel, the bands of correct size were extracted under UV light using a scalpel. A GenElute™ Gel Extraction Kit (MERCK) was used with the extracted bands from the 0.8% agarose gel. The pDNA was eluted in MB water and the yield and impurities were recorded.

2.2.7 Phosphorylation and ligation

After the pDNA was extracted from the band in the 0.8% agarose gel, the following mixture was prepared: 10x T4 DNA Ligase Reaction Buffer (New England Biolabs) 100 µL mL^{-1}, T4 Polynucleotide Kinase (M0201S, New England Biolabs) 50 µL mL^{-1}, pDNA after gel extraction (≥100 ng $µL^{-1}$) 625 µL mL^{-1}, MB water 225 µL mL^{-1}. After mixing gently, the mixture was incubated for 5 minutes at 37°C and was allowed to cool down at RT for 5 minutes. Next, T4 DNA Ligase (M0202T, New England Biolabs) 50 µL mL^{-1} was added, the mixture was inverted gently, and incubated overnight at RT. Next, a PCR clean-up was done to remove the enzymes and any other impurities.

2.2.8 Competent *E. coli* cells preparation

Before the mutated pDNA could be transformed into *E. coli* cells, the cells needed to be made competent. First, *E. coli* cells were grown in LB overnight (180 RPM, 37°C). Next, 1 mL of the overnight culture was used to inoculate 100 mL of LB and incubated at 37°C 180 RPM until the OD_{600} was between 0.4-0.6 (mid-exponential phase). The culture was incubated on ice for 10 minutes. The cells were harvested by centrifugation (5 minutes, 3,000 x *g*, 18°C), resuspended in 20 mL of sterile 4°C 100 mM $CaCl_2$ and incubated on ice for 20 minutes. Next, the cells were harvested by centrifugation (5 minutes, 3,500 x *g*, 18°C) and resuspended in 2.4 mL of 100 mM $CaCl_2$ with 20% glycerol sterile solution. These cells divided in 50 µL aliquots and flash frozen before being stored at -80°C.

2.2.9 Heat shock transformation of *E. coli* TOP10 cells

2 µL of pDNA (≥50 ng $µL^{-1}$) from the PCR clean-up were added to a 50 µL aliquot of competent *E. coli* TOP10 cells and stirred gently. The mixture was incubated on ice for 30 minutes, before being subjected to a 45 second heat shock in a 42°C water bath. Immediately after, the cells were incubated on ice for 2 minutes. After, 200 µL of sterile LB were added, and the mixture was incubated for 45 minutes at 37°C 300 RPM on a ThermoMixer® (Eppendorf). The cells were harvested by centrifugation (2 minutes, 900 x *g*, 18°C) and 150 µL of supernatant were discarded. The pellet was gently resuspended in the remaining supernatant, plated on an LB_{kan} plate using a sterile spreader, and incubated overnight at 37°C. The following day, single colonies

of the transformants were picked and grown overnight (180 RPM, 37°C) in LB_{kan}. The pDNA was extracted and quantified and was ready to be sequenced.

2.2.10 Electroporation transformation of *S. oneidensis* cells

The selected strain of *S. oneidensis* was grown overnight ()180 RPM, 30°C) in LB. 3 mL of overnight culture were harvested by centrifugation (2 minutes, 6,000 x *g*, 18°C). The pellet was transferred to a 1.5 mL Eppendorf and washed three times by gently resuspending in 1 mL of sterile 10% glycerol and centrifuging (1 minute, 6,000 x *g*, 18°C). After the third wash, 930 µL of supernatant were removed and the pellet was resuspended in the remaining 70 µL. Next, 1 µL of pDNA (≥50 ng μL^{-1}) from the PCR clean-up was added to the resuspended cells and stirred gently. The mixture was transferred to a sterile electroporation cuvette (0.1 cm gap, Bio-Rad) and was electroporated at 1.2 kV in a MicroPulser Electroporator (Bio-Rad). Immediately after, 1 mL of SOC medium (dextrose 3.603 g L^{-1}, KCl 0.186 g L^{-1},$MgSO_4$ 4.8 g L^{-1}, tryptone 20 g L^{-1}, yeast extract 5 g L^{-1}) was added to the electroporation cuvette. Next, the cells were transferred back to the 1.5 mL Eppendorf and allowed to recover by incubating 2 hours at 30°C, 180 RPM. Next, the cells were centrifuged (1 minute 3,000 x *g*, 18°C), 900 µL of supernatant was discarded, and the pellet was resuspended in the remaining supernatant. The cells were plated on an LB_{kan} plate and incubated overnight at 37°C. The following day, single colonies of the transformants were picked and grown overnight (180 RPM, 30°C) in LB_{kan}. The pDNA was extracted and quantified and was ready to be sequenced.

2.2.11 DNA sequencing sample preparation

2.5 µL of extracted pDNA (50-100 ng μL^{-1}; See 2.1.1 Plasmid extraction and quantification) were added to a Mix2Seq kit tube (Eurofins Genomics) with 2.5 µL of sequencing primer (10 µM; see Table 2.1) and 5 µL of MB water. The samples were then ready to be collected and sequenced.

Table 2.3. Details of the template plasmid and template strains, as well as the transformed strains used in the experiments of this thesis. All mutageneses were done via PCR mutations, and transformations were done via heat-shock for *E. coli* and electroporation for *S. oneidensis*. In the soluble, plasmid-based *mtrC* mutants, the wild-type *mtrC* signal peptide and lipid anchor had been replaced with the MtrB signal peptide[163] which enabled secretion of soluble forms of MtrC. The naming for the transformed strains consists of the bacteria used "*S. oneidensis* Δ*mtr*", followed by the name of the plasmid "pMTRA$_{rec}$".

Template plasmid	Comments
pBAD_TOPO202	Dose-dependent induction with L-arabinose under the *ara*BAD promoter and *ara*C gene. N-terminal His-Patch thioredoxin for increased solubility and translational efficiency. Kanamycin resistance gene (*kanR*) for selection. pUC origin of replication for both *E. coli* and *S. oneidensis*. The C-terminus hexa histidine and V5 epitope tags were replaced via PCR with a C-terminal Strep (II) tag for purification of fusion proteins.

Template strains	Comments
Shewanella oneidensis MR-1	Wild-type strain.
S. oneidensis MR-1 Δ*mtr*	*mtrC, mtrA, mtrB, mtrD, mtrE, mtrF, omcA* knockout
S. oneidensis MR-1Δ*mtrA*	*mtrA* knockout
S. oneidensis MR-1 Δ*mtrC/omcA*	m*trC* and o*mcA* knockout
Escherichia coli TOP10	Used for high-efficiency cloning as allows for stable replication of high copy number plasmids.

Transformed strains	Comments
S. oneidensis Δ*mtr* pMTRA$_{rec}$	Contains native *mtrA* with a C-terminus Strep (II) tag on pBAD plasmid (**rec**ombinant)
S. oneidensis Δ*mtr* pMTRA$_{H85M}$	Contains *mtrA* with histidine codon at position 85 changed to methionine codon, and a C-terminus Strep (II) tag on pBAD plasmid (**H85M**).
S. oneidensis Δ*mtr* pMTRA$_{H167M}$	Contains *mtrA* with histidine codon at position 167 changed to methionine codon, and a C-terminus Strep (II) tag on pBAD plasmid (**H167M**).
S. oneidensis Δ*mtr* pMTRA$_{H200M}$	Contains *mtrA* with histidine codon at position 200 changed to methionine codon, and a C-terminus Strep (II) tag on pBAD plasmid(**H200M**).
S. oneidensis Δ*mtr* pMTRA$_{triple}$	Contains *mtrA* with histidine codon at positions 85, 167, and 200 changed to methionine codon, and a C-terminus Strep (II) tag on pBAD plasmid (**triple** mutant).
S. oneidensis Δ*mtrA* pMTRA$_{rec}$	Contains native *mtrA* with a C-terminus Strep (II) tag on pBAD plasmid (**rec**ombinant)
S. oneidensis Δ*mtrA* pMTRA$_{triple}$	Contains *mtrA* with histidine codon at positions 85, 167, and 200 changed to methionine codon, and a C-terminus Strep (II) tag on pBAD plasmid (**triple** mutant).

Transformed strains	Comments
S. oneidensis Δ*mtr* soluble $MTRC_{rec}$	Contains *mtrC* with *mtrB* signal peptide, and a C-terminus Strep (II) tag on pBAD plasmid (**rec**ombinant)
S. oneidensis Δ*mtr* soluble $MTRC_{S188V}$	Contains *mtrC* with *mtrB* signal peptide, serine codon at position 188 changed to valine codon, and a C-terminus Strep (II) tag on pBAD plasmid (**S188V**).
S. oneidensis Δ*mtr* soluble $MTRC_{DM}$	Contains *mtrC* with *mtrB* signal peptide, serine codon at position 188 changed to valine codon, asparagine codon at position 251 changed to aspartic acid codon, and a C-terminus Strep (II) tag on pBAD plasmid (**d**ouble **m**utant).
S. oneidensis MR-1 soluble $MTRC_{DI,II}$	Contains *mtrC* with *mtrB* signal peptide, glutamic acid codon at amino acid position 344 changed to amber stop codon on pBAD plasmid, resulting in MtrC **d**omain **I**, and **II.**
S. oneidensis Δ*mtrC/omcA* membrane $MTRC_{rec}$	Contains native *mtrC* with *mtrC* signal peptide on pBAD plasmid (**rec**ombinant)
S. oneidensis Δ*mtrC/omcA* membrane $MTRC_{DM}$	Contains *mtrC* with *mtrC* signal peptide, serine codon at position 188 changed to valine codon, asparagine codon at position 251 changed to aspartic acid codon, and a C-terminus Strep (II) tag on pBAD plasmid (**d**ouble **m**utant).
S. oneidensis Δ*mtrC/omcA* membrane $MTRC_{DI,II}$	Contains *mtrC* with *mtrC* signal peptide, glutamic acid codon at amino acid position 344 changed to amber stop codon on pBAD plasmid, resulting in MtrC **d**omain **I**, and **II.**

2.3 Protein synthesis

2.3.1 Protein expression trials

Once the mutated plasmids that were extracted from the transformants were confirmed by sequencing, protein synthesis was characterised. All protein expression was carried out using L-arabinose to induce the pBAD plasmids containing all the GOIs. Cells were grown overnight (180 RPM, 30°C) in LB_{kan}.1 mL of the overnight culture was used to inoculate 5 x 100 mL LB_{kan} and incubated at 30°C 180 RPM until the OD_{600} was ~ 0.4. Next, 0, 1, 2, 5, or 10 mM of L-arabinose were used in each 100 mL LB_{kan} and incubated overnight (180 RPM, 30°C). The following day, cells were normalised to an OD_{600} of 0.1. For soluble periplasmic proteins and membrane proteins, a whole-cell SDS-PAGE gel was run (see 2.1.7 Whole-cell SDS-PAGE gel preparation). For soluble proteins secreted to the extracellular environment, the cells were pelleted by centrifugation (10 minutes, 3,000 x *g*, 18°C) and the supernatant was used for SDS-PAGE gels (see 2.1.4 SDS-PAGE). Only heme protein expression was relevant, so gels were heme stained (see 2.1.6 Heme-linked peroxidase (heme) staining of SDS-PAGE gels). Arabinose concentrations with the darkest bands on the heme stain were selected for protein purification.

2.3.2 Sodium dodecyl sulfate-polyacrylamide gel electrophoresis

Proteins were separated by size using sodium dodecyl sulfate-polyacrylamide gel electrophoresis (SDS; mPAGE® 4-20% Bis-Tris Precast Gel) that were run with 3-(*N*-morpholino) propanesulfonic acid (MOPS) buffer (MOPS SDS running buffer powder for mPAGE® Bis-Tris gels). Samples were prepared by mixing 1:1 with 2x protein loading dye (6 M urea, 5% SDS, 20% glycerol, 0.2% bromophenol blue, 0.5 M Tris, pH 6.8, in H_2O). The samples were incubated for 10 minutes at 95°C. The protein ladder (Precision Plus Protein™ Dual Color Standards) already contained loading dye, so no 2x protein dye was added. Typically, 20 µL of sample were loaded onto each well. SDS-PAGE gels were limited by voltage at 180 V, until adequate separation of protein bands by size was achieved (until the dye reached the end of the gel). Before staining, SDS-PAGE gels were shaken in a tray with water at 100 RPM for 5 minutes, to remove residual running buffer.

2.3.3 Whole-cell SDS-PAGE gel preparation

For purified protein gels, the proteins were mixed with loading dye before running on an SDS-PAGE gel. For whole-cell SDS-PAGE gels the protocol involved more steps. Cells were grown overnight (180 RPM, 30°C) in LB or LB_{kan}. Next, 10 µL of these overnight cells were added (0.1% inoculum) to 10 mL M72 media with supplements (see 1.1.1. Media preparation), 1 mM L-arabinose, and 10 µL of kanamycin in a Universal tube. A sterile pipette tip was also added to the Universal for increased aeration. The cultures were incubated for 20 hours at 25°C, 120 RPM. Next, 1 mL of cells normalised to an OD_{600} of 0.1 was harvested by centrifugation (10 minutes, 3,000 x *g*, 18°C). Cells were resuspended in 750 µL 20 mM HEPES, 100 mM NaCl, pH 7.8 and were lysed by sonication (Sonics, ultrasonic processor model GE50). This was done in 3 x 30-second bursts, always keeping the cells on ice to prevent overheating. The amplitude was set to the highest value without foaming occurring. After sonication, the lysed cells were subjected to centrifugation (10 minutes, 3,000 x *g*, 18°C) to pellet the cell debris. The supernatant was ultracentrifuged (45 minutes, 200,000 x *g*, 4°C, Beckman Optima™ TLX Ultracentrifuge, TLA120.2 rotor) to separate the membrane fraction (pellet) from the soluble fraction (supernatant). For **soluble** periplasmic proteins, the supernatant was mixed with 2x protein loading dye (see 1.1.4 SDS-PAGE) and incubated for 10 minutes at 95°C before running on an SDS-PAGE gel. For **membrane** proteins, the pellets were resuspended in 100 µL of water before adding 400 µL of cold acetone (stored at -20°C). The solution was incubated at -20°C for 30 minute and then subjected to centrifugation (1 minute, 14,000 x *g*, 4°C). The pellets were resuspended directly in 50 µL 2x protein loading dye (see 1.1.4 SDS-PAGE) and were incubated for 10 minutes at 95°C before running on an SDS-PAGE gel.

2.3.4 Coomassie staining of SDS-PAGE gels

To visualise all proteins in the SDS-PAGE gels, a Coomassie stain was done. After washing the gels in water for 5 minutes, the water was removed and 15-20 mL of Instant*Blue*™ was added. The gel was shaken at 100 RPM, until desired colouration was achieved (usually overnight). The gel was then imaged with white light in a UV transilluminator (Syngene™ G:BOX Chemi XRQ).

2.3.5 Heme-linked peroxidase (heme) staining of SDS-PAGE gels

To visualise only the heme-containing proteins present in the SDS-PAGE gels, a heme stain was done. After washing the gels in water for 5 minutes the water was removed, and 20 mL of sodium acetate (250 mM, pH 5.0) were added. The gels were shaken at 100 RPM for 5 minutes, before adding 20 mL of 3,3',5,5'-Tetramethylbenzidine dihydrochloride hydrate (TMBD) solution (1 mg mL^{-1} in pure methanol). 50 µL of 30% H_2O_2 were added, and the gel was incubated at room temperature (RT; ~ 21°C) until bands started appearing. This usually took 5-10 minutes, but if nothing appeared after this time, a further 50 µL of 30% H_2O_2 were added, or the gel was incubated overnight. Next, the sodium acetate TMBD H_2O_2 solution was removed appropriately, and replaced with water. The gel was imaged with white light in a UV transilluminator.

2.4 Protein purification

Throughout this thesis, many plasmids were used containing WT and mutant versions of the genes found in the *mtr* operon of *S. oneidensis*. The genes were induced, and the final translated protein products were purified using different chromatography columns. Due to this, the protocols differ after obtaining the initial cellular biomass after cell lysis. Proteins with a purification tag were subjected to their respective purification tag columns, regardless of where they were expressed (i.e. periplasm or extracellular environment). Proteins without a purification tag were instead subjected to ionic exchange and size exclusion chromatography columns. The protocols presented here are modified from previous work[79,88]. All purifications were carried out using an ÄKTA Pure Protein Purification System (Cytiva). All buffers and solutions used on the ÄKTA were filter-sterilised (0.4 µm) before use.

2.4.1 Cell lysate preparation

For all purifications, the process for obtaining cell biomass was the same. Cells were grown overnight (180 RPM, 30°C) in LB or LB_{kan}. 20 mL of these overnight cells were added (2% inoculum) to 1 L M72 media with supplements (see 1.1.1. Media preparation) with kanamycin (where necessary) in a 2 L baffled flask. The baffles inside the flasks enhance aeration, resulting in higher cell production. The cultures were incubated at 30°C 180 RPM until the OD_{600} was ~ 0.4. Next, 5 mM L-arabinose was used to induce protein synthesis for all protein purifications (except for

$MtrC_{DI,II}AB$ in which 1 mM was used). The induced cultures were incubated overnight (180 RPM, 30°C) and harvested by centrifugation (20 minutes, 5,500 x *g*, 4°C, JLA-8.1 rotor, Beckman Coulter Avanti™ J-20 Floor Super Speed Refrigerated Centrifuge). After this large volume centrifugation, the supernatant was composed of proteins that were secreted into the extracellularly environment in the spent media (soluble MtrC variants) and the pellet was composed of periplasmic (soluble MtrA variants) and membrane proteins (membrane MtrCAB variants).

2.4.2 Soluble extracellular proteins

2.4.2.1 Soluble MtrC WT/DM (double mutant)

The supernatant from the large volume centrifugation was concentrated using a crossflow cassette (Vivaflow™ 200, 10,000 MWCO) to ~ 100 mL. The concentrated spent media was loaded onto a 5 mL Strep-Tactin™ XT 4Flow™ column (IBA Lifesciences) equilibrated with 100 mM Tris, 150 mM NaCl, pH 8.0 (Strep buffer). After the proteins were applied to the column, the column was washed with Strep buffer. Bound proteins were eluted with 50 mM biotin in Strep buffer. The presence of heme-containing fractions was verified by electronic absorbance spectroscopy at 410 nm. These fractions were run on an SDS-PAGE gel and proteins were visualised by Coomassie and heme staining. Fractions containing bands at the desired size were pooled and concentrated using a centrifugal spin concentrator (Vivaspin® 30,000 MWCO, Sartorius) to ~ 1 mL. To remove any remaining impurities, the concentrated protein was applied to a HiLoad® 16/600 Superdex® 75 pg size exclusion chromatography column pre-equilibrated with 100 mM Tris, 150 mM NaCl, pH 8.1. Heme-containing fractions were selected using spectroscopy at 410 nm and run on an SDS-PAGE gel. Heme and Coomassie staining were used to identify heme proteins and confirm the removal of impurities, respectively. The selected fractions were pooled and concentrated using a centrifugal spin concentrator (Vivaspin® 30,000 MWCO), before being snap-frozen and stored at -80°C for later use.

2.4.2.2 Soluble $MtrC_{DI,II}$ (domain I, II)

The supernatant from the large volume centrifugation was concentrated using a crossflow cassette (Vivaflow™ 200, 10,000 MWCO) to ~ 100 mL. This was further concentrated using a centrifugal concentrator (Vivaspin® 10,000 MWCO) to 200 µL. The concentrate was then diluted in 1 L of 20 mM Tris, 30 mM NaCl, pH 7.8

(diethylaminoethanol (DEAE) sol. buffer) before running on a DEAE cellulose, weak anionic exchange chromatography column preequilibrated with DEAE sol. buffer. The presence of heme-containing fractions was verified via electronic absorbance spectroscopy at 410 nm, and by running proteins on an SDS-PAGE gel. Proteins were identified by heme staining. To remove any remaining impurities, fractions containing heme proteins were pooled and concentrated using a centrifugal concentrator (Vivaspin® 10,000 MWCO) to 1 mL. The concentrated protein was applied to a HiLoad® 16/600 Superdex® 75 pg size exclusion chromatography column pre-equilibrated with 100 mM Tris, 150 mM NaCl, pH 8.1. Fractions containing heme proteins were identified via SDS-PAGE and peroxidase-linked heme stains, before being pooled and concentrated using a centrifugal concentrator (Vivaspin® 10,000 MWCO) before being snap-frozen and stored at -80°C for later use.

2.4.3 Soluble MtrA WT/H85M/H167M/H200M/triple

After the large volume centrifugation (see 2.4.1 Obtaining cell mass), the supernatant was discarded appropriately. The pellets were resuspended in 100 mM Tris, 150 mM NaCl, pH 8.0 (Strep buffer) and DNase and protease inhibitors (cOmplete™, Mini, EDTA-free Protease Inhibitor Cocktail, MERCK) were added. The cells were lysed by three passages on a French Press Cell Disrupter (16,000 PSI, Thermo Electron Corporation). Cellular debris was pelleted by centrifugation (20 minutes, 5,000 x *g*, 4°C) and the supernatant was subjected to ultracentrifugation (2 hours, 185,000 x *g*, 4°C, Beckman Optima™ XL-100K ultracentrifuge, 45 Ti rotor). The supernatant from the ultracentrifugation was loaded onto a 5 mL Strep-Tactin™ XT 4Flow™ column (IBA Lifesciences) equilibrated with 100 mM Tris, 150 mM NaCl, pH 8.0 (Strep buffer). After the proteins were applied to the column, the column was washed with Strep buffer. Bound proteins were eluted with 50 mM biotin in Strep buffer. The presence of heme-containing fractions was verified by electronic absorbance spectroscopy at 410 nm. These fractions were run on an SDS-PAGE gel and proteins were visualised by Coomassie and heme staining. Fractions containing bands at the desired size were pooled and concentrated using a centrifugal spin concentrator (Vivaspin® 3,000 MWCO, Sartorius) to ~ 1 mL. To remove any remaining impurities, the concentrated protein was applied to a HiLoad® 16/600 Superdex® 75 pg size exclusion chromatography column pre-

equilibrated with 100 mM Tris, 150 mM NaCl, pH 8.1. Heme-containing fractions were selected using spectroscopy at 410 nm and run on an SDS-PAGE gel. Heme and Coomassie staining were used to identify heme proteins and confirm the removal of impurities, respectively. The selected fractions were pooled and concentrated using a centrifugal spin concentrator (Vivaspin® 3,000 MWCO), before being snap-frozen and stored at -80°C for later use.

2.4.4 MtrCAB/MtrC$_{DI,II}$AB

After the large volume centrifugation (see 2.4.1 Obtaining cell mass), the supernatant was discarded appropriately. The pellets were resuspended in 100 mM Tris, 150 mM NaCl, pH 8.0 (Strep buffer) and DNase and protease inhibitors (cOmplete™, Mini, EDTA-free Protease Inhibitor Cocktail, MERCK) were added. The cells were lysed by three passages on a French Press Cell Disrupter (16,000 PSI, Thermo Electron Corporation). Cellular debris was pelleted by centrifugation (20 minutes, 5,000 x *g*, 4°C) and the supernatant was subjected to ultracentrifugation (2 hours, 185,000 x *g*, 4°C). The pelleted membrane fraction was resuspended and homogenised in 100 mL (20 mM HEPES, pH 7.8) and left stirring overnight at 4°C. After, *N*-Lauroylsarcosine was added to 2% (w/v) and was left stirring for 40 minutes at 4°C to preferentially solubilise the inner membranes. The membrane fraction was pelleted by ultracentrifugation (2 hours, 185,000 x *g*, 4°C) and the supernatant was discarded. The pellets were resuspended in 100 mL Buffer B (20 mM HEPES, 5% (v/v) Triton X-100, pH 7.8) and left stirring overnight at 4°C to solubilise the outer membranes. The soluble fraction was obtained by centrifugation (2 hours, 185,000 x *g*, 4°C) and was loaded onto a DEAE-Sepharose weak anionic exchange chromatography column, preequilibrated with 20 mM HEPES, 2% (v/v) Triton X-100, pH 7.8 (DEAE memb. buffer). The protein was eluted in a 0-1 M gradient of NaCl in DEAE memb. buffer in 15 mL fractions over 150 mL. The eluant was diluted to 400 mL of DEAE memb. buffer before being loaded onto a Q-Sepharose strong anionic exchange chromatography column, preequilibrated with DEAE memb. buffer. The column was washed with 20 mM HEPES, 5 mM lauryldimethylamine oxide (LDAO), pH 7.8 (LDAO buffer), and the protein was eluted in a 0-1 M gradient of NaCl in DEAE LDAO buffer. The eluted protein was concentrated using a centrifugal concentrator (Vivaspin® 100,000 MWCO) to ~ 0.5 mL. The concentrated protein was applied to a HiLoad® 16/600 Superdex® 200 pg size exclusion chromatography pre-equilibrated

with 20 mM HEPES, 150 mM NaCl, 5 mM LDAO, pH 7.8. Heme-containing fractions were selected using spectroscopy at 410 nm and run on an SDS-PAGE gel. Desired fractions were pooled and concentrated using a centrifugal concentrator (Vivaspin® 100,000 MWCO) to 1 ~ mL. To remove any remaining impurities, the protein was loaded onto a Mono-Q strong anionic exchange chromatography column preequilibrated with LDAO buffer and was eluted with a 0-0.5 M gradient of NaCl in LDAO buffer. Heme-containing fractions were selected using spectroscopy at 410 nm and run on an SDS-PAGE gel. Heme and Coomassie staining were used to identify heme proteins and confirm the removal of impurities, respectively. The selected fractions were pooled and concentrated using a centrifugal spin concentrator (Vivaspin® 100,000 MWCO), before being snap-frozen and stored at -80°C for later use.

2.5 Biophysical and biochemical characterisation

2.5.1 Anaerobic working conditions

Many experiments in this thesis were carried under anaerobic conditions. Two different anaerobic chambers (Belle Technology glove box and MBRAUN UNI Lab Plus glove box) were used for all experiments. They both serve the same function of providing a controlled anoxic environment where all the oxygen has been replaced with nitrogen. For both chambers, conditions were considered anaerobic when the internal oxygen sensors reported oxygen concentrations of <0.5 ppm. Solutions were degassed by sparging with nitrogen before being introduced into the anaerobic chamber. This was done by sealing the solutions with a Suba-seal® and using a needle to bubble nitrogen directly into the liquid sample for ~ 1 minute mL^{-1} of sample to remove dissolved oxygen. The sealed samples were introduced into the anaerobic chamber and left unopened in the anoxic anaerobic atmosphere overnight. Where possible, small solutions were prepared by sparging the headspace of a sealed vial containing a measured solute, transferring the vial into the anaerobic chamber, and adding the appropriate solvent that had already been degassed as above previously. Protein samples were degassed by transferring into an anaerobic chamber and leaving opened for 30-60 minutes depending on volume. Sparging protein samples directly is unadvised as this may cause the sample to evaporate.

2.5.2 Ultraviolet-visible spectroscopy

The redox properties of the purified, soluble heme proteins were determined by taking electronic absorbance spectra on the oxidised and reduced proteins. The proteins were diluted in 20 mM Tris, 30 mM NaCl, pH 7.8 until the Abs at 410 nm was ~ 1.0. To reduce proteins, anaerobic (see 2.1.8 Anaerobic working conditions) sodium dithionite (~ 1 mg mL^{-1}) was titrated slowly until it was in excess, trying to keep the volume of added dithionite as low as possible. Proteins were considered fully reduced when further addition of dithionite did not change the reduced Soret peak (~ 420 nm). Measurements were taken from 350-750 nm, at 600 nm $minute^{-1}$, 1 nm data interval, and 0.1 seconds average time (Cary 60 UV-Vis Spectrophotometer, Agilent). The Beer-Lambert law, $A = \varepsilon cl$, where A is absorbance, ε is molar absorption coefficient (usually M^{-1} cm^{-1}), c is molar concentration (M), and l is optical path length (cm), was used to quantify the concentration of heme proteins at 410 nm using their known molar absorption coefficients (ε). All measurements were taken using a quartz cuvette where possible. Anaerobic measurements were done in a quartz cuvette sealed with a Suba-seal®. When taking anaerobic measurements, solutions were not inverted but shaken gently, as residual oxygen can remain on the inside side of the Suba-seal®.

2.5.3 Ascorbate reduction

To better understand the chemical nature of the heme axial ligand due to the ligand-to-metal charge transfer bands between 750-600 nm[165], the mild reductant ascorbate was used to reduce the proteins. Ascorbate has a potential of ~ +60 mV[166] which would allow it to reduce His/Met hemes much more readily than His/His hemes, due to the more positive potential of the former[167]. Air-oxidised proteins (A_{410} ~ 1.0) were titrated with anaerobic sodium ascorbate (50 mg mL^{-1}) until it was in excess, to partially reduce His/Met hemes, and then with sodium dithionite (10 mg mL^{-1}) to fully reduce all the hemes. Readings were taken immediately after adding ascorbate, and again after incubation for 15 minutes. Measurements were taken from 300-800 nm, at 400 nm $minute^{-1}$, 1 nm data interval, and 0.1 seconds average time (V-650 UV-Vis Spectrophotometer, Jasco). Protein solutions were prepared inside an anaerobic chamber (see 2.1.8 Anaerobic working conditions), sealed with a Suba-seal®, and removed from the chamber for spectrophotometric analysis.

Ascorbate and dithionite were added through the Suba-seal® using a microlitre syringe (Hamilton).

2.5.4 Pyridine hemochromagen assay

To determine the molar absorption coefficients of heme proteins, a pyridine hemochromagen assay was carried out based on a protocol from previously published work[168]. The principle behind the assay is due to pyridine being able to serve as a ligand for reduced hemes. First, a UV-Vis spectrum was taken of the air-oxidised proteins. Next, 50 mM pyridine in sodium hydroxide (1:4, vol:vol) was added 1:1 to the protein solution. This denatures the proteins and allows the pyridine to axially coordinated all the hemes in the sample, making them spectroscopically identical. Next, 100 mM sodium dithionite in 20 mM HEPES, 100 mM NaCl is added to reduce the hemes. As the ε of pyridine is known, the heme concentration can be calculated via the Beer-Lambert law. Based on the number of hemes per protein, the original concentration of protein can be calculated and used to determine the ε of the intact proteins in their oxidised and reduced states. Measurements were taken from 350-800 nm, at 300 nm minute^{-1} (U-3310 UV-Vis spectrophotometer, Hitachi).

2.5.5 Analytical ultracentrifugation

Analytical ultracentrifugation (AUC) can be used to study macromolecules in solution. The radial distribution of a species can be investigated with the use of a centrifuge with spectroscopic capabilities. In this thesis, only sedimentation velocity experiments were conducted (there were no sedimentation equilibrium experiments). Sedimentation over time of species was analysed as samples were centrifuged. Radial distributions are fitted to a series of Lamm equations which explain the sedimentation of a molecule in a cell as a function of the sedimentation coefficient[169]. These analyses can be used to determine if a sample is mono/oligo/polymeric and the heterogeneity of the sample.

Sedimentation analyses were conducted on single proteins as well as protein complexes. Proteins were diluted in appropriate buffers until A_{410} ~ 0.7. Centrifugation was carried out at 128,794 x *g*, 20°C and 200 scans of A_{410} were recorded every 3 minutes (Beckman Optima™ XL^{-1} analytical ultracentrifuge). For data analysis, the buffer viscosity and density were calculated using SEDNTERP

software[170]. The diffusion-deconvoluted sedimentation coefficient distribution c(s) was produced from the 200 scans in SEDFIT[171]. The calculated buffer density and viscosity were used to convert the sedimentation coefficients to standard values ($s_{20,w}$)[172]. Furthermore, 0.73 ml g^{-1} was used as the average partial specific volume was used for the conversion. The data were fitted in SEDFIT[171] using c(s) distribution analysis. The Svedberg equation[170] $\frac{S}{D} = \frac{M(1-\bar{v}\rho)}{RT}$ was used to calculate the molecular weight M of the trimeric complexes, where $\bar{v}$ is the protein partial specific volume, ρ the solvent buffer density, T the temperature, R the gas constant, D the protein diffusion coefficient, and S the protein sedimentation coefficient. The processed data were visualised using GUSSI[173].

2.5.6 Small-angle X-ray scattering (SAXS)

Protein samples were prepared by buffer exchanging into 20 mM HEPES, 100 mM NaCl, pH 7.5 using a centrifugal concentrator of appropriate MWCO. The proteins were then concentrated down to ~ 5 mg mL^{-1}. SAXS was carried out on the B21 beam at the Diamond Light Source Synchrotron (Harwell, Oxfordshire, United Kingdom). The experiments were done with a 10.5 keV 250 µm square X-ray beam and a 10^{12} photons second^{-1} flux. The data were collected on a 1024^2 pixel CCD detector at 4°C with a distance of 4 m between the detector and the sample. Furthermore, the intensity of the transmission was measured with a PIN diode beamstop. Scattering from a dilution range (~ 0.5 mg mL^{-1} to 5 mg mL^{-1}) of the protein solutions was recorded. 25 µL of sample were loaded onto the X-ray beam via capillary tubes (2 µm pathway) and were held in place as 180, 1 second exposures were taken. The first and last exposures were compared for any indications of radiation damage. After confirming no radiation damage had been observed, the 180 images were used to produce an average scattering profile. These average scattering profiles were averaged radially to create a 2D plot of momentum transfer (q) vs intensity (I). The background scattering of the HEPES and NaCl buffer without protein was subtracted. Momentum transfer is directly related to the scattering angle from the incident X-ray beam using the following equation: $q = \frac{4\pi}{\lambda} \cdot \sin\theta$ where q is the momentum transfer, λ is the X-ray wavelength, and 2θ is the scattering angle[174].

The data were processed further using ATSAS[175] software. Dataset scaling was carried out using PRIMUS, and preliminary calculation of the radius of gyration (the

root mean square average of the distance of electrons from the centre of the particle[176]; R_g) was done using AUTORG. This was done by applying the Guinier approximation to estimate R_g and $I(0)$ (extrapolated scattering intensity at zero angle or forward scattering intensity[176]). GNOM[177] was used to generate a real space electron pair-distance distribution p(r) of the average scattering profiles via an indirect Fourier transform method. The overall shape of the protein was visualised by producing *ab initio* models from the p(r) using DAMMIF[178] (oblate spheroid and slow annealing starting parameters). The resulting discrete bead models were averaged with the DAMAVER[179] program, and alignment of consistent intersecting features of all models was done using DAMFILT[180]. Finally, SUPCOMB[181] was used to align the two surface envelopes. The resulting structures were visualised in PyMOL.

2.5.7 Liquid chromatography-mass spectrometry (LC-MS)

LC-MS is a technique that can provide very accurate information on the mass of analysed proteins. For this thesis, LC-MS was carried out by Dr Jessica van Wonderen and Dr Colin Lockwood with help from the Prof Nick Le Brun team at UEA, as previously reported[182]. All proteins were buffer exchanged using a centrifugal spin concentrator of appropriate MWCO into 20 mM Tris, 5 mM NaCl, pH 7.5. 20 µL of protein sample (~ 50 µM) were mixed with 180 µL of 0.3% (v/v) formic acid and 1% (v/v) acetonitrile. This solution caused any cofactors that were not covalently bond to dissociate and resulted in the protein sample becoming denatured. The samples were inserted into a ProSwift RP-1S column (4.6 x 50 mm, Thermo Scientific™) which was part of an Ultimate 3000 uHPLC system (Dionex, Leeds, UK). Samples were eluted on a linear gradient of 2-100% acetonitrile, 0.1% formic acid. A Bruker microQTOF-QIII mass spectrometer was used to carry out positive mode electrospray ionisation mass spectrometry.

2.5.8 X-ray crystallography

To prepare for X-ray crystallography, the purified soluble heme proteins, were applied to a HiLoad® 16/600 Superdex® 75 pg size exclusion chromatography pre-equilibrated with 20 mM HEPES, 100 mM NaCl, pH 7.8. Heme containing fractions were identified by using Abs_{410} and the eluted protein was concentrated using a centrifugal concentrator (Vivaspin® 10,000 MWCO) to 10 mg mL^{-1}. Benjamin Nash helped throughout the protein crystallisation protocol and X-ray data analysis.

Protein crystals were obtained at 4°C from a sitting-drop vapour diffusion set up in a 96-well 1-drop crystallisation plate with 0.2 M magnesium acetate tetrahydrate, 0.1 M sodium cacodylate, 20% (w/v) polyethylene glycol (PEG) 8000, pH 6.5 as the reservoir solution. Total drop volume was 0.5 µL with a 1:1 (protein:reservoir). Crystals were cryoprotected by transfer into 0.2 M magnesium acetate tetrahydrate, 0.1 M MES, 20% (w/v) PEG 8000, 20% ethylene glycol, pH 6.5, before vitrification by plunging into liquid nitrogen.

2.5.9 Protein film electrochemistry

2.5.9.1 Porous ITO electrode preparation

Non-catalytic protein film electrochemistry (PFE) was carried out using hierarchically structured mesoporous indium-tin oxide (ITO) working electrodes (0.25 cm^2 surface area, 20 µm thickness) on glass coated with fluoride-doped tin oxide (FTO), following a previously reported procedure[183,184]. Alex Sutton-Cook helped with PFE electrode preparation, set-up, and cyclic voltammetry.

For the polystyrene-indium tin oxide (ITO) dispersion (PITOD), 35 mg of ITO (Nanotek) were dispersed in 300 µL of methanol solution (methanol:water, 6:1, v/v) by sonication (SW1H ultrasonic bath, Clifton) for three hours. 1 mL of polystyrene beads (750 nm, 2.54% (w/v) suspension in water, Polysciences) was subjected to centrifugation (5 minutes, 17,000 x *g*, 18°C). 900 µL of supernatant were removed and 1000 µL of methanol were added to the pelleted polystyrene beads. This mixture was sonicated for five minutes to ensure dispersion, and then centrifuged again (5 minutes, 17,000 x *g*, 18°C). The supernatant was carefully removed, and the dispersed ITO was added onto the pelleted polystyrene. This mixture was vortexed for two minutes and sonicated for 20 minutes (in an ice-water mixture). The product of this final sonication was the final PITOD.

A 10 cm x 10 cm x 0.3 cm glass slide coated with FTO (surface resistivity ~ 8 Ω sq^{-1}, Sigma-Aldrich) was cut down to 1 cm x 2 cm x 0.3 cm slides. These smaller FTO-coated glass slides were sonicated for 3 minutes in isopropyl alcohol. After, they were sonicated for 3 minutes in ethanol and allowed to dry at RT. To make the ring moulds for the ITO deposition for each slide, a 0.25 cm^2 was cut out of 4 layers of Sellotape using a 0.5 cm diameter hollow, steel, round punch cutter. All the ring moulds were strongly pressed by hand onto the conductive surface of a clean glass

slide coated with FTO (identified with a digital multimeter, Kelvin). The holes were centred on one end of the slides.

4.2 µL of the previously prepared PITOD were added to each ring mould and left to dry at RT for ≥ 4 hours. After, the polystyrene-ITO was redispersed (same method as above), and a further 4.2 µL were added to the ring mould to generate an ITO layer (20 µm thickness; 10 µm 4.2 μL^{-1} of PITOD within the 0.25 cm^2). The slides were left to dry at RT for ≥ 2 hours and the ring moulds were detached. Next, the slides were subjected to a gradually increasing temperature (1°C min^{-1}) until reaching 500°C (ELF 11/6B furnace, Carbolite). The slides were incubated for 20 minutes at 500°C and allowed to cool overnight at RT. The following day the slides were cleaned by submerging into a H_2O_2 (30%):H_2O:NH_4OH (28-30%) mixture (1:5:1) for 15 minutes at 70°C. Finally, the slides were washed gently with deionised water and incubated for 1 hour at 180°C. The final products were the porous hydrophilic hierarchical ITO electrodes.

2.5.9.2 Electrode configuration

Using heat-shrink tubing and a heat gun (TTB77RHTG, Titan), 2-3 cm of platinum wire was fastened to the FTO-coated surface of the electrode, on the end opposite end of the ITO deposition. The electrode was positioned in a glass Petri dish and was allowed to cool down (to ~ 5°C) by placing the Petri dish on ice for 20 minutes. After, 10 µL of protein (40 µM) were added to the electrode and left to adsorb for 15 minutes on the Petri dish on ice. The electrode was introduced into an anaerobic chamber and immediately used as the working electrode in a three-electrode configuration connected to a potentiostat (PGSTAT30 Potentiostat, Metrohm Autolab; controlled by Autolab Nova 2.1.4, Metrohm). Figure 2.2 shows a schematic of the electrode configuration used. The working electrode and a platinum wire counter electrode were placed in the main chamber of an in-house glass housing, both filled with 50 mM HEPES, 100 mM NaCl at pH 7.0. A Ag/AgCl (saturated with KCl) reference electrode was introduced to a side chamber of the glass housing. A Luggin capillary connected the sidearm to the main chamber and defined the sensing point. The section of the working electrode that contained the adsorbed protein was angled perpendicularly (and as close as possible) to the Luggin capillary, to maximise the detectable response.

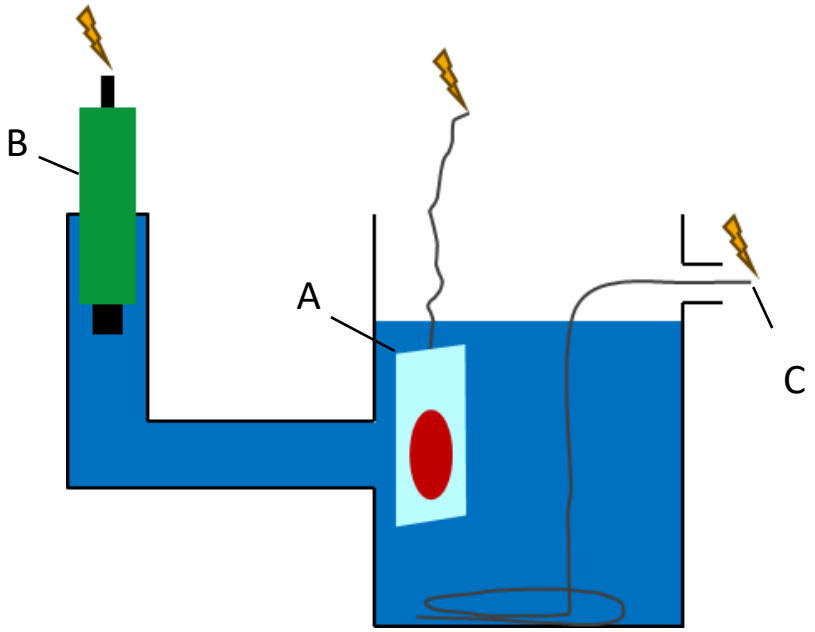

Figure 2.2. Diagram of the three-electrode glass housing configuration for cyclic voltammetry. The protein was adsorbed to an ITO (working) electrode (**A**) and connected to the top of the glass housing. A Ag/AgCl reference electrode (**B**) was connected to the glass housing through a side chamber. A coiled platinum wire counter electrode was positioned inside the glass housing, with an end protruding the glass housing on the right. All three electrodes were connected to the potentiostat at points indicated by yellow lightning bolts.

2.5.9.3 Cyclic voltammetry

Cyclic voltammetry was carried out as 5 linear scan repeats from -0.8 to 0.2 V at 20 mV s^{-1}. Potentials were converted from Ag/AgCl reference electrode to SHE reference electrode by addition of 0.195 V. QSoas 3.2[185] was used to calculate the reductive and oxidative non-catalytic peaks. The following equation can be used to interpret these non-catalytic peaks[186,187]:

$$|i| = \frac{\exp\left(\frac{nF}{RT}(E - E^0)\right)}{\left(1 + \exp\left(\frac{nF}{RT}(E - E^0)\right)\right)^2} \cdot \frac{n^2F^2vA\Gamma}{RT}$$

where $|i|$ is the current magnitude, n is the number of transferred electrons (in the oxidation or reduction reaction), F is Faraday's constant, R is the gas constant, T is the absolute temperature, E is the working electrode potential, E^0 is the reduction potential, v is the voltametric scan rate (V s^{-1}), A is the surface area of the working

electrode (cm^2), and Γ is the protein coverage of the electroactive redox protein (moles cm^{-2})[187]. The proximity of the area under the reductive and oxidative peaks was an indication of the success of the cyclic voltammetry and the reliability of the data. An arbitrary difference of 10% was used to determine whether the data produced were produced solely by the adsorbed protein, or by other molecules in solution. Once the reductive and oxidative areas were confirmed to be similar (± 10%), QSoas was used to subtract the baseline electrode response (ITO electrode without adsorbed protein) from the capacitive (non-Faradaic) current. The capacitive current is due to charging/discharging of the interface between the solution and the electrode; electrons do not transfer this interface. The Faradaic current (produced by electron transfer between the redox-active, adsorbed protein and the electrode)[187] can be calculated by subtracting the baseline electrode response from the capacitive current.

QSoas was also used to fit the Faradaic current peaks to non-catalytic voltammograms for the adsorbed proteins[185]. These fits simulated the distribution of individual heme potentials on the reductive and oxidative peaks, based on the overall potential of the protein. This helps understand if there are/are not hemes that have close, overlapping potentials. The current peaks were fitted to the sum of Z equivalent contributions from individual, n=1 redox centres (where Z is the number of hemes in the experimental electroactive redox protein) using the equation[188]:

$$i_F = \sum_{i=1}^{Z} \frac{X \cdot \exp\left(F\left(\frac{E - E_i}{RT}\right)\right)}{\left(1 + \exp\left(F\left(\frac{E - E_i}{RT}\right)\right)\right)^2}$$

where i_F is the Faradaic current, Z is the number of hemes in the protein, X is used to scale the calculated current to the experimentally measured magnitude, F is Faraday's constant, E is the sample potential, E_i is the reduction potential of centre i, R is the gas constant, and T is the absolute temperature[188]. This fit yielded Z number of peaks for the oxidative and reductive peaks, which were treated as pairs for each individual heme group of a protein containing Z hemes.

2.6 Whole-cell activity assays

2.6.1 Cell viability

When working with cells during *in vivo* experiments, finding a quick way of testing cell viability was imperative for the early experimental design. In protein purification, the state of the cells was of little importance, as the aim was to have the cells produce the highest concentration of protein, regardless of if that eventually became toxic to the cells. For each protein variant, expression trials were carried out (see 2.3.1. Protein expression trials) but instead of lysing the cells and running the lysate on SDS-PAGE gels, the viability of the cells the following day was assessed. This was done by using a resazurin-based cell viability reagent (PrestoBlue™ HS Cell Viability Reagent, Invitrogen™). Resazurin is a molecule that is blue (absorbs ~ 600 nm) and minimally fluorescent, that can easily cross cell membranes until it reaches the cytoplasm without damaging the cells. Once inside the cytoplasm, intracellular NADH or NADPH reduce the resazurin to resorufin, which is red/pink (absorbs ~ 570 nm) and highly fluorescent. It has been suggested that using resazurin produced results that were similar to counting colony-forming units (CFU) and were more sensitive than using the OD_{600}[189].

Before starting the assay, all induced cells need to have been normalised to an appropriate OD_{600}. To start the assay, 180 µL aliquots of normalised cells were added to a 96-well plate (plus 180 µL of the media the cells were grown in as a control). 20 µL of PrestoBlue™ were sequentially added to each well, mixed well, and a timer was started immediately. If the cells are viable (metabolically active), the solution will start to change from blue to pink. If the cells are too metabolically active (or the cell concentration is too high), the reaction can quickly go from blue to pink to then colourless (resorufin can be further reduced to dihydroresorufin which is non-fluorescent). When the cells had an appropriate metabolic activity, the resorufin started to turn pink (within ~ 2 minutes). Before the solution had fully gone pink, the reaction was stopped with 50 µL of 10% SDS. The same incubation time was used for all the samples before adding the 10% SDS. When all reactions had been stopped with the SDS, the plate was inserted into a plate reader (FLUOstar Omega, BMG LABTECH). Measurements were taken from 300-700 nm, 0 RPM, 1.0 nm wavelength step width, 20 flashes $well^{-1}$, 250 µL absorbance path length correction volume, and 1.3605 absorbance path length correction factor.

After extracting the data from the plate reader, the following formula was used to calculate the PrestoBlue™ reagent reduction percentage =

$$\frac{(O_1\, x\, A_1) - (O_2\, x\, A_2)}{(R_1\, x\, M_1) - (R_2 x M_2)} \cdot 100$$

where O_1 is the ε_{600} of oxidised PrestoBlue™ reagent (117,216 M^{-1} cm^{-1}), A_1 is the A_{570} of the sample wells, O_2 is the ε_{570} of oxidised PrestoBlue™ reagent (80,586 M^{-1} cm^{-1}), A_2 is the $A_{600}$of the sample wells, R_1 is the ε_{570} of reduced PrestoBlue™ reagent (155,677 M^{-1} cm^{-1}), M_1 is the A_{600} of the control (media only) wells, R_2 is the ε_{600} of reduced PrestoBlue™ reagent (14,652 M^{-1} cm^{-1}), and M_2 is the is the A_{570} of the control (media only) wells. *S.* oneidensis cells that had PrestoBlue™ reagent reduction percentages that were ±10% were considered adequate, and acceptable for normalisation.

This cell viability assay was employed each time an activity assay was done for the first time, or each time a new protein variant was expressed in a *S. oneidensis* strain. From that point moving forwards, the OD_{600} of overnight cultures compared to the controls was used as an indicator for cell viability. Also, after each activity assay was carried out for the first time, the normalised cells were kept and run on an SDS-PAGE whole-cell gel (see 2.1.7 Whole-cell SDS-PAGE gel preparation, and 2.3.1 Protein expression trials).

2.6.2 Ferrozine assay

Several of the activity assays involved quantifying the reduction of soluble Fe(III) to Fe(II) by *S. oneidensis* cells. To do so, an assay was developed based on previous work[190]. The ferrozine solution was composed of 10 mM ferrozine (3-(2-Pyridyl)-5,6-diphenyl-1,2,4-triazine-4',4''-disulfonic acid sodium salt) and 100 mM ammonium acetate in RO water. The ferrozine solution was filter-sterilised (0.2 µm filter) before use. As the reduced Fe(II) can be reoxidised by oxygen, any assayed sample was maintained anaerobic for as long as possible, before quickly carrying out the ferrozine assay. First, 750 µL of sample were carefully extracted from a Suba-sealed container using a syringe and a thin needle (23G x 1”, BD Microlance™ 3). The samples were immediately subjected to centrifugation (5 minutes, 20,000 x *g*, 18°C) to pellet any insoluble components. 500 µL of the supernatant were transferred to a polystyrene cuvette, 30 µL of ferrozine solution were added and mixed thoroughly, and the solution was incubated for 60 seconds. As the results from the ferrozine

assay are largely dependent on incubation time (amongst other things) the 60 seconds must be the same for all samples. Measurements were taken from 400-800 nm, at 600 nm min^{-1}, 1 nm data interval, and 0.1 seconds average time (Cary 60 UV-Vis Spectrophotometer, Agilent).

The ferrozine solution reacts with Fe(II) (but not with Fe (III)) and turns purple/blue. The absorbance maximum is at 562, so the A_{562} was used to quantify soluble Fe(III) concentrations. To do so, a standard curve was prepared using known $Fe(II)Cl_2$ concentrations (see Figure 2.3). The linear regression formula was rearranged and used to extrapolate measured absorbances during the activity assays and convert them to concentration of Fe(II).

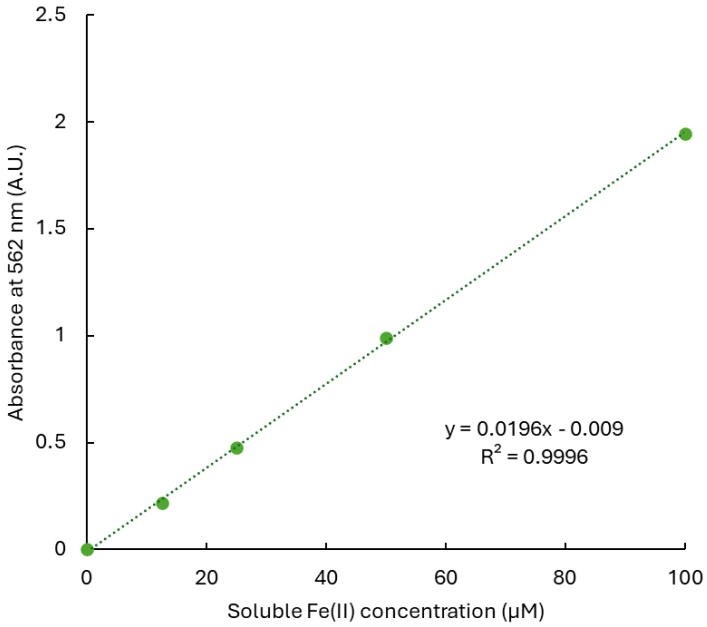

Figure 2.3. Standard curve used for ferrozine assay. 0, 12.5, 25, 50, and 100 µM $Fe(II)Cl_2$ were used. The formula for converting absorbance to concentration was rearranged so that $x = \frac{y+0.009}{0.0196}$ where x is concentration of Fe(II) in µM, and y is A_{562} in A.U.

2.6.3 Flavin mononucleotide reduction assay

The protocol for the flavin mononucleotide (FMN) reduction experiments was based on work by Coursolle *et al.*[113]. FMN can act as an electron shuttle that facilitates EET by transferring electrons from outer-membrane multiheme cytochromes such as MtrC, to the terminal electron acceptor. The FMN molecules can go from a fully

oxidised state to a one-electron reduced state (flavin semiquinone), and finally to a two-electron reduced state (fully reduced).

To begin single colonies were picked to make cultures that were grown overnight (180 RPM, 30°C) in LB or LB_{kan}. These cultures were then used as a 0.1% inoculum for 10 mL of M72 media with supplements (see 1.1.1. Media preparation), 1 mM L-arabinose, and 10 µL of kanamycin (where necessary) in a sealed Universal tube. These cells were incubated for 18 hours at 25°C 120 RPM, and (without opening the lid) were transferred to an anaerobic chamber. As the incubation progressed, the cells used up most of the oxygen within the sealed container, but to become fully anaerobic, they were left opened in the anaerobic chamber for one hour to remove any residual oxygen. After an hour (the oxygen sensor in the anaerobic chamber reading should have gone down to <0.5 ppm), 5 mL of cells were anaerobically harvested by centrifugation (10 minutes, 3,000 x *g*, 18°C) and resuspended in 4 mL of SMM (Shewanella minimal medium, see 2.1.1. Media preparation) supplemented with fresh, 20 mM anaerobic sodium DL-lactate and kanamycin where necessary. An anaerobic FMN stock (1 mM) was also introduced and opened into the anaerobic chamber to remove residual oxygen. The final concentration of FMN in solution was 12 µM, so 36 µL of 1 mM FMN were used in these experiments. The cells were normalised so that adding 2,964 µL of cells and 36 µL of FMN, resulted in an OD_{600} of 0.1. Inside the glovebox, 2,974 µL of normalised cells were added to a 3 mL quartz fluorescence cuvette and sealed with a lid that the addition of FMN with a microlitre syringe (Hamilton). >36 µL of FMN (1 mM) were taken up into the microlitre syringe inside the glovebox, before introducing the sealed cuvette to the fluorimeter (Cary Eclipse Fluorescence Spectrophotometer, Agilent). The fluorimeter was set to excitation at 365 nm and emission at 525 nm, medium detector voltage, taking a read every second for 10 minutes. The background fluorescence of the cells was recorded for a few seconds (to confirm nothing unusual was happening) before anaerobically adding 36 µL of 1 mM FMN (12 µM final concentration) to the fluorescence cuvette. Absorbance data were converted to rates of reduction using the Beer Lambert law.

2.6.4 Soluble OmcA reduction

OmcA usually exchanges electrons with MtrC on the surface of the outer membrane of *S. oneidensis*. OmcA has a heme coordination similar to that of MtrC, where there is a possibility for electrons to be transferred laterally between adjacent MtrC and OmcA proteins. To investigate this, soluble OmcA was used as an electron acceptor, and reduction with *S. oneidensis* strains expressing membrane-bound MtrC variants was reported spectroscopically.

S. oneidensis cells were induced, cultured, harvested, and resuspended in SMM supplemented with 20 mM anaerobic sodium DL-lactate , as above (see 2.6.3 Flavin mononucleotide reduction assay). Cells were normalised to an OD_{600} of 1.0.Purified, soluble OmcA was introduced into the glovebox and opened for one hour before use to remove any residual oxygen. The soluble OmcA was diluted in the same SMM 20 mM lactate, until the A_{410} ~ 1.0. The 96-well plates used in this experiment were introduced into the glovebox the day before to remove residual oxygen. In each test well, 25 µL of normalised *S. oneidensis* cells were added to 225 µL of the diluted OmcA in SMM lactate, resulting in a final OD_{600} of 0.1 of the cells. Control wells were prepared similarly, with the addition of 1 µL of sodium dithionite (10 mg mL^{-1}). These controls served as a reference point for full reduction of the OmcA and helped monitor the anaerobic conditions of the 96-well plate during the experiment. Immediately after adding the cells to the OmcA SMM lactate solution inside the glovebox, the 96-well plates were sealed with a plate seal (Adhesive PCR Plate Seals, Thermo Scientific™) to prevent oxygen from entering. Quickly, the sealed plate was removed from the glovebox, and a thin layer of poly cement (Poly Cement Colle Polystyrene, Humbrol™) was applied to the edge of the plate. The poly cement works by melting the plastic on the edge of the plate and inside of the plate lid, which allows them to be “welded”, forming a strong bond, and further limit any oxygen from entering the plate. The plate was rapidly introduced into the plate reader (FLUOstar Omega, BMG LABTECH), and electronic absorbance measurements were recorded from 350-700nm at varying intervals (every 1, 3, 5, 15, or 20 minutes), 0 RPM, with 2 nm data interval, and a path length of 7.89 mm (250 µL absorbance path length correction). The sharpening of the alpha (~ 552 nm), beta (~ 525 nm), and Soret (when oxidised ~ 410 nm, upon reduction ~ 420 nm)

bands was used to monitor the reduction of OmcA. Data measurements were taken until the reduction no longer continued.

The increase in A_{552} (alpha band) was used to quantify the reduction of OmcA. Calculations were done based on the fraction of reduction when compared to full reduction (the control wells with sodium dithionite). The fraction reduced was then converted to concentration of OmcA using the Beer Lamber law with a ε_{410} of 1,670 mM^{-1} cm^{-1} [191] .

2.6.5 Ferric citrate reduction

S. oneidensis can transfer electrons directly to Fe(III) (ferric) complexes reducing them to Fe(II) (ferrous) complexes. To investigate differences in EET rates across cells expressing membrane-bound MtrC variants, a reduction assay using the physiological electron acceptor Fe(III) citrate was designed.

S. oneidensis cells were grown overnight (180 RPM, 30°C) in LB or LB_{kan}. They were harvested by centrifugation (10 minutes, 3,000 x *g*, 18°C) and resuspended to an OD_{600} of 0.1 in 25 mL of SMM supplemented with 20 mM sodium DL lactate, 1 mM L-arabinose, 5 mM ferric citrate, and kanamycin where necessary (filter-sterilised, 0.4 µm). The 25 mL samples were prepared in 25 mL Universal tubes, which were sealed with a Suba-Seal®, resulting in a very reduced headspace. The cells were incubated at 30°C, 0 RPM, and measurements were taken every 2 hours. This was done by carefully extracting samples through the Suba-Seal® and assessing their Fe(II) concentration via the Ferrozine assay (see 2.6.2 Ferrozine assay) and the linear regression from a ferrous chloride standard curve (Figure 2.1).

As the Suba-Seal® provided a contained environment within the Universal tube, withdrawing volume through the syringe for Fe(II) quantification lowered the pressure inside the sealed environment. With a decreased pressure, there is a higher likelihood for environmental oxygen to be drawn into the Universal. To counteract this decreasing pressure, after every two reads (or every four hours), all the samples were sparged for one second with sterile nitrogen (the nitrogen was channelled through a 0.2 µm filter) through the Suba-Seal® using a sterile needle. This made the pressure inside the sealed Universal more positive and helped prevent oxygen from re-entering.

2.6.6 Ferric EDTA reduction

Similarly to Fe(III) citrate, *S. oneidensis* can use Fe(III) EDTA as an electron acceptor in EET. This experiment was the same as the 2.6.5 Ferric citrate protocol, except that 5 mM Fe(III) EDTA was used instead of 5 mM Fe(III) citrate. The solution was also filter-sterilised (0.4 µm) before use. The ferrozine assay was used to determine the reduction of Fe(III) to Fe(II) in solution.

2.6.7 Azo dye reduction

To have a better understanding of the effect modifying the outer-membrane cytochromes had on EET in *S. oneidensis*, three non-physiological electron acceptors were selected, Reactive Black 5 (RB5), Amaranth, and Methyl orange (MO). These are all azo dyes which are bright and colourful. However, upon reduction of the azo bond (-N=N-), the dyes become colourless. This allows for a way to easily assess the reductive capacities of *S. oneidensis* strains expressing MtrC variants.

In these experiments, a 96-well plate was prepared in the same was as 2.6.4 Soluble OmcA reduction. Each well contained 250 µL of azo dye (60 µM RB5, 30 µM Amaranth, or 60 µM MO, all in anaerobic RO water) with cells at a final OD_{600} of 0.1. Controls were also prepared with 1 µL of sodium dithionite (10 mg mL^{-1}) to monitor any oxygen leaking into the sealed 96-well plate. Measurements were taken from 350-700 nm, 0 RPM, every 20 minutes for 12 hours, 2 nm data interval, with a path length of 7.89 mm (250 µL absorbance path length correction).

Chapter 3

Increased angle within MtrC

3. MtrC S188V N251D

3.1 Introduction

MtrC is one of the terminal reductases in *S. oneidensis*' extracellular electron transfer (EET) that enables the electrons produced during intracellular metabolism to be transported onto an extracellular terminal electron acceptor. It forms part of the MtrCAB heterotrimer, comprised of a decaheme cytochrome, MtrA, which is embedded in a 26 β-strand porin, MtrB[88]. This MtrAB dimer sits within the outer membrane of *S. oneidensis*, with the N-terminus of MtrA receiving electrons from the periplasm, and the C-terminus transferring them to MtrC on the cell surface. Once the electrons are passed onto MtrC, they can then be directly transported to a soluble or insoluble terminal electron acceptor, such as Fe(III)/Mn(IV) oxides, or indirectly via electron shuttles, such as flavins, that mediate the EET to the terminal electron acceptor[131]. However, due to the "staggered cross" arrangement of the MtrC hemes, it is also possible for the electrons to be passed laterally to other acceptors, such as the decaheme OmcA[191,192]. This is possible because the ten hemes within MtrC lie within two separate domains, with five hemes in domain II and five hemes in domain IV. Previous work[88] has suggested that domains I and II displayed movement relative to domains III and IV. This movement was centred around residues 289-300 which are located in the α-helix that links domains II and III. It was also suggested that such a movement at this hinge location would not be restricted in the MtrCAB complex[88].

Here, we sought to investigate this movement between domains I, II and domains III, IV. To do so, two codons on *mtrC* were mutated (Figure 3.1). The serine 188 codon (TCT) was mutated a valine codon (GTG), changing the polarity of the side chain from polar to non-polar (hydrophobic). This would result in a disruption of hydrogen bonding, as valine is non-polar and can therefore only participate in van der Waals interactions. Next, the asparagine 251 codon (AAT) was mutated an aspartic acid codon (GAC), changing the side chain from polar to having a negative charge. This would again disrupt hydrogen bonding, but also introduce electrostatic changes. As the exposed propionates on MtrC have an overall negative charge, it would be expected that the aspartic acid would be repelled by the propionates to a certain extent. We hypothesise that changing two amino acid residues in MtrC will

result in a change in local polarity and charge, which will consequently disrupt the hydrogen bonding and increase the electrostatic repulsion between domains I, II and domains III, IV, affecting the EET capacity of the protein.

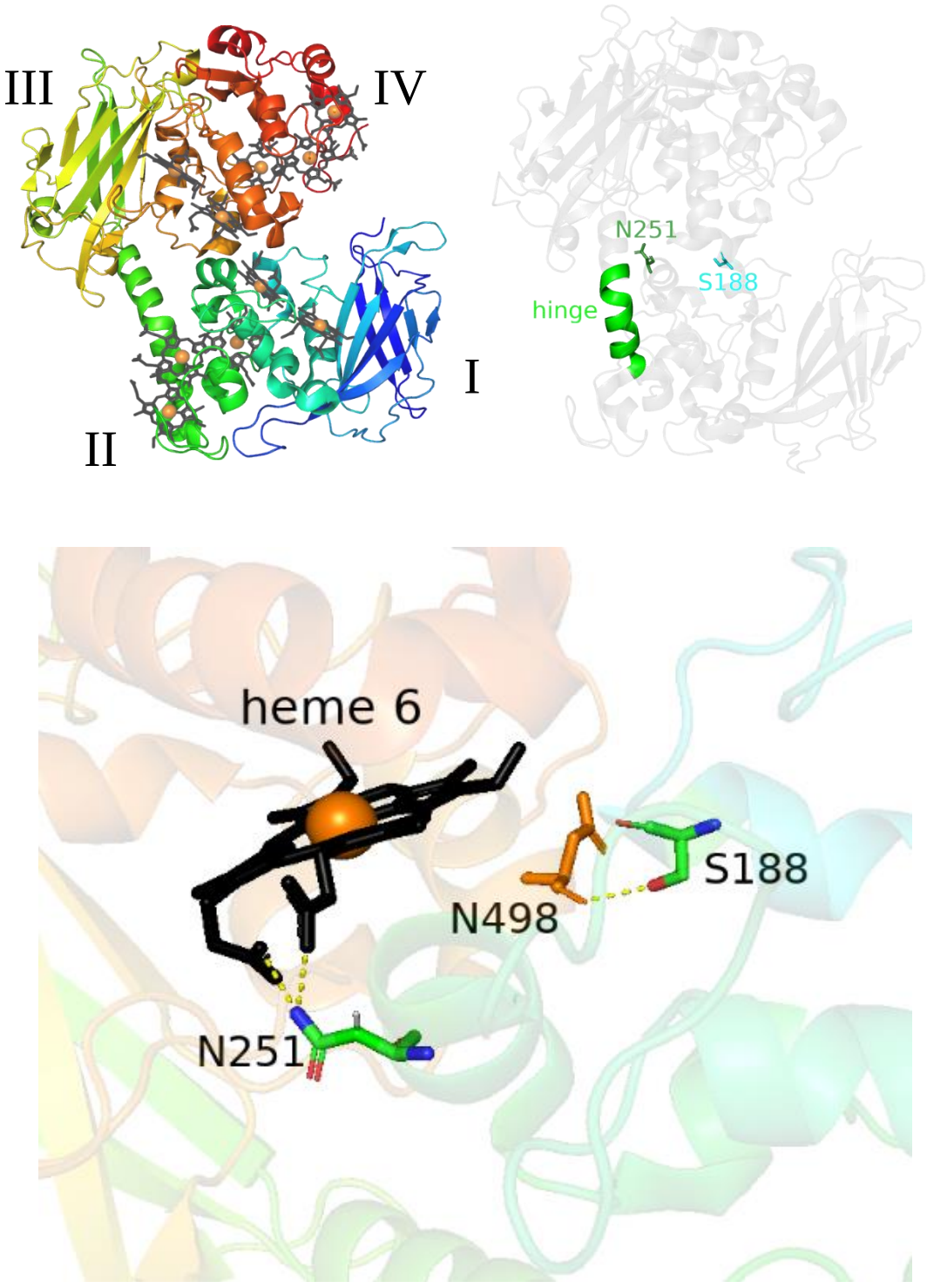

Figure 3.1. Crystal structure of MtrC from *S. oneidensis* (PDB:4LM8). **Top, left.** MtrC is represented as a cartoon, with the four domains numbered in roman numerals. The ten hemes are shown too. **Top, right.** The MtrC structure is shown in grey, with the hinge region, serine 188 (S188), and asparagine 251 (N251) coloured in green, dark green, and cyan, respectively. **Bottom**. Interactions between S188 and N251 and neighbouring molecules. The hydrogen bonds between the S188 and asparagine 498, and between N251 and heme 6 are indicated with yellow dashed lines. Hemes are show in black with the iron core as an orange sphere. Figure created in PyMOL.

3.2 Results and discussion

3.2.1 Plasmid design and generation

3.2.1.1 Production of soluble pMTRC$_{DM}$ plasmid

A pBAD plasmid containing the soluble (without a lipid anchor) WT version of MtrC (soluble pMTRC$_{rec}$) with a Strep(II) tag was obtained from the laboratory repository at the University of East Anglia, Norwich (Table 2.3 in Methods 2.2.11). The plasmid DNA (pDNA) was sequenced (Methods 2.2.10) and was successfully aligned in Benchling to *mtrC* WT (NCBI: QKG96446), with all DNA bases aligning as expected.

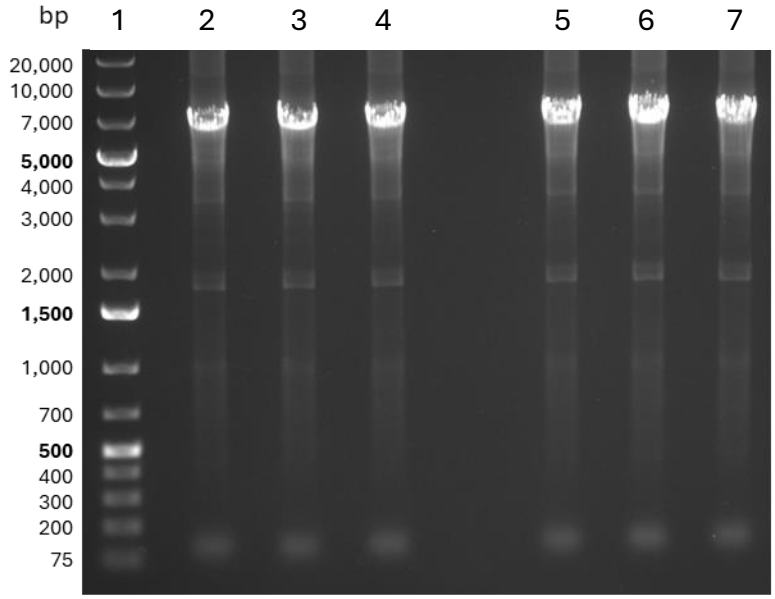

Figure 3.2. 0.8% agarose gel of the PCR products after the soluble MtrC S188V and N251D PCR. An annealing temperature gradient was done to optimise the success rate. The lanes are as follow: molecular marker (lane 1), annealing at: 60°C (lane 2), 58°C (lane 3), 54°C (lane 4), 52°C (lane 5), 50°C (lane 6), 48°C (lane 7). The bright bands around 7,000 bp are the successful PCR products.

After the DNA sequence from the template soluble pMTRC$_{rec}$ plasmid was determined to be correct, a PCR was carried out to replace the serine codon at amino acid position 188 with the valine codon (S188V) resulting in the pMTRC$_{S188V}$ plasmid. Then, a second PCR was done to replace the asparagine codon at amino acid position 251 with the aspartic acid codon (N251D) resulting in a double mutant plasmid that contained both amino acid changes (*mtrC* double mutant, pMTRC$_{DM}$)

The PCR primers used are detailed in Table 2.2 in Methods 2.2.3, and the PCR conditions are shown in Methods 2.2.3. The PCR products (pMTRC$_{DM}$) were

visualised on a 0.8% agarose gel (Methods 2.1.3) to confirm the amplification (Figure 3.2).

Once the PCR was confirmed to have worked via the gel electrophoresis, a DpnI digest was carried out (Methods 2.2.4) on the soluble pMTRC$_{DM}$ PCR product. Next, the DpnI and the buffers used in the reaction were removed by using a PCR clean-up kit. After, the soluble pMTRC$_{DM}$ was transformed into competent *E. coli* TOP10 cells via heat shock (Methods 2.2.7 and 2.2.8). The pDNA was extracted from the transformants and sent for sequencing to confirm the S188V and N251D mutations in the DNA had occurred successfully.

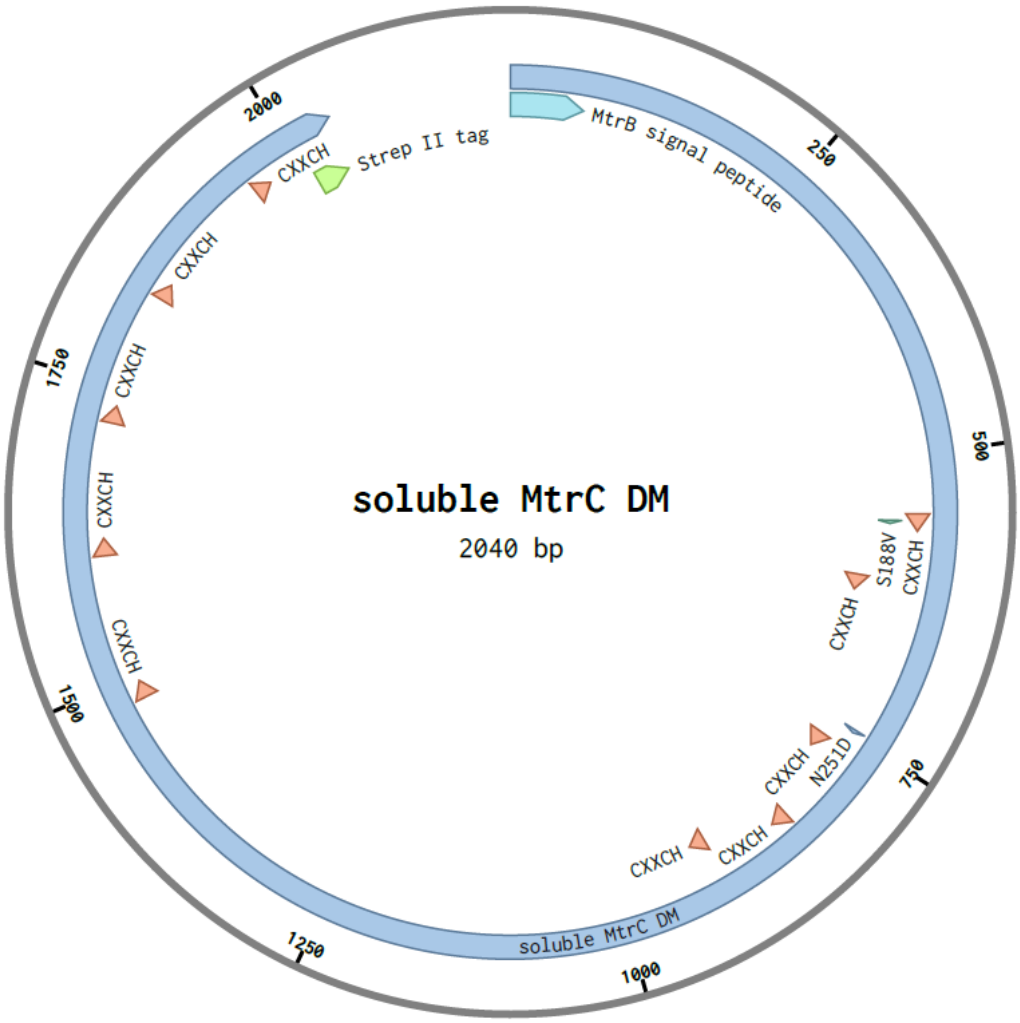

Figure 3.3. Sequencing data from soluble pMTRC$_{DM}$ obtained from Eurofins and visualised in Benchling. As this is the soluble and not lipid-anchored form, the MtrB signal peptide (light blue arrow) replaces the native MtrC signal peptide. CXXCH heme binding motifs are shown with red arrows. The Strep(II) tag is shown with a light green arrow. The locations for the S188V and N251D mutations are shown with a dark green and dark blue arrows, respectively. Note: even though the sequencing data is linear, it has been shown as circular to better visualise the components.

Finally, the plasmid was transformed into a *S. oneidensis* Δ*mtr* strain via electroporation (Methods 2.2.9). This strain was selected because the soluble protein was intended for purification, therefore production of MtrA and MtrB proteins was not necessary. To check if any unwanted mutations had been introduced during the electroporation into *S. oneidensis* cells, the pDNA was extracted and sent for sequencing (Figure 3.3). Upon confirmation of the correct pDNA sequence, protein expression trials were commenced.

Figure 3.4 shows the full, mature translated DNA sequence for $MtrC_{DM}$, with the CXXCH binding motifs, as well as the location of the two amino acid residue changes.

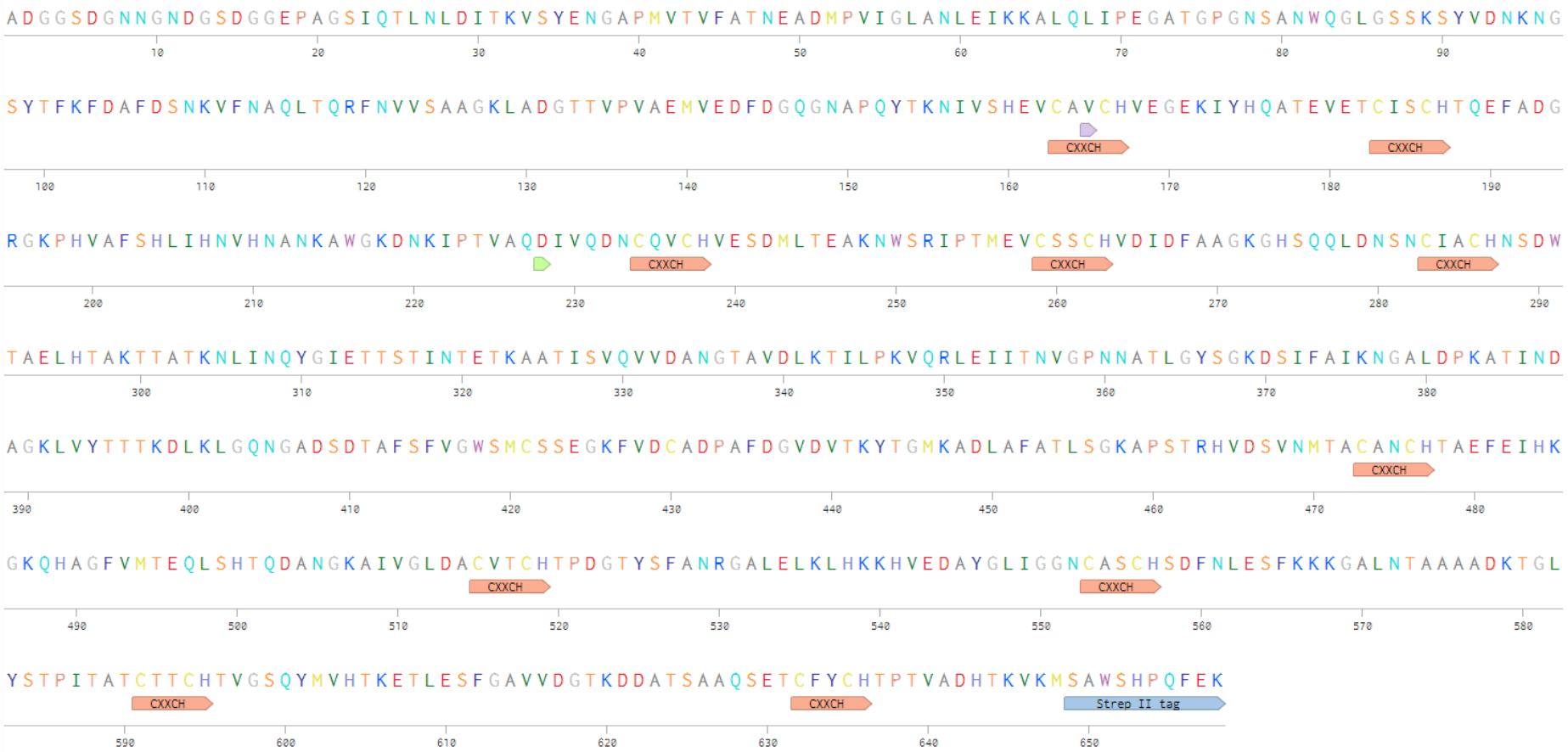

Figure 3.4. Translated DNA sequence for mature, soluble $MtrC_{DM}$. The first amino acid residue shown is the alanine immediately after the MtrB signal peptide cut site. The sequence ends with the Strep(II) tag (blue arrow).The CXXCH motifs are shown within the orange arrow labels over the sequence. The two locations for the codon mutations are shown, S188V (purple arrow) and N251D (green arrow). The mutations on the soluble $MtrC_{DM}$ sequence are not at the expected positions, as the native *mtrC* signal peptide was replaced for the *mtrB* one, which is of a different length. Figured produced in Benchling.

3.2.1.2 Production of membrane pMTRC$_{DM}$ plasmid

A pBAD plasmid with the lipid-anchored (membrane-bound) MtrC WT (membrane pMTRC$_{rec}$) was obtained from the laboratory repository at the University of East Anglia, Norwich (Table 2.3 in Methods 2.2.11). The pDNA was extracted and sent for sequencing (Methods 2.2.10). The plasmid was aligned to *mtrC* WT with no mismatches.

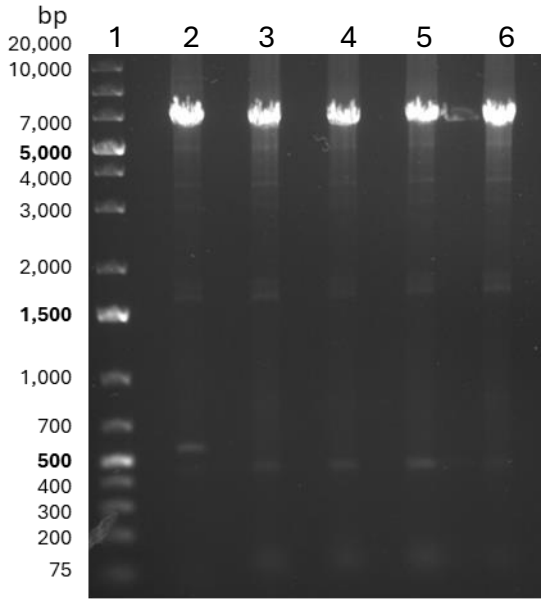

Figure 3.5. 0.8% agarose gel of the PCR products after the membrane MtrC S188V and N251D PCR. An annealing temperature gradient was done to optimise the success rate. The lanes are as follow: molecular marker (lane 1), annealing at: 60°C (lane 2), 58°C (lane 3), 54°C (lane 4), 52°C (lane 5), 50°C (lane 6). The bright bands at ~ 7,000 bp are the successful PCR products.

After checking that the pMTRC$_{rec}$ sequence was correct, a PCR was done to replace serine at amino acid position 188 with valine (S188V). Then, a second PCR was done to replace asparagine at amino acid position 251 with aspartic acid (N251D). The PCR conditions and primers are detailed in Methods 2.2.3 and Table 2.2. The PCR products (membrane pMTRC$_{DM}$) were visualised on a 0.8% agarose gel (methods 2.1.3) to confirm the success of the PCR (Figure 3.5).

After confirming the success of the PCR via gel electrophoresis (Figure 3.5), a DpnI digest (Methods 2.2.4) and PCR clean-up (Methods 2.2.7) were done. Next, the membrane pMTRC$_{DM}$ was transformed into competent *E. coli* TOP10 cells (Methods 2.2.8). The pDNA was extracted from the *E. coli* and sequenced to confirm the S188V and N251D mutations in the DNA had occurred successfully. Lastly, the

pMTRC$_{DM}$ was transformed into a *S. oneidensis* Δ*mtrC/omcA* strain via electroporation (methods 2.2.9).

To confirm that no unwanted mutations had been introduced into the pDNA during the electroporation, membrane pMTRC$_{DM}$ was extracted and sent for sequencing (Figure 3.6). After confirming that the plasmid sequence was correct, protein expression trials were started. All plasmids used in this chapter are shown in Table 3.1.

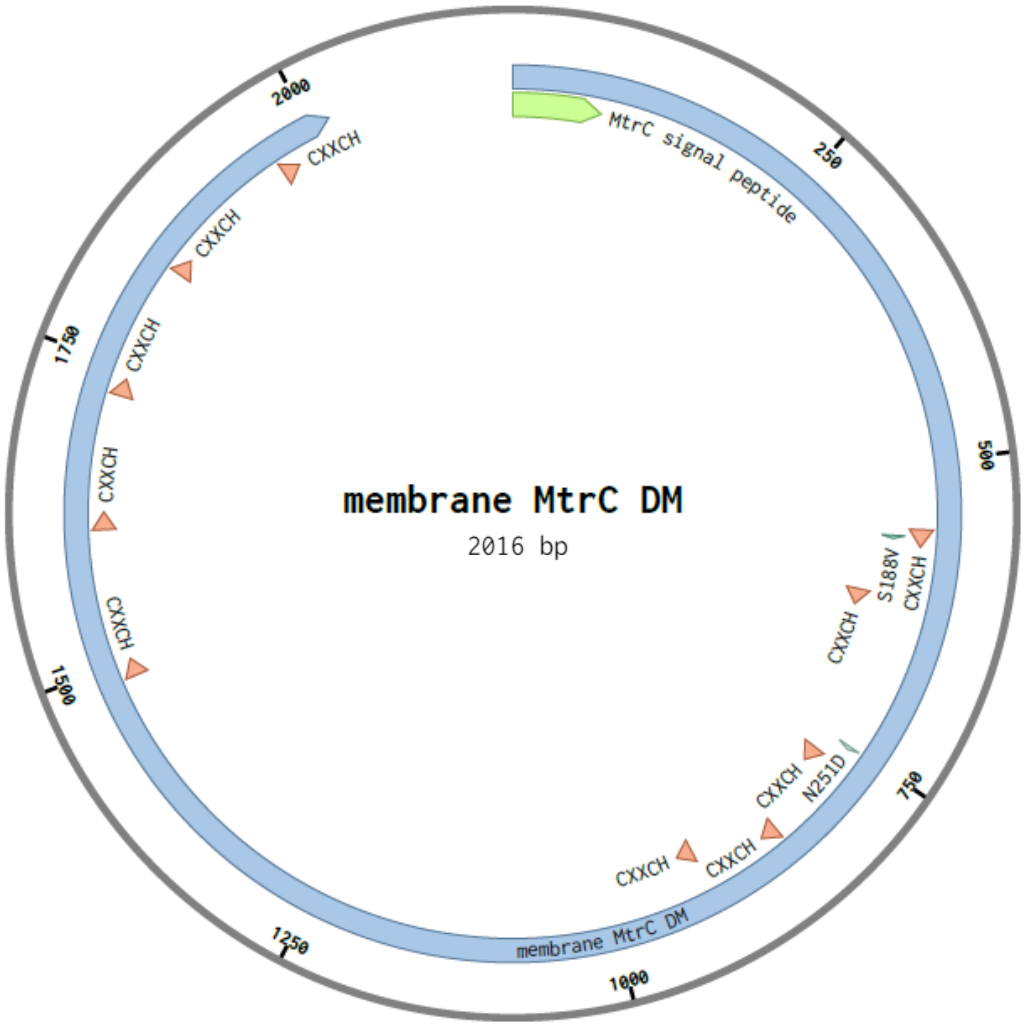

Figure 3.6. Sequencing data from membrane pMTRC$_{DM}$ obtained from Eurofins and visualised in Benchling. The MtrC signal peptide (green arrow), CXXCH heme binding motifs (orange arrows), and locations for S188V (dark blue arrow) and N251D (dark green arrow) mutations are shown. Note: even though the sequencing data is linear, it has been shown as circular to better visualise the components.

Table 3.1. Plasmids used in this chapter with indicated relevant features. Text in bold forms part of each plasmid name.

Plasmid	Features
Soluble pMTRC$_{rec}$	*mtrB* signal peptide, no lipid anchor; no more modifications to *mtrC* (**rec**ombinant)
Soluble pMTRC$_{S188V}$	*mtrB* signal peptide, no lipid anchor; **s**erine codon at amino acid position **188** of *mtrC* changed to **v**aline codon
Soluble pMTRC$_{DM}$	*mtrB* signal peptide, no lipid anchor; serine codon at amino acid position 188 of *mtrC* changed to valine codon; asparagine codon at position 251 changed to aspartic acid codon (**d**ouble **m**utant)
Membrane pMTRC$_{rec}$	Native *mtrC* signal peptide, lipid anchor; no modifications to *mtrC,* (**rec**ombinant)
Membrane pMTRC$_{S188V}$	Native *mtrC* signal peptide, lipid anchor; **s**erine codon at amino acid position **188** of *mtrC* changed to **v**aline codon
Membrane pMTRC$_{DM}$	Native *mtrC* signal peptide, lipid anchor; serine codon at amino acid position 188 of *mtrC* changed to valine codon; asparagine codon at position 251 changed to aspartic acid codon (**d**ouble **m**utant)

3.2.2 Soluble MtrC$_{DM}$ expression trials

An expression trial was done to confirm the correct production and secretion of soluble MtrC$_{DM}$ by the *S. oneidensis* Δ*mtr* cells with soluble pMTRC$_{DM}$ plasmid (Methods 2.3.1). Gene expression was induced with 5 mM L-arabinose. Six hours after induction of expression, the cells were harvested by centrifugation and discarded. The spent media samples and controls were run on an SDS-PAGE gel (Methods 2.3.3) and stained for heme (Methods 2.3.5).

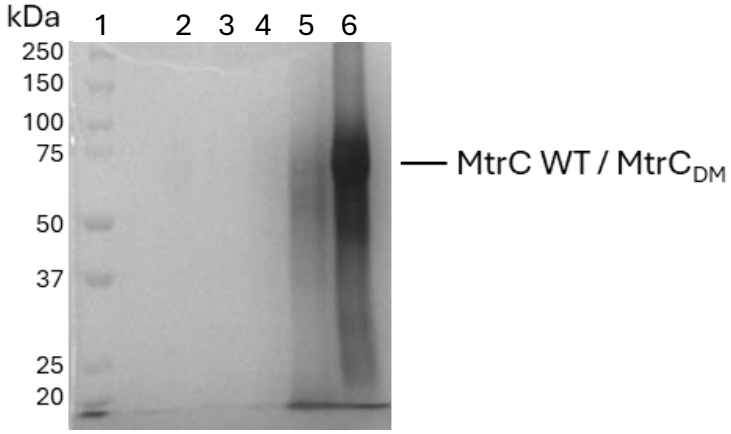

Figure 3.7. Heme-stained SDS-PAGE gel from the spent media of the of *S. oneidensis* Δ*mtr* cells with the soluble pMTRC$_{DM}$ plasmid expression trial. Lanes are as follows: molecular marker (lane 1), MR-1 (lane 2), Δ*mtr* (lane 3), Δ*mtr* cells with uninduced pMTRC$_{DM}$ plasmid (lane 4), Δ*mtr* cells with pMTRC$_{DM}$ plasmid induced with 5 mM L-arabinose (lane 5), Δ*mtr* cells with pMTRC$_{rec}$ plasmid induced with 5 mM L-arabinose (lane 6). MtrC$_{rec}$ (WT) and MtrC$_{DM}$ are indicated with lines.

Figure 3.7 shows the heme-stained gel with strong banding where MtrC was expected to be (~ 76 kDa). As the sample contains only the cell-free spent media, the gel does not show banding of fumarate reductase (~ 65 kDa) in any strain, which can appear as a false positive in SDS-PAGE gels of MtrC. Furthermore, some of the fumarate reductase is also removed during the centrifugation step. The difference in the MtrC band is also clear between the uninduced sample (Figure 3.7, lane 4) and induced samples (Figure 3.7 lanes 5, 6).

3.2.3 Soluble $MtrC_{DM}$ purification

After confirming with the expression trials that the proteins were being expressed correctly, a larger-scale purification protocol was carried out. To purify the proteins, cells were cultured, and proteins were extracted as detailed before (Methods 2.4.1 and Methods 2.4.3). Purification was carried out using the Strep(II) tag on the C-terminus of $MtrC_{DM}$ (Figure 3.8). After the Strep(II) tag column, size-exclusion chromatography (SEC) on a Superdex 16/600 75 pg was carried out on the proteins to further remove any impurities. shows a single, principal peak for both the absorbance at 410 nm and 280 nm.

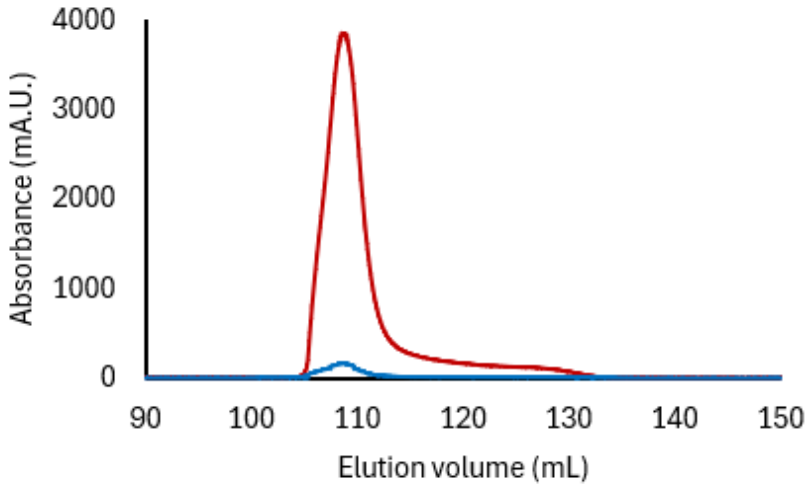

Figure 3.8. ÄKTA traces from Strep(II)-tag column purification of soluble $MtrC_{DM}$. The A_{410} and A_{280} are shown as red and blue lines, respectively. The A_{410} was used to select which fractions to run on SDS-PAGE gels to assess the purity of the proteins. Proteins were purified from a 4 L culture.

3.2.4 Liquid chromatography-mass spectrometry on soluble $MtrC_{DM}$

Once the soluble $MtrC_{DM}$ was determined to be of sufficiently high purity by SDS-PAGE gels the protein samples were submitted for LC-MS (Methods 2.5.6). Figure 3.9 shows the processed data from the LC-MS with a large primary peak at 76,267 Da corresponding to $MtrC_{DM}$.

Benchling was used to predict a mass of 70,113 Da for the mature soluble $MtrC_{DM}$ polypeptide backbone on its own, and 76,265 Da when adding the mass of 10 *c*-type hemes (615.71[193] Da $heme^{-1}$). The observed experimental molecular mass obtained from the LC-MS was 76,267 Da (Figure 3.9), putting it 2 Da away from the predicted molecular mass of soluble $MtrC_{DM}$. For soluble $MtrC_{rec}$, Benchling predicted a protein backbone mass of 70,100 Da, resulting in a predicted mass of 76,257 Da for the mature protein with 10 hemes. The mass of soluble $MtrC_{rec}$ was previously reported to be 76,252 Da[194].

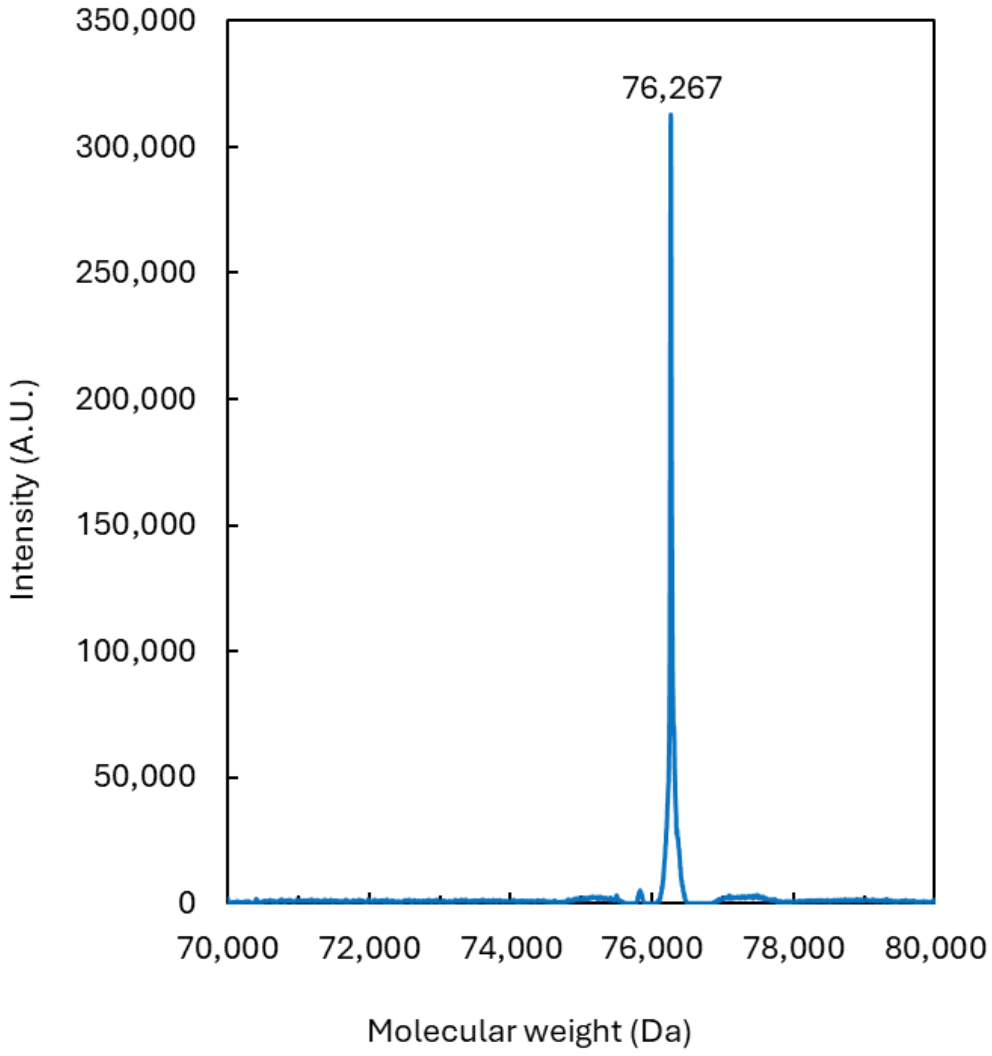

Figure 3.9. $MtrC_{DM}$ LC-MS data analysis showing the detected intensity units as a function of molecular weight. The maximum value for the intensity is shown as a data label on the graph and corresponds to the experimental molecular weight of soluble $MtrC_{DM}$.

3.2.5 Ultraviolet-visible spectroscopy on soluble $MtrC_{DM}$

After confirming that the purified soluble $MtrC_{DM}$ had been produced correctly and at the right molecular weight (± 2 Da), the redox properties were analysed. Investigating the characteristic heme protein spectroscopic features can provide insight on the structure and redox properties by using UV-Vis spectroscopy (Methods 2.5.1). These analyses provide information on both the redox functionality and the protein folding integrity.

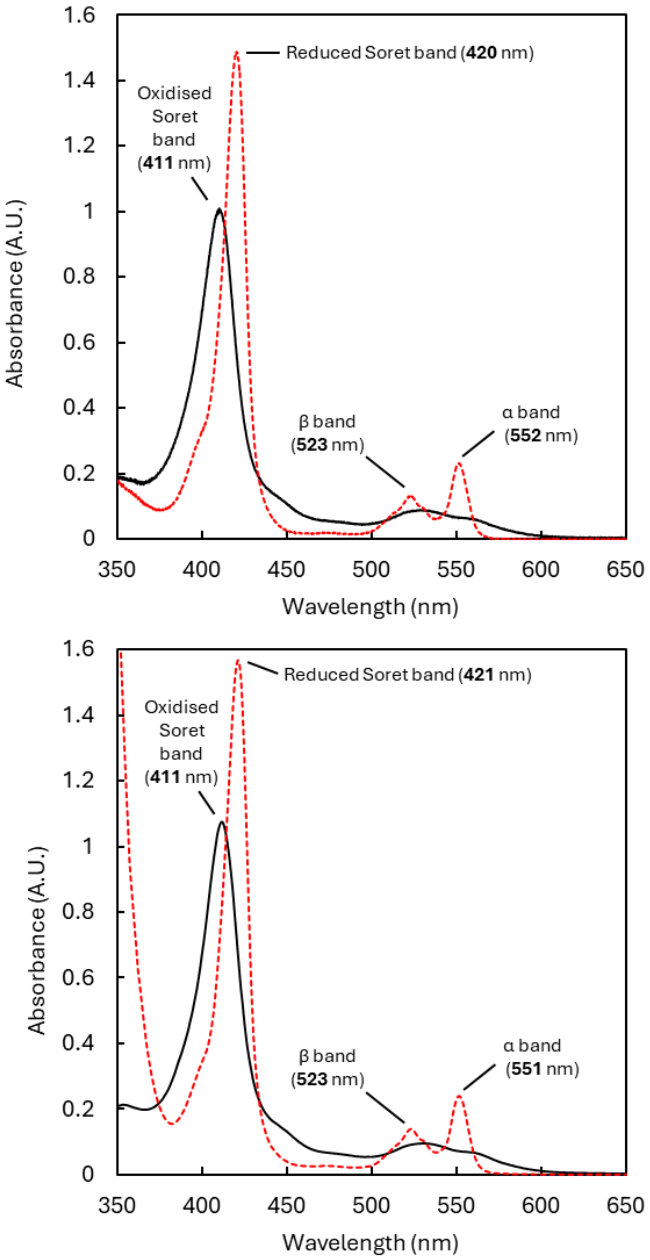

Figure 3.10. Electronic absorbance of soluble $MtrC_{DM}$ (**top**), and soluble $MtrC_{rec}$ (**bottom**) showing the oxidised state (solid black line) and dithionite-reduced state (red dashed line). Characteristic heme protein features and their corresponding wavelengths are labelled on the spectra. Proteins were diluted in 20 mM Tris, 30 mM NaCl, pH 7.8, to ~ 0.8 µM.

Figure 3.10 shows the electronic absorbance spectra of the oxidised and reduced states of soluble $MtrC_{DM}$ and $MtrC_{rec}$, respectively. In $MtrC_{DM}$ (Figure 3.10, top) the Soret band was shifted from 411 nm to 420 nm upon reduction. Also, the α- and β (552 nm and 523 nm, respectively) became sharper and more evident. These features are indicative of a heme protein that has folded correctly and displays typical redox capabilities. For $MtrC_{rec}$ (Figure 3.10, bottom), the Soret band shifted from 411 nm to 421 nm, and the sharpening of the α- and β bands occurred at 551 nm and 523 nm, respectively. These peak maxima suggest that there is little to no difference in the spectroscopic properties of soluble $MtrC_{rec}$ and soluble $MtrC_{DM}$.

3.2.6 Small angle X-ray scattering on soluble $MtrC_{DM}$

Small angle X-ray scattering (SAXS) was carried out to investigate the structural properties of soluble $MtrC_{DM}$. SAXS is particularly useful when investigating proteins that do not readily crystallise and for observing dynamic conformations in solution. Several crystallisation trials were carried out on purified soluble $MtrC_{DM}$. These trials involved using commercially available screening trays, as well as using the known crystallisation conditions[88] for soluble $MtrC_{rec}$ as a starting point. However, all trials were unsuccessful, and no crystals were formed during the trials.

The purified soluble $MtrC_{DM}$ samples were placed in an X-ray beam, and the radially isotropic scattering patterns were collected and interpreted. The SAXS sample preparation and data processing protocols are detailed in Methods 2.5.6. The processed SAXS data for soluble $MtrC_{rec}$ and $MtrC_{DM}$ are shown in Figure 3.11 A to D and Figure 3.11 E to H, respectively. SAXS data can be represented as intensity as a function of scattering vector s, where $s = \frac{2 \sin \theta}{\lambda}$. θ is the scattering angle and λ is the wavelength. The data presented in Figures 3.11 were processed in ATSAS and reported using the scattering vector (s) units.

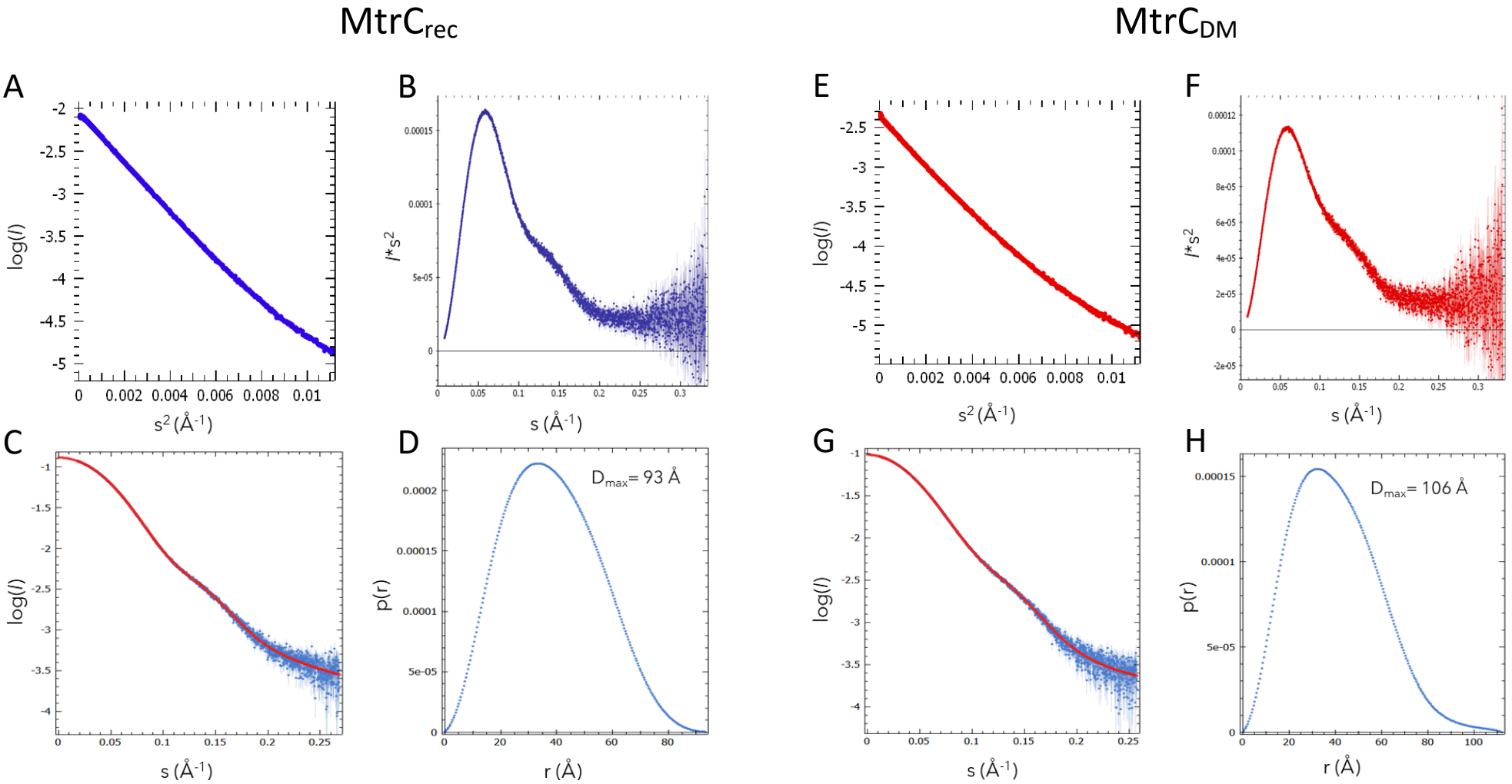

Figure 3.11. SAXS data analyses for soluble MtrC$_{rec}$ (A-D) and soluble MtrC$_{DM}$ (E-H). **A, E**. Guinier plots of the scattering curves, with linearity at low s^2, suggesting no protein aggregation. **B, F**. Kratky plots of the merged scattering curve, suggesting the proteins were correctly folded. **C, G**. log(*I*) vs s scattering curve plots (blue circles) with the fit line (red line). **D, H**. Particle pair distance distribution p(r) plots showing a maximum intramolecular distance (D$_{max}$) of 93 Å for soluble MtrC$_{rec}$ and 106 Å for soluble MtrC$_{DM}$. Intensity (*I*), scattering vector (s), and intramolecular radius (r) are shown on the axes.

Any background scattering and noise caused by the buffer were removed by subtracting the buffer scattering profiles from the protein scattering profiles. The radius of gyration (R_g) for both proteins was determined by Guinier approximation analyses using AUTORG[176]. Guinier plots for soluble $MtrC_{rec}$ and $MtrC_{DM}$ are shown in Figure 3.11, A, and Figure 3.11, E, respectively. The R_g was also calculated from particle pair distance distribution, p(r), plots for soluble $MtrC_{rec}$ and $MtrC_{DM}$ shown in Figure 3.11, A and Figure 3.11, H, respectively. Both plots produced single peaks of particle distances, without any other peaks, which suggested that both proteins were monomeric.

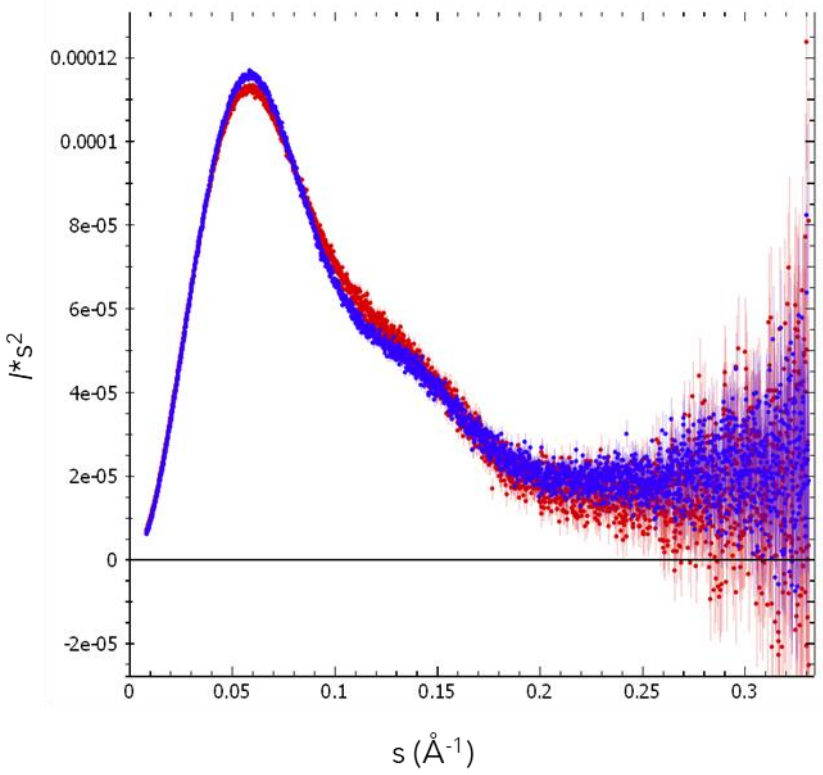

Figure 3.12. Overlay of the Kratky plots of the merged scattering curves of soluble $MtrC_{rec}$ (blue) and $MtrC_{DM}$ (red). The data around s values of 0.05 and 0.1 provide insight into the globularity of the proteins, while the data around s values of 0.1 and 0.15, are provide insight into the flexibility of the proteins.

The soluble $MtrC_{rec}$ R_g was calculated from the p(r) plot to be 29.7 Å (±0.13 Å) with a maximum intramolecular distance (D_{max}) of 93.31 Å (Figure 3.11, D). For $MtrC_{DM}$ the R_g was calculated from the p(r) plot to be 31.23 Å (±0.1 Å) with a maximum intramolecular distance (D_{max}) of 106.33 Å (Figure 3.11, H). For both proteins, the R_g calculated from the Guinier approximation and p(r) function were identical (±0.02 Å). The R_g is the average distribution of mass around the protein, with an axis

crossing the protein through the centre of mass, which can provide insight into the protein shape.

An overlay of the Kratky analyses of the scattering curves for soluble $MtrC_{rec}$ and $MtrC_{DM}$ is shown in Figure 3.12. This overlay suggested that $MtrC_{DM}$ is slightly less globular than $MtrC_{DM}$ (Figure 3.12). The mutations introduced in soluble $MtrC_{DM}$ were designed to produce a variant MtrC that had a higher degree of flexibility between domains I, II and domains III, IV. Therefore, there was an expected slight decrease in globularity in $MtrC_{DM}$ which was confirmed by the SAXS. Furthermore, the overlay also suggested that $MtrC_{DM}$ is slightly more flexible than $MtrC_{rec}$ (Figure 3.12). Again, this was predicted to be the case because of the introduced mutations in $MtrC_{DM}$.

A variety of software (Methods 2.5.6) were used to produce a final model of the $MtrC_{DM}$ structure based on the SAXS data. Figure 3.13, A, shows a structure of $MtrC_{rec}$ with the two locations where the amino acid changes were produced. Figure 3.13, B, shows the generated structure from the SAXS results. Figure 3.13, C, shows the model created from the SAXS data superposed to the structure of $MtrC_{rec}$. This superposition suggests an increase in the angle between the N terminus of MtrC (comprised of domains I and II) and the C terminus (comprised of domains III and IV).

The changes in the amino acid residues of MtrC were expected to change the flexibility of the hinge between domains I, II and domains III, IV within MtrC. Serine (with a polar, uncharged R group) was changed to valine (nonpolar, hydrophobic R group). The change in polarity and hydrophobicity of these amino acids were expected to produce a slight repulsion from the rest of the structure when the serine was changed to valine. Furthermore, asparagine (polar, uncharged R group) was changed to aspartic acid (negatively charged R group). The consequent change in charge of the amino acid was also expected to produce a change in the flexibility and angle between domains I, II and domains III, IV in $MtrC_{DM}$.

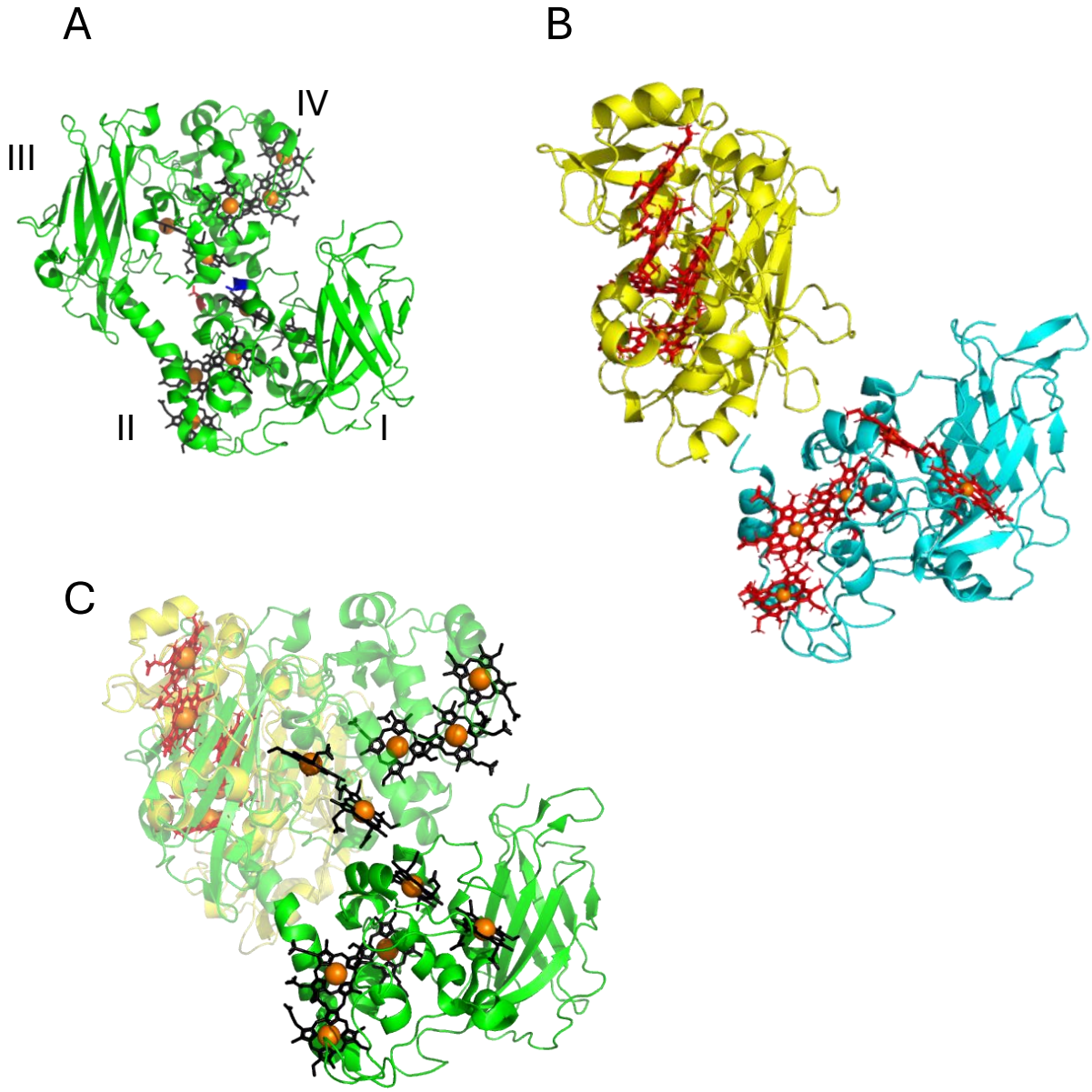

Figure 3.13. MtrC structures. (**A**). Soluble $MtrC_{rec}$ (PDB: 4LM8) shown in green with the hemes shown in black and Fe centres shown as orange spheres. The two locations where mutations were introduced to change serine 188 to valine (blue) and asparagine 251 to aspartic acid (red) are shown on the structure. **(B)** Soluble $MtrC_{DM}$ subunits model generated from SAXS data. As the angle between the N and C termini of the protein was increased, each terminus was treated as a separate subunit. The purified protein, however, does not have separate subunits; it is one continuous polypeptide chain. Domains I and II are shown in cyan and domains III and IV are shown in yellow. **(C)**. Superposition of MtrC WT (PDB: 4LM8, green) and $MtrC_{DM}$ (yellow) produced from the SAXS data. Domains I and II of both proteins were superposed perfectly (opaque green). The superposition of domains III and IV of MtrC WT (translucent green) and $MtrC_{DM}$ (translucent yellow) reveals the modelled increased angle between domains I, II and domains III, IV of $MtrC_{DM}$. MtrC WT and $MtrC_{DM}$ hemes are shown in black and red, respectively. Fe centres are shown as orange spheres. Domains indicated with roman numerals. Structures and models visualised using PyMOL[222].

3.2.7 Membrane $MtrC_{DM}$ expression and cell viability trials

An expression trial was done to confirm the correct production of membrane $MtrC_{DM}$ by *S. oneidensis* Δ*mtrC/omcA* cells (Methods 2.3.1). a 0.1% inoculum was used in M72 media (with supplements and kanamycin). These cells were immediately induced with 0.5 and 1 mM L-arabinose and incubated overnight. As the membrane $MtrC_{DM}$ would have formed a complex with native MtrAB, the health of the cells was more important than the yield of protein. To assess this, a cell viability assay was carried out on the *S. oneidensis* cells with the induced $pMTRC_{DM}$ plasmid (Methods 2.6.1). The cell viability assay served the purpose of helping understand if the assayed cells were healthy or not. However, as the reaction was stopped arbitrarily at the point before the reactant changes colour too much, the quantitative value of the data cannot be too high.

Instead, the processed data generated by the assay should be considered qualitative, i.e. whether the cells were metabolically active (healthy) or metabolically inactive (dead). Moreover, for some of the cells containing plasmids, too high a concentration of L-arabinose led to premature cell death. Consequently, it is difficult to normalise the total amount of healthy cells as the OD_{600} also includes unhealthy or lysed cells. However, for cells without a plasmid, a turbid culture the following day almost always meant the cells grew properly and were healthy. Therefore, this cell viability assay primarily evaluated the viability of the induced, plasmid-containing cells. Table 3.2 shows the results of the cell viability assay done on two samples induced with different L-arabinose concentrations. The values listed in Table 3.2 indicated that all the assayed cells were metabolically active.

Table 3.2. Processed data converted from the electronic absorbance taken during the cell viability assay of *S. oneidensis ΔmtrC/omcA* cells containing the $pMTRC_{DM}$ plasmid. Numbers represent averages from three replicates, and ±indicates standard error of mean. Control indicates a cell-free sample only containing

L-arabinose concentration	PrestoBlue™ Reagent percentage reduction
0 mM	47.53 (± 2.37)
0.5 mM	45.48 (± 3.90)
1 mM	49.96 (± 1.18)
control	2.62 (± 0.09)

Cell viability was assessed before doing any activity assays for all the strains that were used on the day. However, as it had been shown that the plasmid-containing cells were healthy (Table 3.2) using a spectrophotometer and plate reader, subsequent cell viability assays were done using microfuge tubes and no spectrophotometer. Instead, a noticeable colour change within a few minutes of adding the cell viability reagent was determined to mean that the cells were healthy.

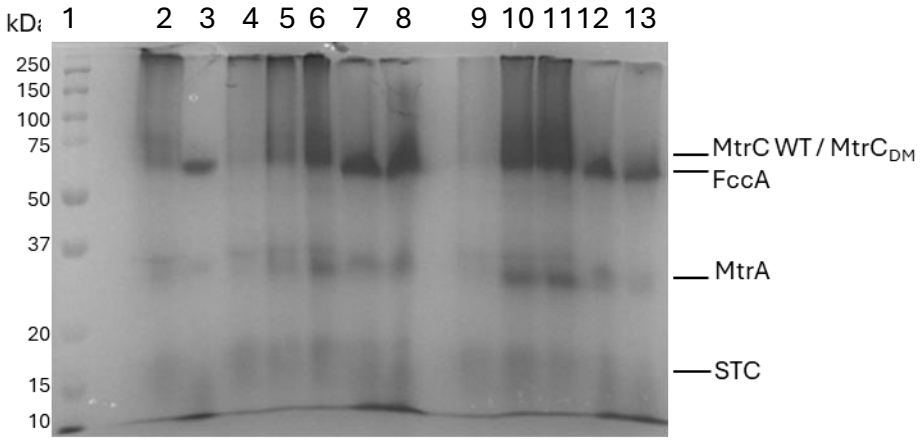

Figure 3.14. Heme-stained SDS-PAGE whole-cell gel from expression trial of *S. oneidensis ΔmtrC/omcA* with the membrane MtrC$_{DM}$ plasmid. Lanes are as follows: molecular marker (lane 1); MR-1, membrane fraction (lane 2); MR-1, soluble fraction (lane 3); membrane fraction of Δ*mtrC/omcA* cells expressing MtrC$_{rec}$ with L-arabinose at: 0 mM (lane 4), 0.5 mM (lane 5), and 1 mM (lane 6); soluble fraction of Δ*mtrC/omcA* cells expressing MtrC$_{rec}$ with L-arabinose at: 0 mM (lane 7) and 1 mM (lane 8); membrane fraction of Δ*mtrC/omcA* cells expressing MtrC$_{DM}$ with L-arabinose at: 0 mM (lane 9), 0.5 mM (lane 10), and 1 mM (lane 11); and soluble fraction of Δ*mtrC/omcA* cells expressing MtrC$_{DM}$ with L-arabinose at: 0 mM (lane 12) and 1 mM (lane 13). Fumarate reductase (FccA), MtrC WT (MtrC$_{rec}$), MtrC$_{DM}$, and small tetraheme cytochrome (STC) are indicated with lines.

After having confirmed that the *S. oneidensis* Δ*mtrC/omcA* cells with the induced pMTRC$_{DM}$ plasmid were metabolically active after induction, the production of proteins was assessed by running a whole-cell gel (Methods 2.1.7) and doing a heme stain on the gel. Figure 3.14 shows the heme-stained gel after the expression trial after confirming the viability of the cells. The gel shows the difference between the membrane and soluble fractions of the MR-1 as well as the Δ*mtrC/omcA* cells producing membrane MtrC$_{rec}$ or MtrC$_{DM}$. For all three strains, the soluble fraction produced much darker bands on the gel around 70 kDa, which was predicted to be due to high concentrations of fumarate reductase. The gel also shows that1 mM L-arabinose induction produced bands that were much darker than 0 mM and slightly darker than 0.5 mM. Consequently, 1 mM L-arabinose was chosen for all future inductions of the pMTRC$_{DM}$ plasmid. The MtrA band was the strongest in the

membrane fraction of all strains, especially the 1 mM L-arabinose induction of cells with either $pMTRC_{rec}$ or $pMTRC_{DM}$. Furthermore, there did not seem to be much basal level expression (or "leaky" expression) of the pBAD plasmid in the 0 mM L-arabinose induction cells. The whole-cell gel (Figure 3.14) also shows other heme proteins found within the *S. oneidensis* cells, including fumarate reductase (FccA) and small tetraheme cytochrome (STC).

3.2.8 Membrane MtrC activity assays

After confirming that $MtrC_{DM}$ was expressed correctly and appeared to be localised to the membrane, functional effects of having the membrane $MtrC_{DM}$ were investigated. SAXS had confirmed that the angle between domains I, II and domains III, IV of MtrC had been increased slightly after introducing the S188V and N251D mutations. However, it was unknown if this would have any effects on the electron transfer rates through $MtrC_{DM}$AB. The EET was investigated in different *S. oneidensis* strains through the reduction of flavin mononucleotide (FMN). Under anaerobic conditions and when supplemented with lactate, the intracellular metabolism of *S. oneidensis* generated electrons that required a terminal electron acceptor (such as FMN to complete EET.

3.2.8.1 Reduction of flavin mononucleotide

Flavin mononucleotide (FMN) is capable of mediating EET between MtrC or OmcA and certain terminal electron acceptors such as ferrihydrite (Fe(III) oxide) and electrodes[127]. Oxidised FMN has a bright yellow colour and fluoresces intensely with peak excitation and emission wavelengths of 365 nm and 525 nm, respectively. Upon reduction, the FMN loses the capacity to fluoresce, a property that is extremely useful in investigating electron transfer rates. Figure 3.15 shows the change in fluorescence intensity of 36 µM FMN (Figure 3.15, left) and the rate of FMN reduction in the presence of *S. oneidensis* cells with an OD_{600} ~ 0.1 (Figure 3.15, right).The fluorescence intensity decreased rapidly with the strains expressing either membrane $MtrC_{rec}$ or $MtrC_{DM}$. Additionally, the data suggested that there was a small difference in the capabilities of the strains producing membrane $MtrC_{rec}$ and $MtrC_{DM}$ to reduce FMN. The change in intensity was also decreased for MR-1, but not as much nor as fast. As the strains producing plasmid-based protein variants employ an overexpression system, higher reduction rates when compared to MR-1

were expected. The Δ*mtrC/omcA* mutant showed little to no change in the fluorescence intensity from the unprocessed data.

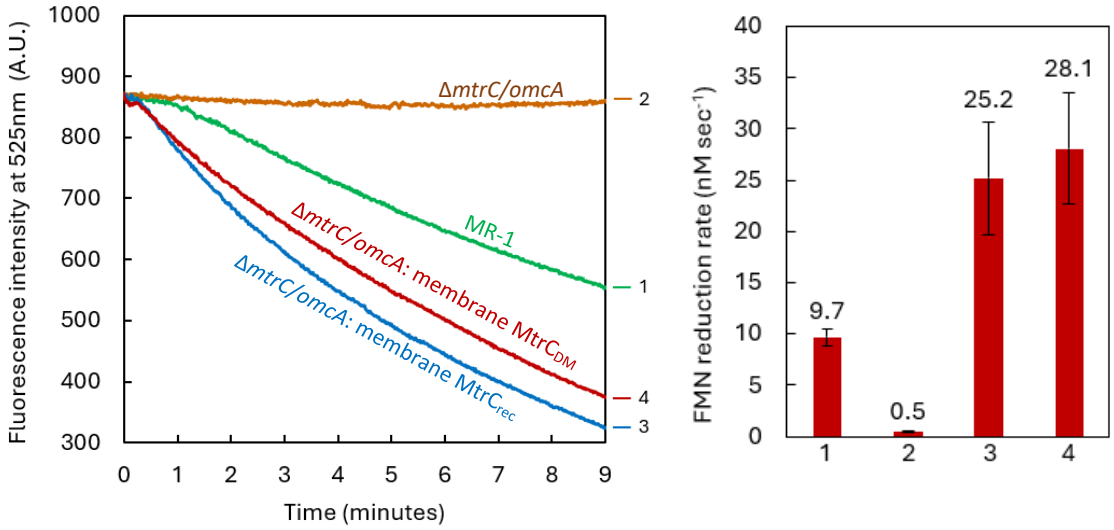

Figure 3.15. Results from the $MtrC_{DM}$ FMN reduction assay. **Left.** Change in fluorescence intensity at 525 nm of four *S. oneidensis* strains over a period of 9 minutes. **Right.** Processed data from the FMN assay, where change in fluorescence was converted to a rate of FMN reduction. Strains shown include: MR-1 (**1**); *ΔmtrC/omcA* (**2**); *ΔmtrC/omcA* producing membrane $MtrC_{rec}$(**3**); and *ΔmtrC/omcA* producing membrane $MtrC_{DM}$ (**4**). The assay was carried out with cells at a starting OD_{600} of 0.1 induced with 1 mM L-arabinose. The initial concentration of FMN was 12 μM. Experiments were done in triplicate and error bars show standard error of mean. No statistical tests were carried out on the data.

The transfer of electrons from the *S. oneidensis* cells to FMN happened rapidly, as was seen from the decreasing gradient of the fluorescence intensity with time. Consequently, the initial (within two to three minutes) change in fluorescence was largely used in the FMN reduction rate calculations. Furthermore, using the initial change was advantageous to try to mitigate against any false positive readings from any oxygen that may have leaked into the cuvette and sequestered the intracellular electrons. The FMN reduction rates shown in this thesis (Figure 3.15, right) corroborated previous work[113] showing the incapability for *ΔmtrC/omcA* mutants to reduce FMN. The *ΔmtrC/omcA* mutant did have a very small FMN reduction rate suggesting a small level of electron transfer does occur between *S. oneidensis* *ΔmtrC/omcA* cells and FMN. Additionally, the *ΔmtrC/omcA* mutant producing membrane $MtrC_{rec}$ had a faster rate than MR-1, which was expected as this construct has increased expression of MtrC when compared to MR-1. This suggested the experimental design was appropriate and the produced membrane $MtrC_{rec}$ protein transferred electrons from the endogenous MtrAB to the exogenous FMN.

When MtrC is reduced, and under anaerobic conditions, the FMN can interact with MtrC which increases EET rates. However, it is unknown where on the MtrC scaffold these interactions take place. It has been suggested[131] that the closest heme to the MtrC disulfide bond (located in domain III) is heme 7 (located in domain IV). Here the effect of increasing the angle between domains I, II and domains III, IV in $MtrC_{DM}$ on electron transfer was investigated. However, the results from the FMN reduction assay would indicate that there were no noticeable differences between EET through membrane $MtrC_{rec}$ and $MtrC_{DM}$. Even though the SAXS results for soluble $MtrC_{DM}$ indicate that $MtrC_{DM}$ was more flexible than $MtrC_{rec}$, this did not seem to impact electron transfer to FMN.

3.3 Conclusion and future work

The outer-membrane decaheme, MtrC, is comprised of four domains. Two structural, β-barrel domains (domains I and III) and two pentaheme, α-helical domains (domains II and IV). It was reported[88] that in the crystallised MtrC in MtrCAB from *Shewanella baltica* OS185 (which is very similar to MtrC from *S. oneidensis* MR-1[131]), domains I, II showed movement relative to domains III, IV. This movement was centred around MtrC residues 289-300, which form part of the alpha helix located in the hinge region between domains II and III. It was suggested that the location of this flexible hinge would not restrict MtrCAB, enabling MtrC the flexibility to change its conformation[88].

To further investigate the role of these flexible conformational states of MtrC, an MtrC variant ($MtrC_{DM}$) with two mutations (S188V, N251D) was produced. These residue changes were predicted to cause the angle between domains I, II and domains III, IV to be increased due to differences in the hydrophobicity and charge of the modified amino acid residues. The results presented here show that there were no appreciable differences between the UV-Vis spectra of soluble $MtrC_{rec}$ and $MtrC_{DM}$. The processed SAXS data suggested an increased radius of gyration (R_g) and maximum intramolecular distance (D_{max}) in $MtrC_{DM}$. In the models produced from the SAXS data, domains I, II of soluble $MtrC_{DM}$ overlay perfectly with domains I, II of soluble $MtrC_{rec}$. Domains III, IV, however, were predicted to be located at an increased angle from domains I, II, which is in alignment with the increased R_g and D_{max}.

To investigate any functional effects of increasing the angle between domains I, II and domains III, IV, in $MtrC_{DM}$, a flavin mononucleotide (FMN) reduction assay was carried out on several *S. oneidensis* strains. This assay determines the rate at which electrons are transferred from *S. oneidensis* cells, through MtrCAB, to FMN. The results from this assay suggest that there were no significant differences between the electron transfer rates of cells producing MtrCAB or $MtrC_{DM}$AB. It would appear that, even though there is a greater distance between domains I, II and domains III, IV, there are no major changes in the electron transfer rate. This could be because FMN is suggested[131] to form a complex with MtrC, which might bring domains III, IV closer to domains I, II, regardless of the increased angle between the two sets of domains. As the FMN is predicted to bind near heme 7, on domain III, then it would

not be advantageous for the cells if domains III, IV were far enough from domains I, II to hinder electron transport. If the distance between the two sets of pentahemes within MtrC were to be increased, then electron transfer rates would go down, as they would have to travel farther.

Furthermore, previous work has proposed that the disulfide near heme 7 is essential for FMN reduction [131,134]. So even though the hinge between domains I, II and domains III, IV has increased flexibility in $MtrC_{DM}$, the disulfide remains. This may be the reason as to why the rates of EET through membrane $MtrC_{DM}$ are comparable to those through membrane $MtrC_{rec}$. Moreover, the rates of heme-to-heme electron transfer have been previously[195] suggested to be in the order of 10^9 s^{-1} with edge-to-edge distances of 3.7-4.3 Å. Consequently, even though the distance between domains I, II and domains III, IV was increased in $MtrC_{DM}$, these proposed electron transfer rates are fast enough to sustain the reduction of FMN.

The SAXS results presented here show that $MtrC_{DM}$ is more flexible than $MtrC_{rec}$. This flexibility, however, seems to have no impact on the rate of EET to FMN. This could be the case if the changes observed in the SAXS do not affect the EET rate sufficiently to affect FMN reduction, or if the EET rates are not affected by the mutations. Another possibility is that the FMN does not bind to MtrC near domain III or IV, even though the disulfide is important. It is hypothesised that disruption of the disulfide bridge in MtrC forces a fixed change in domain III or IV that affects FMN reduction. If this is true, then removal of domains III and IV will prevent catalytic reduction of substrates that interact with either domain. Consequently, other assays should be done with different types of electron acceptors.

Chapter 4

Removing domains III and IV of MtrC

4. MtrC domains I and II

4.1 Introduction

Shewanella oneidensis has the capacity to survive in environment with little to no oxygen, by respiring extracellular metals such as Fe(III) and Mn(IV) oxides. To do so, it can transfer the electrons generated from intracellular metabolism to the extracellular electron acceptors via the MtrCAB heterotrimer. This complex is comprised of MtrA (outer-membrane decaheme) enveloped by MtrB (porin), and MtrC (cell-surface decaheme). Electrons can be transferred to the acceptor from MtrC directly, by going through OmcA (another cell-surface decaheme) first, or indirectly via electron shuttles like flavins[131,191]. Lateral electron transfer between MtrC and OmcA is possible due to the "staggered cross" heme arrangement of MtrC. This is possible as MtrC has its 10 hemes divided into domains II (hemes 1-5) and IV (hemes 6-10). Within domain III of MtrC, the 444 and 453 cysteines form a disulfide bond when oxygen is present [131,134]. Under reducing conditions, however, this bond is broken. It has been suggested that the binding of flavins to MtrC occurs near a hydrophobic cleft adjacent to heme 7. However, upon exposure to oxygen, the flavin cofactor is rapidly released as the disulfide bond reforms[88,131,134]. The crystal structure reveals that the edge-to-edge distances for the MtrA hemes are 3.9-6.5 Å[88]. Furthermore, the distance between heme 10 from MtrA (at the C terminus) and heme 5 of MtrC (at the N terminus, next to MtrA) was 8 Å. Additionally, the hinge between domains I, II and domains III, IV of MtrC is located around residues 289-300[88]. This hinge region allows some flexibility between the C and N termini of MtrC. Perhaps it allows MtrC to have subtle conformational changes that enable the binding of cofactors such as flavins, or direct contact with metal oxide acceptors.

In the previous chapter, the angle and distance between domains I, II and domains III, IV of MtrC was increased. However, there were no significant differences in the biophysical properties nor the reductase activity of the MtrC variant when compared to WT MtrC. To better understand the effects of increasing the distances between domains I, II and domains III, IV, another MtrC variant was generated that only contained domains I and II. This variant was used to investigate changes in EET when domain III and IV (which contain the disulfide bridge and heme 7, respectively) were removed. Our hypothesis is that MtrC can open and close to regulate electron transfer, and if this were to be the case, then we would expect to find physiological

substrate binding sites within domains III and IV. By removing both these domains, the location of binding sites for substrates like iron oxides or flavins will become clearer.

4.2 Results and discussion

4.2.1 Plasmid design and generation

4.2.1.1 Production of soluble pMTRC$_{DI,II}$ plasmid

A pBAD plasmid containing the soluble (no lipid anchor) MtrC E344Amber (soluble pMTRC$_{DI,II}$) was kindly provided by Dr Colin Lockwood, from the Butt group at the University of East Anglia, Norwich (Table 2.3 in Methods 2.2.11). The pDNA had recently been confirmed by sequencing to have the correct DNA sequence, with the glutamic acid codon (E; GAA) replaced with an amber stop codon (Amber; TAG) at amino acid residue position 344 in MtrC.

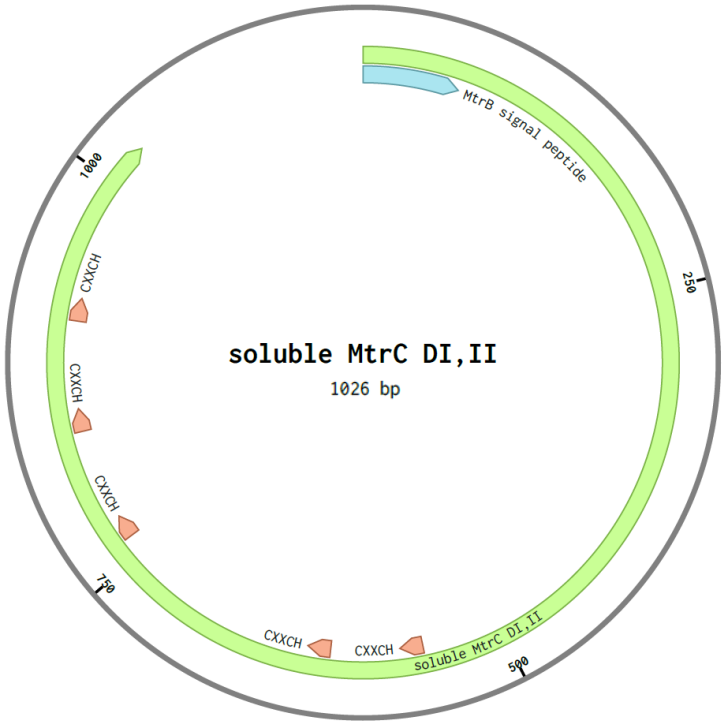

Figure 4.1. Sequencing data from soluble pMTRC$_{DI,II}$ obtained from Eurofins and visualised on Benchling. The MtrB signal peptide is shown as a green arrow, CXXCH heme binding motifs are shown with red arrows. As a premature stop codon is introduced at position 344, the gene ends up being 1026 bp, which is around half the length of *mtrC* WT which is 2016 bp (NCBI: QKG96446). Note: even though the sequencing data is linear, it has been shown as circular to better visualise the components.

Next, the pDNA was transformed into *S. oneidensis* MR-1 cells (Methods 2.2.9). After, the pDNA was extracted and sequenced (Figure 4.1). Upon confirmation of the correct sequence, protein expression trials were started.

4.2.1.2 Production of membrane pMTRCDI,II plasmid

A pBAD plasmid containing the MtrC WT with the native *mtrC* signal peptide that anchored MtrC to the extracellular face of the outer membrane (membrane $pMTRC_{rec}$) was obtained from the laboratory repository at the University of East Anglia, Norwich (Table 2.3 in Methods 2.2.11). The plasmid DNA (pDNA) was prepared and sent for sequencing (Methods 2.2.10). The sequenced plasmid was successfully aligned in Benchling to *mtrC* WT (NCBI: QKG96446), with all DNA bases aligning as expected.

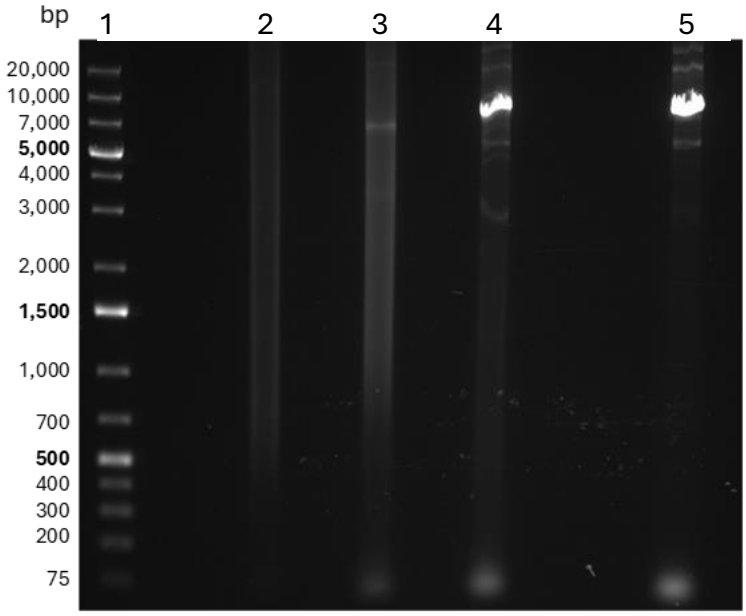

Figure 4.2. 0.8% agarose gel of the PCR products from the E344Amber PCR. An annealing temperature gradient was done to optimise the protocol. The lanes are as follows: molecular marker (lane 1), annealing at: 60°C (lane 2), 58°C (lane 3), 54°C (lane 4), and a positive control using the same primers on another MtrC WT template plasmid with annealing at 54°C (lane 5). The bright bands around 7,000 bp in lanes IV and V are the successful PCR products.

Once it had been determined that the template membrane $pMTRC_{rec}$ plasmid had no anomalies, PCR was used to replace the glutamic acid codon (E; GAA) with a premature amber stop codon (Amber; TAG) at amino acid residue position 344 of MtrC. The PCR conditions are detailed in Methods 2.2.3 and the PCR primers used are shown in Table 2.2 in Methods 2.2.3. After the PCR, the PCR products ($pMTRC_{DI,II}$) were visualised on a 0.8% agarose gel (Methods 2.1.3) to confirm the PCR had been successful (Figure 4.2).

When the plasmids are *in vivo* they remain tightly wound or supercoiled. When they are extracted, single stranded breaks can occur which leads to a nicked or open-

circular conformation. If there is a double stranded break, then the plasmid becomes linear. Plasmids of the same size can run differently on agarose gels depending on their conformation, with supercoiled running the fastest, then linear, then open-circular. This is why the bands in the agarose gel (Figure 4.2) may appear to be ~7,000-10,000 base pairs (bp) when pMTRC$_{DI,II}$ is ~ 6,500 bp.

After confirming with the gel electrophoresis that the PCR had worked, a DpnI digest was done (Methods 2.2.4) on the membrane pMTRC$_{DI,II}$ PCR product. The DpnI enzyme digests methylated template DNA (but cannot digest the non-methylated PCR product), therefore removing any remaining template DNA. After, the DpnI enzyme and associated buffers used in the digest were removed with a PCR clean-up kit. Next, the membrane pMTRC$_{DI,II}$ was transformed by heat shock into competent *E. coli* TOP10 cells (Methods 2.2.7 and 2.2.8). The *E. coli* can repair any nicks in the PCR, and because they are the TOP10 strain, they enable stable replication of high copy number plasmids.

pDNA was extracted from the transformants and sent for sequencing to confirm that the DNA had not changed after introducing the plasmid and then extracting from *E. coli* TOP10 cells. Once the sequencing confirmed this, the pDNA was transformed into a *S. oneidensis* Δ*mtrC/omcA* strain via electroporation (Methods 2.2.9). This way the produced lipid-anchored (membrane) MtrC$_{DI,II}$ from the inducible plasmid could form a complex with the endogenously produced MtrA and MtrB.

In the unlikely event that the plasmids may have had mutations introduced during the electroporation into *S. oneidensis* cells, pDNA was extracted and sequenced again. Upon confirmation of the correct sequence (Figure 4.3), protein expression trials were started. All plasmids used in this chapter are shown in Table 4.1.

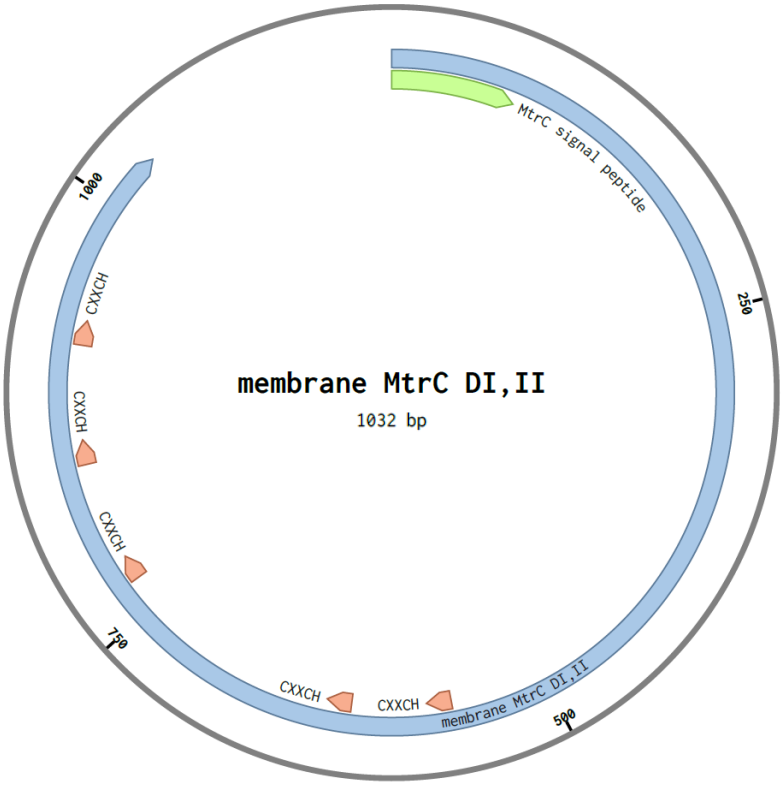

Figure 4.3. Sequencing data from membrane pMTRC$_{DI,II}$ obtained from Eurofins and visualised on Benchling. The MtrC signal peptide (green arrow) is maintained instead of the MtrB signal peptide, as this is the lipid-anchored form. CXXCH heme binding motifs are shown with red arrows. As a premature stop codon is introduced at position 344, the gene ends up being around half the length of *mtrC* WT. Note: even though the sequencing data is linear, it has been shown as circular to better visualise the components.

Table 4.1. Plasmids used in this chapter with indicated relevant features. Text in bold forms part of each plasmid name.

Plasmid	Features
Soluble pMTRC$_{rec}$	*mtrB* signal peptide, no lipid anchor; no more modifications to *mtrC* (**rec**ombinant)
Soluble pMTRC$_{DI,II}$	*mtrB* signal peptide, no lipid anchor; glutamic acid codon at amino acid position 344 of *mtrC* changed to amber stop codon, resulting in MtrC **d**omain **I**, and **II**
Membrane pMTRC$_{rec}$	Native *mtrC* signal peptide, lipid anchor; no modifications to *mtrC,* (**rec**ombinant)
Membrane pMTRC$_{DI,II}$	Native *mtrC* signal peptide, lipid anchor; glutamic acid codon at amino acid position 344 of *mtrC* changed to amber stop codon, resulting in MtrC **d**omain **I**, and **II**

4.2.2 Soluble $MtrC_{DI,II}$ expression trials

To confirm correct production and secretion of soluble $MtrC_{DI,II}$ by the *S. oneidensis* MR-1 cells, an expression trial was done (Methods 2.3.1). Expression was induced with 5 mM L-arabinose (Methods 2.3.1). 20 hours after inducing protein expression, the cells were harvested by centrifugation and discarded.

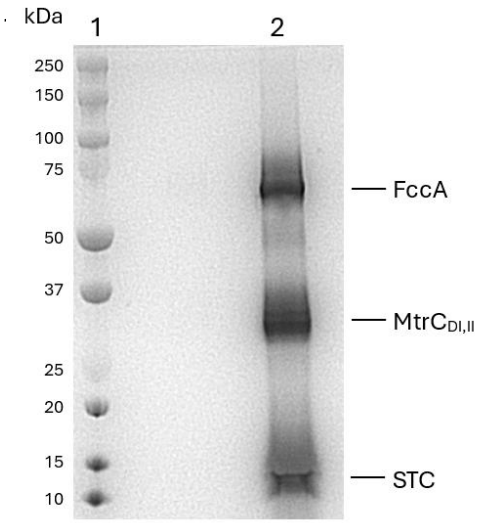

Figure 4.4. Heme-stained SDS-PAGE gel from expression trial of *S. oneidensis* MR-1 cells with the soluble $MtrC_{DI,II}$ plasmid. Lanes are as follows: molecular marker (lane 1) and 12.5 µL spent media sample (lane 2). Fumarate reductase (FccA), $MtrC_{DI,II}$, and small tetraheme cytochrome (STC) are indicated with lines.

The spent media samples were run on an SDS-PAGE gel and stained for heme (Methods 2.1.6). Figure 4.4 shows the heme-stained gel with strong bands where $MtrC_{DI,II}$ was expected to be. MtrC WT has a molecular weight of ~ 76 kDa (protein backbone and 10 bis-his heme cofactors), and $MtrC_{DI,II}$ was expected to have a molecular weight of ~ 35 kDa (protein backbone and 5 bis-his heme cofactors). Even though the gel shows samples secreted to the extracellular environment, fumarate reductase (FccA) and small tetraheme cytochrome (STC) are also seen. These proteins are both periplasmic, but they are produced in high quantities. As cells die and lyse in solution during incubation, these proteins get mixed with the $MtrC_{DI,II}$ and can show up on the heme-stained SDS-PAGE gels. This is especially true of expression trial gels such as Figure 4.4 where nothing is done to try to remove FccA and STC, as it is not necessary at this stage.

4.2.3 Soluble $MtrC_{DI,II}$ purification

After appropriate synthesis was determined with the expression trials, a large-scale purification protocol was employed. To purify soluble $MtrC_{DI,II}$, cells were cultured, and the proteins extracted as detailed before (Methods 2.4.1 and Methods 2.4.2.2). SDS-PAGE gels were carried out throughout the purification process and stained for heme. Figure 4.5 A and C show the ÄKTA trace and heme-stained SDS-PAGE gel after

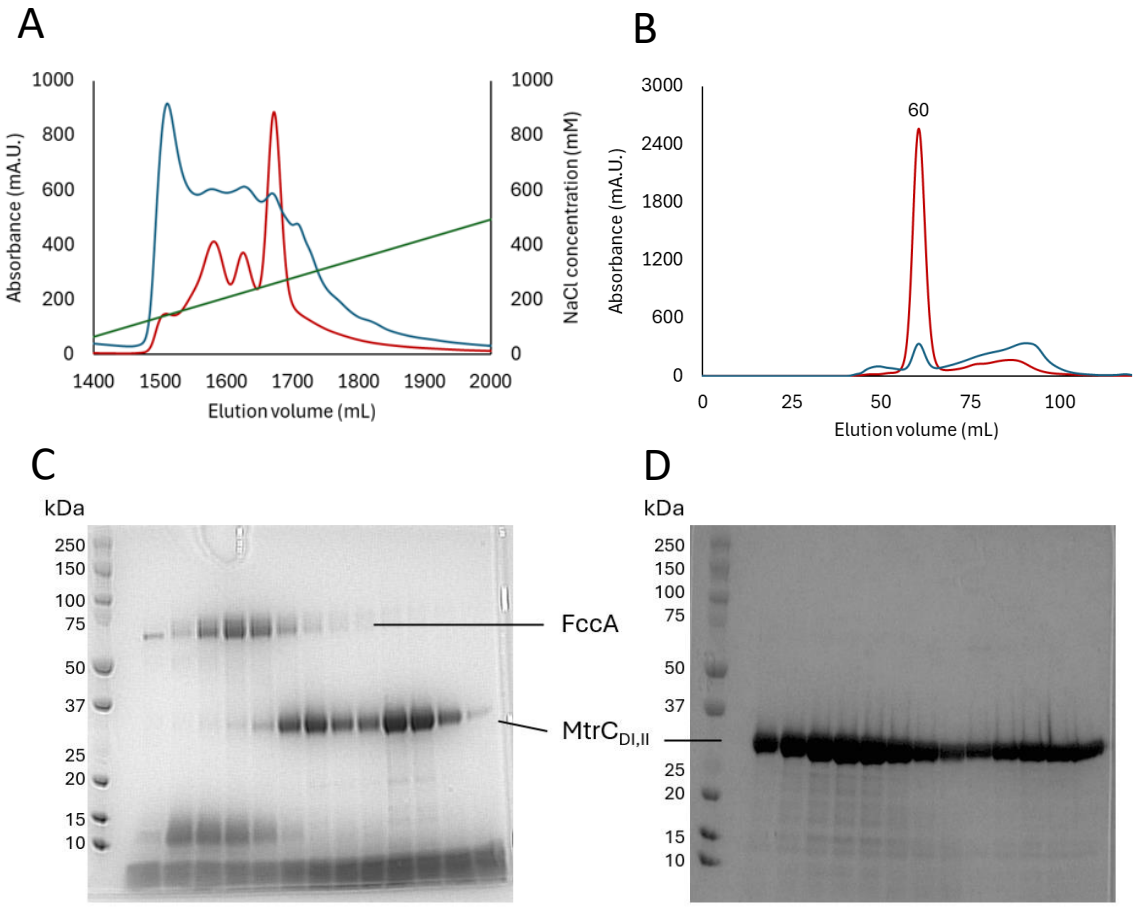

Figure 4.5. ÄKTA traces from DEAE anionic exchange (**A**) and size exclusion (**B**) chromatographic columns used to purify soluble $MtrC_{DI,II}$. The A_{410},A_{280} and NaCl concentration are shown in red, blue, and green lines, respectively. Heme-stained SDS-PAGE gels showing fractions after elution from a DEAE anionic exchange chromatography column (**C**), and a size exclusion chromatography (SEC) column (**D**) from the soluble $MtrC_{DI,II}$ protein purification. Molecular weights (kDa) are labelled on the leftmost lane. FccA is almost entirely removed after the SEC, and the sample is largely composed of soluble $MtrC_{DI,II}$.

the DEAE column, respectively. The different constituents of the prep eluted with increasing NaCl concentration as seen on the trace (Figure 4.5, A). This became more apparent as seen by the different bands on the heme-stained SDS-PAGE gel, which was used to select which eluted fractions would be applied to a size exclusion chromatography (SEC) column. Figure 4.5 B and D show the ÄKTA trace and heme-

stained SDS-PAGE gel after the SEC column, respectively. After the SEC column, the great majority of the impurities were removed.

Finally, the purified $MtrC_{DI,II}$ was run on an SDS-PAGE alongside MtrC WT as a control, to confirm the purity of the purification as well as an obvious size difference between the variant and WT version of MtrC. Figure 4.6 left and 4.6 right show the proteins on an SDS-PAGE gel that was heme-stained, or stained with Coomassie, respectively.

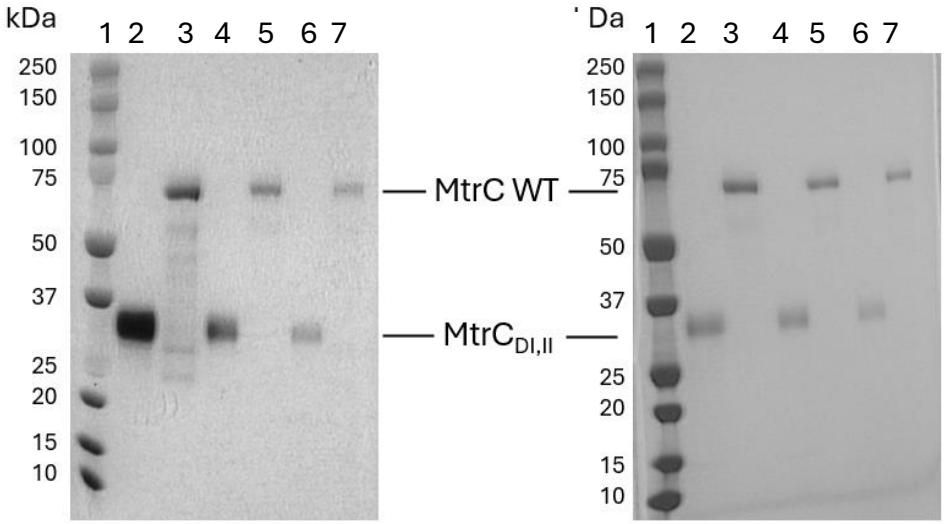

Figure 4.6. SDS-PAGE gel showing MtrC WT and $MtrC_{DI,II}$ subjected to a heme stain (**left**) or stained with Coomassie (**right**). For both gels, the lanes shown are as follows: molecular marker (lane 1); 20 µL, 10 µL, and 5 µL of $MtrC_{DI,II}$ (lanes 2, 4, and 6, respectively); 20 µL, 10 µL, and 5 µL of MtrC WT (lanes 3, 5, and 7, respectively).

4.2.4 Soluble $MtrC_{DI,II}$ liquid chromatography-mass spectrometry

Once the $MtrC_{DI,II}$ had been established to be of sufficiently high purity by the absence of any extra bands on SDS-PAGE gels (Figure 4.6), the protein samples were prepared for LC-MS (Methods 2.5.6). Figure 4.7, Top shows the processed data from LC-MS with a large peak at 35,364 Da corresponding to $MtrC_{DI,II}$, as well as several adjacent peaks corresponding to impurities or truncated forms of $MtrC_{DI,II}$. Benchling was used to predict a mass of 32,285 Da for the mature $MtrC_{DI,II}$ polypeptide backbone on its own, and of 35,361 Da when adding the mass of 5 *c*-type hemes (at 615.71[193] Da $heme^{-1}$). The experimental molecular weight obtained from the LC-MS was 3 Da away from the predicted molecular mass of $MtrC_{DI,II}$.

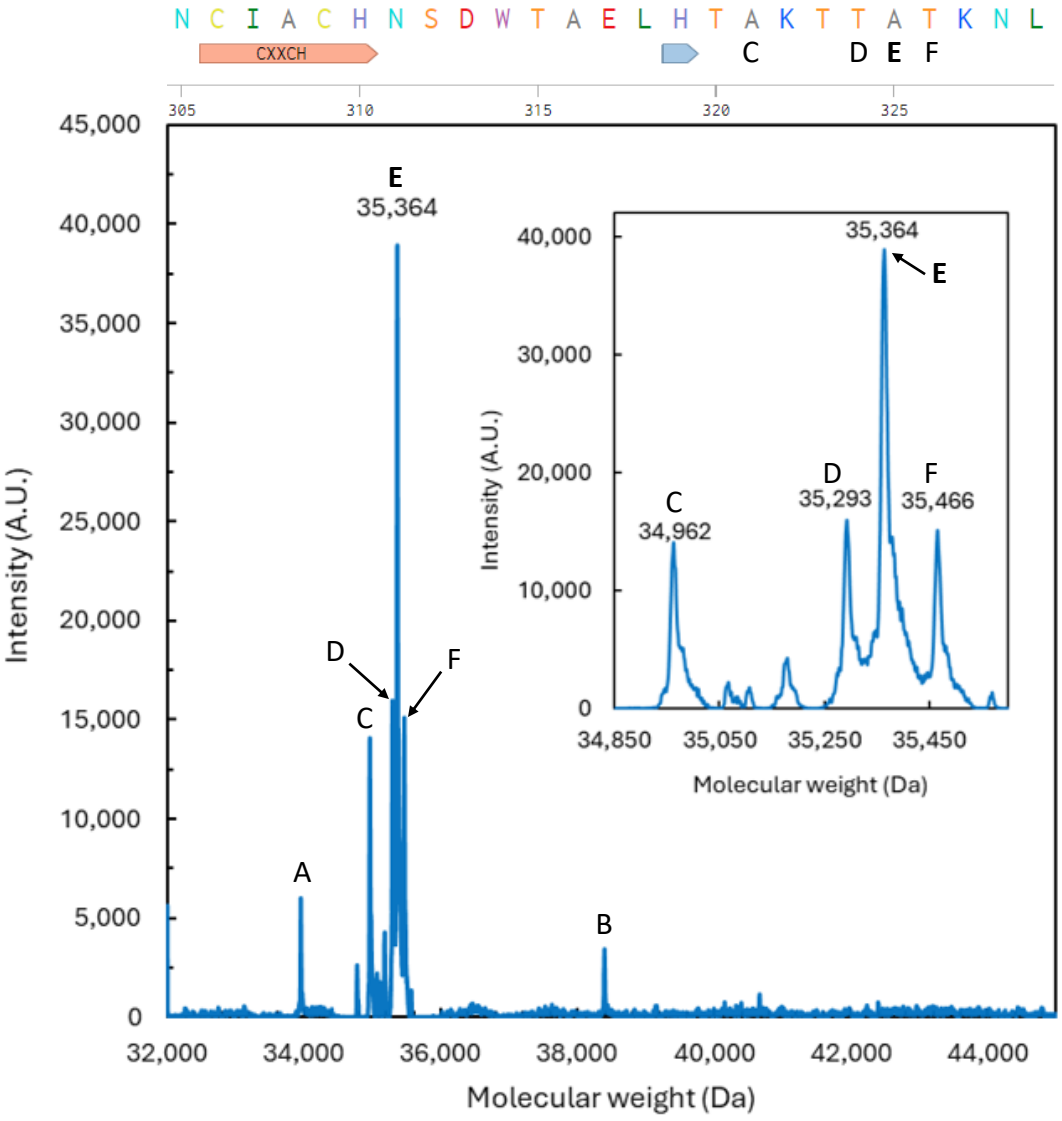

Peak	Composition	Percentage of total sample
A	Impurity	2.7 %
B	Impurity	3.5 %
C	MtrC truncated to residue A321	15.6 %
D	MtrC truncated to residue T324	17.6 %
E	**$MtrC_{DI,II}$ terminating at residue A325**	**43.6 %**
F	MtrC truncated to residue A326	16.9 %

Figure 4.7. Top. $MtrC_{DI,II}$ LC-MS data analysis showing the detected intensity units as a function of molecular weight. The maximum value for the intensity is shown as a data label on the graph and corresponds to the experimental molecular weight of soluble $MtrC_{DI,II}$. Inset: other adjacent, high intensity peaks are also labelled. The amino acid sequence above shows the predicted truncation site of the proteins corresponding to the high intensity peaks. **Bottom.** Description of the main peaks from the LC-MS. The percentage of total sample was calculated using the intensity of each peak when compared to the total intensity of the complete sample. Benchling was used to determine the truncation site based on the predicted mass.

The neighbouring peaks, however, matched perfectly with predicted MtrC variants with different truncation sites. Therefore, the LC-MS results would indicate the final $MtrC_{DI,II}$ residue to be A325. Benchling was used to calculate the predicted molecular masses of three MtrC variants that had truncation sites of -4, -1, and +1 amino acid residues with respect to the expected $MtrC_{DI,II}$ cut site (Figure 4.7, bottom). These predicted masses were the same (±<1 Da) as the experimental masses from the smaller peaks from the LC-MS (Figure 4.7, top inset). Consequently, it was concluded that the majority of the purified protein was $MtrC_{DI,II}$, with a range of C terminus truncation sites . Figure 4.8 shows the translated DNA sequence for $MtrC_{DI,II}$ as well as the predicted truncation sites based on the LC-MS data and Benchling mass calculations.

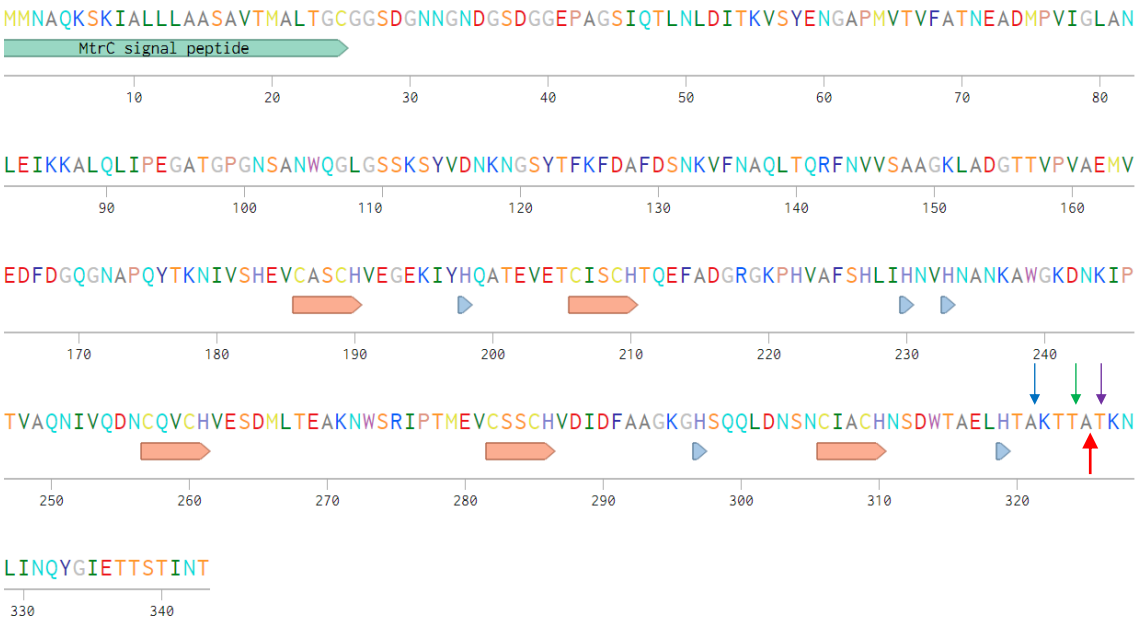

Figure 4.8. Translated DNA sequence for $MtrC_{DI,II}$ with native signal peptide. The final residue is the threonine (T343) before the E344Amber stop codon site. The large red arrow indicates the predicted cut site for $MtrC_{DI,II}$ from the LC-MS data with a mass of 35,364 Da. The three smaller arrows indicate predicted cut sites for the other truncated variants from the LC-MS. The blue, green, and purple small arrows correspond to MtrC proteins truncated at A321 (34,962 Da), T324 (35,293 Da), and T326 (35,466 Da), respectively. The CXXCH motifs are indicated with wide orange arrows over the sequence. The distal histidines for the five hemes are indicated with wide blue arrows. Figure produced on Benchling.

4.2.5 Ultraviolet-visible spectroscopy on soluble $MtrC_{DI,II}$

Once it was confirmed that the purified $MtrC_{DI,II}$ was produced correctly and at the right molecular weight (± 3 Da), the redox capacities were assessed. Insight on the structure of a heme protein can be obtained by investigating if characteristic features can be observed in the electronic absorbance which was measured by UV-Vis spectroscopy (Methods 2.5.1). Not only does this provide information on the correct folding of the protein, but also correct functionality.

Figure 4.9 shows the electronic absorbance spectra of the oxidised and reduced states of $MtrC_{DI,II}$ and MtrC WT. For $MtrC_{DI,II}$ (Figure 4.9, top), the Soret band shifted from 410 nm to 420 nm upon reduction. Also, the α- and β bands (552 nm, 523 nm, respectively) became much sharper and more evident. These features are indicative of a properly folded protein with typical redox activity. For MtrC WT (Figure 4.9, bottom) the Soret band shifted from 411 nm to 421 nm, and the sharpening of the α- and β bands occurred at 551 nm and 523 nm, respectively.

The data from Figure 4.9 would suggest that the differences in the UV-Vis spectra between $MtrC_{DI,II}$ and MtrC WT are very subtle, and that proteins behave very similarly upon reduction with dithionite.

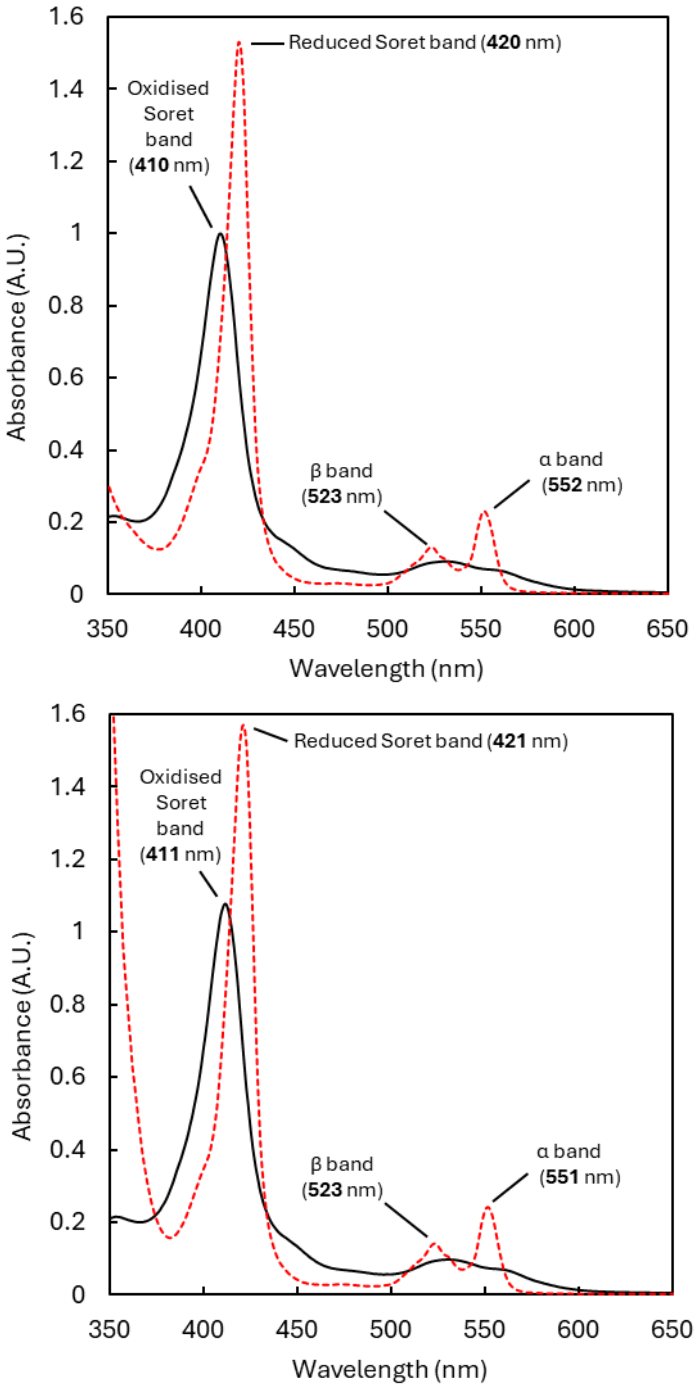

Figure 4.9. Electronic absorbance of purified soluble $MtrC_{DI,II}$ (**top**), and MtrC WT (**bottom**) showing the oxidised state (solid black line) and dithionite-reduced state (red dashed line). Characteristic heme protein features and their corresponding wavelengths are labelled on the spectra. $MtrC_{DI,II}$ and MtrC WT were diluted in 20 mM Tris, 30 mM NaCl, pH 7.8, to ~ 0.8 and ~ 1.6 μM, respectively.

4.2.6 X-ray crystallography on soluble $MtrC_{DI,II}$

To better understand the structure of $MtrC_{DI,II}$, protein crystals were produced with the help of Benjamin Nash (Clarke lab) following the protocol in 2.5.7 X-ray crystallography. After a few days of incubation at 4°C in 0.2 M magnesium acetate tetrahydrate, 0.1 M sodium cacodylate, 20% (w/v) polyethylene glycol (PEG) 8000, pH 6.5, red crystals started to form. Figure 4.10 shows photographs taken of the crystals under a microscope.

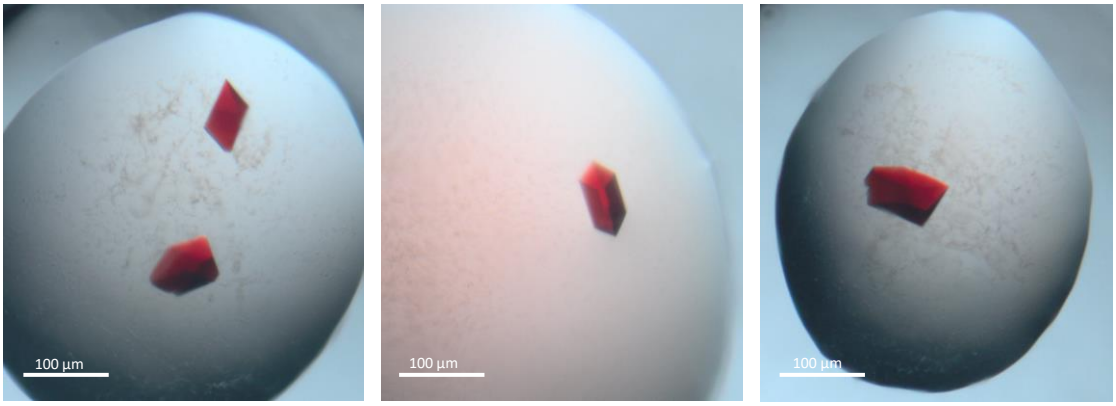

Figure 4.10. $MtrC_{DI,II}$ crystals in the crystallisation plates visualised under a microscope with 50x magnification. The crystallisation conditions were 4°C in 0.2 M magnesium acetate tetrahydrate, 0.1 M sodium cacodylate, 20% (w/v) polyethylene glycol (PEG) 8000, pH 6.5.

The crystals were harvested and shipped to Diamond Light Source where beam I24 was used for X-ray diffraction. Figure 4.11 shows the crystal setup at Diamond Light Source.

Figure 4.11. $MtrC_{DI,II}$ crystal mounted on a LithoLoop under stream of gaseous nitrogen in I24 hutch at Diamond Light Source, during data collection.

The data were collected from beamline I24 at Diamond Light Source (Table 4.2). The average cell dimensions of the crystals were a = 74.36 Å, b = 77.15 Å, c = 96.52 Å, with space group $P2_12_12_1$. Data were collected using an X-ray wavelength of 1 ~ Å and processed using Xia2 DIALS[196] and AIMLESS[197]. A molecular replacement model was produced based on MtrC (PDB:4LM8). This model was refined using Phenix[198] and Refmac5[199] to a final resolution of 1.8 Å.

Table 4.2. Data collection and refinement statistics for MtrC domains I and II crystal structure

MtrC domains I, II	
Data collection	
Space group	P $2_1 2_1 2_1$
Cell dimensions	
a, *b*, *c* (Å)	74.28 77.35 96.53
α, β, γ (°)	90.00, 90.00, 90.00
Resolution (Å)	58.87 - 1.80 (1.86 - 1.80)
$CC_{1/2}$ (%)	99.4 (80.2)
$I / \sigma I$	6.92 (0.63)
Completeness (%)	99.8 (99.9)
Multiplicity	12.5 (12.7)

Refinement	
Resolution (Å)	1.80
No. reflections	52134
R_{work} / R_{free}	0.190/0.221
No. atoms	
Protein	2128
Ligand/ion	228
Water	367
B-factors	
Protein	29.03
Ligand/ion	23.04
Water	39.30
R.m.s. deviations	
Bond lengths (Å)	0.020
Bond angles (°)	2.06

The diffraction data was processed by Benjamin Nash (Methods 2.5.7) using a molecular replacement model based on MtrC (PDB: 4LM8) to produce a crystal structure of $MtrC_{DI,II}$ at 1.8 Å (Figure 4.12 A). The structure was resolved to residue A321, with the final four residues (KTTA) not being resolved in the crystal structure. The LC-MS data showed that the highest intensity peak corresponded to a protein predicted to terminate at residue A325. However, the LC-MS also suggested another peak with lower intensity that corresponded to a protein predicted to terminate at residue A321. This could have been the MtrC form that crystallised, as opposed to the predicted $MtrC_{DI,II}$ with termination at A324. The $MtrC_{DI,II}$ crystal structure was deposited on the PDB with a PDB ID of 9EOV. Figure 4.12, B shows how domains I and II from MtrC are maintained in $MtrC_{DI,II}$.

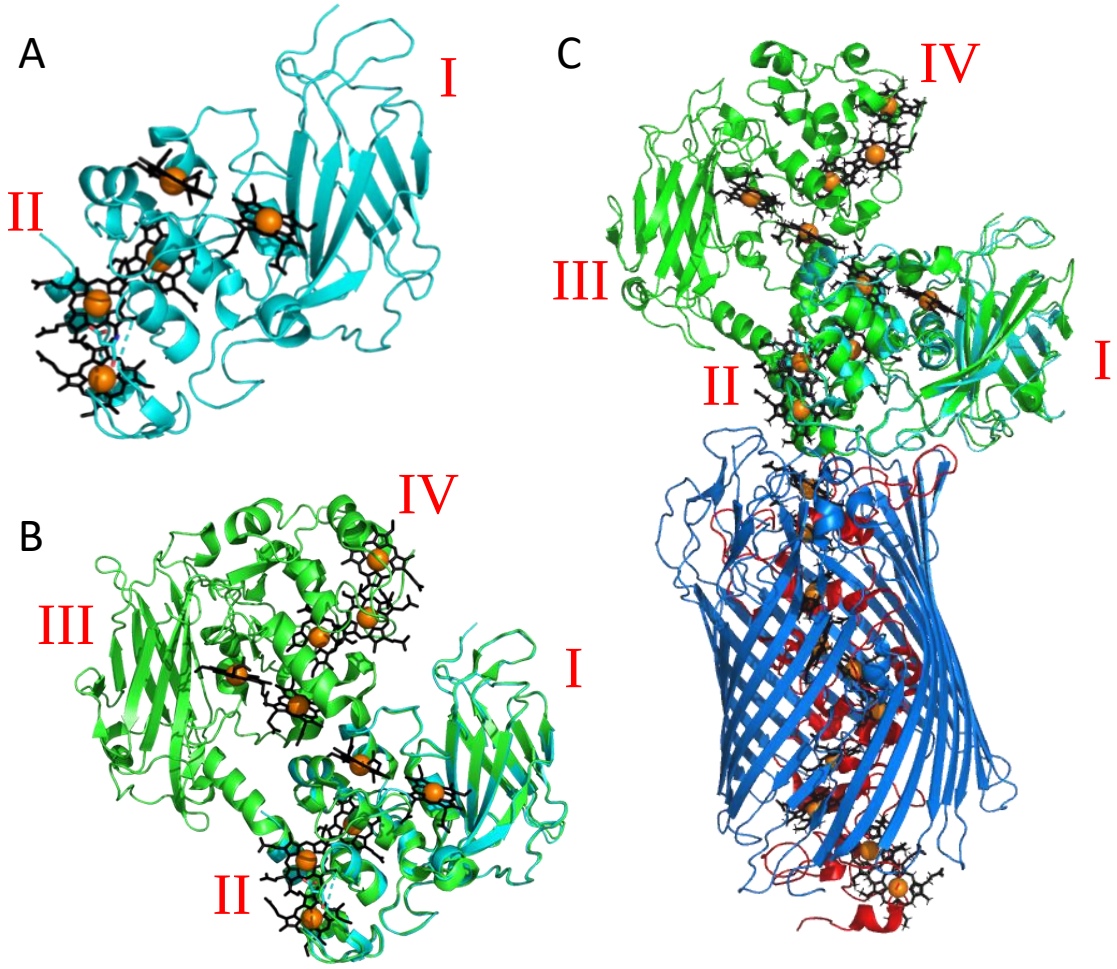

Figure 4.12. $MtrC_{DI,II}$ crystal structure and models. **(A)**. Crystal structure of $MtrC_{DI,II}$ resolved to residue A321 at 1.8 Å (PDB:9EOV). **(B)**. $MtrC_{DI,II}$ crystal structure (cyan) superposed with the crystal structure of MtrC from *S. oneidensis* MR-1 (green; PDB: 4LM8) with an RMSD of 0.380 Å. **(C)**. $MtrC_{DI,II}$ crustal structure (cyan) superposed with the crystal structure for MtrCAB from *S. baltica* OS185 (PDB:6R2Q) with an RMSD of 1.029 Å. *S. baltica* MtrC is shown in green, MtrA in red, and MtrB in blue. MtrC domains are shown in red Roman numerals. Crystal structures and models visualised using PyMOL Molecular Graphics System, version 3.0[222].

Superposing the $MtrC_{DI,II}$ crystal structure to domains I and II of the crystal structure of MtrC WT (Figure 4.12, B) yielded a root mean square displacement (RMSD) of 0.380 Å. This RMSD showed that the structure was identical to that of MtrC domains I, II. The $MtrC_{DI,II}$ structure was superposed to the MtrCAB structure (PDB:6R2Q) of *S. baltica* in Figure 4.12, C. Furthermore, the electron density maps shown in Figure 4.13, also indicate that there was no more density at the C-terminus of the crystallised structure. Consequently, it would appear that domains I and II are enough for MtrC to be produced and folded properly, for the hemes to be incorporated correctly, and for the protein to be secreted correctly to the extracellular space.

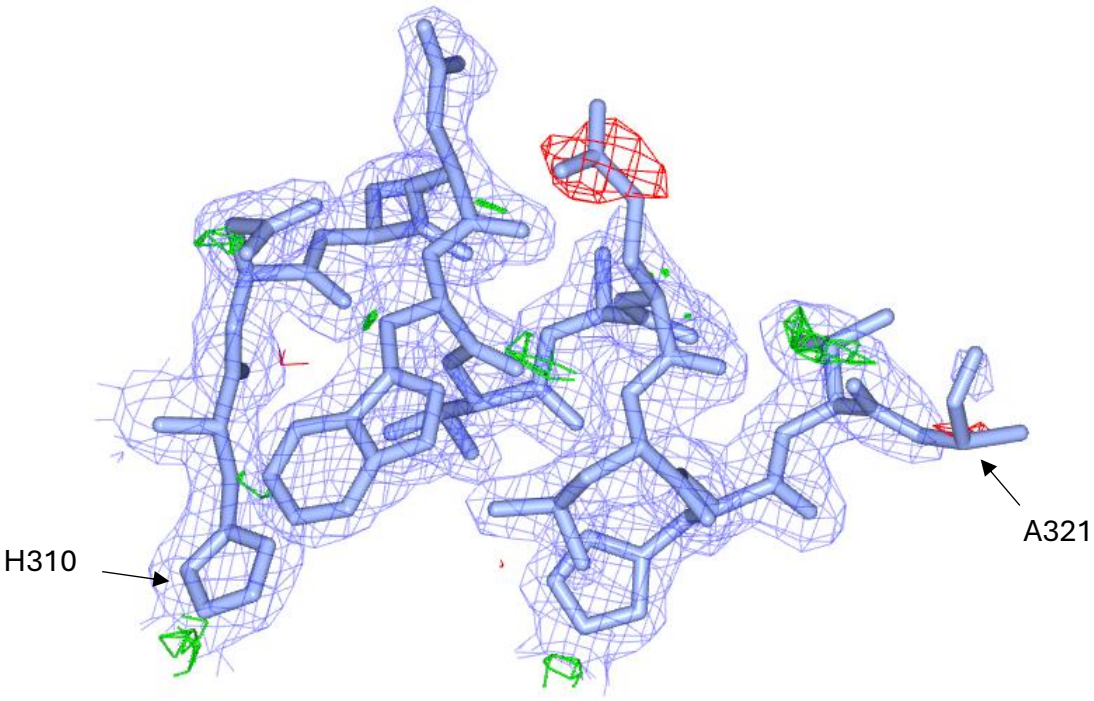

Figure 4.13. Electron density maps for amino acid residues H310 to A321 of $MtrC_{DI,II}$. The Fo-Fc map is shown in blue mesh, while the 2Fo-Fc map is shown in green and red mesh. Figure created using the crystal structure for $MtrC_{DI,II}$ (PDB:9EOV) using *CCP4mg*[223].

4.2.7 Protein film electrochemistry on soluble $MtrC_{DI,II}$

To investigate the electrochemical properties of the hemes in $MtrC_{DI,II}$, non-catalytic protein film electrochemistry was carried out. To do so, cyclic voltammetry (CV) was carried out on purified $MtrC_{DI,II}$ (Methods 2.5.8).

The CV was carried out as 5 linear scans (Methods 2.5.8.3), and the data were analysed and processed in QSoas 3.2[185]. First, CV was done on the ITO electrode

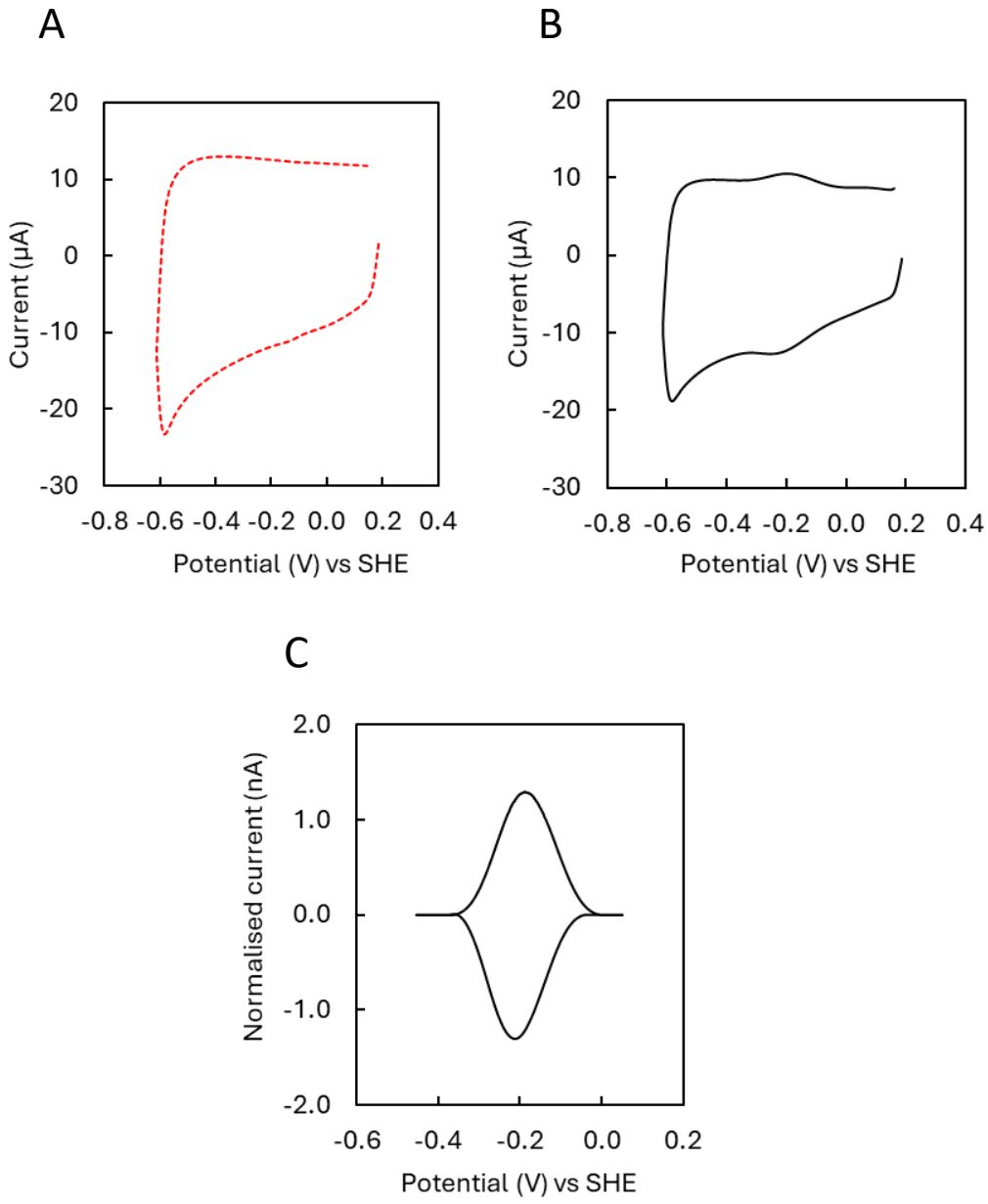

Figure 4.14. Non-catalytic protein film voltammetry of $MtrC_{DI,II}$. (**A**) Voltammogram showing capacitive current of the ITO electrode with no protein adsorbed to it. (**B**) Voltammogram showing capacitive current of $MtrC_{DI,II}$ adsorbed onto the ITO electrode. (**C**) Voltammogram showing Faradaic current of $MtrC_{DI,II}$ adsorbed onto the ITO electrode. Buffer electrolyte solution was composed of anaerobic 50 mM HEPES, 100 mM NaCl, pH 7.0. Cyclic voltammetry was carried out as 5 linear scan repeats from -0.8 V to 0.2 V at 20 mV s^{-1}.

itself, to confirm that the experiment was setup correctly (Figure 4.14, A). Next, CV was carried out on $MtrC_{DI,II}$ adsorbed to the ITO electrode (Figure 4.14, B). The capacitive current of the ITO electrode was subtracted from the capacitive current of the $MtrC_{DI,II}$ adsorbed electrode, resulting in the Faradaic current of $MtrC_{DI,II}$ (Figure 4.14, C).

The experiment was repeated using MtrC WT to compare with $MtrC_{DI,II}$ and see if removing domains III and IV would have any effect on the working reduction potential window of $MtrC_{DI,II}$. Figure 4.15 shows an overlay of the Faradaic currents of MtrC WT and $MtrC_{DI,II}$. When comparing the two, there appeared to be a slight shift towards a more negative potential for the reductive curve of $MtrC_{DI,II}$, and virtually no change in the oxidative curve. This would suggest that even though domains III and IV are no longer present, the difference between MtrC WT and $MtrC_{DI,II}$ is not significant.

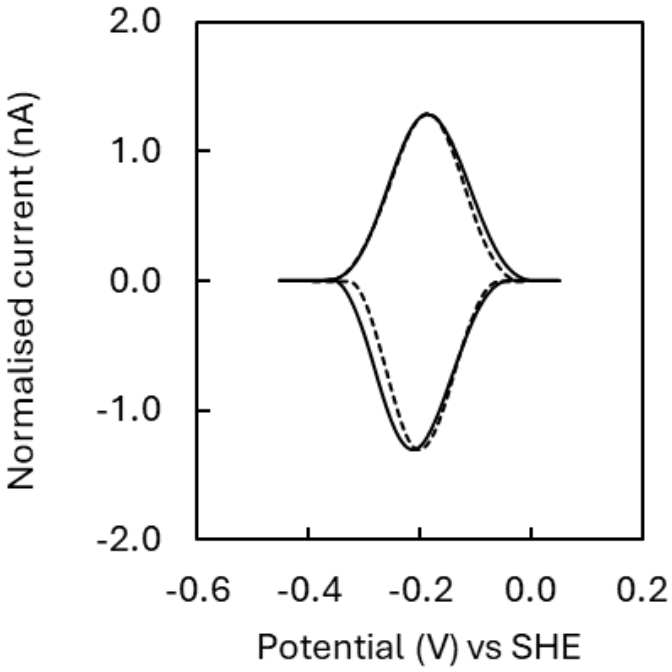

Figure 4.15. Non-catalytic protein film voltammetry of $MtrC_{DI,II}$ (solid line) and MtrC WT (dashed line). The voltammograms show the Faradaic currents of both proteins from cyclic voltammetry. Buffer electrolyte solution was composed of anaerobic 50 mM HEPES, 100 mM NaCl, pH 7.0. Cyclic voltammetry was carried out as 5 linear scan repeats from -0.8 V to 0.2 V at 20 mV s^{-1}.

To better understand the predicted reduction potential contributions of each individual heme, QSoas[185] was used to fit the simulated reduction potentials of five species to the Faradaic current of the protein for both the reductive and oxidative

peaks (Figure 4.16). A sum of five equivalent contributions from individual n=1 redox centres was also generated and fit to the Faradaic current of $MtrC_{DI,II}$ (Methods 2.5.8.3). This model generated five simulated peaks for each the reductive and oxidative Faradaic current peaks, which were treated as pairs for each modelled individual heme group of $MtrC_{DI,II}$.

Figure 4.16 shows the Faradaic current for $MtrC_{DI,II}$ and the simulated individual heme reduction potentials. Notably, for the reductive curve only three different potentials were modelled, when compared to the five of the oxidative curve (Figure 4.16), which suggested that several hemes may have shared very similar reduction potentials. This corroborates previous experiments[195] where the reduction potentials of each of the 10 individual hemes of two MtrC variants were simulated. Their simulations suggested that only 5 hemes had their own different potentials, while the remaining 5 were grouped into two groups of different potentials.

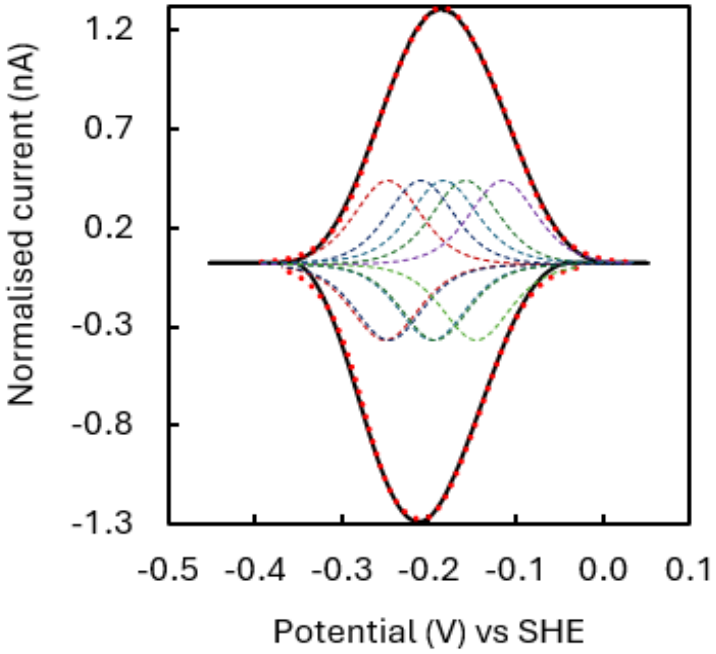

Figure 4.16. Non-catalytic protein film electrochemistry of $MtrC_{DI,II}$. The simulation of five individual hemes (dashed colour lines) fitted to baseline-subtracted cyclic voltammogram (Faradaic current, solid black line) is shown. The fit of the simulation is also shown (red dotted line). The protein was adsorbed onto an indium tin oxide electrode, and voltammetry was recorded at 20 mV s^{-1} in 50 mM HEPES, 100 mM NaCl at pH 7.0.

Table 4.3 shows the simulated reductive and oxidative potential minima and maxima, respectively, of the five individual hemes of $MtrC_{DI,II}$. Table 4.3 also shows the midpoint potentials for MtrC WT and $MtrC_{DI,II}$, which were experimentally calculated to be -0.194 V and -0.199 V vs SHE, respectively, by averaging the potentials at the oxidative and reductive Faradaic current maximum and minimum, respectively.

Table 4.3. Simulated reduction potentials of the individual hemes I, II, III, IV, V, in coloured text. Experimental reduction potentials of the $MtrC_{DI,II}$ and MtrC WT peaks from cyclic voltammetry (black text, bold) are also shown.

heme	I	II	III	IV	V	$MtrC_{DI,II}$	MtrC WT
oxidised E_{red} (V)	-0.249	-0.210	-0.183	-0.158	-0.114	**-0.187**	**-0.185**
reduced E_{red} (V)	-0.250	-0.245	-0.197	-0.194	-0.146	**-0.211**	**-0.202**
overall E_{red} (V)	-0.250	-0.228	-0.190	-0.176	-0.130	**-0.199**	**-0.194**

Previous work[200] has shown the calculated free-energy landscape of MtrC, with predicted reduction potential for each individual heme. They concluded that the net driving force for electrons between hemes 5 and 10 of MtrC and MtrF (*S. oneidensis* MtrC homolog), appeared to be small[200]. Consequently, this symmetrical, free-energy landscape allows bidirectional EET across the MtrCAB complex[201]. It was suggested [200] that heme 7 acted as an electron sink due to its more positive reduction potential (due to nearby positively charged residues), and that upon reduction electron transfer to heme 6 was slowed down. However, if the cells are grown without an electron acceptor, the intracellular electrons accumulate, and all of the hemes within MtrCAB become reduced. Regardless of the heme 7 electron sink, as soon as an acceptor becomes available, the electrons are quickly transferred from the reduced hemes to the acceptor, allowing more intracellular electrons to traverse the MtrCAB conduit. The proportion of MtrA and MtrC hemes that become reduced at the same time depends heavily on the potential of the acceptor. Consequently, this could lead to fewer electrons traversing the heme proteins at any given time [200]. Moreover, as electrons start to reduce the hemes in the multiheme proteins, it becomes increasingly difficult for more electrons to be transferred onto the proteins until they are all transferred onto the acceptor[202].

4.2.8 Membrane $MtrC_{DI,II}$ expression trials for purification

To confirm correct production of membrane $MtrC_{DI,II}$ by the *S. oneidensis* Δ*mtrC/omcA* cells, an expression trial was done (Methods 2.3.1). First, the *S. oneidensis ΔmtrC/omcA* containing the $pMTRC_{DI,II}$ plasmid were incubated overnight in 10 mL of LB_{kan}. The following day, a 0.1% inoculum of the overnight cells was prepared in 4 x 10 mL of M72 media (with supplements and kanamycin). The cells were immediately induced with 0, 1, 3, and 5 mM L-arabinose and incubated overnight again. The produced membrane $MtrC_{DI,II}$ was not secreted to the extracellular environment, but instead would have formed a complex with natively produced MtrAB. Consequently, the cells needed to be cultured at conditions where the induced plasmid led to optimal protein overexpression, but the cells were still viable and healthy. Therefore, the following day a viability assay was performed on the *S. oneidensis ΔmtrC/omcA* with the induced $pMTRC_{DI,II}$ plasmid (Methods 2.6.1). The cell viability assay served the purpose of helping understand if the assayed cells were healthy or not. However, as the reaction is stopped arbitrarily at the point before the reactant changes colour too much, the quantitative value of the data cannot be too high.

Table 4.4. Processed data converted from the electronic absorbance taken during the cell viability assay of *S. oneidensis ΔmtrC/omcA* cells containing the $pMTRC_{DI,II}$ plasmid. Numbers represent averages from three replicates, and ±indicates standard error of mean. Control indicates a cell-free sample only containing media.

L-arabinose concentration	PrestoBlue™ Reagent percentage reduction
0 mM	61.95 (±5.75)
1 mM	57.55 (±2.25)
3 mM	52.4 (±3.1)
5 mM	60.2 (±2.9)
control	2.62 (±0.09)

Instead, the processed data generated by the assay should be considered qualitative, i.e. whether the cells were metabolically active (healthy) or metabolically inactive (dead). Table 4.4 shows the results of the cell viability assay done on two groups of the same L-arabinose concentration range. The values listed in Table 4.4 indicated that all the assayed cells were metabolically active.

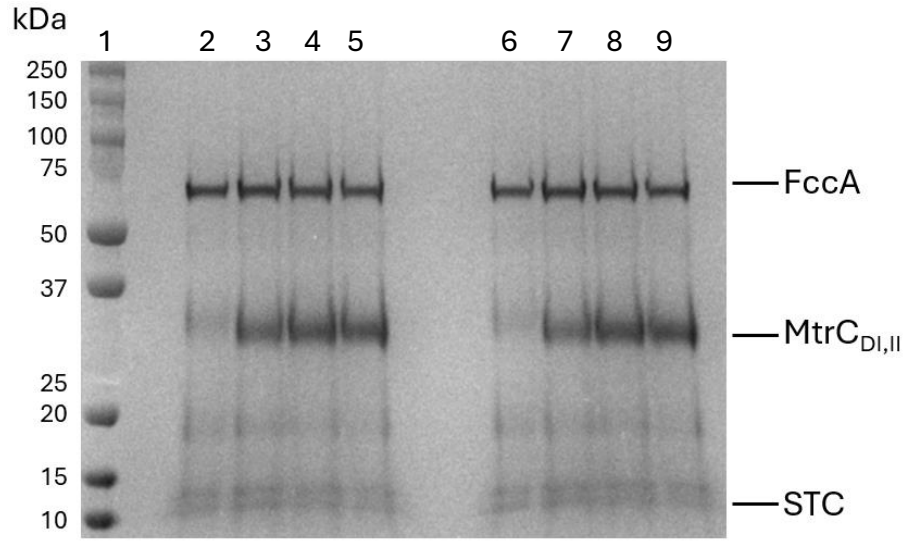

Figure 4.17. Heme-stained SDS-PAGE gel from expression trial of *S. oneidensis ΔmtrC/omcA* with the membrane pMTRC$_{DI,II}$ plasmid. Samples were done in duplicate and are composed of lysed cells. Lanes are as follows: molecular marker (lane 1); induction with 0 mM L-arabinose (lanes 2, 6); induction with 1 mM L-arabinose (lanes III, VII); induction with 3 mM L-arabinose (lanes 4, 8); and induction with 5 mM L-arabinose (lanes 5, 9). Fumarate reductase (FccA), membrane (lipid-anchored) MtrC$_{DI,II}$, and small tetraheme cytochrome (STC) are indicated with lines.

After having confirmed that the *S. oneidensis* Δ*mtrC/omcA* cells with the induced pMTRC$_{DI,II}$ plasmid were metabolically active, protein expression was investigated by running a whole-cell gel (Methods 2.1.7) and performing a heme stain on the gel. Figure 4.17 shows the heme-stained gel from the expression trial after confirming the cells were viable. The gel suggests that induction with 1, 3, and 5 mM of L-arabinose resulted in a produced protein with a size of ~ 35 kDa. This is the expected weight of MtrC$_{DI,II}$, therefore it was concluded that the protein had been produced correctly, regardless of the concentration of L-arabinose used. Furthermore, there appeared to be a fainter band in the 0 mM L-arabinose samples (lanes II and VI, Figure 4.17) at the same size. It is known that there is basal level expression (or "leaky" expression) of the pBAD plasmid, which is what is seen in the SDS-PAGE gel; however, the bands at 0 mM L-arabinose were much fainter than the bands at 1, 3, and 5 mM L-arabinose. The whole-cell gel (Figure 4.17) which includes the membranes, shows heme proteins found inside the lysed cells (the secreted proteins were removed after cell lysis) including fumarate reductase (FccA) and small tetraheme cytochrome (STC). 1 mM L-arabinose was selected for all future inductions of membrane MtrC$_{DI,II}$ plasmid.

A second SDS-PAGE gel (Figure 4.18) was run with *S. oneidensis* MR-1 cells, *S. oneidensis ΔmtrC/omcA* cells, and *S. oneidensis ΔmtrC/omcA* cells with the pMTRC$_{DI,II}$ plasmid to further confirm the production of MtrC$_{DI,II}$. The expression trial and SDS-PAGE gel were carried out as above, and the gel was heme-stained. The gel shows *S. oneidensis* MR-1 producing MtrC WT (~ 76 kDa) and MtrA (~ 35 kDa), as expected. Furthermore, the *S. oneidensis ΔmtrC/omcA* cells produce MtrA but not MtrC. It becomes less clear, but in the uninduced cells (lanes IV, VI, Figure 4.18) the band around 35 kDa is slightly broader than the double knockout cells. Again, this is due to leaky expression from the pBAD plasmids. However, the induced cells (lanes V, VII, Figure 4.18) show a much more intense band at ~ 35 kDa. Unfortunately, MtrC$_{DI,II}$ and MtrA are extremely close in size, so distinguishing the two on an SDS-PAGE gel is quite subjective. However, Figure 4.18 suggests that the MtrC$_{DI,II}$ band has a slightly smaller size, thus suggesting a difference from MtrA. Nevertheless, to fully confirm the formation of the MtrC$_{DI,II}$AB trimer, the purification of the whole complex was necessary.

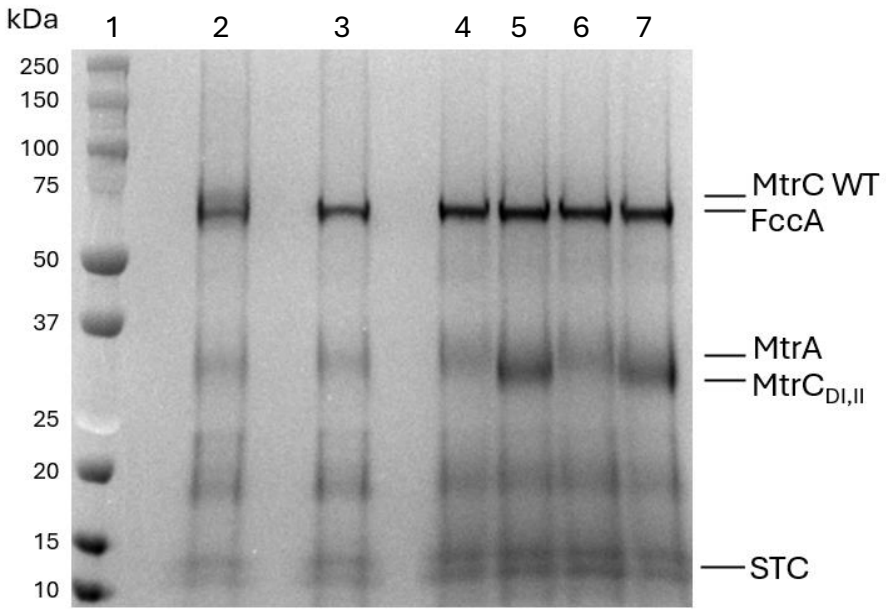

Figure 4.18. Heme-stained SDS-PAGE gel with three *S. oneidensis* strains. Lanes are as follows: molecular marker (lane 1); *S. oneidensis* MR-1 cells (lane 2); *S. oneidensis ΔmtrC/omcA* cells (lane 3); uninduced *S. oneidensis ΔmtrC/omcA* cells with pMTRC$_{DI,II}$ plasmid (lanes 4, 6); and *S. oneidensis ΔmtrC/omcA* cells with pMTRC$_{DI,II}$ plasmid induced with 1 mM L-arabinose (lanes 5, 7). Fumarate reductase (FccA), MtrC WT, MtrA, MtrC$_{DI,II}$, and small tetraheme cytochrome (STC) are indicated with lines.

A final whole-cell SDS-PAGE gel was run comparing protein production of the following *S. oneidensis* strains MR-1 (wild-type), *ΔmtrA*, *ΔmtrC/omcA*, *ΔmtrC/omcA* containing the $pMTRC_{rec}$ plasmid (producing MtrC WT), and *ΔmtrC/omcA* containing the $pMTRC_{DI,II}$ plasmid (Figure 4.19). The differences in production of MtrC WT, $MtrC_{DI,II}$ and MtrA are more apparent in this gel. The MR-1 cells (lane II, Figure 4.19) produce both MtrC WT and MtrA. However, the *ΔmtrA* (lane III, Figure 4.19) and *ΔmtrC/omcA* (lane IV, Figure 4.19) have no band where MtrC WT would be expected to be. The *ΔmtrC/omcA* cells with the $pMTRC_{rec}$ and $pMTRC_{DI,II}$ (lanes V and VI, Figure 4.19, respectively) both produce MtrA. However, it is difficult to distinguish the MtrA and $MtrC_{DI,II}$ bands from this gel, as they are so close to each other. However, the MtrC WT is clearly visible only in the cells with the $pMTRC_{rec}$ plasmid. Furthermore, the fumarate reductase (FccA) is also seen across the whole gel, highlighting the high levels of expression of this protein.

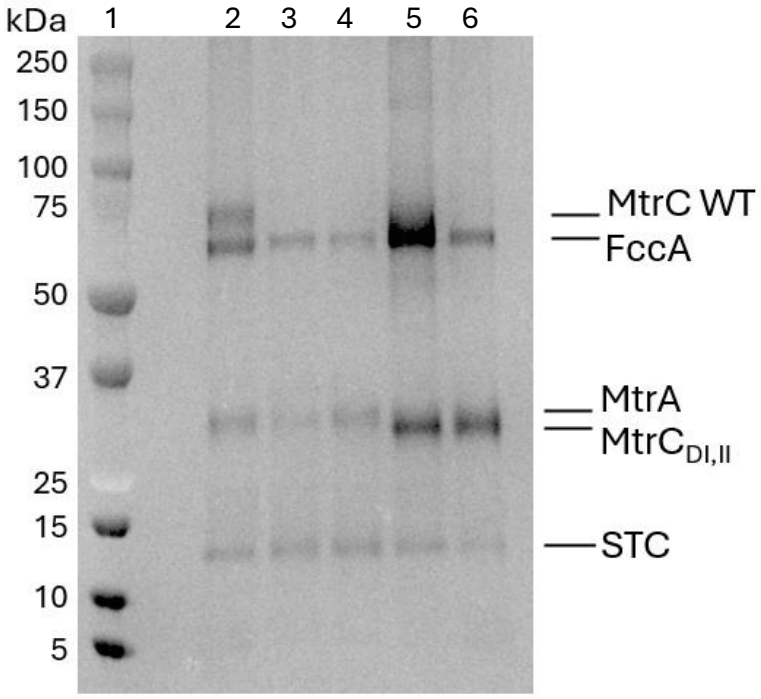

Figure 4.19. *S. oneidensis* whole-cell SDS-PAGE gel visualised by heme-stain. *S. oneidensis* strains are as follows: molecular marker (lane 1); MR-1 (wild-type, lane 2); *ΔmtrA* (lane 3); *ΔmtrC/omcA* (lane 4); *ΔmtrC/omcA* with $pMTRC_{rec}$ (producing MtrC WT, lane 5); *ΔmtrC/omcA* with $pMTRC_{DI,II}$ (lane 6). Cells were normalised to an OD_{600} of 0.1 and precipitated with acetone. Fumarate reductase (FccA), MtrC WT, MtrA, $MtrC_{DI,II}$, and small tetraheme cytochrome (STC) are indicated with lines.

4.2.9 $MtrC_{DI,II}AB$ complex purification

After confirming correct protein production with the expression trials, a large-scale protein purification protocol was used. As the membrane $MtrC_{DI,II}$ had a lipid anchor, it was expected that it would form a complex with the endogenously produced MtrAB, resulting in a $MtrC_{DI,II}AB$ trimer complex. Therefore, the trimer complex was purified as a whole, as opposed to just $MtrC_{DI,II}$. Cells were grown as detailed before (Methods 2.4.1) and the "2.4.4 Membrane proteins" protocol was followed. SDS-PAGE gels were done throughout the purification process and subjected to both heme and Coomassie stains. Figure 4.20 top and 4.20 bottom show heme- and Coomassie-stained SDS-PAGE gels of several steps of the purification protocol, respectively. The heme-stained SDS-PAGE gels were used to monitor the presence of heme proteins throughout the purification protocol. MtrCAB with MtrC WT was also loaded on the gel as a control. This was particularly important to compare the size of MtrA and MtrB between the purified MtrCAB and $MtrC_{DI,II}AB$. Figure 4.20 highlights the necessity of running a SEC column to remove any final impurities.

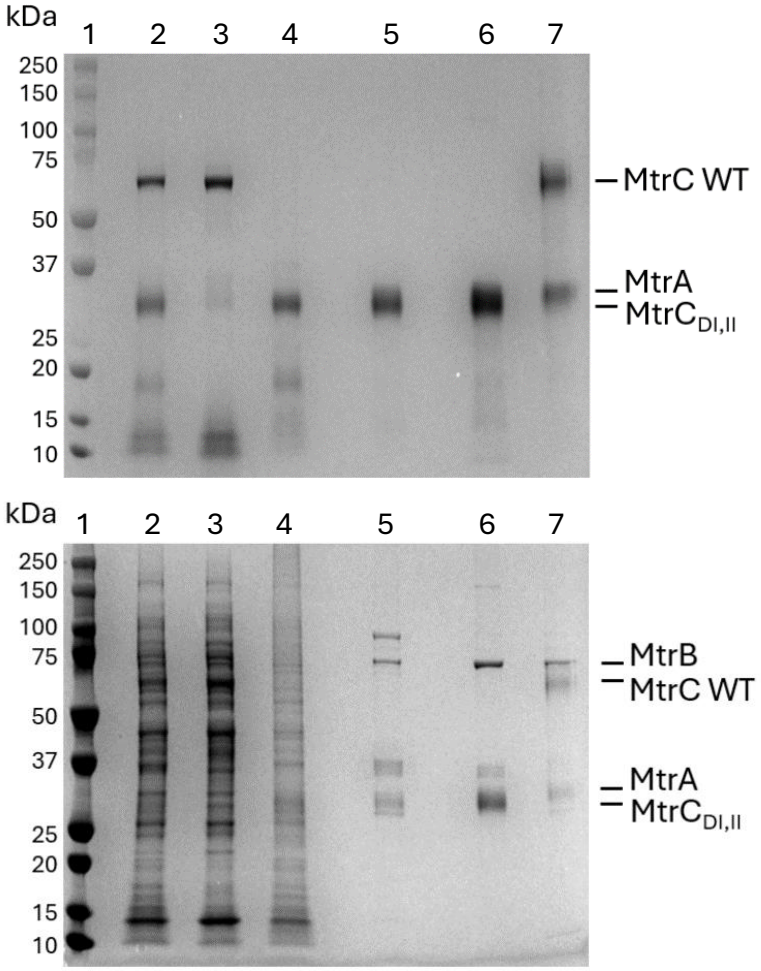

Figure 4.20. SDS-PAGE gels of MtrC$_{DI,II}$AB purification steps. Gels shown were heme-stained (**top**) or stained with Coomassie (**bottom**). For both gels, lanes are as follows: molecular marker (lane 1); lysed cells after French Press (lane 2); membrane fraction after first ultra centrifugation (lane 3); membrane fraction after preferentially solubilising inner membranes (lane 4); pooled eluted fractions after DEAE anionic exchange chromatography column (lane 5); pooled eluted fractions after SEC column (lane 6); purified MtrCAB (with MtrC WT) as a control (lane 7). Fumarate reductase (FccA), MtrB, MtrC WT, MtrA, MtrC$_{DI,II}$, and small tetraheme cytochrome (STC) are indicated with lines.

However, after the elution from the SEC column (lane VI, Figure 4.20) the sample still contained minor impurities. To remove these, the proteins were loaded onto a Mono-Q anionic exchange column (Methods 2.4.4). The ÄKTA trace for the SEC and Mono-Q columns of both MtrCAB and MtrC$_{DI,II}$AB are shown in Figure 4.21.

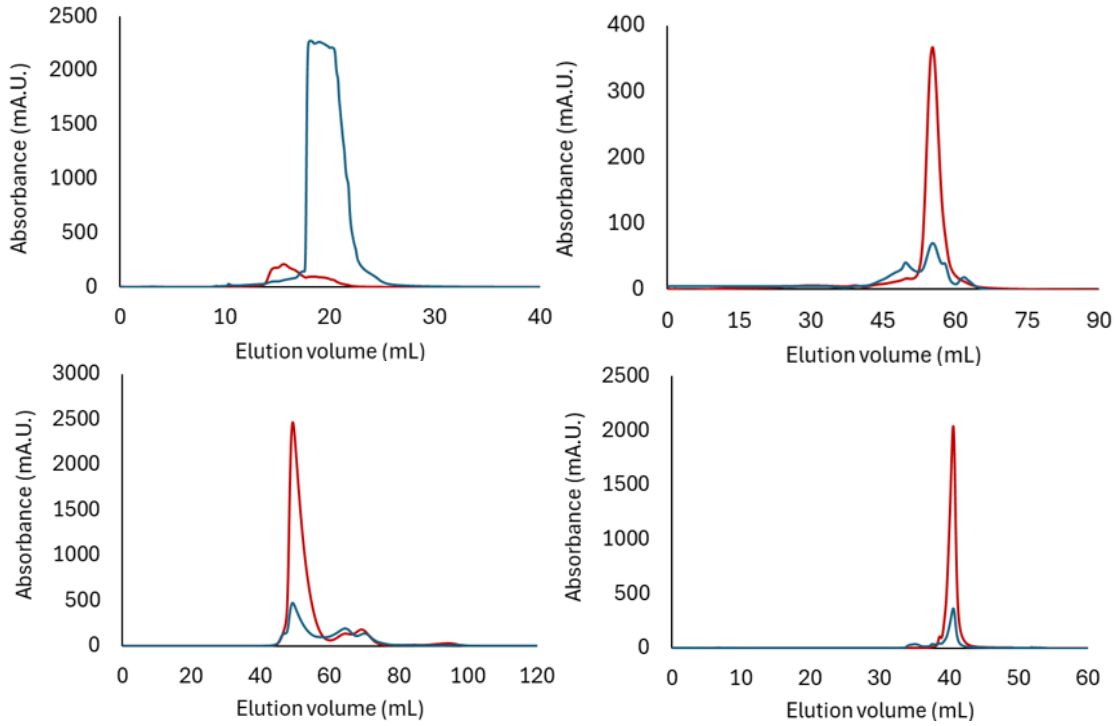

Figure 4.21. ÄKTA traces showing: MtrCAB eluted from SEC Superdex 16/60 200 pg column (**top, left**), MtrCAB eluted from MonoQ column (**top, right**), $MtrC_{DI,II}AB$ eluted from SEC Superdex16/60 200 pg column (**bottom, left**), and $MtrC_{DI,II}AB$ eluted from MonoQ column (**bottom, right**). The electronic absorbance is shown for absorbance at. The A_{410} and A_{280} are shown as red and blue lines, respectively.

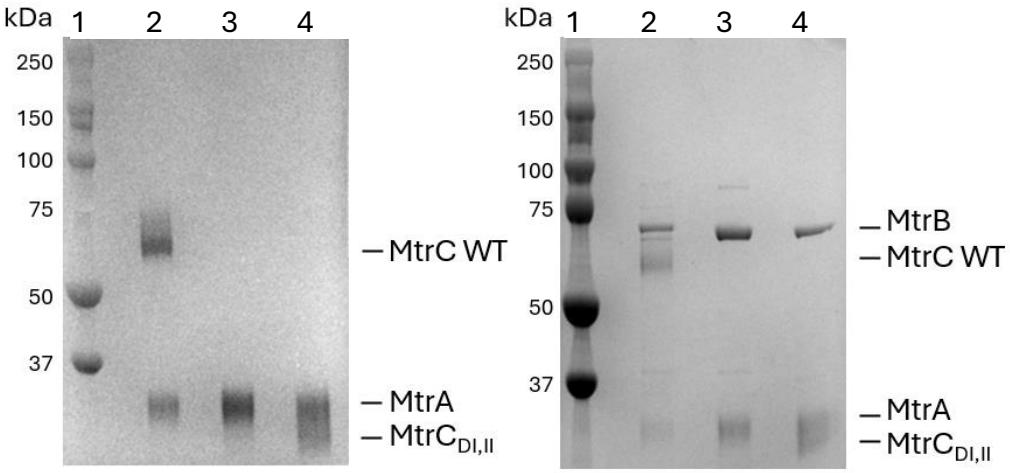

Figure 4.22. SDS-PAGE gels of purified MtrCAB, MtrAB, and $MtrC_{DI,II}AB$. Gels shown were heme-stained (**left**) or stained with Coomassie (**right**). For both gels, lanes are as follows: molecular marker (lane 1); MtrCAB (lane 2); MtrAB (lane 3); and $MtrC_{DI,II}AB$ (lane 4).

Differences between the size and charge of the MtrCAB and $MtrC_{DI,II}AB$ can be seen on the SEC and MonoQ columns, respectively due to their different elution volumes.

These differences were indicative of physical differences between the two purified proteins.

The fractions eluted from the Mono-Q column were confirmed to have virtually no impurities as seen in Figure 4.22. These results suggested that a complex had successfully formed comprised of the plasmid-based membrane $MtrC_{DI,II}$ and the native MtrAB.

4.2.10 Analytical ultracentrifugation of $MtrC_{DI,II}AB$

The ÄKTA traces (Figure 4.21) suggested that the $MtrC_{DI,II}AB$ had been purified as a single, trimeric complex. Additionally, the SDS-PAGE gels (Figure 4.22) suggested that the purified complex was comprised of $MtrC_{DI,II}$, MtrB, and MtrA. However, more evidence was required to increase the level of confidence that the trimer was forming correctly as a whole complex, as opposed to as MtrAB with $MtrC_{DI,II}$ attached due to hydrostatic interactions. Furthermore, the differences in band sizes on the SDS-PAGE gels between MtrA and $MtrC_{DI,II}$ were quite small, therefore discerning between the two bands was quite subjective. To further confirm the formation of the $MtrC_{DI,II}AB$ complex, analytical ultracentrifugation (AUC) was used (Methods 2.5.4). Sedimentation velocity analyses were conducted by repeatedly measuring the electronic absorbance at 410 nm during centrifugation. These analyses were done on $MtrC_{DI,II}$ as well as MtrCAB and MtrAB as controls. After obtaining the A_{410} spectra for all three proteins, the Lamm equation[203] was used to fit

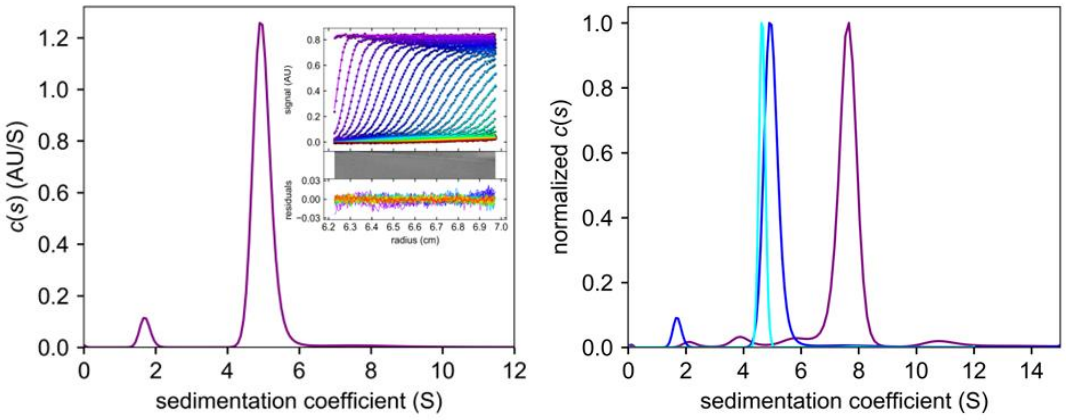

Figure 4.23. Left. Sedimentation coefficient distribution of $MtrC_{DI,II}AB$. **Inset**: $MtrC_{DI,II}AB$ sedimentation velocity analysis observed by absorbance at 410 nm (markers). Data was fit (lines) to Lamm equation and any fitted data residual absorption is shown in the lower panel. **Right.** Overlay of deconvoluted diffusion sedimentation coefficient distribution S of MtrAB (cyan line), $MtrC_{DI,II}AB$ (blue line), and MtrCAB (purple line). All proteins were diluted in 20 mM HEPES, 150 mM NaCl, 5 mM LDAO, pH 7.8.

the data (Figure 4.23, left). From the fitted data, a c(S) distribution was determined (Figure 4.23, right)

Figure 4.23 left shows the data fitted with the Lamm equation for $MtrC_{DI,II}AB$ as well as the fit residuals. The fitted data yielded a predominant peak of 5.22 S, with a much smaller peak around ~ 1.5 S. This secondary peak was probably due to residual impurities after the Mono-Q chromatography column. Figure 4.23 right shows the distribution of the diffusion sedimentation coefficients (S) for all three protein complexes. The sedimentation coefficients for MtrAB and $MtrC_{DI,II}AB$ were relatively close, but for MtrCAB was higher. This could be due to the higher mass and extended length of MtrCAB. The sedimentation coefficient provides information on the rate at which the particles migrate through the buffer or settle out of suspension (sedimentation) under centrifugal force. However, because the detergent micelles impact the buoyancy, and consequently the sedimentation, of the membrane protein complexes, comparisons of the sedimentation coefficient across the three proteins should take this into consideration.

Table 4.5 Processed results from sedimentation velocity AUC experiments. The deconvoluted diffusion sedimentation coefficient distribution and frictional coefficients show differences between MtrAB, $MtrC_{DI,II}AB$, and MtrCAB. In the MtrAB sample, MtrAB accounted for 99% of the experimental mass, sedimentation coefficient and frictional coefficient. For the $MtrC_{DI,II}AB$ sample, $MtrC_{DI,II}AB$ accounted for 92% of the experimental mass, sedimentation coefficient, and frictional coefficient. For the MtrCAB sample, MtrCAB accounted for 86% of the experimental mass, sedimentation coefficient, and frictional coefficient. The partial specific volume for all samples was 0.72 mg mL^{-1}. All samples were in 20 mM HEPES, 150 mM NaCl, 5 mM LDAO, pH 7.8.

Sample	Experimental mass (kDa)	Predicted mass (kDa)	Sedimentation coefficient (S)	Frictional coefficient $\left(\frac{f}{f_0}\right)$
MtrAB	95	114	4.8	1.55
$MtrC_{DI,II}AB$	135	149	5.2	1.82
MtrCAB	183	185	7.4	1.56

The predominant $MtrC_{DI,II}AB$ species had a sedimentation coefficient of 5.22 S and a frictional coefficient ratio $\left(\frac{f}{f_0}\right)$ of 1.82 (Table 4.5), where f is the $MtrC_{DI,II}AB$ frictional coefficient, and f_0 is the frictional coefficient of a perfect sphere of equal viscosity, mass, and hydration[79]. MtrAB, however, had a sedimentation coefficient of 4.81 S and a frictional coefficient ratio of 1.55 (Table 4.5). After accounting for the

whole cell SDS-PAGE and the AUC data, it was concluded that the likelihood of $MtrC_{DI,II}$ forming a stable complex with MtrAB was quite high.

Table 4.5 shows the predicted and experimental masses for the three proteins, as well as their corresponding calculated sedimentation and frictional coefficients. The differences between the predicted and experimental masses were likely due to the buoyant effect the detergent micelle had on the overall sedimentation of the proteins. The data from the ÄKTA traces, SDS-PAGE gels and the AUC further increased the likelihood of having purified the full $MtrC_{DI,II}AB$ complex successfully.

4.2.11 Ultraviolet-visible spectroscopy of $MtrC_{DI,II}AB$

To begin to assess the redox capabilities of the purified $MtrC_{DI,II}AB$ complex, UV-Visible spectroscopy was carried out (Methods 2.5.1). To do so, the oxidised proteins were reduced with sodium dithionite and the electronic absorbance spectra were taken. Figure 4.24, top shows the oxidised and reduced $MtrC_{DI,II}AB$. As expected, when the heme protein is reduced with sodium dithionite, the Soret band shifts from ~ 410 nm (oxidised) to ~ 420 nm (reduced). Also, the alpha (~ 552 nm), beta (~ 525 nm), and Soret bands all become more pronounced upon reduction. Figure 4.24, bottom shows the same spectrum but for MtrCAB, also showing the characteristic features of heme protein reduction. There is a very small difference of 1 nm and 2 nm in the wavelength of the reduced Soret and α bands, respectively, between MtrCAB and $MtrC_{DI,II}AB$. The β band, however, remained the same. The oxidised Soret wavelengths had a difference of 1 nm as well. These data suggest that there do not appear to be any dramatic differences in the redox capacities of MtrCAB and $MtrC_{DI,II}AB$ when reduced with sodium dithionite. These results are similar to the UV-Vis spectra of soluble $MtrC_{DI,II}$ and soluble MtrC.

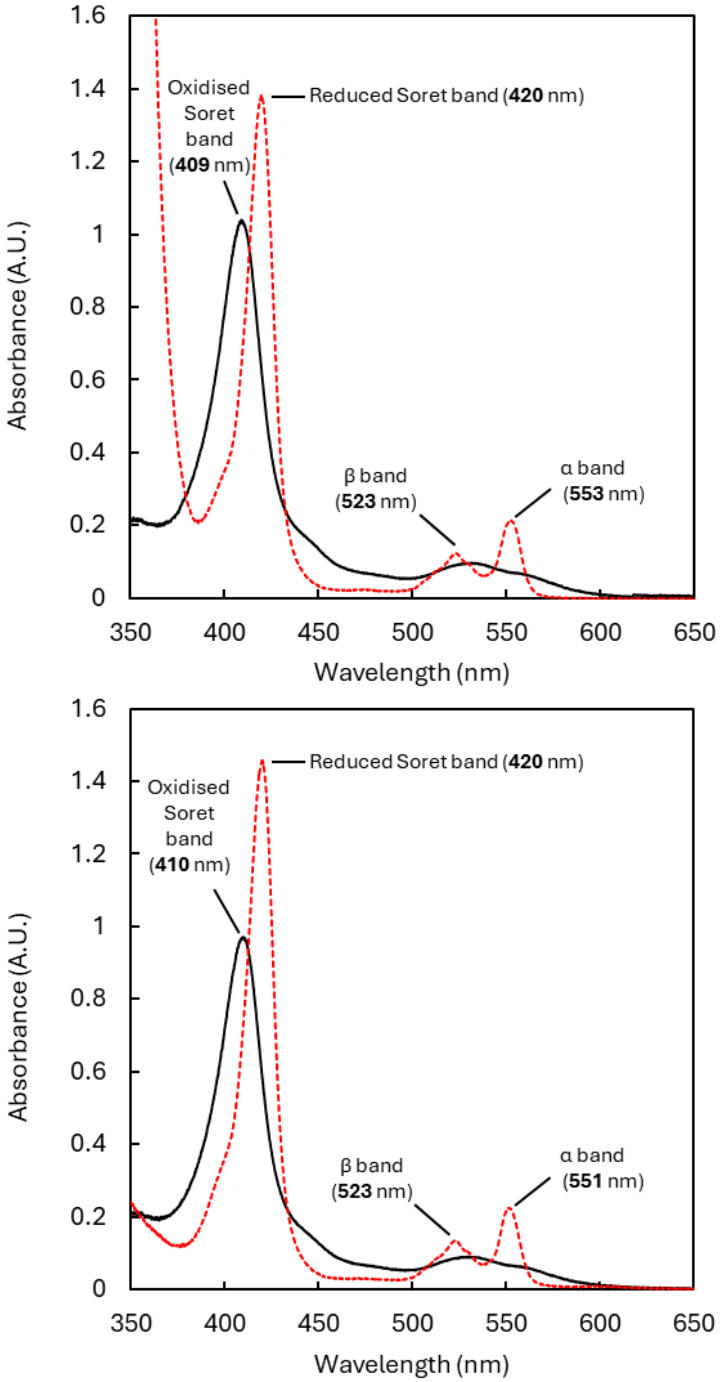

Figure 4.24. Electronic absorbance of soluble $MtrC_{DI,II}AB$ (**top**), and MtrCAB (**bottom**) showing the oxidised state (solid black line) and dithionite-reduced state (red dashed line). Characteristic heme protein features and their corresponding wavelengths are labelled on the spectra. Proteins were diluted in 20 mM Tris, 30 mM NaCl, 5 mM LDAO, pH 7.8.

4.2.12 Functional characterisation of $MtrC_{DI,II}AB$

Once it had been confirmed that the membrane $MtrC_{DI,II}$ was forming a complex with MtrAB to form the trimer $MtrC_{DI,II}AB$, and some biophysical characterisation had been done on the =purified complex itself, the focal point of this thesis was shifted towards the *in vivo* effects that removing domains III and IV of MtrC would have on the functionality of the $MtrC_{DI,II}AB$ complex. To do, the electron transfer through the complex was investigated largely through reduction assays. When supplemented with lactate and under anaerobic conditions, the intracellular metabolism of *S. oneidensis* generated electrons that required a terminal electron acceptor to complete EET. A variety of physiological as well as non-physiological electron acceptors were assayed for this purpose. Furthermore, reduction assays were carried out on several mutant *S. oneidensis* strains, with and without $MtrC_{DI,II}$.

4.2.12.1 Membrane $MtrC_{DI,II}AB$ cell viability trials for functional assays

To begin, all *S. oneidensis* cells assayed in all reduction experiments needed to be healthy and metabolically active. The reduction experiments, however, were carried out on the same *S. oneidensis ΔmtrC/omcA* cells containing the membrane $pMTRC_{DI,II}$ plasmid. These same cells already had been shown to be viable and metabolically active (Methods 4.2.2.2) so further viability assays were not necessary on this strain. However, this assay was used to simply determine if the cells had grown properly overnight, and to confirm the L-arabinose induction had not led to cell death. Table 4.6 shows the results from the cell viability assay on *S. oneidensis ΔmtrC/omcA* cells containing the $pMTRC_{rec}$ plasmid (producing MtrC WT).

Table 4.6. Processed data converted from the electronic absorbance taken during the cell viability assay of *S. oneidensis ΔmtrC/omcA* cells containing the $pMTRC_{rec}$ plasmid. Cells were induced with 1 mM L-arabinose. Control indicates a cell-free sample only containing media.

Sample	PrestoBlue™ Reagent percentage reduction
A	50.3 (±3.54)
B	47.4 (±4.02)
control	2.62 (±0.09)

For the remaining *S. oneidensis* strains that did not contain plasmids (MR-1, *Δmtr*, and *ΔmtrC/omcA* with no plasmid) a faster, bench version of the assay was carried out. However, these samples were not analysed using a plate reader or spectrophotometer. After the reaction was stopped, a visual inspection of the wells was enough to determine if the cells were metabolically active. Only the overnight cultures of plasmid-less *S. oneidensis* cells that went turbid were subjected to the fast, bench version of the cell viability assay.

This fast version of the viability assay could only be done with the plasmid-free *S. oneidensis* cells. This was because *S. oneidensis* cells that contained a plasmid could multiply successfully (and consequently increase the OD_{600} and turbidity of the media), but if the L-arabinose concentration used for induction was too high, the cells would end up dying. This would result in an overnight culture that was highly turbid, but with little to no metabolic activity.

4.2.12.2 Reduction of flavin mononucleotide

Flavin mononucleotide (FMN) is a known redox shuttle for *Shewanella* and is secreted by the cells to help in EET[204]. A feature of FMN that is extremely useful in biochemical analyses, is the fluorescence of the molecule. However, only the oxidised form can fluoresce (excitation at 365 nm and emission at 525 nm). Upon reduction, the FMN loses its capacity to fluoresce. Therefore, the decrease in fluorescence of the FMN over a determined amount of time can be converted into rate of electron transfer onto the FMN molecules.

Figure 4.25 shows both the raw fluorescence data from the fluorimeter (Figure 4.25, left) and the data converted to rate of FMN reduction (Figure 4.25, right). From the raw data, it could be visually seen that the fastest drop in fluorescence intensity was due to the electrons transported in the *ΔmtrC/omcA* producing the MtrC WT (red line). As the plasmid-based proteins are largely overexpressed, higher reduction rates than the WT were expected. MR-1 (green line) was the positive control and the decrease in fluorescence intensity was clear, but not as dramatic as the overexpressed MtrC WT mutant. The *Δmtr*, *ΔmtrC/omcA*, and overexpressed $MtrC_{DI,II}$ mutants showed similar results, where little to no change in fluorescence intensity was observed (orange, blue, and purple lines, respectively).

The transfer of electrons from the *S. oneidensis* cells to FMN happened quickly, as was seen from the decreasing gradient of the fluorescence intensity with time. Consequently, the initial (within two to three minutes) change in fluorescence was largely used in the FMN reduction rate calculations. Furthermore, using the initial change was advantageous to try to mitigate against any false positive readings from any oxygen that may have leaked into the cuvette and sequestered the intracellular electrons. The FMN reduction rates shown in this thesis (Figure 4.25, right) corroborated previous work[113] showing the incapability for *Δmtr* and *ΔmtrC/omcA* mutants to reduce FMN. The *ΔmtrC/omcA* mutant did have a slightly higher rate than the *Δmtr* mutant, suggesting a small level of electron transfer does occur between MtrA and FMN. Reassuringly, the *ΔmtrC/omcA* mutant producing MtrC WT had a faster rate than MR-1, suggesting the experimental design was appropriate and the produced MtrC WT protein transferred electrons from the endogenous MtrAB onto the FMN.

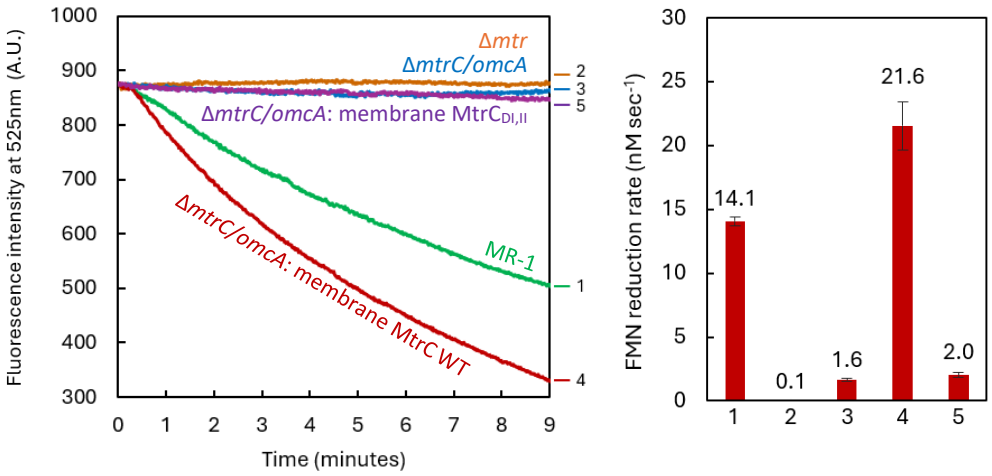

Figure 4.25. Results from the $MtrC_{DI,II}$ FMN reduction assay. **Left.** Change in fluorescence intensity at 525 nm of five *S. oneidensis* strains over a period of 9 minutes. **Right.** Processed data from the FMN assay, where change in fluorescence was converted to a rate of FMN reduction. Strains shown include: MR-1 (**1**); *Δmtr* (**2**); *ΔmtrC/omcA* (**3**); *ΔmtrC/omcA* producing MtrC WT (**4**); and *ΔmtrC/omcA* producing $MtrC_{DI,II}$ (**5**). The assay was carried out with cells at a starting OD_{600} of 0.1 induced with 1 mM L-arabinose. The initial concentration of FMN was 12 μM. Experiments were done in triplicate and error bars show standard error of mean. No statistical tests were carried out on the data.

Under anaerobic conditions and when MtrC is reduced, FMN can form a putative MtrC-FMN complex which increases EET rates. However, this is only possible when the CX_8C disulfide bond in MtrC remains reduced. Upon interaction with oxygen, the disulfide reforms and the FMN cofactor is lost. It has been suggested[131] that the closest heme to the MtrC disulfide bond is heme 7 within domain III of MtrC. Here,

the presented $MtrC_{DI,II}AB$ system does not contain domains III or IV, therefore does not have this disulfide redox switch nor heme 7. Therefore, the formation of MtrC-FMN complex would not be possible. The *ΔmtrC/omcA* cells producing $MtrC_{DI,II}$ showed no significant increase in the FMN reduction rate when compared to just *ΔmtrC/omcA* with no plasmid. These results corroborated previous hypotheses that the FMN binding socket on MtrC is located near heme 7 in domain III. However, molecular simulations have also been carried out[205] where computational docking was utilised to predict the preferred interaction site between MtrC and FMN. This work concluded that heme 2 would be the docking site for FMN on MtrC by comparing the predicted dissociation constants (K_d). However, the work presented in this chapter disproves these predictions. The results from the FMN reduction assay would suggest that electrons cannot be transferred from $MtrC_{DI,II}$ onto FMN, indicating that a MtrC-FMN complex may not be able to form without domains III and IV containing hemes 6 to 10, especially heme 7 and the neighbouring disulfide bond.

4.2.12.3 Reduction of OmcA

Like MtrC, OmcA is an outer-membrane decaheme with 10 bis-his ligated hemes. It is known that the OmcA can take the electrons from MtrC before donating them to the terminal electron acceptor. However, the mechanism for electron transfer between MtrC and OmcA is not fully defined. To further investigate this electron transfer, an OmcA reduction assay was carried out with the $MtrC_{DI,II}$. As OmcA is a heme protein, its spectral properties can be used to determine when the protein is reduced. These characteristic features were used as the basis for the design of the OmcA reduction assay. Like with the FMN reduction assay, *S. oneidensis* cells are made anaerobic and supplemented with lactate. This drives their internal metabolism and generates intracellular electrons that need an extracellular acceptor. Soluble OmcA can then be added, and the change in electronic absorbance at a given wavelength can be used to infer electron transfer rates. The alpha band (A_{552}) was used to determine the reduction of the OmcA over an hour. As the OmcA gets more reduced, the alpha band becomes sharper, and the A_{552} increases accordingly. Figure 4.26 shows the results from the OmcA reduction assay carried out on *S. oneidensis* MR-1, *Δmtr*, *ΔmtrC/omcA*, *ΔmtrC/omcA* producing MtrC WT, and *ΔmtrC/omcA* producing $MtrC_{DI,II}$.

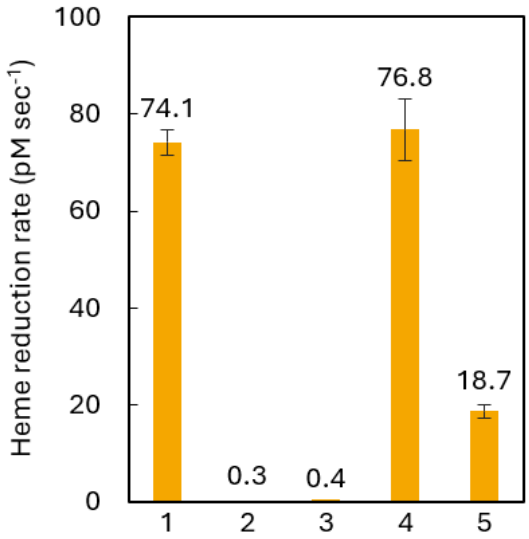

Figure 4.26. Processed data from the soluble OmcA reduction assay where reduction of OmcA was converted to heme reduction rate. Strains shown include: MR-1 (**1**); *Δmtr* (**2**); *ΔmtrC/omcA* (**3**); *ΔmtrC/omcA* producing MtrC WT (**4**); and *ΔmtrC/omcA* producing $MtrC_{DI,II}$ (**5**). The assay was carried out with cells at a starting OD_{600} of 0.1 induced with 1 mM L-arabinose. Experiments were done in triplicate and error bars show standard error of mean.

Similarly to FMN reduction, the capacity for electrons to be transported to OmcA appeared to be impaired when domains III and IV of MtrC were absent in the *ΔmtrC/omcA* producing $MtrC_{DI,II}$ (5, Figure 4.26). Furthermore, both the *Δmtr* and *ΔmtrC/omcA* strains were incapable of reducing soluble OmcA (2, 3, Figure 4.26). The *ΔmtrC/omcA* mutant producing MtrC (4, Figure 4.26), as expected, had a rate slightly higher than the WT (1, Figure 4.26). In the FMN reduction assay, having MtrA without MtrC allowed for some minor electron transfer to FMN, but that did not seem to be the case with OmcA.

MtrC and OmcA have been shown[120,206] to interact on the extracellular surface, both acting as terminal reductases that can transfer electrons to the terminal acceptor directly or indirectly (via electron shuttles like flavins). These interactions are thought to enhance the reductase activity synergistically[206]. Extracellular electron transfer rates though MtrCAB have been shown to be fast enough (in the nanosecond range) to conclude that the rate limiting step of electron transfer between intracellular metabolism and extracellular terminal electron acceptor is not transfer through the MtrCAB conduit, but perhaps the transfer between the terminal reductase (MtrC or OmcA) and the acceptor directly [195]. The results from

the OmcA reduction assay indicate that removing hemes 6 to 10 in MtrC decreased the rate of electron flow from MtrC to OmcA. Figure 4.26 shows almost a four-fold decrease in the reduction rate of the *ΔmtrC/omcA* cells producing $MtrC_{DI,II}$ when compared to the WT. These results suggest some binding between MtrC and OmcA might occur within domain III. However, these results still showed that electron transfer could occur, albeit at reduced rates, between $MtrC_{DI,II}$ and OmcA, but not between MtrA and OmcA.

4.2.12.4 Reduction of ferric citrate

The MtrCAB complex allows *S. oneidensis* to survive in anoxic environments, such as iron and manganese rich lakes. They can use Fe (III) and Mn (IV) as terminal electron acceptors in EET. Fe(III) can complex with oxygen to produce a variety of Fe (III) oxides but can also join with citrate to produce Fe(III) (ferric) citrate. Like FMN and OmcA, Ferric citrate is a physiologically relevant electron acceptor for *S. oneidensis*. The Fe(III) is reduced to Fe(II), and this enables the bacteria to continue respiring.

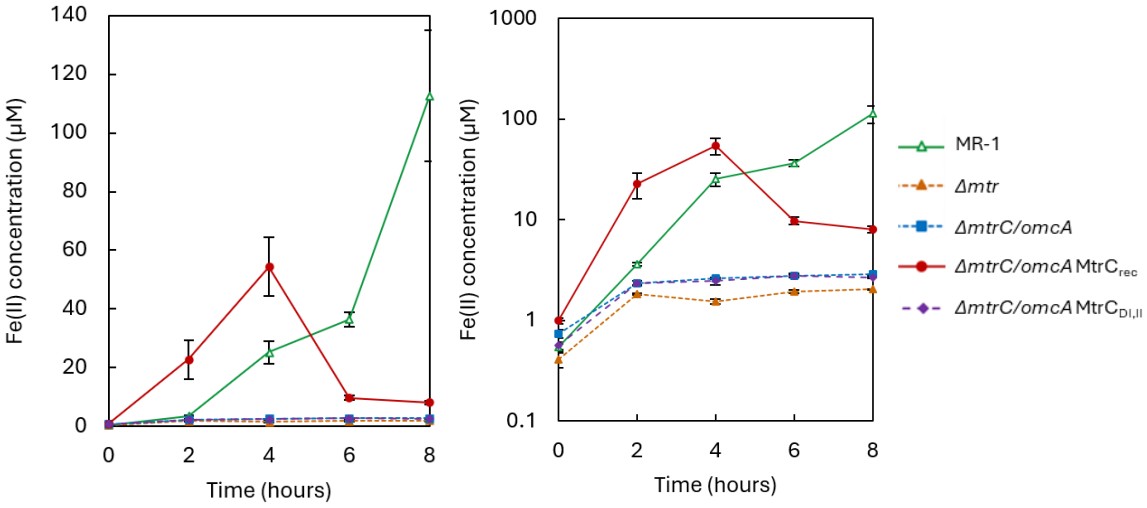

Figure 4.27. Concentration of Fe(II) over 8 hours in the ferric citrate experiment. Data is shown on a non-logarithmic (**left**) and logarithmic (**right**) Y-axis. The *S. oneidensis* strains shown are listed in the legend on the right.). The assay was carried out with cells at a starting OD_{600} of 0.1 induced with 1 mM L-arabinose. Experiments were done in triplicate and error bars show standard error of mean.

A way to monitor the reduction of Fe(III) to Fe(II), is by quantifying the concentration of Fe(II) in solution using ferrozine solution (Methods 2.6.2). As the starting concentration of Fe(III) is known, the concentration of Fe(II) can be calculated. The same five strains from FMN and OmcA reduction assays were used in these experiments (Methods 2.6.5). Figure 4.27 shows a time course of the Fe(II) concentration over 8 hours. The increase in Fe(II) concentration over time can be converted into a rate of Fe(III) reduction (Figure 4.28).

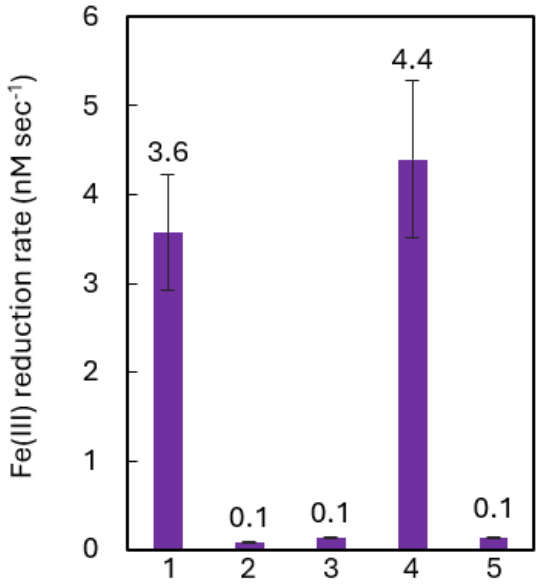

Figure 4.28. Processed data from the ferric citrate reduction assay. Strains shown include: MR-1 (**1**); *Δmtr* (**2**); *ΔmtrC/omcA* (**3**); *ΔmtrC/omcA* producing MtrC WT (**4**); and *ΔmtrC/omcA* producing $MtrC_{DI,II}$ (**5**). The assay was carried out with cells at a starting OD_{600} of 0.1 induced with 1 mM L-arabinose. Experiments were done in triplicate and error bars show standard error of mean.

Similarly to the previous assays, MR-1 and the *ΔmtrC/omcA* producing MtrC had the two highest Fe(III) reduction rates (1, 4, Figure 4.28, respectively). In accordance with previous work[113], the rate of ferric citrate reduction in the *ΔmtrC/omcA* cells (3, Figure 4.28) was much lower than that of MR-1 or the *ΔmtrC/omcA* cells producing MtrC. It seems that the presence of MtrAB is not enough to enable reduction of the ferric citrate, as the *Δmtr* cells (2, Figure 4.28) were also incapable. The *ΔmtrC/omcA* cells producing $MtrC_{DI,II}$ had virtually the same rate of reduction as the both the knockout strains. These rates can differ due to a variety of factors, including the structure of the Fe(III) citrate, the difference in reduction potential between the

electron donator/acceptor, interaction between the ferric citrate and MtrC, and any differences in charge between the MtrC and the ferric citrate[139]. Furthermore, depending on the ratio of Fe(III) to citrate, higher order complexes can form such as Fe(III) citrate trimers, which may also impact the rate of reduction. As seen above (Table 4.3 in 4.2.7 Protein film electrochemistry), MtrC WT and $MtrC_{DI,II}$ were calculated to have midpoint reduction potentials of ~ 200 mV vs SHE. Fe(III) citrate has been calculated to have a midpoint reduction potential of ~ 0 mV vs SHE[207]. Consequently, this would indicate that the lack of electron transfer from $MtrC_{DI,II}$ to ferric citrate was not due to differences in reduction potentials. It is more likely that, similarly to FMN binding, there is a physical docking site within domains III and IV.

Furthermore, the solvent-exposed heme propionates of MtrC (and MtrF, an MtrC homolog) give most of the surface of the protein a negative charge[88,139]. However, it has been suggested that UndA (an undecaheme that substitutes OmcA in several *Shewanella* species) has a positively charged surface near heme 7, as the lysine and arginine residues neutralise the negatively charged propionates in the heme 7 environment[139,208]. This positive charge is proposed to facilitate the association between ferric citrate and UndA. MtrC, however, does not have a positively charged heme 7 environment. This would again suggest the presence, or absence, of a physical ferric citrate docking site in MtrC, or $MtrC_{DI,II}$, respectively.

4.2.12.5 Reduction of ferric EDTA

Like ferric citrate, ferric EDTA is another iron complex that *S. oneidensis* can use as a terminal electron acceptor. The experimental design was identical to that of the ferric citrate reduction assay (Methods 2.6.6). Ferrozine solution was again used to quantify the amount of Fe(II) in solution. The same five strains used in the FMN, OmcA, and ferric citrate reduction assays were used (Figure 4.29, left). Additionally, two new strains were assayed in this experiment, a *Δmtr* strain containing the $pMTRC_{rec}$ plasmid and a *Δmtr* strain containing the $pMTRC_{DI,II}$ plasmid (Figure 4.29, right). The purpose of adding these two new strains was to investigate if (over)expressing membrane $MtrC_{DI,II}$ (or MtrC WT) would permeabilise the membrane and allow electrons to bypass the $MtrC_{DI,II}$ AB/MtrCAB conduit and be taken by the electron acceptor directly. As both strains acted as controls to test the permeability of the outer membrane, adding them to every other reduction assay

was not required. The changes in Fe(II) concentration over time were converted to Fe(III) reduction rates which are shown in Figure 4.30.

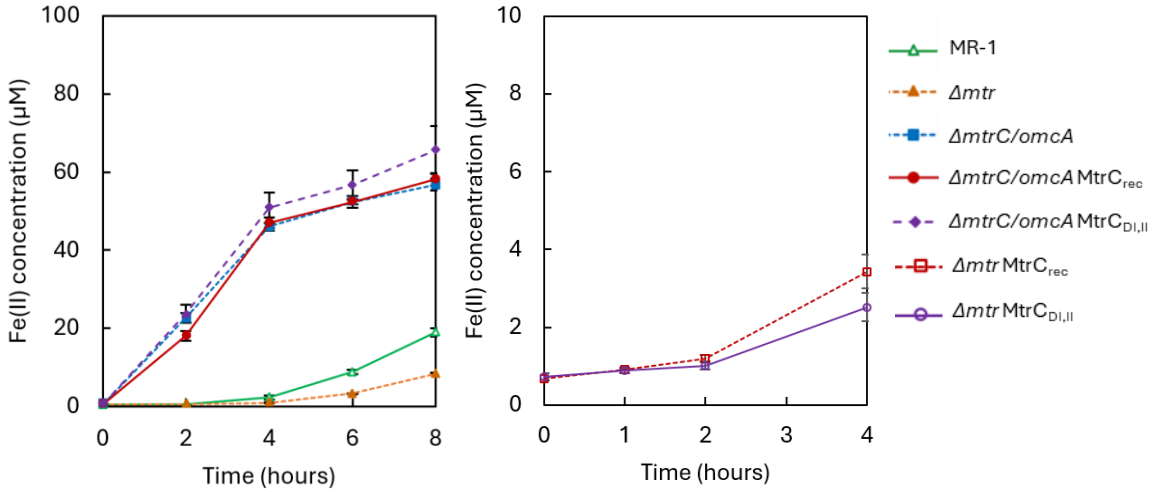

Figure 4.29. Increase in concentration of Fe(II) over 8 hours in the ferric EDTA reduction assay. **Left.** Strains used: *S. oneidensis* MR-1, Δ*mtr*, Δ*mtrC/omcA*, Δ*mtrC/omcA* cells with the pMTRC$_{rec}$ plasmid, and Δ*mtrC/omcA* cells with the pMTRC$_{DI,II}$ plasmid. **Right**. Strains used: *S. oneidensis* Δ*mtr* cells with the pMTRC$_{rec}$ plasmid, and Δ*mtr* cells with the pMTRC$_{DI,II}$ plasmid. The assay was carried out with cells at a starting OD$_{600}$ of 0.1 induced with 1 mM L-arabinose. Experiments were done in triplicate and error bars show standard error of mean. Note: the Y-axis range is different between the two graphs.

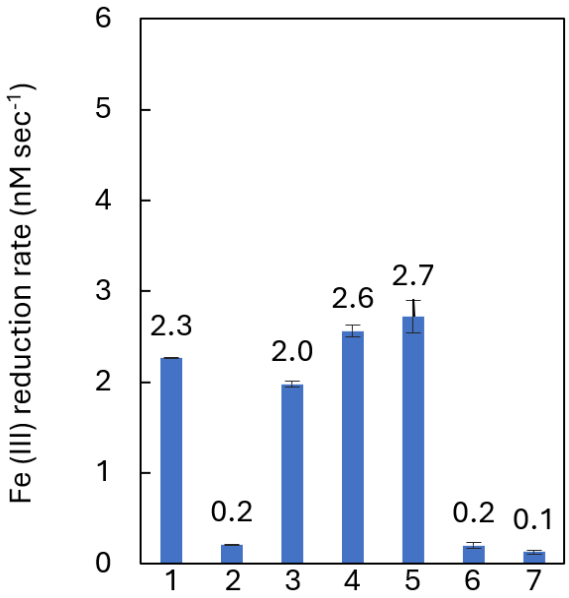

Figure 4.30. Processed data from the ferric EDTA reduction assay. Strains shown include: MR-1 (**1**); *Δmtr* (**2**); *ΔmtrC/omcA* (**3**); *ΔmtrC/omcA* producing MtrC WT (**4**); *ΔmtrC/omcA* producing MtrC$_{DI,II}$ (**5**); *Δmtr* producing MtrC WT (**6**); and *Δmtr* producing MtrC$_{DI,II}$ (**7**). The assay was carried out with cells at a starting OD$_{600}$ of 0.1 induced with 1 mM L-arabinose. Experiments were done in triplicate and error bars show standard error of mean.

Previous work[209] has shown that ferric citrate reduction was significantly slower than ferric EDTA reduction. However, this work looked at purified proteins interacting with the ferric complexes directly, showing *in vitro* rates. The *in vivo* rates in Figure 4.30 showed the opposite pattern, with ferric citrate having a slightly higher rate than ferric EDTA. Furthermore, the difference in rate between the *S. oneidensis* MR-1 cells (1, Figure 4.30), and the three *ΔmtrC/omcA* strains (3, 4, 5, Figure 4.30) was minor, regardless of the presence or absence of an MtrC variant. The results suggest that having MtrA is the only requirement for electron transfer onto ferric EDTA. Moreover, the three *Δmtr* strains (2, 6, 7, Figure 4.30) had also very similar rates. These, however, were significantly lower than the strains that expressed MtrA. This would suggest that the electrons can be transferred from MtrA directly onto the ferric EDTA complex. Furthermore, the data show there are virtually no differences between the rate of electron flow through MtrC WT when compared to $MtrC_{DI,II}$, which indicated that ferric EDTA (unlike ferric citrate) would not appear to need a specific binding pocket to interact with the cytochromes.

The reduction potential of ferric EDTA at pH 7 has been shown to be ~ 100 mV vs SHE[210] as opposed to the ~ 0 mV vs SHE[207] of ferric citrate. Consequently, the ferric EDTA could function as a stronger oxidising agent, suggesting that electrons would be transferred more readily from the reduced MtrA to the ferric EDTA, even in the absence of an MtrC variant. The last 3 to 4 hemes of MtrA protrude ~ 15-20 Å[88] into the extracellular environment from the outer membrane. This would further facilitate any interaction between MtrA and the ferric complexes directly. These factors combined are perhaps what allowed the electrons to be transferred from MtrA directly to ferric EDTA.

4.2.12.6 Reduction of azo dyes

To further investigate electron transfer through $MtrC_{DI,II}$ to an electron acceptor, non-physiological azo dyes were selected for reduction assays. Even though these dyes are not the usual terminal electron acceptors for *Shewanella* species, their biophysical properties are very useful in reduction assays. This is because upon reduction of the azo bond, the reaction products are colourless amines; this is known as decolourisation[211]. *S. oneidensis* WL-7 has been shown to be able to decolourise azo dyes such as Reactive Black 5 (RB5), Methyl Red, and Reactive Blue 19, amongst others. Furthermore, *S. oneidensis* MR-1 has been shown to be able to

reduce Amaranth[212] and Methyl Orange (MO)[213,214]. Once it was concluded that RB5, Amaranth, and MO were all suitable azo dyes to investigate electron transfer through $MtrC_{DI,II}$ AB, whole-cell reduction assays were carried out (Methods 2.6.7). The absorbances of each azo dye at their corresponding wavelength over 12 hours is shown in Figure 4.31. The preliminary results showed that the *ΔmtrC/omcA* strain producing $MtrC_{DI,II}$ had a different capacity to reduce each of the three assayed azo dyes.

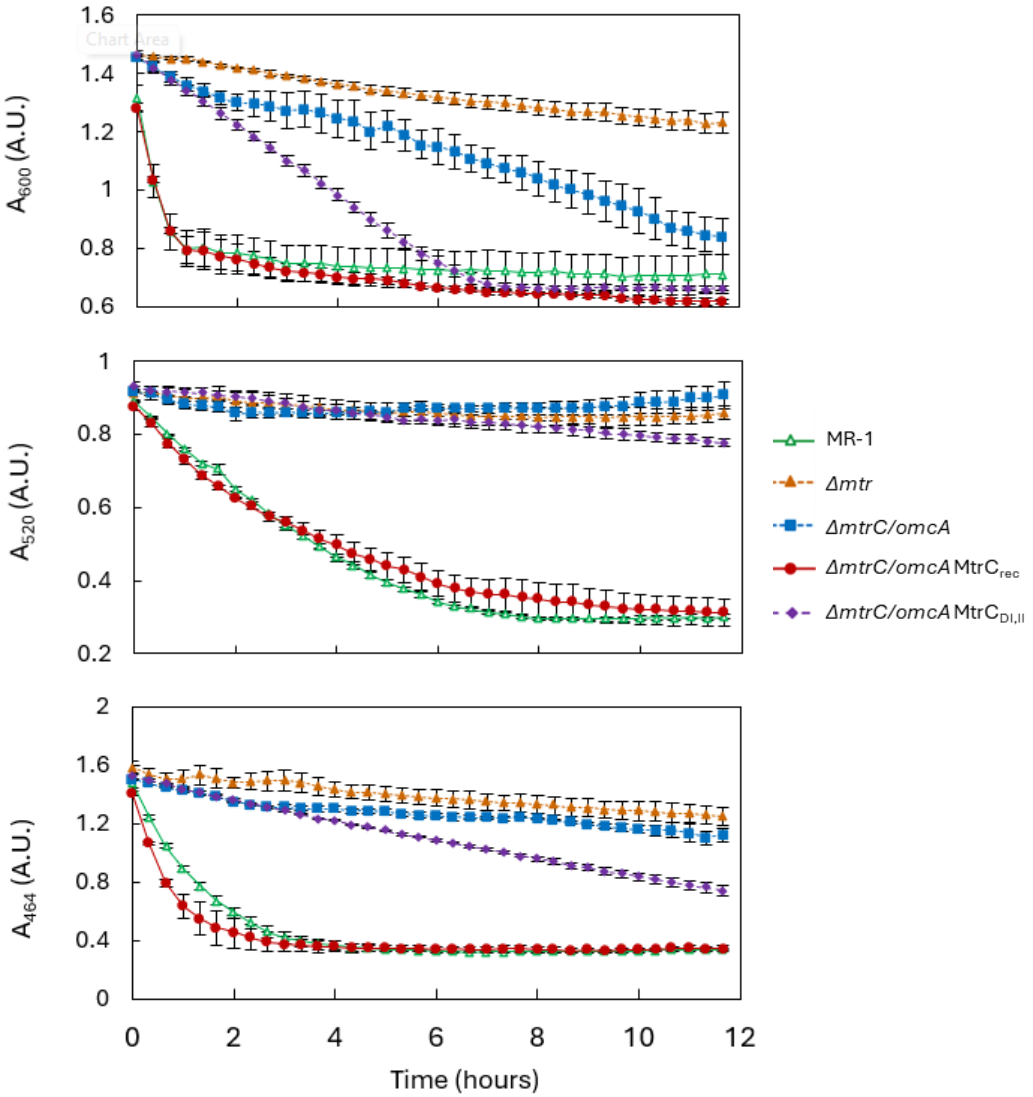

Figure 4.31. Absorbance of each azo dye at the corresponding wavelength over 12 hours during the azo dye reduction experiment. The assayed dyes are Reactive Black 5 (**top**), Amaranth (**centre**), and Methyl Orange (**bottom**). The *S. oneidensis* strains shown are listed in the legend on the right. The assay was carried out with cells at a starting OD_{600} of 0.1 induced with 1 mM L-arabinose. Experiments were done in triplicate and error bars show standard error of mean. No statistical tests were carried out on the data. Note: the Y-axis range is different across the graphs.

To better understand these differences, the changes in absorbance were converted to total concentration of reduced dye (Figure 4.32)

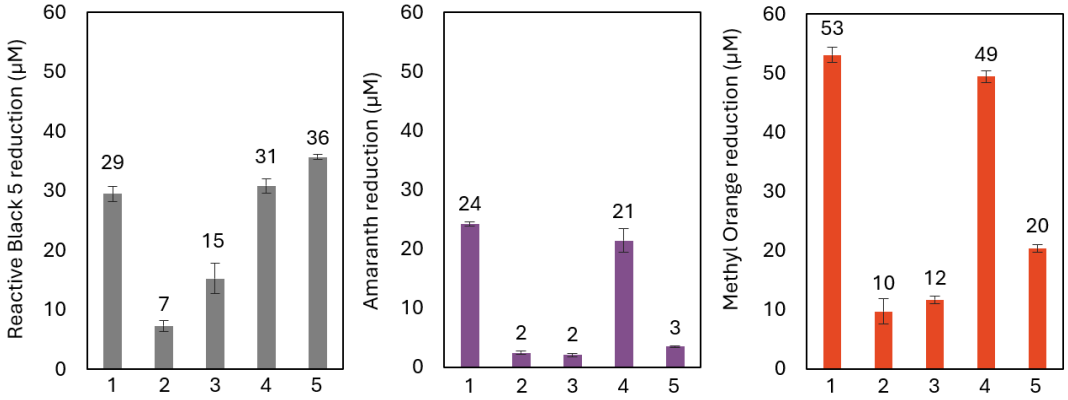

Figure 4.32. Processed data from the azo dyes reduction experiment. The assayed dyes are Reactive Black 5 (**left**), Amaranth (**centre**), and Methyl Orange (**right**). Strains shown include: MR-1 (**1**); *Δmtr* (**2**); *ΔmtrC/omcA* (**3**); *ΔmtrC/omcA* producing MtrC WT (**4**); and *ΔmtrC/omcA* producing $MtrC_{DI,II}$ (**5**). The assay was carried out with cells at a starting OD_{600} of 0.1 induced with 1 mM L-arabinose. Experiments were done in triplicate and error bars show standard error of mean. No statistical tests were carried out on the data. Data shows the total reduction of dye concentration after 6 hours.

The data shown in Figure 4.32 show the differences in the total reduction of RB5, Amaranth, and MO across the 5 assayed strains. In accordance with previous work[211–214], *S. oneidensis* MR-1 could reduce all three azo dyes. As expected, the *Δmtr* cells decolourised the lowest amount of each dye, with *ΔmtrC/omcA* being the same (Amaranth, MO) or slightly higher (RB5). The *ΔmtrC/omcA* cells that expressed MtrC WT had comparable rates to MR-1 across all three dyes. Intriguingly, the total dye reduced by the *ΔmtrC/omcA* cells producing $MtrC_{DI,II}$ varied depending on the dye. RB5 had a rate which was close to MR-1(Figure 4.32, left), which suggested that the full ten hemes were not necessary to decolourise RB5. Perhaps the 5 hemes within domains I and II were enough to bring electrons close enough for reduction of the RB5. However, having MtrA alone was not enough for this electron transfer to occur at the same rate. For Amaranth, there was virtually no difference between the *Δmtr*, *ΔmtrC/omcA*, and *ΔmtrC/omcA* cells producing $MtrC_{DI,II}$ (Figure 4.32, centre), which suggested the necessity for having the ten hemes in MtrC present. Perhaps there is a physical binding site (similarly to FMN and OmcA) that is required for Amaranth reduction and that is missing when domains III and IV are removed. Finally, the capacity of the *ΔmtrC/omcA* cells producing $MtrC_{DI,II}$ to reduce MO falls somewhere between MR-1 and the *Δmtr* and *ΔmtrC/omcA* cells. As these azo dyes

are not present in the usual *S. oneidensis* environments they are not physiological electron acceptors. This makes it difficult to ascertain whether reduction occurred due to the proximity of the azo dye to the terminal heme in the EET (heme 10 for MtrC WT or heme 1 or 2 for $MtrC_{DI,II}$) or due to a specific binding site present/absent in MtrC WT/$MtrC_{DI,II}$, respectively.

4.3 Conclusion and future work

It is well known that the outer-membrane multiheme cytochromes of *S. oneidensis*, have an unusual staggered-cross heme arrangement. In MtrCAB, this allows electrons to be transferred from heme 10 in MtrA to heme 5 in MtrC. The electrons travel through MtrC and can be transferred laterally to OmcA or continue through the heme chain and be donated to the electron acceptor from heme 10. However, it is not entirely understood why MtrC has this heme arrangement or if all 10 hemes are needed for EET. In this chapter, both a soluble and membrane-bound isoform were successfully expressed and characterised from a plasmid-based system. There can sometimes be issues with overexpressing *c*-type cytochromes variants, as their heme incorporation and maturation pathways are not yet fully understood.

The soluble $MtrC_{DI,II}$ (domains I and II) which lacked domains III and IV was successfully expressed inside *S. oneidensis* cells. The size was confirmed by LC-MS to be within what was expected meaning the hemes were incorporated properly into the protein backbone. UV-Vis spectroscopy revealed that the soluble pentaheme behaved as a redox-active heme protein would behave, with the characteristic Soret band shift and tightening of the alpha and beta band upon reduction. After this initial characterisation, the purified protein was successfully crystallised, and the structure was resolved to 1.8 Å (PDB: (9EOV). Cyclic voltammetry suggested little to no differences in the active redox potential window or the midpoint reduction potential when compared to soluble MtrC WT. After confirming the correct expression of the soluble $MtrC_{DI,II}$, its capacity to form a complex with native MtrAB was assessed. SDS-PAGE confirmed the presence of a band around the size of MtrA (~ 35 kDa) which was only present when the plasmid containing the mutated gene was induced. A single peak on the SEC column suggested that only one species was present in the purification products. Furthermore, differences in the sedimentation and frictional coefficients of $MtrC_{DI,II}$AB when compared to MtrAB and MtrCAB, increased the confidence that the $MtrC_{DI,II}$ was in fact forming a trimer. Also, a variety of reduction assays with both physiological and non-physiological electron acceptors were carried out to further investigate the functional effects that removing domains III and IV would have on the capacity of MtrC to transfer electrons.

The results from these whole-cell activity assays would suggest that there is a need for a physical binding site located within domains III and IV for correct reduction of FMN and OmcA. As FMN and OmcA are both molecules that are usually present in the vicinity of MtrC, this would make sense. Without the disulfide found near heme 7, it would seem that it was impossible for MtrC to form a flavocytochrome complex with FMN. Similarly, the electron transfer rates to OmcA were suggested to be drastically reduced when only hemes 1 to 5 were present in MtrC. Reduction of ferric citrate was not possible with $MtrC_{DI,II}$, suggesting again that a physical binding site was removed when domains III and IV were eliminated. For ferric EDTA, it seems that MtrA was capable of donating the electrons directly, meaning the lack of domains III and IV played no role in the electron transfer rates. Finally, the differences in reduction of three different azo dyes highlighted the varying magnitude of the impact of not having hemes 6 to 10 in MtrC.

It would seem that, depending on the electron acceptor, a pentaheme minimal system for EET is possible as seen in $MtrC_{DI,II}$. Perhaps evolutionarily, there was an original set of 5 hemes that enabled *Shewanella* to respire in environments where it could not before. A gene duplication event might have led this synthesised pentaheme protein to form into a decaheme, further allowing the bacteria to thrive in previously uninhabitable environments. As the electrons can get all the way to the end of $MtrC_{DI,II}$, then another protein could be fused to the C-terminus of the $MtrC_{DI,II}$. This allow for a system where lactate-driven intracellular metabolism produces electrons that can be transferred to the extracellular environment of *S. oneidensis* cells. This could then be coupled to a tailored protein of choice that could interact with a variety of electron acceptors that *S. oneidensis* would not usually be able to use to complete its EET.

Chapter 5

His/Met ligation in MtrA

5. MtrA axial ligand coordination

5.1 Introduction

The previous chapters have investigated EET in *S. oneidensis* by changing the interactions between the MtrC domains. In this chapter, the heme coordination of MtrA is investigated. As previously discussed, MtrCAB is comprised of an extracellular decaheme cytochrome, MtrC, which receives electrons from MtrA, another decaheme cytochrome, which lies within MtrB, a β-barrel porin located in the outer-membrane[88]. In MtrC and MtrA, the closely-packed hemes enable Fe(III)⇔Fe(II) transitions of the neighbouring sites, transporting periplasmic electrons to the extracellular terminal acceptor[79]. The ten hemes of MtrA all have bis-his axial ligand heme coordination, and they are positioned so that neighbouring pairs alternate between perpendicular and parallel porphyrin ring planes. The edge-to-edge distances of these porphyrins range from 3.9 to 6.5 Å[88]. The arrangement of smaller cytochromes from *Shewanella* such as STC, is very similar to that of MtrA. The STC heme chain can be superposed over hemes 6-9 and 2-5 of MtrA, with root-mean-square deviations (RMSD) of 1.64 and 1.52 Å, respectively. The conservation of the arrangement of the hemes in these structures suggest there is a possibility for MtrA and STC of sharing a common ancestor, and that MtrA might have been the result of a gene duplication event[88].

Homologs of both *mtrA* and *mtrB* can also be found in other bacteria, such as the iron-oxidiser *Rhodopseudomonas palustris* TIE-1, where they are named *pioA* and *pioB*, respectively. The *pioA* gene product is predicted to transfer electrons from an extracellular donor, across the outer membrane, and into the periplasm of *R. palustris* TIE-1[79]. Similarly to MtrA, PioA contains ten hemes that enable electron transfer. However, the iron transitions are Fe(II)⇔Fe(III) instead of Fe(III)⇔Fe(II) as the electron transfer direction is opposite to MtrA. Furthermore, in PioA, 3 out of the 10 hemes have His/Met coordination instead of bis-his. Previous work[79] has stated that hemes displaying His/Met ligation contribute to redox activities at a potential more positive than bis-his ligated hemes[79].

We hypothesise that the three His/Met hemes in PioA (with more positive potentials) act as electron sinks, storing electrons from the oxidation of Fe(II) before transferring them to the periplasmic acceptors. We also hypothesise that these His/Met hemes enable PioA to transfer electrons intracellularly, even when the

intracellular potential is more negative than the extracellular one. To test this, we produced an *mtrA* mutant with three distal histidines mutated to methionines, at MtrA amino acid positions 85, 167, and 200, which correspond to hemes 3, 2, and 7, respectively. These were selected as these are the hemes in PioA that have His/Met ligation. Biophysical characterisation was carried out on the purified protein and activity assays were done on cells expressing the mutant *mtrA* gene product designed to contain three His/Met hemes.

5.2 Results and discussion

5.2.1 Plasmid design and generation

A pBAD plasmid containing *mtrA* was obtained from the laboratory repository at the University of East Anglia, Norwich (Table 2.3 in Methods 2.2.11). Before any DNA modifications were carried out, a Strep(II) tag was added using PCR mutagenesis to the C-terminus of *mtrA* on the pBAD plasmid, for downstream purification. The PCR primers are listed in Table 2.2 in Methods 2.2.3, and the PCR conditions are detailed in Methods 2.2.3. The PCR products were visualised on a 0.8% agarose gel (Methods 2.1.3) to confirm the success of the PCR (Figure 5.1).

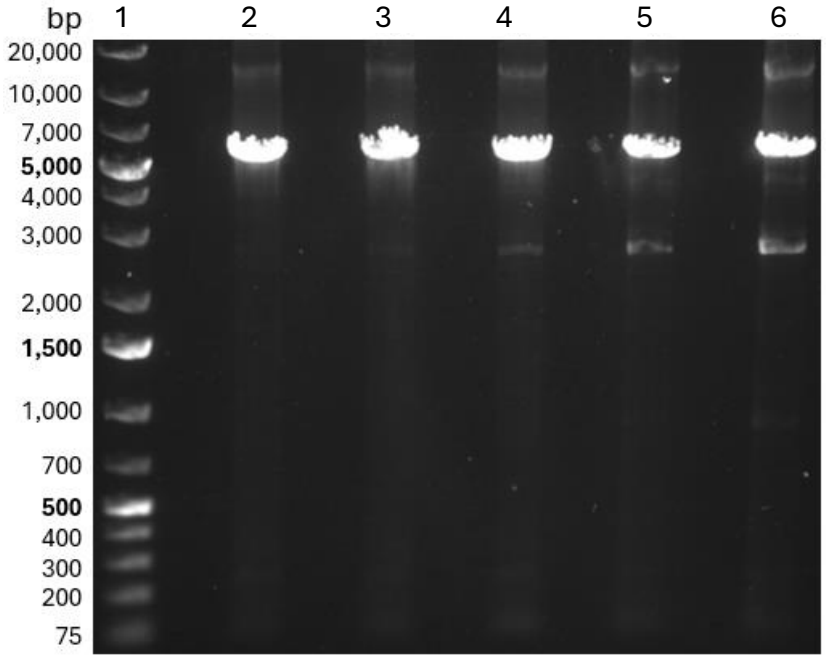

Figure 5.1. 0.8% agarose gel of the PCR products after the *mtrA* Strep(II) tag PCR. An annealing temperature gradient was done to optimise the success rate. The lanes are as follow: molecular marker (lane 1), annealing at: 64°C (lane 2), 62.5°C (lane 3), 61°C (lane 4), 57.9°C (lane 5), and 56°C (lane 6). The bright bands around 6,000 bp are the successful PCR products.

After confirming that the template DNA had been amplified during the PCR (Figure 5.1), the bands were excised from the gel (Methods 2.2.6). After, they were subjected to a phosphorylation and ligation step (Methods 2.2.7), to re-ligate any nicks in the DNA after the Strep(II) tag PCR. Next, the pDNA that had been phosphorylated and ligated was transformed into competent *E. coli* TOP cells via heat shock (Methods 2.2.7 and 2.2.8). The pDNA was extracted and sequenced, to confirm that the *mtrA* sequence had no mutations and had the Strep(II) tag added to the C-terminus. This

plasmid containing *mtrA* with a Strep(II) tag (pMTRA$_{rec}$) was used for all downstream PCR mutagenesis.

Three mutations were introduced to change the distal histidine codon (CAC) to the methionine codon (ATG) of three hemes: heme 3 (H85M), heme 2 (H167M), and heme 7 (H200M). These were all done sequentially via individual PCR mutagenesis as with the Strep(II) tag, but because the PCR primers were designed to bridge any nicks during the PCR itself, there was no need for band extraction from the gel nor phosphorylation and ligation. Instead, a DpnI digest was carried out (Methods 2.2.4) on the PCR products after the His/Met mutagenesis.

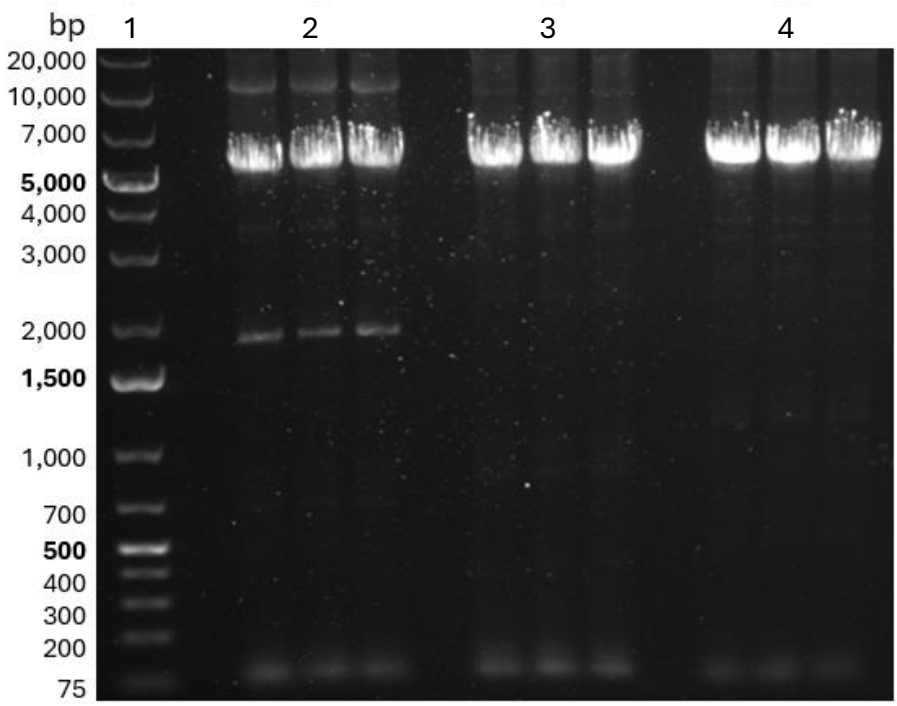

Figure 5.2. 0.8% agarose gel of the PCR products after the third round of His/Met mutations was done on three different *mtrA* double mutants. The lanes are as follow: molecular marker (lane 1); *mtrA* H85M, H167M after the H200M PCR (lane 2); *mtrA* H85M, H200M after the H167M PCR (lane 3); and *mtrA* H167M, H200M after the H85M PCR (lane 4). Each PCR product lane is composed of three samples (left, centre, and right) carried out with annealing temperatures of 52°C, 50°C, and 48°C, respectively. The bright bands around 6,000 bp are the successful PCR products.

After, the DpnI enzyme and corresponding reaction buffers were removed via a PCR clean-up kit. Next, the plasmid was transformed into competent *E. coli* TOP cells via heat shock (Methods 2.2.7 and 2.2.8). After producing the three single His/Met codon mutants, the same set of primers and protocols were used to create three double mutants (one with H85M and H167M, one with H85M and H200M, and one with H167M and H200M). These were sequenced to confirm correct mutagenesis. From these double mutants, three triple mutants were produced that had all three H85M, H167M, and H200M codon mutations, regardless of which order they were done in. Figure 5.2 shows three triple mutants produced from three different double mutants. In theory, the three triple mutants should have been identical, but there were slightly different bands on the agarose gel done after the PCR (Figure 5.2). To confirm that the three His/Met mutations had been introduced at the correct locations and without any unwanted mutations at other sites, the pDNA was extracted and sent for sequencing.

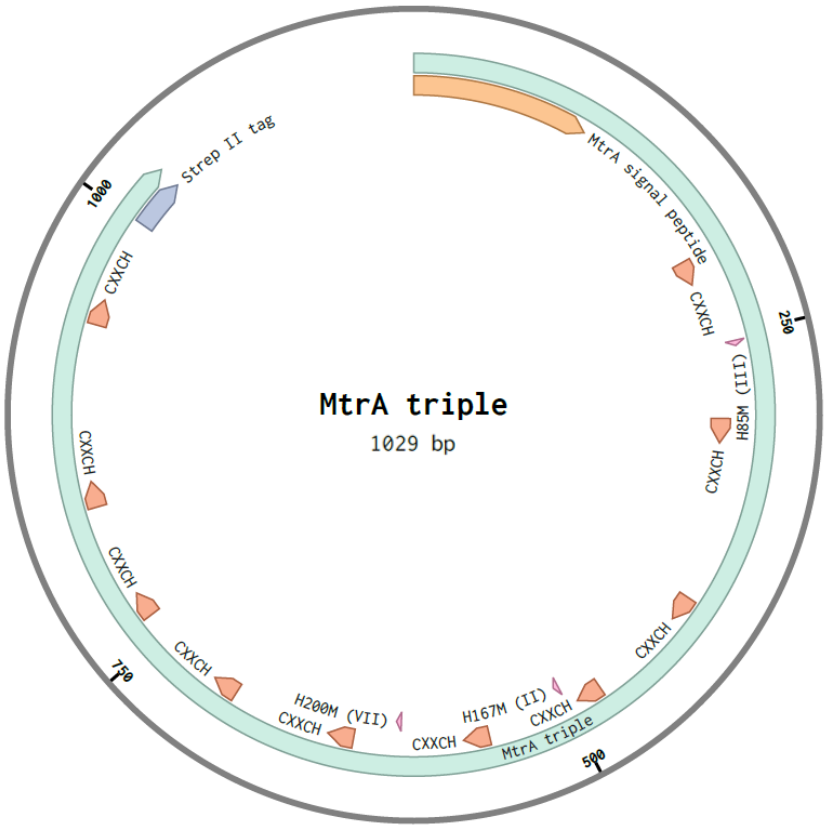

Figure 5.3. Sequencing data from pMTRA$_{triple}$ obtained from Eurofins and visualised on Benchling. The MtrA signal peptide (orange arrow), CXXCH heme binding motifs (red arrows), and Strep(II) tag (navy arrow) are shown. The locations for the three His/Met mutations are shown with a pink arrow, with the corresponding heme indicated in roman numerals. Note: even though the sequencing data is linear, it has been shown as circular to better visualise the components.

Figure 5.3 shows the sequenced pMTRA$_{triple}$ (triple mutant) with the added Strep(II) tag and the three His/Met mutations. All the plasmids from this chapter are listed in Table 5.1.

Table 5.1. Plasmids used in this chapter with indicated relevant features. Text in bold forms part of each plasmid name.

Plasmid	Features
pMTRA$_{rec}$	*mtrA* signal peptide; C-terminus Strep(II) tag; no modifications to *mtrA* (**rec**ombinant)
pMTRA$_{H85M}$	*mtrA* signal peptide; C-terminus Strep(II) tag; **h**istidine codon at amino acid position **85** in *mtrA* changed to **m**ethionine codon (**H85M**)
pMTRA$_{H167M}$	*mtrA* signal peptide; C-terminus Strep(II) tag; **h**istidine codon at amino acid position **167** in *mtrA* changed to **m**ethionine codon (**H167M**)
pMTRA$_{H200M}$	*mtrA* signal peptide; C-terminus Strep(II) tag; **h**istidine codon at amino acid position **200** in *mtrA* changed to **m**ethionine codon (**H200M**)
pMTRA$_{triple}$	*mtrA* signal peptide; C-terminus Strep(II) tag; histidine codon at amino acid positions 85 167, and 200 in *mtrA* changed to methionine codon (**triple** mutant)

After confirming the correct incorporation of the His/Met mutations in the three individual mutants as well as the triple mutant, the plasmids were each transformed into a *S. oneidensis* Δ*mtr* strain via electroporation (Methods 2.2.9). As these proteins were intended for purification, the whole MtrCAB complex was not necessary. To check the pDNA were all correct, the plasmids were sent for sequencing again. After confirming this protein expression trials were started on the *S. oneidensis* cells with the pMTRA$_{rec}$, pMTRA$_{H85M}$, pMTRA$_{H167M}$, pMTRA$_{H200M}$, and pMTRA$_{triple}$ plasmids.

5.2.2 MtrA expression trials

To confirm the correct production of MtrA variants (WT, three single mutants, and the triple mutant) in the *S. oneidensis* Δ*mtr* cells, an expression trial was carried out (Methods 2.3.1). Gene expression was induced with 2.5 mM and 5 mM L-arabinose. 6 hours after induction of expression, the cells were harvested by centrifugation and heat-lysed (95°C, 10 minutes). The lysed whole-cell samples and controls were run on an SDS-PGAE gel (Methods 2.3.3.) and stained for heme and Coomassie (Methods 2.3.5, and 2.3.4, respectively).

The heme stained SDS-PAGE gel shows a faint band in the induced cells (Figure 5.4, left, lanes 2 and 5) just below 35 kDa which corresponds to MtrA WT (~ 39 kDa). This is more apparent in the gel stained with Coomassie (Figure 5.4, right, lanes 2 and 5).

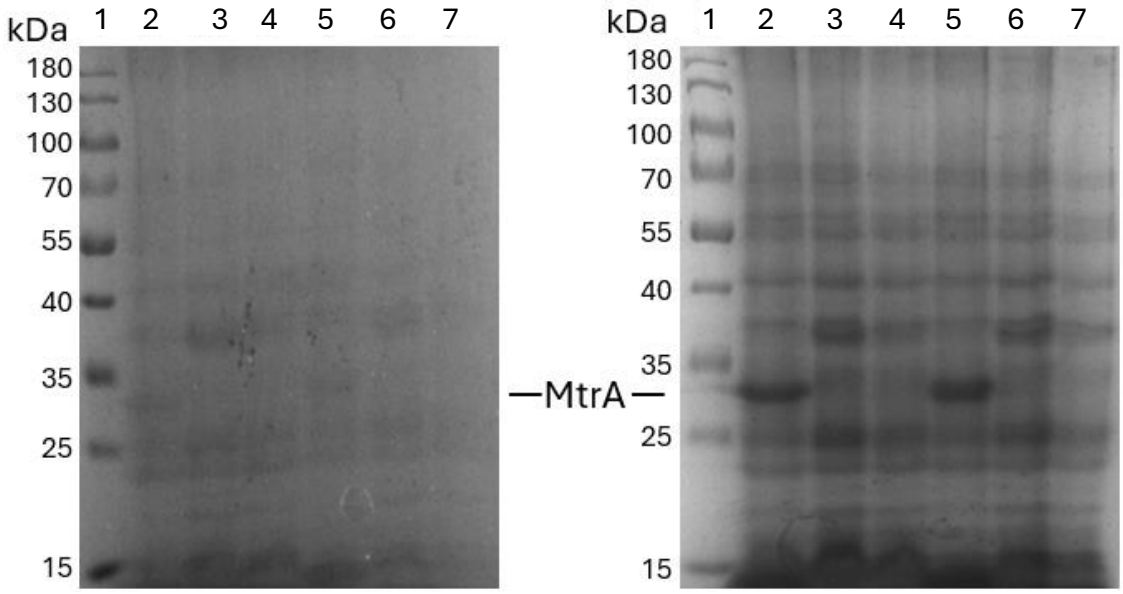

Figure 5.4. SDS-PAGE gel from expression trial of *S. oneidensis* Δ*mtr* cells with the pMTRA$_{rec}$ plasmid, stained with heme (**left**) and Coomassie (**right**). Lanes are as follows: molecular marker (lane 1); *S. oneidensis* Δ*mtr* cells with pMTRA$_{rec}$ plasmid (lanes 2, 5); *S. oneidensis* Δ*mtr* (lanes 3, 6); *S. oneidensis* MR-1 (lanes 4, 7). Plasmids were induced with 5 mM L-arabinose. MtrA is indicated with lines.

The gel stained with Coomassie also shows the presence of many other proteins in the samples, but the lanes containing the induced plasmid show a band (MtrA) that is darker than the rest. As the MtrA in *S. oneidensis* forms a complex with MtrB, there is no strong band on the SDS-PAGE gels, as the membrane fraction (containing MtrAB) was removed before preparing the samples.

A gel was run (Figure 5.5) showing a variety *S. oneidensis* cells, including MR-1 (the WT), Δ*mtr*, Δ*mtrA*, and Δ*mtr* with plasmids expressing the five MtrA variants (WT, three individual mutants, and the triple mutant). The proteins were normalised before loading onto the gel. The gel shows how the MtrA band shows in MR-1 (lane II), as expected, but also faintly in Δ*mtr* (lane 3) and Δ*mtrA* (lane 4). This could be due to MtrD, a *S. oneidensis* MtrA homologue.

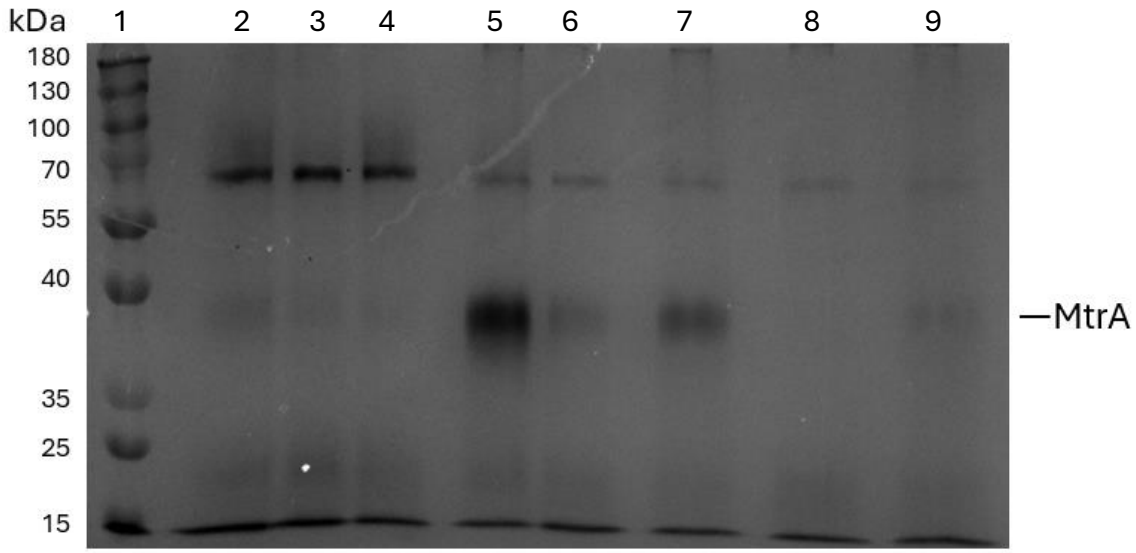

Figure 5.5. Normalised heme-stained SDS-PAGE gel comparing MtrA expression across different *S. oneidensis* cells. Lanes are as follows: molecular marker (lane 1); *S. oneidensis* MR-1 (lane 2); *S. oneidensis* Δ*mtr* (lane 3); *S. oneidensis* Δ*mtrA* (lane 4); *S. oneidensis* Δ*mtr* cells with $pMTRA_{rec}$ plasmid (lane 5); *S. oneidensis* Δ*mtr* cells with $pMTRA_{H85M}$ plasmid (lane 6); *S. oneidensis* Δ*mtr* cells with $pMTRA_{H167M}$ plasmid (lane 7); *S. oneidensis* Δ*mtr* cells with $pMTRA_{H200M}$ plasmid (lane 8); and *S. oneidensis* Δ*mtr* cells with $pMTRA_{triple}$ mutant plasmid (lane 9). Plasmids were induced with 5 mM L-arabinose. MtrA is indicated with lines.

The MtrA band is the strongest in the Δ*mtr* cells producing MtrA WT (lane 5). The three single mutants show different levels of relative expression between the Δ*mtr* cells producing MtrA H85M (lane 6), H167M (lane 7), and H200M (lane 8). The band for the MtrA H200M sample was extremely faint. The MtrA triple mutant (lane 9) displayed a band intensity that was higher than MR-1 but not as high as the Δ*mtr* cells producing MtrA WT. As this was a variant with three amino acid modifications, it was expected that the expression would be the lowest as it was the protein that had the most different amino acid sequence from MtrA WT.

5.2.3 Purification of MtrA variants

After determining the correct production of all five MtrA variants, large scale purifications of each protein were carried out. To purify the MtrA variants, cells were cultured, and the proteins were extracted as detailed before (Methods 2.4.1 and Methods 2.4.3). Purification was done using the Strep(II) tag that had been added to the template pMTRA$_{rec}$ before any of the His/Met mutations had been introduced. The ÄKTA trace of the Strep(II) tag purification for the MtrA WT and the three single MtrA mutants can be seen in Figure 5.6. The MtrA WT had the highest absorbance at 410 nm when compared to the three single His/Met mutants. This highlights the fact that producing a soluble MtrA variant protein is more difficult for the *S. oneidensis* cells when compared to MtrA with no modifications.

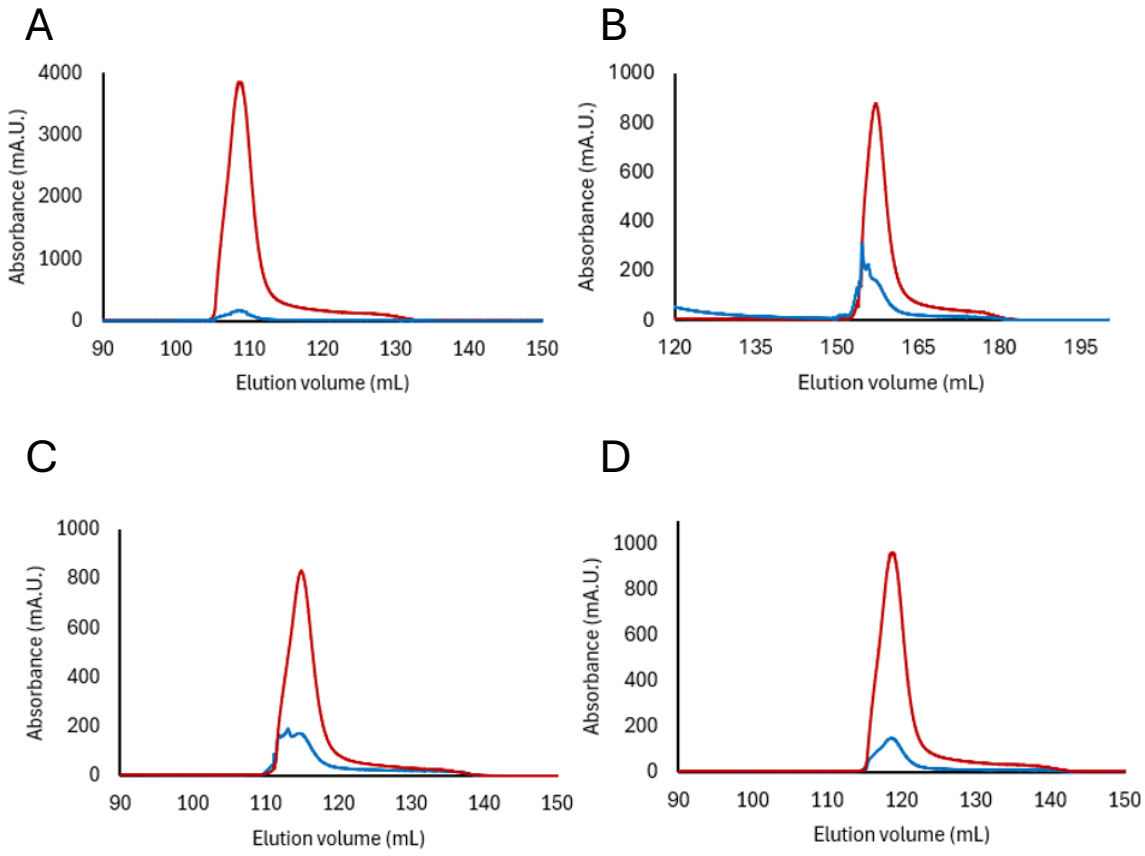

Figure 5.6. ÄKTA traces from Strep(II) column purification of MtrA WT (**A**), MtrA H85M (**B**), MtrA H167M (**C**), and MtrA H200M (**D**). The A_{410} and A_{280} are shown as red and blue lines, respectively. The A_{410} was used to select which fractions to run on SDS-PAGE gels to assess the purity of the proteins. All four variants were purified from a 6 L culture.

For the MtrA triple His/Met mutant, size-exclusion chromatography (SEC) was done after the Strep(II) tag purification (Figure 5.7). The yield for the triple mutant was considerably lower than the single mutants and the WT, again corroborating the hypothesis that the cells struggle more to produce a soluble MtrA variant protein that is less similar to the native version.

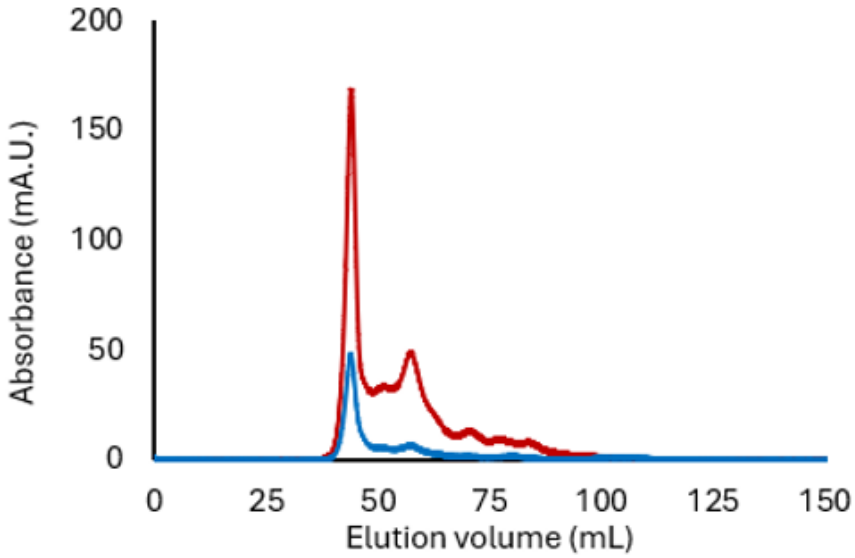

Figure 5.7. ÄKTA traces from SEC purification of MtrA triple His/Met mutants. The A_{410} and A_{280} are shown\ as red and blue lines, respectively. The A_{410} peaks were used to select which fractions to run on an SDS-PAGE gel to further assess the purity of the protein.

Different optimisation attempts at increasing the yield MtrA triple mutant were carried out including: modifying the concentration of L-arabinose used at induction, changing the OD_{600} induction point, increasing the incubation time of *S. oneidensis* cells before harvesting, and increasing the starting inoculum. However, the yield (determined by the 410 nm absorbance during the ÄKTA run) remained relatively low after changing all these variables.

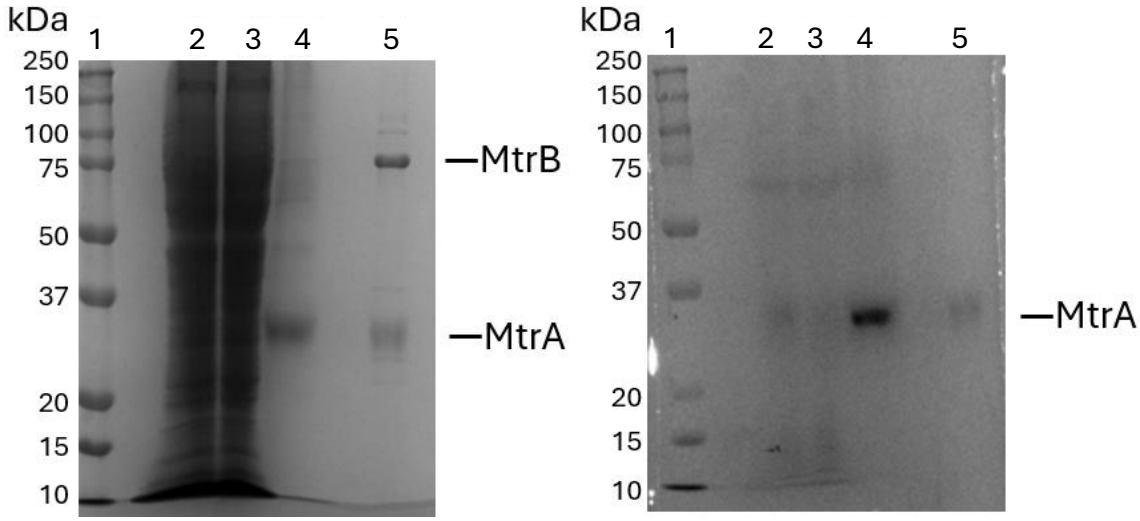

Figure 5.8. SDS-PAGE gels showing purification of MtrA triple from *S. oneidensis* Δ*mtr* cells containing pMTRA$_{triple}$ after SEC. Gels were stained for Coomassie (**left**) and heme (**right**). For both gels, lanes are as follows: molecular marker (lane 1), lysed cells (lane 2), ÄKTA flow through that did not bind to the Strep(II) column (lane 3), purified MtrA triple after SEC (lane 4), purified MtrAB control (lane 5). MtrA and MtrB are indicated with lines. Plasmid induction was done with 5 mM L-arabinose.

Throughout the purification process, SDS-PAGE gels were carried out and stained for heme. Figure 5.8 shows the purified MtrA triple after elution from a Strep column. Both gels show a clear band for MtrA at ~ 37 kDa. The Coomassie gel also shows the MtrB band for the MtrAB control (lane V) that is not seen in the heme stain, as MtrB contains no hemes. The gels both suggest the purification of MtrA triple was done successfully and there were few impurities. Even though the heme-stained gel shows a faint MtrA band for the cell lysate samples and the ÄKTA flow through samples, the band is diffuse and not very strong. This highlights how overexpressed the proteins are in the pBAD system. The gels from the purifications of MtrA WT, H85M, H167M, and H200M were very similar to Figure 5.8 and are not shown for concision.

Figure 5.9 shows the translation of the sequenced pMTRA$_{triple}$ plasmid, with the three corresponding His/Met mutations. Protein expression of MtrA triple was lower than the WT or single mutants. This is suggested to have been due to having three mutations as opposed to just one. The impact of these mutations on the tertiary structure of MtrA was unknown, but the decrease in protein expression was apparent.

Figure 5.9. Top. Translated DNA sequence for mature, MtrC triple. The first amino acid residue shown is the serine immediately after the MtrA signal peptide cut site. The H85M, H167M, and H200M amino acid modifications are shown with purple, dark blue, and dark green arrows, respectively. The CXXCH motifs are shown within the brown arrow labels over the sequence. The Strep(II) tag is shown with a light blue arrow. **Bottom.** DNA alignment of MtrA WT and MtrA$_{triple}$ showing the histidines (CAC) being mutated to methionines (ATG). Mutated methionines are shown with pink arrows. Figures produced using Benchling.

5.2.4 UV-Vis spectroscopy

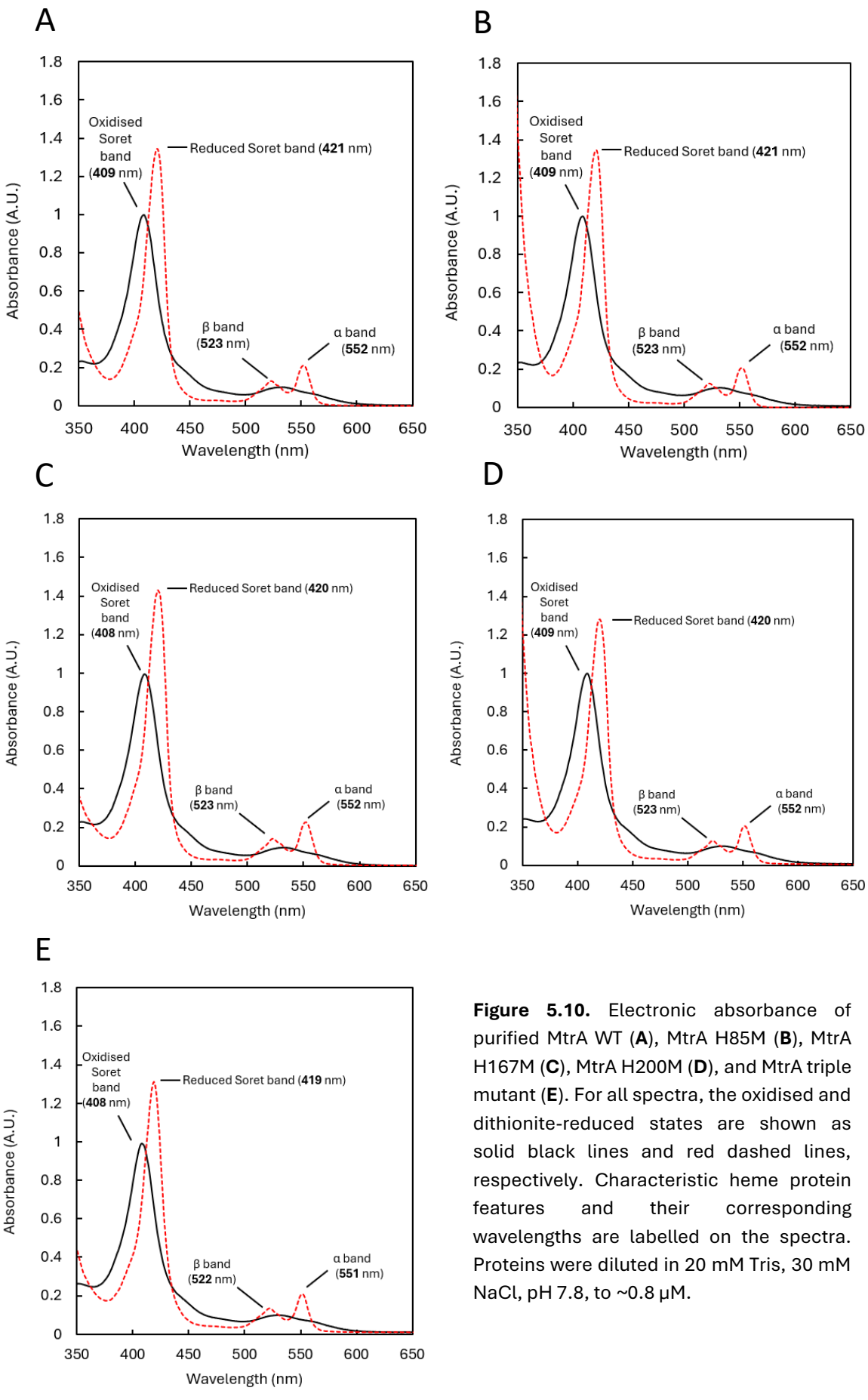

Figure 5.10. Electronic absorbance of purified MtrA WT (**A**), MtrA H85M (**B**), MtrA H167M (**C**), MtrA H200M (**D**), and MtrA triple mutant (**E**). For all spectra, the oxidised and dithionite-reduced states are shown as solid black lines and red dashed lines, respectively. Characteristic heme protein features and their corresponding wavelengths are labelled on the spectra. Proteins were diluted in 20 mM Tris, 30 mM NaCl, pH 7.8, to ~0.8 µM.

After confirming that the DNA sequence was correct and the produced proteins were at the appropriate size on an SDS-PAGE gel, the redox capacities of all variants were assessed. UV-Vis spectroscopy (Methods 2.5.1) can be used to provide insight on the structures of heme proteins by observing their characteristic features. This provides information not only on the structure, folding, and heme incorporation, but also on the correct redox functionality.

Table 5.2. Summary of the MtrA variants' spectral features obtained from UV-Vis spectroscopy. The maxima for the three characteristic peak features are listed for the oxidised (black text) and reduced (red text) states.

	λ_{max} (nm)									
Peak	WT		H85M		H167M		H200M		Triple	
Soret	409	421	409	421	408	420	409	420	408	419
Alpha (α)		552		552		552		552		551
Beta (β)		523		523		523		523		522

Figure 5.10 shows the UV-Vis spectra of the purified MtrA and the four MtrA variants in their reduced and oxidised states. A comparison of the Soret, α and β peak features across the five MtrA variants is shown in Table 5.2. The results from the UV-Vis spectra data indicate that there were no significant differences in the maxima for the alpha and beta bands across all five variants. The most notable shift was in the reduced Soret band maxima of the triple mutant, which decreased by 2 nm. This suggests that the three His/Met modifications might have slightly impacted the tertiary structure or electron orbital configuration of MtrA triple. Within the porphyrin inside hemes, the Soret band feature arises from a characteristic π- π* absorption region. These occur as the electrons take in the light energy and are transferred from the S_0 ground state (highest occupied molecular orbital ((HOMO)) to the second S_2 excited state (the least unoccupied molecular orbital (LUMO + 1)) in the 400-450 nm range[215]. By having methionine instead of histidine as the distal ligand, the local electron orbital environment is changed. Therefore, this may explain the subtle changes in the Soret maxima of the MtrA triple when compared to the single mutants and MtrA WT.

5.2.5 Pyridine hemochromagen assay

To determine the molar absorption coefficients (ε) of heme proteins, the pyridine hemochromagen assay can be used. These coefficients can vary depending on the protein environment and axial ligands to the heme. Heme proteins are denatured before pyridine is added, which axially coordinates all hemes in the sample. As they all become spectroscopically identical, and the ε for pyridine is known, the original concentration of the intact protein can be calculated. The Beer-Lambert law can then be used to calculate the ε for the assayed protein. The pyridine hemochromagen assay was done following the protocol listed in Methods 2.5.4.

Table 5.3. Molar absorption coefficients (ε) calculated by the pyridine hemochromagen assay. ‡From published work[224] using a similar protocol.

Protein	ε (mM^{-1} cm^{-1})
MtrA‡	1320
MtrA WT	1317
MtrA H85M	1295
MtrA H167M	1288
MtrA H200M	1303
MtrA Triple	1276

Table 5.3 shows the calculated ε of the five MtrA variants, as well as a published MtrA (WT) one. There was no significant difference between the published ε, and the one obtained for MtrA WT. For the three single mutants, there was a slight decrease in the ε; however, the difference was minute. The largest difference was with the MtrA triple, as this seemed to have the lowest calculated ε out of all of the variants. These results are similar to previous results[195] where the *S. oneidensis* outer-membrane decaheme MtrC was investigated. In the study, two MtrC variants were analysed. Both had a Y657C mutation, but one had all ten bis-his hemes while the other had a single His/Met heme. Their results suggested the ε of the His/Met MtrC variant was ~ 25 mM^{-1} cm^{-1} lower than that of the MtrC with all ten bis-his hemes. However, the robustness of the data produced from the pyridine hemochromagen assay varies greatly, as it depends on several factors including: the purity of the assayed protein, the stability of the pyridine solution, operator error, the environment the assayed protein is in. Consequently, interpretation of the data should be taken with a more qualitative than quantitative approach. Therefore, it was concluded that introducing single or triple His/Met mutations in MtrA resulted

in changes to the ε that were too subtle to be detected by the pyridine hemochromagen assay.

5.2.6 Ascorbate reduction assay

To confirm the correct incorporation of the distal methionine to the corresponding hemes in MtrA, an ascorbate reduction assay was carried out (Methods 2.5.3). The sequenced plasmid indicated that the DNA sequence was correct, but that does not necessarily mean that the methionine was correctly incorporated into the protein. Moreover, the change from histidine to methionine might have caused structural instability that could lead to the ligand falling off the heme. The assay is based on the principle that with certain sets of ligands, oxidised hemes show ligand-to-metal charge-transfer bands from 600-750 nm. These energies are indicative of the chemical properties of their axial ligands[165].

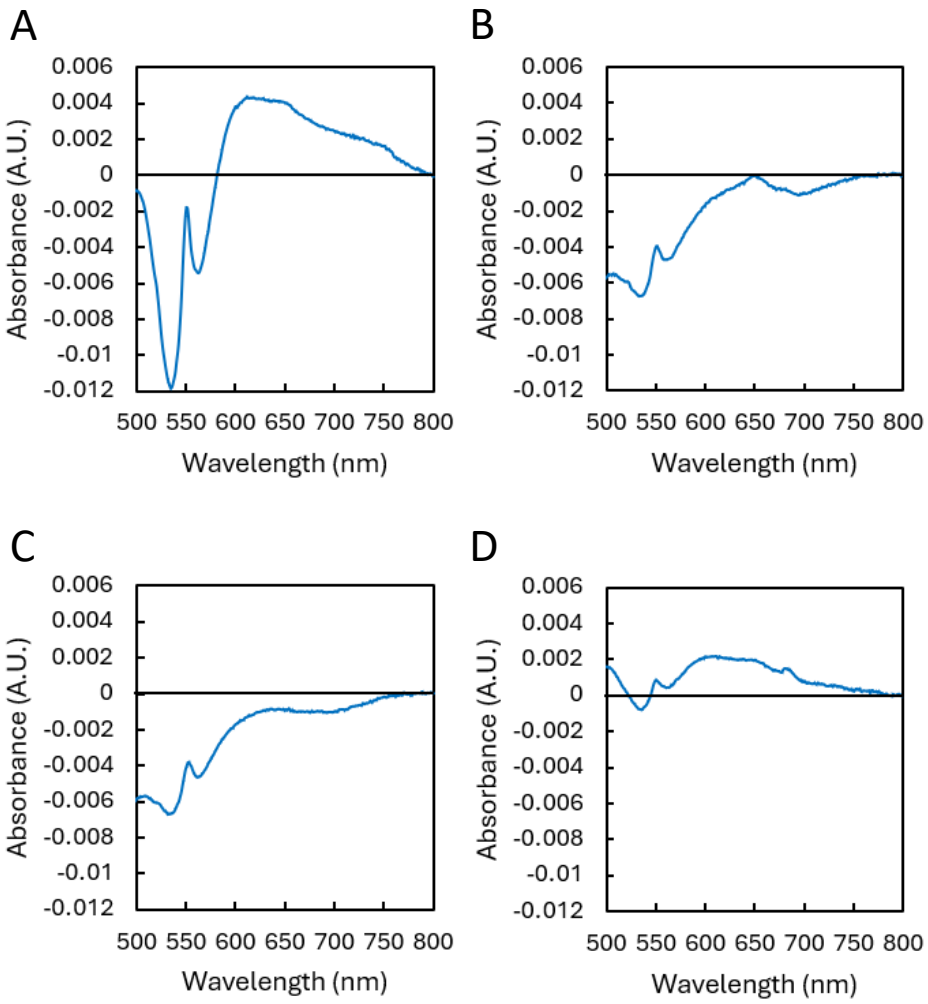

Figure 5.11. Difference spectra showing ascorbate-reduced minus oxidised states as blue lines. Proteins shown are MtrA WT (**A**), H85M (**B**), H167M (**C**), and H200M (**D**). Samples were in 20 mM Tris, 30 mM NaCl, pH 7.8. Absorbance was normalised to 800 nm.

To take advantage of this, a difference spectrum can be taken of the ascorbate-reduced spectra minus the oxidised spectra (Figure 5.11). To verify that similar features do not occur when reduced with sodium dithionite, a difference spectrum was taken of the dithionite reduced minus oxidised (Figure 5.12)

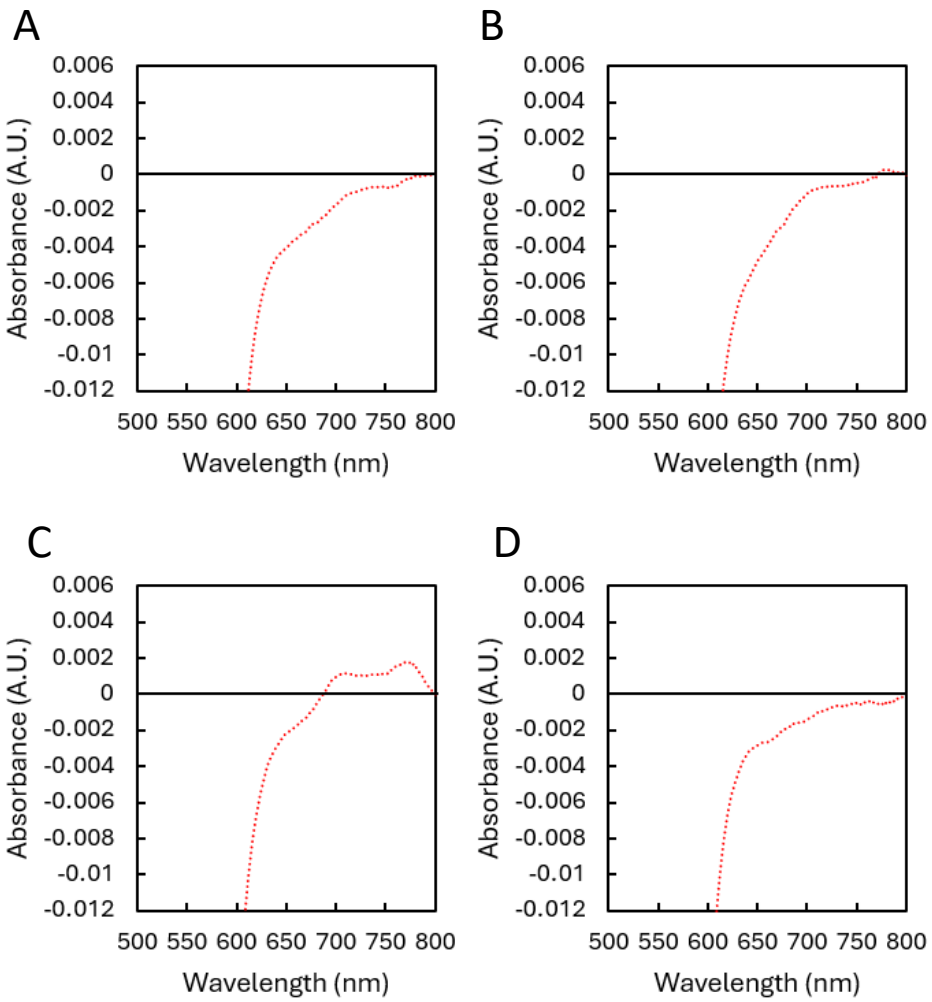

Figure 5.12. Difference spectra showing dithionite reduced minus oxidised states as red dotted lines. Proteins shown are MtrA WT (**A**), H85M (**B**), H167M (**C**), and H200M (**D**). Samples were in 20 mM Tris, 30 mM NaCl, pH 7.8. Absorbance was normalised to 800 nm.

Previous work[79] has suggested that the ascorbate-reduced minus oxidised difference spectrum (Figure 5.11) can reveal two negative features that may provide information on the axial ligands. First, a trough centred at 630 nm has been reported to be indicative of reduction of a high-spin (with unpaired electrons) Fe(III) heme, predicted to have His/H_2O ligation[79]. Second, a trough centred at 700 nm would be indicative of reduction of a low-spin (with no unpaired electrons) Fe(III) heme with His/Met ligation. The difference spectrum for MtrA H200M (Figure 5.11, D) shows what would appear to be a very shallow trough at 630 nm, which suggests the

methionine might have fallen off the heme, and there is a H2O-ligated heme or heme with no ligand. For MtrA H85M (Figure 5.11, B) and H167M (Figure 5.11, C), a trough centred around 700 nm appears more pronounced, suggesting correct incorporation of the distal methionine to the heme. MtrA WT (Figure 5.11, A) does not appear to show either of these features. A dithionite reduction was carried out on the same four MtrA variants on the same day. The dithionite reduced minus oxidised difference spectra (Figure 5.12) do not suggest that any of the four MtrA variants have a trough at neither 630 nm nor 700 nm, indicating that ascorbate is necessary to observe these features. These results suggest that MtrA H85M and H167M had the methionine incorporated correctly, whereas it might have fallen off in H200M. These results are consistent with previously investigated heme proteins with His/Met hemes[79], but are not conclusive. Furthermore, the purification of

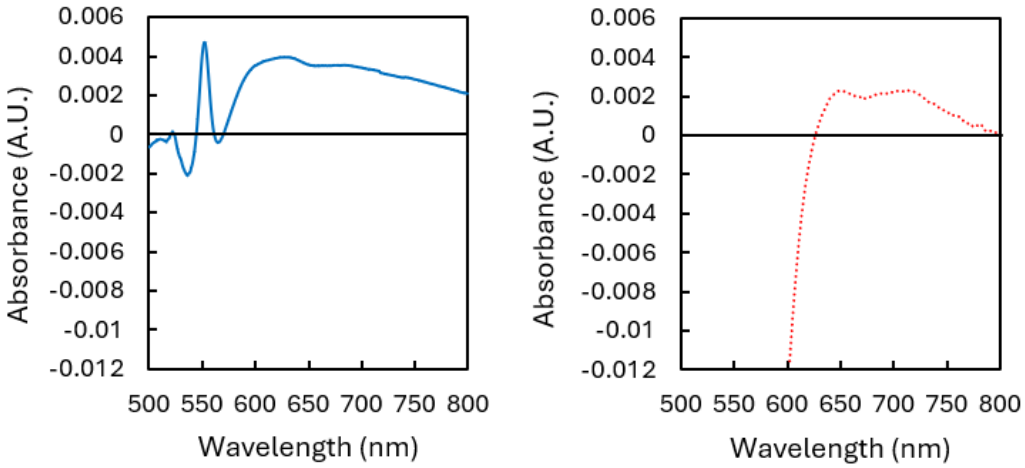

Figure 5.13. Difference spectra showing ascorbate-reduced minus oxidised as a solid blue line (**left**) and dithionite-reduced minus oxidised as a dotted red line (**right**). Samples were in 20 mM Tris, 30 mM NaCl, pH 7.8. Absorbance was normalised to 800 nm.

functional MtrA variants that were not all bis-his ligated was successful, and these variants all showed typical spectroscopic features of heme proteins.

Next, the same assay was carried out on MtrA triple to investigate what would happen when methionine was intended as the axial distal ligand in three hemes instead of one. Figure 5.13 left and right show the difference spectra for purified MtrA triple when reduced with ascorbate and dithionite, respectively. The data for MtrA triple are less conclusive than for the other variants. The spectra do not show any troughs at neither 630 nor 700 nm, suggesting that there are no hemes with neither His/Met nor His/H_2O ligation. However, finding these predicted thoughts in

the UV-Vis difference spectra can be quite subjective and the data is not robust enough to be able to conclude possible methionine ligation. Furthermore, due to the extremely low yields of the purified MtrA triple, other techniques such as nuclear magnetic resonance (NMR) that would be better for ascertain the ligand environment of hemes, were not feasible. After many attempts at optimising the purification protocol, the average yields were still ~ 500 µg of purified MtrA triple from 12 L of cultured cells.

5.2.7 Activity assays

To better understand the effect of the His/Met modifications on the distal heme ligands of MtrA, functional assays were carried out. These investigated any impact of having changed the heme ligands on the capacity for *S. oneidensis* cells to carry out EET. The five MtrA plasmids (WT, three single mutants, and the triple mutant; MtrA 5.2.1.1) were transformed into a *S. oneidensis* Δ*mtrA* strain for these activity assays (Methods 2.2.9). This way, the MtrA variants would form a complex with the native MtrB and MtrC.

5.2.7.1 Protein expression trials on Δ*mtrA* mutants

Before starting the functional assays, the relative protein expression of each variant was assessed in the *S. oneidensis* Δ*mtrA* cells.

Figure 5.14 compares the expression of the five different MtrA variants in the *S. oneidensis* Δ*mtr* cells with corresponding pMTRA plasmids. The gel suggests little to no difference in expression between MtrA WT and the three single mutants. The gel also indicated that there was not much difference when inducing the triple mutant with 2.5 mM, 5 mM, or 10 mM L-arabinose. 5 mM was selected as an appropriate concentration of L-arabinose to use for future induction of the $pMTRA_{triple}$ plasmid.

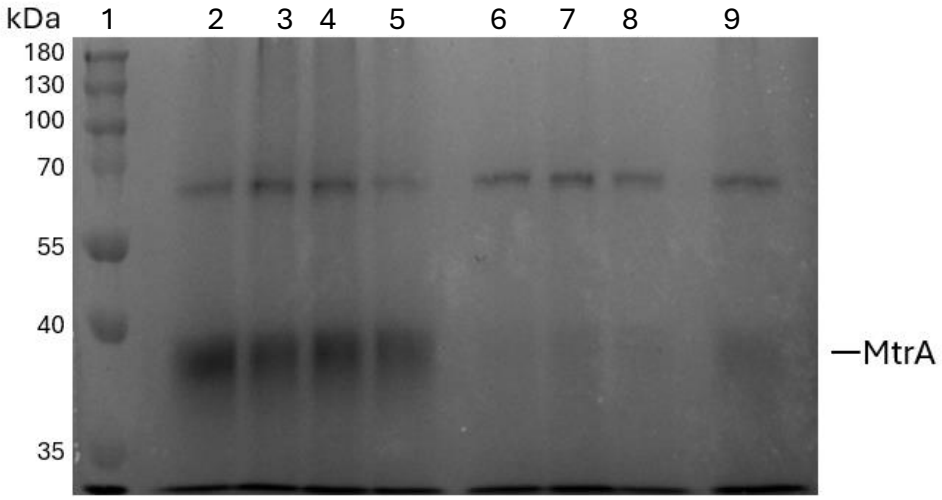

Figure 5.14. Normalised heme-stained SDS-PAGE gel comparing MtrA expression across different *S. oneidensis* cells. Lanes are as follows: molecular marker (lane 1); *S. oneidensis* Δ*mtrA* cells with $pMTRA_{rec}$ plasmid (lane 2); *S. oneidensis* Δ*mtrA* cells with $pMTRA_{H85M}$ plasmid (lane 3); *S. oneidensis* Δ*mtrA* cells with $pMTRA_{H167M}$ plasmid (lane 4); *S. oneidensis* Δ*mtrA* cells with $pMTRA_{H200M}$ plasmid (lane 5); *S. oneidensis* Δ*mtrA* cells with $pMTRA_{triple}$ mutant plasmid induced with 2.5 mM, 5 mM, and 10 mM L-arabinose (lanes 6, 7, and 8, respectively); and *S. oneidensis* Δ*mtrA* cells with $pMTRA_{triple}$ mutant plasmid induced with 5 mM L-arabinose and supplemented with 20 mM Fe (III) citrate during growth phase (lane 9). MtrA is indicated with lines.

5.2.7.2 Flavin mononucleotide reduction

Flavin mononucleotide (FMN) can be used to determine the rate of EET in *S. oneidensis* cells. The FMN act as electron shuttles that accept the electrons from heme 10 of MtrC and can donate them to the terminal electron acceptor. As the oxidised form of FMN can fluoresce (excitation at 365 nm and emission at 525 nm), the rate at which the FMN is reduced can be monitored with fluorescence spectroscopy. Changes in fluorescence over time can be converted into rate of electron transfer onto FMN molecules.

Figure 5.15 shows the unprocessed fluorescence intensity data from the fluorimeter (Figure 5.15, left) and the processed data converted to FMN reduction rate (Figure 5.15, right). The data showed that the fastest decrease in fluorescence intensity was due to electrons transported in the Δ*mtrA* producing MtrA WT (red line). Due to the plasmid-based overexpression system, reduction rates higher than those of the WT

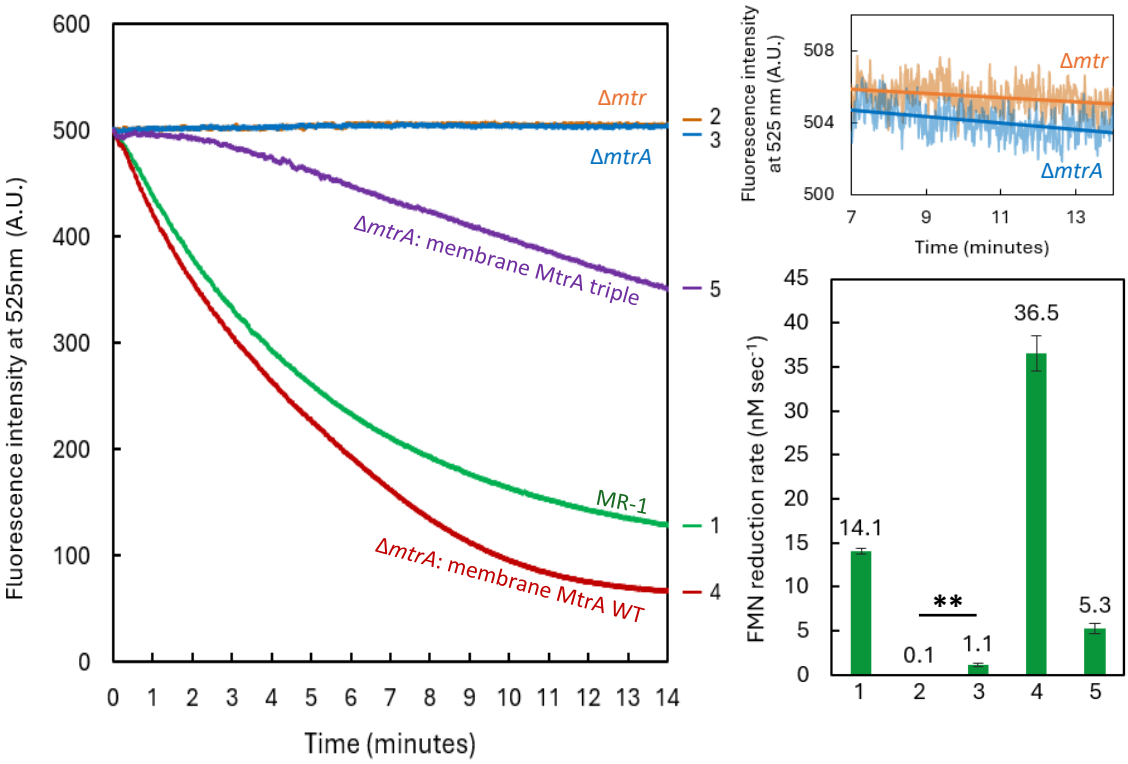

Figure 5.15. Results from the MtrA triple FMN reduction assay. **Left.** Change in fluorescence intensity at 525 nm of five *S. oneidensis* strains over a period of 14 minutes. **Top right.** Higher magnification of figure on the left, showing Δ*mtr* (orange) and Δ*mtrA* (blue). A linear trendline was added to visualise the difference in rate with more ease. **Bottom right.** Processed data from the FMN assay, where change in fluorescence was converted to a rate of FMN reduction. Strains shown include: MR-1 (**1**); *Δmtr* (**2**); *ΔmtrA* (**3**); *ΔmtrA* producing MtrA WT (**4**); and *ΔmtrA* producing MtrA triple (**5**). An unpaired *t* test indicated a statistically significant difference ($p < 0.01$) represented with two asterisks (**). The assay was carried out with cells at a starting OD_{600} of 0.1 induced with 1 mM L-arabinose. The initial concentration of FMN was 12 μM. Experiments were done in triplicate and error bars show standard error of mean.

were to be expected. The positive control, MR-1 (green line), also showed a large decrease in the fluorescence intensity, but not as significant as the mutant overexpressing MtrA WT. The Δ*mtr* (orange line) and Δ*mtrA* (blue line) mutants showed identical results ,with no change in the fluorescence intensity over the 14 minutes. The transfer of electrons from the *S. oneidensis* cells to the oxidised FMN molecules occurred quickly as shown in Figure 5.15, left, by the steeper gradient within the first few minutes. Consequently, the change in fluorescence over this initial period was used in the FMN reduction rate calculations. Furthermore, the initial rate was also used to mitigate any unwanted interactions with any remaining oxygen molecules.

The FMN reduction rates presented in this thesis (Figure 5.15, right) corroborated previous work[113] indicating the incapability for the Δ*mtr* and Δ*mtrA* mutants to significantly reduce FMN. In previous work, the Δ*mtrA* mutant showed a rate that

was higher than the Δ*mtr* mutant, and the difference was statistically significant ($p < 0.01$). It is hypothesised that, as *S. oneidensis* has other mechanisms for EET, then the outer-membrane MtrC (even if MtrA is not present) might act as an electron acceptor/donor. Yet, the rate is only marginally higher, so the effect might not be appreciable. The Δ*mtrA* cells producing MtrA WT had the highest rate, more than twice the rate of MR-1. Again, this was due to the overexpression plasmid-based system used in these experiments. Additionally, it confirmed that the experimental design was appropriate and suggested that the MtrCAB complex was formed by the plasmid-based MtrA and the native MtrB and MtrC and electrons could be transported by the trimer. The rate for the Δ*mtrA* producing MtrA triple was lower than both MR-1 and the Δ*mtrA* producing MtrA WT; however, it was higher than the Δ*mtr* and Δ*mtrA* mutants. These results would indicate that the MtrA triple is forming a complex with the native MtrB and MtrC, but the electrons cannot traverse the trimer as quickly as they did when MtrA had all bis-his coordinated hemes. However, it is unknown if this was because of having methionine as the distal ligand, or because the methionine had fallen off any of the mutated His/Met hemes in MtrA triple resulting in His/H_2O ligation or no distal ligand. Furthermore, for the Δ*mtr* strains producing MtrA variants, the likelihood of MtrAB (comprised of a variant MtrA and a native MtrB) forming a complex with MtrC to produce a functional MtrCAB is unknown. Even though the MtrA variants are overexpressed, they still need MtrB in a 1:1 ratio to be able to be correctly incorporated into the outer membrane. However, if there are more MtrAB produced than MtrC, then rates of EET could be artificially low as there are not enough MtrC to accept the electrons from MtrA and donate to FMN. Consequently, it is difficult to be sure of the ratio of MtrAB:MtrCAB:MtrC. Therefore, changes in FMN reduction rates could also be due to this uncertainty. It is also notable that, as shown earlier in the chapter, the capacity of *S. oneidensis* to produce the soluble MtrA variants is lower than the MtrA WT. Consequently, the rates might be lower in the mutants producing MtrA triple because the relative expression of the cytochrome is lower than in MR-1, producing lower rates of EET.

5.3 Conclusion and future work

S. oneidensis can transport electrons across its outer membrane via the MtrCAB conduit. The decaheme MtrA is embedded within the porin MtrB, which results in an MtrAB complex through which electrons enter at the periplasmic side of MtrA and are transferred onto the outer-membrane decaheme MtrC. All ten hemes in MtrA (as well as MtrC) have histidine as the distal axial ligand to the heme. Most other studied *c*-type cytochromes involved in EET in *S. oneidensis* and other electroactive bacteria have hemes with bis-his ligation. However, there are other *c*-type cytochromes such as PgcA from the iron-reducing *Geobacter sulfurreducens* and PioA from the iron-oxidising *Rhodopseudomonas palustris* TIE-1 that have methionine as the distal ligand instead of histidine. PioA is homologous to MtrA but contains three His/Met hemes and seven bis-his hemes. It has been proposed[79], that having these methionines enables PioA to operate at reduction potentials that are more positive than those that MtrA or MtrCAB would operate at. Furthermore, these methionines with more positive reduction potentials could function as electron sinks, preventing electrons from going backwards in the heme chain. Therefore, it has been hypothesised that these methionines enable PioA to transport electrons from Fe(II) oxides into the cells, even when the intracellular reduction potential is more negative than the extracellular one.

To investigate this further, the distal histidines of hemes 2, 3, and 7 of a plasmid-based MtrA from *S. oneidensis* were mutated into methionines. This was done first with three single His/Met mutants and then a triple mutant. Alongside a plasmid-based MtrA WT, the MtrA variants were all purified with a C-terminus Strep(II) tag that was added before doing the His/Met mutations. The purified MtrA variants were all analysed using UV-Vis spectroscopy and their molar absorption coefficients (ε) were calculated using a pyridine hemochromagen protocol. The calculated ε for the single mutants and triple mutant did not differ significantly from the MtrA WT one nor from the published MtrA ε. Furthermore, the UV-Vis spectra for all five variants showed that the proteins were all redox active and the Soret, α and β peak maxima were within a few nm of each other. With an ascorbate reduction assay, two out of the three single mutants were suggested to have methionine as the heme distal ligand. In the data for the other single mutant and the triple mutant, however, the presence of methionine was not observed. Finally, the FMN reduction rates for the

Δ*mtrA* cells producing MtrA triple were ~ 3-fold and 7-fold lower when compared to MR-1 and Δ*mtrA* cells producing MtrA WT, respectively.

Ultimately, the work in this thesis chapter confirmed that the modification of histidine to methionine as the distal ligands in three of the MtrA hemes was possible. The purification of these four variants was also possible by a Strep(II) tag. However, only two (H85M and H167M) out of the four variants were suggested to have the methionine attached to the heme via the ascorbate reduction assay. To better understand the local heme environment, nuclear magnetic resonance (NMR) or magnetic circular dichroism (MCD) could be employed. However, due to low purification yields, this was not possible in this thesis. Furthermore, electrochemistry techniques such as cyclic voltammetry, could further explore if the methionines were correctly ligated to the heme. Regardless of which technique is used, as the other 9/10 hemes (or 7/10 in the triple mutant) have bis-his hemes, discerning between bis-his and His/Met hemes would remain a challenge.

The FMN assay results suggested that having three methionines impaired the ability for the *S. oneidensis* cells to transfer electrons onto FMN as quickly as the controls. However, the FMN reductase activity was still maintained, suggesting a functional MtrCAB complex was formed that likely contained the MtrA triple. The $MtrCA_{triple}B$ complex was still capable of EET, indicating that the His/Met hemes did not restrict the direction of electron flow. However, further work is necessary to corroborate this. First, the correct incorporation of methionine as the distal ligand should be better explored. After, reduction assays with other physiological and non-physiological electron acceptors would provide insight onto the functional effects of having His/Met as opposed to bis-his hemes.

Chapter 6

Discussion

6. Final discussion

6.1 Summary and conclusions

6.1.1 Increased flexibility in MtrC

The work presented in this thesis has endeavoured to further the understanding of the decaheme cytochromes from MtrCAB found in *Shewanella oneidensis*. In the extracellular cytochrome MtrC, two amino acid residues were changed, S188V and N251D ($MtrC_{DM}$). These changes in the residues were predicted to increase the angle between domains I,II and domains III, IV, as a consequence of differences in the charge and hydrophobicity of the modified amino acid residues. The SAXS results suggest that the angle and flexibility between domains was increased in the $MtrC_{DM}$ variant. However, there were no significant differences in the spectroscopic properties of soluble $MtrC_{DM}$ when compared to the WT, suggesting that the heme environments remained intact. Functional characterisation of membrane $MtrC_{DM}$ by the FMN reduction assay indicated no significant differences in the EET capacities of MtrCAB compared to $MtrC_{DM}$AB. These results suggest that, regardless of the increased angle and distance between domains, MtrC can maintain efficient FMN reductase capacity. This could be because FMN is suggested[131] to form a complex with MtrC, which might bring domains III, IV closer to domains I, II, regardless of the increased angle between the two sets of domains. As the FMN is predicted to bind near heme 7, on domain III, then it would not be advantageous for the cells if domains III, IV were far enough from domains I, II to hinder electron transport. If the distance between the two sets of pentahemes within MtrC were to be increased, then electron transfer rates would go down, as they would have to travel farther. The results in this thesis suggest that the rate limiting step of *in vivo* flavin reduction is not through the MtrC domain interface. This is surprising as it is known that disruption of the disulfide in domain III affects the interaction between MtrC and flavins[131,134]. Perhaps by further increasing the distance between domains I,II and III, IV in MtrC the rate of electron transfer to acceptors would be disrupted more significantly.

6.1.2 Absence of domains III and IV in MtrC

Continuing the work from the previous chapter, the effect of removing domains III and IV of MtrC was explored. The secretion of soluble $MtrC_{DI,II}$ of the predicted mass

was confirmed by LC-MS. The protein was crystallised and the structure resolved to 1.8 Å (PDB: (9EOV). Superposition of the crystal structure onto MtrC (PDB: 4LM8) indicated that the hemes were correctly incorporated with identical angles of His/His ligation to the hemes. There were no significant differences in the spectroscopic properties, in the active redox potential window, nor in the midpoint reduction potential of soluble of $MtrC_{DI,II}$ compared to MtrC. To confirm the association of $MtrC_{DI,II}$ to MtrAB, sedimentation velocity experiments were conducted and the functional effects of removing domains III and IV were investigated by a variety of reduction assays. Reduction rates of FMN, OmcA, ferric citrate, Amaranth, and Methyl Orange, was significantly decreased in *S. oneidensis* Δ*mtrC/omcA* mutants expressing $MtrC_{DI,II}$. However, the reduction rate of Reactive Black 5 was sustained in the same mutants, suggesting EET to this azo dye was successful. More reduction assays with different electron acceptors should be conducted to further explore the effects on EET. It is concluded that $MtrC_{DI,II}$ can function as a minimal model for EET in *S. oneidensis*. However, the substrates it can reduce are limited. The results in this thesis suggest that there are discrete binding sites on MtrC that interact with physiologically relevant electron acceptors, in particular flavins. This aligns with the hypothesis that flavin reduction is prevented by the MtrC disulfide and also furthers the understanding of this proposed mechanism of action. To further evidence this, a variant comprised solely of domains III and IV would be designed, which would be able to bind FMN but might not be able to take electrons from MtrA.

6.1.3 His/Met ligation in MtrA

In the outer-membrane cytochrome, MtrA, the distal axial ligands of hemes 2, 3, and 7 heme groups were changed from histidines to methionines. This was done to replicate the heme ligand configuration of PioA, an MtrA homologue found in *Rhodopseudomonas palustris* TIE-1[79]. This thesis confirmed that the modification of histidine to methionine in the three MtrA hemes was possible, but only two soluble variants (H85M and H167M) showed the indication of having the methionine attached to the heme, as confirmed by ascorbate reduction; the other two variants (H200M and triple mutant) did not. Biophysical characterisation of the MtrA variants showed negligible differences in the spectroscopic properties when compared to WT MtrA. The functional characterisation results from the FMN reduction assay

suggested that having three His/Met hemes impaired the ability for *S. oneidensis* cells to transfer electrons to FMN as efficiently as the WT MtrA. It was hypothesised that these methionines functioned as electron sinks, reducing the capacity for electrons to quickly traverse MtrA onto MtrC. The electrons that have passed the His/Met hemes might be drawn back due to the more positive reduction potential of methionine when compared to histidine. However, further investigation is needed to corroborate this. First, other techniques like NMR should be used to definitively confirm the ligation of methionines to the heme. Next, reduction assays with different electron acceptors should be conducted to further explore the effects of having methionine-ligated hemes on EET. Finally, a variant MtrA with more than three His/Met hemes could be designed. It would be expected that this putative variant might have a lower rate of electron transfer. However, electron transfer might be completely disrupted if the protein can no longer maintain its tertiary structure.

6.2 Future work

S. oneidensis shows potential for biotechnological applications ranging from wastewater treatment to biomining. However, increasing our understanding of EET in the bacteria is essential to further these applications. The work shown here on the modification of the distal ligands of three hemes in MtrA yields insight into the predicted electron sink behaviour of these methionines. In PioA, it is hypothesised that these three methionines allow for electron transport into the cell, even when against a reduction potential gradient. A modified MtrA might enable *S. oneidensis* to respire in environments where the extracellular reduction potential is lower than the intracellular one. To explore this, the number of His/Met hemes in MtrA could be increased. However, regardless of the number of His/Met hemes, more robust techniques should be used to confirm correct ligation of methionine to the heme.

However, most research relating to MtrCAB is conducted on MtrC itself, as this cytochrome is usually the last or second to last step in EET to the terminal electron acceptor. Here the distance between domains I, II and domains III, IV was increased in one chapter, with no significant biophysical nor functional differences when compared to WT MtrC. In another, domains III and IV were removed entirely. The results indicate negligible biophysical differences when compared to WT MtrC. Functionally, however, EET reduction rates of most analysed substrates were largely impaired by the removal of domains III and IV. To further investigate the

consequences of removing these two domains, more physiological and non-physiological electron acceptors should be assayed. The results would suggest that the reason for no EET to most acceptors was because of no binding sites. To explore this in more detail, an MtrC variant comprised of domains III and IV could be designed and purified. Then, restoration of reductase activity upon the addition of this new MtrC variant could be explored. Alternatively, other protein domains could be fused to $MtrC_{DI,II}$. For example, domains III and IV of MtrF (MtrC homologue) or OmcA would be ideal candidates to start. This work demonstrates that the electrons can traverse domains I and II of MtrC, so if the fusion proteins are designed appropriately, EET through them would be expected. Furthermore, domains from cytochromes not from *Shewanella* could also be fused to $MtrC_{DI,II}$, enabling *S. oneidensis* mutants to respire substrates that MR-1 cannot.

References

1. Verma, A. K. Relevancy of Three Domain System of Biological Classification in modern context. *International Journal on Biological Sciences* **7**, 35–39 (2016).

2. Woese, C. R., Kandler, O. & Wheelis, M. L. Towards a natural system of organisms: proposal for the domains Archaea, Bacteria, and Eucarya. *Proc Natl Acad Sci U S A* **87**, 4576 (1990).

3. Jayashantha, E. *Archaea Morphology, Physiology, Biochemistry and Applications*. (2015). doi:10.13140/RG.2.1.4382.9281.

4. Bini, E. Archaeal transformation of metals in the environment. *FEMS Microbiol Ecol* (2010) doi:10.1111/j.1574-6941.2010.00876.x.

5. Kosman, D. J. The teleos of metallo-reduction and metallo-oxidation in eukaryotic iron and copper trafficking. *Metallomics* **10**, 370–377 (2018).

6. Gerald, B. *Basic Cell and Molecular Biology*. (LibreTexts, 2024).

7. Moissl-Eichinger, C. *et al.* Archaea Are Interactive Components of Complex Microbiomes. *Trends Microbiol* **26**, 70–85 (2018).

8. Bang, C. & Schmitz, R. A. Archaea associated with human surfaces: not to be underestimated. *FEMS Microbiol Rev* **39**, 631–648 (2015).

9. Chow, C., Padda, K. P., Puri, A. & Chanway, C. P. An Archaic Approach to a Modern Issue: Endophytic Archaea for Sustainable Agriculture. *Curr Microbiol* **79**, 1–9 (2022).

10. Hartman, H. & Fedorov, A. The origin of the eukaryotic cell: A genomic investigation. *Proceedings of the National Academy of Sciences* **99**, 1420–1425 (2002).

11. Donoghue, P. C. J. *et al.* Defining eukaryotes to dissect eukaryogenesis. *Current Biology* **33**, R919–R929 (2023).

12. Roger, K. & Kadner, R. J. Bacteria. *Encyclopedia Britannica* https://www.britannica.com/science/bacteria (2020).

13. Melnicki, M. R., Sutter, M. & Kerfeld, C. A. Evolutionary relationships among shell proteins of carboxysomes and metabolosomes. *Curr Opin Microbiol* **63**, 1–9 (2021).

14. Peter Jurtshuk, Jr. Bacterial Metabolism. in *Medical Microbiology* (ed. Baron, S.) (University of Texas Medical Branch at Galveston, Galveston, 1996).

15. Silhavy, T. J., Kahne, D. & Walker, S. The bacterial cell envelope. *Cold Spring Harbor perspectives in biology* vol. 2 Preprint at https://doi.org/10.1101/cshperspect.a000414 (2010).

16. Scott, J. R. & Barnett, T. C. Surface proteins of gram-positive bacteria and how they get there. *Annual Review of Microbiology* vol. 60 397–423 Preprint at https://doi.org/10.1146/annurev.micro.60.080805.142256 (2006).

17. Gerbino, E., Carasi, P., Mobili, P., Serradell, M. A. & Gómez-Zavaglia, A. Role of S-layer proteins in bacteria. *World J Microbiol Biotechnol* **31**, 1877–1887 (2015).

18. Fagan, R. P. & Fairweather, N. F. Biogenesis and functions of bacterial S-layers. *Nature Reviews Microbiology 2014 12:3* **12**, 211–222 (2014).

19. Cooper, G. M. Metabolic Energy. in *The Cell: A Molecular Approach* (Sinauer Associates, 2000).

20. Mitchell, P. Coupling of Phosphorylation to Electron and Hydrogen Transfer by a Chemi-Osmotic type of Mechanism. *Nature* **191**, 144–148 (1961).

21. Farha, M. A., Verschoor, C. P., Bowdish, D. & Brown, E. D. Collapsing the Proton Motive Force to Identify Synergistic Combinations against *Staphylococcus aureus*. *Chem Biol* **20**, 1168–1178 (2013).

22. Minamino, T., Morimoto, Y. V, Kinoshita, M., Aldridge, P. D. & Namba, K. The bacterial flagellar protein export apparatus processively transports flagellar proteins even with extremely infrequent ATP hydrolysis. *Sci Rep* **4**, 7579 (2014).

23. Eiler, A. Evidence for the ubiquity of mixotrophic bacteria in the upper ocean: Implications and consequences. *Applied and Environmental Microbiology* vol. 72 7431–7437 Preprint at https://doi.org/10.1128/AEM.01559-06 (2006).

24. Yafremava, L. S. *et al.* A general framework of persistence strategies for biological systems helps explain domains of life. *Front Genet* **4**, (2013).

25. Bryce, C. *et al.* Microbial anaerobic Fe(II) oxidation – Ecology, mechanisms and environmental implications. *Environ Microbiol* **20**, 3462–3483 (2018).

26. Barros, M. E., Rawlings, D. E. & Woods, D. R. Mixotrophic Growth of a Thiobacillus ferrooxidans Strain. *Appl Environ Microbiol* **47**, 593–5 (1984).

27. White, G. F. *et al.* Mechanisms of Bacterial Extracellular Electron Exchange. *Adv Microb Physiol* **68**, 87–138 (2016).

28. Sapkota, A. Electron Transport Chain: Steps, Products, Diagram. *Microbe Notes* https://microbenotes.com/electron-transport-chain/ (2024).

29. Anraku, Y. Bacterial electron transport chains. *Annual Review of Biochemistry* vol. 57 101–132 Preprint at https://doi.org/10.1146/annurev.bi.57.070188.000533 (1988).

30. Kracke, F., Vassilev, I. & Krömer, J. O. Microbial electron transport and energy conservation - The foundation for optimizing bioelectrochemical systems. *Frontiers in Microbiology* vol. 6 575 Preprint at https://doi.org/10.3389/fmicb.2015.00575 (2015).

31. Dolin, M. Survey of microbial electron transport mechanisms. *The bacteria* **2**, 319 (2012).

32. Richardson, D. J. Bacterial respiration: a flexible process for a changing environment. *Microbiology (N Y)* **146**, 551–571 (2000).

33. Simon, J., van Spanning, R. J. M. & Richardson, D. J. The organisation of proton motive and non-proton motive redox loops in prokaryotic respiratory systems. *Biochimica et Biophysica Acta - Bioenergetics* vol. 1777 1480–1490 Preprint at https://doi.org/10.1016/j.bbabio.2008.09.008 (2008).

34. Read, A. D., Bentley, R. E., Archer, S. L. & Dunham-Snary, K. J. Mitochondrial iron-sulfur clusters: Structure, function, and an emerging role in vascular biology. *Redox Biol* **47**, 102164 (2021).

35. Alvarez, A. F., Rodriguez, C. & Georgellis, D. Ubiquinone and Menaquinone Electron Carriers Represent the Yin and Yang in the Redox Regulation of the ArcB Sensor Kinase. *J Bacteriol* **195**, 3054–3061 (2013).

36. Franza, T. & Gaudu, P. Quinones: more than electron shuttles. *Res Microbiol* **173**, 103953 (2022).

37. Sikora, A., Detman, A., Chojnacka, A. & Blaszczyk, M. K. Anaerobic Digestion: I. A Common Process Ensuring Energy Flow and the Circulation of Matter in Ecosystems. II. A Tool for the Production of Gaseous Biofuels. in *Fermentation Processes* (InTech, 2017). doi:10.5772/64645.

38. Mitchell, P. Keilin's respiratory chain concept and its chemiosmotic consequences. *Science* vol. 206 1148–1159 Preprint at https://doi.org/10.1126/science.388618 (1979).

39. Madsen, C. S. & TerAvest, M. A. NADH dehydrogenases Nuo and Nqr1 contribute to extracellular electron transfer by <i>Shewanella oneidensis<i/> MR-1 in bioelectrochemical systems. *Sci Rep* **9**, 14959 (2019).

40. Flamholz, A., Noor, E., Bar-Even, A., Liebermeister, W. & Milo, R. Glycolytic strategy as a tradeoff between energy yield and protein cost. *Proc Natl Acad Sci U S A* **110**, 10039–10044 (2013).

41. TeSlaa, T., Ralser, M., Fan, J. & Rabinowitz, J. D. The pentose phosphate pathway in health and disease. *Nature Metabolism 2023 5:8* **5**, 1275–1289 (2023).

42. Godbey, W. T. Fermentation, beer, and biofuels. *Biotechnology and its Applications* 369–387 (2022) doi:10.1016/B978-0-12-817726-6.00016-2.

43. Unden, G. & Bongaerts, J. Alternative respiratory pathways of Escherichia coli: energetics and transcriptional regulation in response to electron acceptors. *Biochimica et Biophysica Acta (BBA) - Bioenergetics* **1320**, 217–234 (1997).

44. Richter, K., Schicklberger, M. & Gescher, J. Dissimilatory reduction of extracellular electron acceptors in anaerobic respiration. *Applied and Environmental Microbiology* vol. 78 913–921 Preprint at https://doi.org/10.1128/AEM.06803-11 (2012).

45. Vignais, P. M. & Billoud, B. Occurrence, classification, and biological function of hydrogenases: An overview. *Chemical Reviews* vol. 107 4206–4272 Preprint at https://doi.org/10.1021/cr050196r (2007).

46. Borisov, V. B. *et al.* Bacterial Oxidases of the Cytochrome bd Family: Redox Enzymes of Unique Structure, Function, and Utility As Drug Targets. *Antioxid Redox Signal* **34**, 1280–1318 (2021).

47. Stolz, J. F. & Basu, P. Unraveling the inner workings of respiratory arsenate reductase. *Proc Natl Acad Sci U S A* **115**, 9051–9053 (2018).

48. Pester, M., Knorr, K. H., Friedrich, M. W., Wagner, M. & Loy, A. Sulfate-Reducing Microorganisms in Wetlands – Fameless Actors in Carbon Cycling and Climate Change. *Front Microbiol* **3**, (2012).

49. Graf, J. S. *et al.* Anaerobic endosymbiont generates energy for ciliate host by denitrification. *Nature* **591**, 445 (2021).

50. Chaudhry, R. & Varacallo, M. Biochemistry, Glycolysis. *StatPearls* (2023).

51. Oren, A. Anaerobic Respiration. in *Encyclopedia of Life Sciences* (Wiley, 2009). doi:10.1002/9780470015902.a0001414.pub2.

52. Pereira, M., Matuszewska, K., Glogova, A. & Petrik, J. Mutant p53, the Mevalonate Pathway and the Tumor Microenvironment Regulate Tumor Response to Statin Therapy. *Cancers 2022, Vol. 14, Page 3500* **14**, 3500 (2022).

53. Sacco, N. J., Bonetto, M. C. & Cortón, E. Isolation and characterization of a novel electrogenic bacterium, *Dietzia* sp. RNV-4. *PLoS One* **12**, e0169955 (2017).

54. Kato, S. Biotechnological aspects of microbial extracellular electron transfer. *Microbes Environ* **30**, 133–139 (2015).

55. Watanabe, K., Manefield, M., Lee, M. & Kouzuma, A. Electron shuttles in biotechnology. *Current Opinion in Biotechnology* vol. 20 633–641 Preprint at https://doi.org/10.1016/j.copbio.2009.09.006 (2009).

56. Marsili, E. *et al. Shewanella* secretes flavins that mediate extracellular electron transfer. *Proc Natl Acad Sci U S A* **105**, 3968–3973 (2008).

57. Okegbe, C., Price-Whelan, A. & Dietrich, L. E. P. Redox-driven regulation of microbial community morphogenesis. *Curr Opin Microbiol* **18**, 39–45 (2014).

58. Shi, L., Squier, T. C., Zachara, J. M. & Fredrickson, J. K. Respiration of metal (hydr)oxides by *Shewanella* and *Geobacter* : a key role for multihaem *c* -type cytochromes. *Mol Microbiol* **65**, 12–20 (2007).

59. Castelle, C. *et al.* A new iron-oxidizing/O2-reducing supercomplex spanning both inner and outer membranes, isolated from the extreme acidophile *Acidithiobacillus ferrooxidans*. *Journal of Biological Chemistry* **283**, 25803–25811 (2008).

60. Okamoto, A., Hashimoto, K., Nealson, K. H. & Nakamura, R. Rate enhancement of bacterial extracellular electron transport involves bound flavin semiquinones. *Proc Natl Acad Sci U S A* **110**, 7856–7861 (2013).

61. Pirbadian, S. *et al. Shewanella oneidensis* MR-1 nanowires are outer membrane and periplasmic extensions of the extracellular electron transport components. *Proc Natl Acad Sci U S A* **111**, 12883–12888 (2014).

62. Shi, L. *et al.* Extracellular electron transfer mechanisms between microorganisms and minerals. *Nature Reviews Microbiology* vol. 14 651–662 Preprint at https://doi.org/10.1038/nrmicro.2016.93 (2016).

63. Nevin, K. P. *et al.* Electrosynthesis of organic compounds from carbon dioxide is catalyzed by a diversity of acetogenic microorganisms. *Appl Environ Microbiol* **77**, 2882–2886 (2011).

64. Banerjee, A., Leang, C., Ueki, T., Nevin, K. P. & Lovley, D. R. Lactose-inducible system for metabolic engineering of *Clostridium ljungdahlii*. *Appl Environ Microbiol* **80**, 2410–2416 (2014).

65. Zhang, T. *et al.* Improved cathode materials for microbial electrosynthesis. *Energy Environ Sci* **6**, 217–224 (2013).

66. Ehrlich, H. L. Are gram-positive bacteria capable of electron transfer across their cell wall without an externally available electron shuttle? *Geobiology* **6**, 220–224 (2008).

67. Wrighton, K. C. *et al.* A novel ecological role of the Firmicutes identified in thermophilic microbial fuel cells. *ISME Journal* **2**, 1146–1156 (2008).

68. Marshall, C. W. & May, H. D. Electrochemical evidence of direct electrode reduction by a thermophilic Gram-positive bacterium, *Thermincola ferriacetica*. *Energy Environ Sci* **2**, 699–705 (2009).

69. Byrne-Bailey, K. G. *et al.* Complete genome sequence of the electricity-producing '*Thermincola potens*' strain JR. *Journal of Bacteriology* vol. 192 4078–4079 Preprint at https://doi.org/10.1128/JB.00044-10 (2010).

70. Carlson, H. K. *et al.* Surface multiheme c-type cytochromes from *Thermincola potens* and implications for respiratory metal reduction by Gram-positive bacteria. *Proc Natl Acad Sci U S A* **109**, 1702–1707 (2012).

71. Costa, N. L. *et al.* How thermophilic gram-positive organisms perform extracellular electron transfer: Characterization of the cell surface terminal reductase OcwA. *mBio* **10**, (2019).

72. Edwards, M. J., Richardson, D. J., Paquete, C. M. & Clarke, T. A. Role of multiheme cytochromes involved in extracellular anaerobic respiration in bacteria. *Protein Science* vol. 29 830–842 Preprint at https://doi.org/10.1002/pro.3787 (2020).

73. Bird, L. J., Bonnefoy, V. & Newman, D. K. Bioenergetic challenges of microbial iron metabolisms. *Trends in Microbiology* vol. 19 330–340 Preprint at https://doi.org/10.1016/j.tim.2011.05.001 (2011).

74. Shi, L., Fredrickson, J. K. & Zachara, J. M. Genomic analyses of bacterial porin-cytochrome gene clusters. *Front Microbiol* **5**, 657 (2014).

75. Liu, Y. *et al.* A trans-outer membrane porin-cytochrome protein complex for extracellular electron transfer by *Geobacter sulfurreducens* PCA. *Environ Microbiol Rep* **6**, 776–785 (2014).

76. Emerson, D. & Moyer, C. Isolation and characterization of novel iron-oxidizing bacteria that grow at circumneutral pH. *Appl Environ Microbiol* **63**, 4784–4792 (1997).

77. Shi, L., Rosso, K. M., Zachara, J. M. & Fredrickson, J. K. Mtr extracellular electron-transfer pathways in Fe(III)-reducing or Fe(II)-oxidizing bacteria: A genomic perspective. in *Biochemical Society Transactions* vol. 40 1261–1267 (Portland Press, 2012).

78. Liu, J. *et al.* Identification and characterization of MtoA: A decaheme c-type cytochrome of the neutrophilic Fe(ll)-oxidizing bacterium *Sideroxydans lithotrophicus* ES-1. *Front Microbiol* **3**, (2012).

79. Li, D. B. *et al.* His/Met heme ligation in the PioA outer membrane cytochrome enabling light-driven extracellular electron transfer by *Rhodopseudomonas palustris* TIE-1. *Nanotechnology* **31**, 354002–354013 (2020).

80. Liu, J. *et al.* $Fe_{3-x}Ti_xO_4$ nanoparticles as tunable probes of microbial metal oxidation. *J Am Chem Soc* **135**, 8896–8907 (2013).

81. Beckwith, C. R. *et al.* Characterization of MtoD from *Sideroxydans lithotrophicus*: A cytochrome c electron shuttle used in lithoautotrophic growth. *Front Microbiol* **6**, 332 (2015).

82. Zhou, N., Keffer, J. L., Polson, S. W. & Chan, C. S. Unraveling Fe(II)-Oxidizing Mechanisms in a Facultative Fe(II) Oxidizer, *Sideroxydans lithotrophicus* Strain ES-1, via Culturing, Transcriptomics, and Reverse Transcription-Quantitative PCR. *Appl Environ Microbiol* **88**, (2022).

83. Zhou, N., Kupper, R. J., Catalano, J. G., Thompson, A. & Chan, C. S. Biological Oxidation of Fe(II)-Bearing Smectite by Microaerophilic Iron Oxidizer *Sideroxydans lithotrophicus* Using Dual Mto and Cyc2 Iron Oxidation Pathways. *Environ Sci Technol* **56**, 17443–17453 (2022).

84. Jiao, Y., Kappler, A., Croal, L. R. & Newman, D. K. Isolation and characterization of a genetically tractable photoautotrophic Fe(II)-oxidizing bacterium, Rhodopseudomonas palustris strain TIE-1. *Appl Environ Microbiol* **71**, 4487–4496 (2005).

85. Jiao, Y. & Newman, D. K. The *pio* operon is essential for phototrophic Fe(II) oxidation in *Rhodopseudomonas palustris* TIE-1. *J Bacteriol* **189**, 1765–1773 (2007).

86. Gupta, D. *et al.* Photoferrotrophs produce a PioAB electron conduit for extracellular electron uptake. *mBio* **10**, (2019).

87. Bose, A., Gardel, E. J., Vidoudez, C., Parra, E. A. & Girguis, P. R. Electron uptake by iron-oxidizing phototrophic bacteria. *Nat Commun* **5**, 3391 (2014).

88. Edwards, M. J., White, G. F., Butt, J. N., Richardson, D. J. & Clarke, T. A. The Crystal Structure of a Biological Insulated Transmembrane Molecular Wire. *Cell* **181**, 665-673.e10 (2020).

89. Bird, L. J. *et al.* Nonredundant roles for cytochrome c_2 and two high-potential iron-sulfur proteins in the photoferrotroph *Rhodopseudomonas palustris* TIE-1. *J Bacteriol* **196**, 850–858 (2014).

90. Levar, C. E., Hoffman, C. L., Dunshee, A. J., Toner, B. M. & Bond, D. R. Redox potential as a master variable controlling pathways of metal reduction by *Geobacter sulfurreducens*. *ISME Journal* **11**, 741–752 (2017).

91. Morgado, L., Brulx, M., Pessanha, M., Londer, Y. Y. & Salgueiro, C. A. Thermodynamic characterization of a triheme cytochrome family from *Geobacter sulfurreducens* reveals mechanistic qnd functional diversity. *Biophys J* **99**, 293–301 (2010).

92. Zacharoff, L., Chan, C. H. & Bond, D. R. Reduction of low potential electron acceptors requires the CbcL inner membrane cytochrome of *Geobacter sulfurreducens*. *Bioelectrochemistry* **107**, 7–13 (2016).

93. Liu, Y., Fredrickson, J. K., Zachara, J. M. & Shi, L. Direct involvement of ombB, omaB, and omcB genes in extracellular reduction of Fe(III) by *Geobacter sulfurreducens* PCA. *Front Microbiol* **6**, 1075 (2015).

94. Ding, Y. H. R. *et al.* Proteome of *Geobacter sulfurreducens* grown with Fe(III) oxide or Fe(III) citrate as the electron acceptor. *Biochim Biophys Acta Proteins Proteom* **1784**, 1935–1941 (2008).

95. Levar, C. E., Chan, C. H., Mehta-Kolte, M. G. & Bond, D. R. An inner membrane cytochrome required only for reduction of high redox potential extracellular electron acceptors. *mBio* **5**, (2014).

96. Hunt, K. A., Flynn, J. M., Naranjo, B., Shikhare, I. D. & Gralnick, J. A. Substrate-level phosphorylation is the primary source of energy conservation during anaerobic respiration of *Shewanella oneidensis* strain MR-1. *J Bacteriol* **192**, 3345–3351 (2010).

97. Myers, C. R. & Nealson, K. H. Bacterial manganese reduction and growth with manganese oxide as the sole electron acceptor. *Science Science* **240**, 1319–1321 (1988).

98. Yang, C. *et al.* Comparative Genomics and Experimental Characterization of N-Acetylglucosamine Utilization Pathway of *Shewanella oneidensis*. *Journal of Biological Chemistry* **281**, 29872–29885 (2006).

99. Luo, S., Guo, W., Nealson, K. H., Feng, X. & He, Z. 13C Pathway Analysis for the Role of Formate in Electricity Generation by *Shewanella oneidensis* MR-1 Using Lactate in Microbial Fuel Cells. *Scientific Reports 2016 6:1* **6**, 1–8 (2016).

100. Duhl, K. L., Tefft, N. M. & TerAvest, M. A. *Shewanella oneidensis* MR-1 utilizes both sodium- and proton-pumping NADH dehydrogenases during aerobic growth. *Appl Environ Microbiol* **84**, (2018).

101. Kane, A. L. *et al.* Formate metabolism in *Shewanella oneidensis* generates proton motive force and prevents growth without an electron acceptor. *J Bacteriol* **198**, 1337–1346 (2016).

102. Kasai, T., Suzuki, Y., Kouzuma, A. & Watanabe, K. Roles of D-lactate dehydrogenases in the anaerobic growth of <i>Shewanella oneidensis<i/> MR-1 on sugars. *Appl Environ Microbiol* **85**, (2019).

103. Pinchuk, G. E. *et al.* Pyruvate and Lactate Metabolism by *Shewanella oneidensis* MR-1 under Fermentation, Oxygen Limitation, and Fumarate Respiration Conditions. *Appl Environ Microbiol* **77**, 8234 (2011).

104. Bertling, K. Mechanisms and Regulation of Aerobic Respiration in Shewanella Oneidensis MR-1. *Theses* (University of Wisconsin, Milwaukee, 2020).

105. Thöny-Meyer, L. Biogenesis of respiratory cytochromes in bacteria. *Microbiology and Molecular Biology Reviews* **61**, (1997).

106. Jasaitis, A. *et al.* Electrogenic reactions of cytochrome bd. *Biochemistry* **39**, (2000).

107. Bertling, K., Banerjee, A. & Saffarini, D. Aerobic Respiration and Its Regulation in the Metal Reducer Shewanella oneidensis. *Front Microbiol* **12**, (2021).

108. Gao, H. *et al.* Impacts of Shewanella oneidensis c-type cytochromes on aerobic and anaerobic respiration. *Microb Biotechnol* **3**, (2010).

109. Kouzuma, A., Hashimoto, K. & Watanabe, K. Influences of aerobic respiration on current generation by Shewanella oneidensis MR-1 in single-chamber microbial fuel cells. *Biosci Biotechnol Biochem* **76**, (2012).

110. Le Laz, S. *et al.* Expression of terminal oxidases under nutrient-starved conditions in Shewanella oneidensis: Detection of the A-type cytochrome c oxidase. *Sci Rep* **6**, (2016).

111. Nakagawa, G. *et al.* Metabolic Characteristics of a Glucose-Utilizing *Shewanella oneidensis* Strain Grown under Electrode-Respiring Conditions. *PLoS One* **10**, e0138813 (2015).

112. Tokunou, Y., Hashimoto, K. & Okamoto, A. Extracellular electron transport scarcely accumulates proton motive force in Shewanella oneidensis MR-1. *Bull Chem Soc Jpn* **88**, (2015).

113. Coursolle, D. & Gralnick, J. A. Modularity of the Mtr respiratory pathway of *Shewanella oneidensis* strain MR-1. *Mol Microbiol* **77**, 995–1008 (2010).

114. McMillan, D. G. G. *et al.* Protein-protein interaction regulates the direction of catalysis and electron transfer in a redox enzyme complex. *J Am Chem Soc* **135**, 10550–10556 (2013).

115. Sturm, G. *et al.* A dynamic periplasmic electron transfer network enables respiratory flexibility beyond a thermodynamic regulatory regime. *ISME Journal* **9**, 1802–1811 (2015).

116. Richardson, D. J. *et al.* The 'porin-cytochrome' model for microbe-to-mineral electron transfer. *Mol Microbiol* **85**, 201–212 (2012).

117. Shi, L. *et al.* Direct involvement of type II secretion system in extracellular translocation of *Shewanella oneidensis* outer membrane cytochromes MtrC and OmcA. *J Bacteriol* **190**, 5512–5516 (2008).

118. Dietrich, H. M. *et al.* Soluble versions of outer membrane cytochromes function as exporters for heterologously produced cargo proteins. *Microb Cell Fact* **18**, (2019).

119. Edwards, M. J. *et al.* Structural modeling of an outer membrane electron conduit from a metal-reducing bacterium suggests electron transfer via periplasmic redox partners. *Journal of Biological Chemistry* **293**, 8103–8112 (2018).

120. Shi, L. *et al.* Isolation of a high-affinity functional protein complex between OmcA and MtrC: Two outer membrane decaheme c-type cytochromes of *Shewanella oneidensis* MR-1. *J Bacteriol* **188**, 4705–4714 (2006).

121. Kouzuma, A., Kasai, T., Hirose, A. & Watanabe, K. Catabolic and regulatory systems in *Shewanella oneidensis* MR-1 involved in electricity generation in microbial fuel cells. *Frontiers in Microbiology* vol. 6 609 Preprint at https://doi.org/10.3389/fmicb.2015.00609 (2015).

122. Lomize, M. A., Pogozheva, I. D., Joo, H., Mosberg, H. I. & Lomize, A. L. OPM database and PPM web server: Resources for positioning of proteins in membranes. *Nucleic Acids Res* **40**, D370–D376 (2012).

123. White, G. F. *et al.* Rapid electron exchange between surface-exposed bacterial cytochromes and Fe(III) minerals. *Proc Natl Acad Sci U S A* **110**, 6346–6351 (2013).

124. Ross, D. E., Flynn, J. M., Baron, D. B., Gralnick, J. A. & Bond, D. R. Towards electrosynthesis in *Shewanella*: energetics of reversing the *mtr* pathway for reductive metabolism. *PLoS One* **6**, e16649 (2011).

125. Ford, K. C. & TerAvest, M. A. The electron transport chain of Shewanella oneidensis MR-1 can operate bidirectionally to enable microbial electrosynthesis. *Appl Environ Microbiol* **90**, (2024).

126. Pirbadian, S. & El-Naggar, M. Y. Multistep hopping and extracellular charge transfer in microbial redox chains. *Physical Chemistry Chemical Physics* **14**, 13802–13808 (2012).

127. Kotloski, N. J. & Gralnick, J. A. Flavin electron shuttles dominate extracellular electron transfer by *Shewanella oneidensis*. *mBio* **4**, 553–565 (2013).

128. Coursolle, D., Baron, D. B., Bond, D. R. & Gralnick, J. A. The Mtr respiratory pathway is essential for reducing flavins and electrodes in *Shewanella oneidensis*. *J Bacteriol* **192**, 467–474 (2010).

129. Edwards, M. J. *et al.* The X-ray crystal structure of *Shewanella oneidensis* OmcA reveals new insight at the microbe-mineral interface. *FEBS Lett* **588**, 1886–1890 (2014).

130. Clarke, T. A. *et al.* Structure of a bacterial cell surface decaheme electron conduit. *Proc Natl Acad Sci U S A* **108**, 9384–9389 (2011).

131. Edwards, M. J. *et al.* Redox Linked Flavin Sites in Extracellular Decaheme Proteins Involved in Microbe-Mineral Electron Transfer. *Sci Rep* **5**, 11677 (2015).

132. Shi, Z., Zachara, J. M., Wang, Z., Shi, L. & Fredrickson, J. K. Reductive dissolution of goethite and hematite by reduced flavins. *Geochim Cosmochim Acta* **121**, 139–154 (2013).

133. Wang, Z. *et al.* Effects of soluble flavin on heterogeneous electron transfer between surface-exposed bacterial cytochromes and iron oxides. *Geochim Cosmochim Acta* **163**, 299–310 (2015).

134. Norman, M. P. *et al.* A Cysteine Pair Controls Flavin Reduction by Extracellular Cytochromes during Anoxic/Oxic Environmental Transitions. *mBio* **14**, (2023).

135. Breuer, M., Rosso, K. M., Blumberger, J. & Butt, J. N. Multi-haem cytochromes in *Shewanella oneidensis* MR-1: structures, functions and opportunities. *J R Soc Interface* **12**, (2015).

136. Lower, B. H. *et al. In vitro* evolution of a peptide with a hematite binding motif that may constitute a natural metal-oxide binding archetype. *Environ Sci Technol* **42**, 3821–3827 (2008).

137. Barrozo, A., El-Naggar, M. Y. & Krylov, A. I. Distinct Electron Conductance Regimes in Bacterial Decaheme Cytochromes. *Angewandte Chemie International Edition* **57**, 6805–6809 (2018).

138. Jiang, X. *et al.* Kinetics of trifurcated electron flow in the decaheme bacterial proteins MtrC and MtrF. *Proc Natl Acad Sci U S A* **116**, 3425–3430 (2019).

139. Edwards, M. J. *et al.* The Crystal Structure of the Extracellular 11-heme Cytochrome UndA Reveals a Conserved 10-heme Motif and Defined Binding Site for Soluble Iron Chelates. *Structure* **20**, 1275–1284 (2012).

140. Clarke, T. A. *et al.* Structure of a bacterial cell surface decaheme electron conduit. *Proc Natl Acad Sci U S A* **108**, 9384–9389 (2011).

141. Taylor, P., Pealing, S. L., Reid, G. A., Chapman, S. K. & Walkinshaw, M. D. Structural and mechanistic mapping of a unique fumarate reductase. *Nature Structural Biology 1999 6:12* **6**, 1108–1112 (1999).

142. Ing, N. L., El-Naggar, M. Y. & Hochbaum, A. I. Going the Distance: Long-Range Conductivity in Protein and Peptide Bioelectronic Materials. *Journal of Physical Chemistry B* vol. 122 10403–10423 Preprint at https://doi.org/10.1021/acs.jpcb.8b07431 (2018).

143. Su, L. & Ajo-Franklin, C. M. Reaching full potential: bioelectrochemical systems for storing renewable energy in chemical bonds. *Current Opinion in Biotechnology* vol. 57 66–72 Preprint at https://doi.org/10.1016/j.copbio.2019.01.018 (2019).

144. Garg, K. *et al.* Direct evidence for heme-assisted solid-state electronic conduction in multi-heme: *c*-type cytochromes. *Chem Sci* **9**, 7304–7310 (2018).

145. Kikuchi, T. & Tanaka, S. Biological removal and recovery of toxic heavy metals in water environment. *Critical Reviews in Environmental Science and Technology* vol. 42 1007–1057 Preprint at https://doi.org/10.1080/10643389.2011.651343 (2012).

146. Lovley, D. R. *et al.* Geobacter: The Microbe Electric's Physiology, Ecology, and Practical Applications. in *Advances in Microbial Physiology* vol. 59 1–100 (Academic Press, 2011).

147. Stolz, J. F. & Oremland, R. S. Bacterial respiration of arsenic and selenium. *FEMS Microbiol Rev* **23**, 615–627 (1999).

148. Yamamura, S. & Amachi, S. Microbiology of inorganic arsenic: From metabolism to bioremediation. *Journal of Bioscience and Bioengineering* vol. 118 1–9 Preprint at https://doi.org/10.1016/j.jbiosc.2013.12.011 (2014).

149. Wang, Y. T. & Shen, H. Bacterial reduction of hexavalent chromium. *J Ind Microbiol* **14**, 159–163 (1995).

150. Lovley, D. R. & Coates, J. D. Bioremediation of metal contamination. *Curr Opin Biotechnol* **8**, 285–289 (1997).

151. Vera, M., Schippers, A. & Sand, W. Progress in bioleaching: Fundamentals and mechanisms of bacterial metal sulfide oxidation-part A. *Applied Microbiology and Biotechnology* vol. 97 7529–7541 Preprint at https://doi.org/10.1007/s00253-013-4954-2 (2013).

152. Lloyd, J. R. Microbial reduction of metals and radionuclides. *FEMS Microbiology Reviews* vol. 27 411–425 Preprint at https://doi.org/10.1016/S0168-6445(03)00044-5 (2003).

153. Konishi, Y. *et al.* Bioreductive deposition of platinum nanoparticles on the bacterium *Shewanella algae* . *J Biotechnol* **128**, 648–653 (2007).

154. Gregory, K. B., Bond, D. R. & Lovley, D. R. Graphite electrodes as electron donors for anaerobic respiration. *Environ Microbiol* **6**, 596–604 (2004).

155. Logan, B. E. *et al.* Microbial fuel cells: Methodology and technology. *Environmental Science and Technology* vol. 40 5181–5192 Preprint at https://doi.org/10.1021/es0605016 (2006).

156. Logan, B. E. & Rabaey, K. Conversion of wastes into bioelectricity and chemicals by using microbial electrochemical technologies. *Science* vol. 337 686–690 Preprint at https://doi.org/10.1126/science.1217412 (2012).

157. Miyahara, M., Hashimoto, K. & Watanabe, K. Use of cassette-electrode microbial fuel cell for wastewater treatment. *J Biosci Bioeng* **115**, 176–181 (2013).

158. Logan, B. E. Scaling up microbial fuel cells and other bioelectrochemical systems. *Applied Microbiology and Biotechnology* vol. 85 1665–1671 Preprint at https://doi.org/10.1007/s00253-009-2378-9 (2010).

159. Kaku, N., Yonezawa, N., Kodama, Y. & Watanabe, K. Plant/microbe cooperation for electricity generation in a rice paddy field. *Appl Microbiol Biotechnol* **79**, 43–49 (2008).

160. Ren, H., Lee, H. S. & Chae, J. Miniaturizing microbial fuel cells for potential portable power sources: promises and challenges. *Microfluidics and Nanofluidics* vol. 13 353–381 Preprint at https://doi.org/10.1007/s10404-012-0986-7 (2012).

161. Bond, D. R., Holmes, D. E., Tender, L. M. & Lovley, D. R. Electrode-reducing microorganisms that harvest energy from marine sediments. *Science (1979)* **295**, 483–485 (2002).

162. Baron, D., LaBelle, E., Coursolle, D., Gralnick, J. A. & Bond, D. R. Electrochemical Measurement of Electron Transfer Kinetics by *Shewanella oneidensis* MR-1. *J Biol Chem* **284**, 28865 (2009).

163. Lockwood, C. W. J. *et al.* Membrane-spanning electron transfer proteins from electrogenic bacteria: Production and investigation. *Methods Enzymol* **613**, 257–275 (2018).

164. Liu, H. & Naismith, J. H. An efficient one-step site-directed deletion, insertion, single and multiple-site plasmid mutagenesis protocol. *BMC Biotechnol* **8**, 91 (2008).

165. Cheesman, M. R., Watmough, N. J., Gennis, R. B., Greenwood, C. & Thomson, A. J. Magnetic-circular-dichroism studies of *Escherichia coli* cytochrome bo Identification of high-spin ferric, low-spin ferric and ferryl [Fe(IV)] forms of heme o. *Eur J Biochem* **219**, 595–602 (1994).

166. Jenner, L. P. *et al.* Heme ligation and redox chemistry in two bacterial thiosulfate dehydrogenase (TsdA) enzymes. *Journal of Biological Chemistry* **294**, 18002–18014 (2019).

167. Zheng, Z. & Gunner, M. R. Analysis of the electrochemistry of hemes with Ems spanning 800 mV. *Proteins* **75**, 719 (2009).

168. Barr, I. & Guo, F. Pyridine Hemochromagen Assay for Determining the Concentration of Heme in Purified Protein Solutions. *Bio Protoc* **5**, (2015).

169. Brautigam, C. A. Using Lamm-Equation Modeling of Sedimentation Velocity Data to Determine the Kinetic and Thermodynamic Properties of Macromolecular Interactions. *Methods* **54**, 4 (2011).

170. Laue, T. M., Shah, B. D., Ridgeway, T. M. & Pelletier, S. L. Analytical ultracentrifugation in biochemistry and polymer science. *Anal Chim Acta* **306**, 365 (1995).

171. Schuck, P. Size-distribution analysis of macromolecules by sedimentation velocity ultracentrifugation and Lamm equation modeling. *Biophys J* **78**, 1606–1619 (2000).

172. Firer-Sherwood, M. A., Ando, N., Drennan, C. L. & Elliott, S. J. Solution-Based Structural Analysis of the Decaheme Cytochrome, MtrA, by Small-Angle X-ray Scattering and Analytical Ultracentrifugation. *J Phys Chem B* **115**, 11208 (2011).

173. Brautigam, C. A. Calculations and Publication-Quality Illustrations for Analytical Ultracentrifugation Data. in *Methods in Enzymology* vol. 562 109–133 (Academic Press, 2015).

174. Mertens, H. D. T. & Svergun, D. I. Structural characterization of proteins and complexes using small-angle X-ray solution scattering. *J Struct Biol* **172**, 128–141 (2010).

175. Petoukhov, M. V., Konarev, P. V., Kikhney, A. G. & Svergun, D. I. ATSAS 2.1 – towards automated and web-supported small-angle scattering data analysis. *urn:issn:0021-8898* **40**, s223–s228 (2007).

176. Choi, K. H. & Morais, M. Use of Small-Angle X-ray Scattering to Investigate the Structure and Function of Dengue Virus NS3 and NS5. *Methods Mol Biol* **1138**, 241 (2014).

177. Svergun, D. I. & IUCr. Determination of the regularization parameter in indirect-transform methods using perceptual criteria. *urn:issn:0021-8898* **25**, 495–503 (1992).

178. Franke, D. & Svergun, D. I. DAMMIF, a program for rapid ab-initio shape determination in small-angle scattering. *urn:issn:0021-8898* **42**, 342–346 (2009).

179. Volkov, V. V. & Svergun, D. I. Uniqueness of ab initio shape determination in small-angle scattering. *J Appl Crystallogr* **36**, 860–864 (2003).

180. Svergun, D. I. Restoring low resolution structure of biological macromolecules from solution scattering using simulated annealing. *Biophys J* **76**, 2879–2886 (1999).

181. Kozin, M. B. & Svergun, D. I. Automated matching of high- and low-resolution structural models. *urn:issn:0021-8898* **34**, 33–41 (2001).

182. van Wonderen, J. H. *et al.* Photosensitised Multiheme Cytochromes as Light-Driven Molecular Wires and Resistors. *ChemBioChem* **19**, 2206–2215 (2018).

183. Mersch, D. *et al.* Wiring of Photosystem II to Hydrogenase for Photoelectrochemical Water Splitting. *J Am Chem Soc* **137**, 8541–8549 (2015).

184. Jenner, L. P. *et al.* Reaction of Thiosulfate Dehydrogenase with a Substrate Mimic Induces Dissociation of the Cysteine Heme Ligand Giving Insights into the Mechanism of Oxidative Catalysis. *J Am Chem Soc* **144**, 18296–18304 (2022).

185. Fourmond, V. QSoas: A Versatile Software for Data Analysis. *Anal Chem* **88**, 5050–5052 (2016).

186. Laviron, E. General expression of the linear potential sweep voltammogram in the case of diffusionless electrochemical systems. *J Electroanal Chem Interfacial Electrochem* **101**, 19–28 (1979).

187. Butt, J. N., Jeuken, L. J. C., Zhang, H., Burton, J. A. J. & Sutton-Cook, A. L. Protein film electrochemistry. *Nature Reviews Methods Primers* **3**, 77 (2023).

188. Doyle, R. M. A. S., Richardson, D. J., Clarke, T. A. & Butt, J. N. Freely diffusing versus adsorbed protein: Which better mimics the cellular state of a redox protein? *Electrochim Acta* **110**, 73–78 (2013).

189. Costa, P., Gomes, A. T. P. C., Braz, M., Pereira, C. & Almeida, A. Application of the Resazurin Cell Viability Assay to monitor *Escherichia coli* and *Salmonella typhimurium* Inactivation Mediated by Phages. *Antibiotics (Basel)* **10**, (2021).

190. Viollier, E., Inglett, P. W., Hunter, K., Roychoudhury, A. N. & Van Cappellen, P. The ferrozine method revisited: Fe(II)/Fe(III) determination in natural waters. *Applied Geochemistry* **15**, 785–790 (2000).

191. Ross, D. E., Brantley, S. L. & Tien, M. Kinetic Characterization of OmcA and MtrC, Terminal Reductases Involved in Respiratory Electron Transfer for Dissimilatory Iron Reduction in *Shewanella oneidensis* MR-1. *Appl Environ Microbiol* **75**, 5218–5226 (2009).

192. Meitl, L. A. *et al.* Electrochemical interaction of *Shewanella oneidensis* MR-1 and its outer membrane cytochromes OmcA and MtrC with hematite electrodes. *Geochim Cosmochim Acta* **73**, 5292–5307 (2009).

193. Yang, F. *et al.* Characterization of purified c-type heme-containing peptides and identification of c-type heme-attachment sites in *Shewanella oneidenis* cytochromes using mass spectrometry. *J Proteome Res* **4**, 846–854 (2005).

194. van Wonderen, J. H. *et al.* Liquid-chromatography mass spectrometry describes post-translational modification of Shewanella outer membrane proteins. *Biochim Biophys Acta Biomembr* **1866**, (2024).

195. van Wonderen, J. H. *et al.* Nanosecond heme-to-heme electron transfer rates in a multiheme cytochrome nanowire reported by a spectrally unique His/Met-ligated heme. *Proc Natl Acad Sci U S A* **118**, e2107939118 (2021).

196. Winter, G. Xia2: An expert system for macromolecular crystallography data reduction. *J Appl Crystallogr* **43**, 186–190 (2010).

197. Evans, P. R. & Murshudov, G. N. How good are my data and what is the resolution? *Acta Crystallogr D Biol Crystallogr* **69**, 1204–1214 (2013).

198. Liebschner, D. *et al.* Macromolecular structure determination using X-rays, neutrons and electrons: recent developments in Phenix. *Acta Crystallogr D Struct Biol* **75**, 861–877 (2019).

199. Murshudov, G. N. *et al.* REFMAC5 for the refinement of macromolecular crystal structures. *urn:issn:0907-4449* **67**, 355–367 (2011).

200. Barrozo, A., El-Naggar, M. Y. & Krylov, A. I. Distinct Electron Conductance Regimes in Bacterial Decaheme Cytochromes. *Angewandte Chemie International Edition* **57**, 6805–6809 (2018).

201. White, G. F. *et al.* Rapid electron exchange between surface-exposed bacterial cytochromes and Fe(III) minerals. *Proc Natl Acad Sci U S A* **110**, 6346–6351 (2013).

202. Breuer, M. *et al.* Molecular structure and free energy landscape for electron transport in the decahaem cytochrome MtrF. *Biochem Soc Trans* **40**, 1198–1203 (2012).

203. Laue, T. M., Shah, B. D., Ridgeway, T. M. & Pelletier, S. L. *Analytical Ultracentrifugation in Biochemistry and Polymer Science*. *Analytical ultracentrifugation in biochemistry and polymer science* (Royal Society of Chemistry, Cambridge [England] :, 1992). doi:10.1016/0003-2670(95)90401-8.

204. Von Canstein, H., Ogawa, J., Shimizu, S. & Lloyd, J. R. Secretion of Flavins by *Shewanella* Species and Their Role in Extracellular Electron Transfer. *Appl Environ Microbiol* **74**, 615–623 (2008).

205. Breuer, M., Rosso, K. M. & Blumberger, J. Flavin Binding to the Deca-heme Cytochrome MtrC: Insights from Computational Molecular Simulation. *Biophys J* **109**, 2614–2624 (2015).

206. Shi, L. *et al.* Molecular underpinnings of Fe(III) oxide reduction by *Shewanella oneidensis* MR-1. *Front Microbiol* **3**, 17420 (2012).

207. Adam, F. I., Bounds, P. L., Kissner, R. & Koppenol, W. H. Redox properties and activity of iron-citrate complexes: Evidence for redox cycling. *Chem Res Toxicol* **28**, 604–614 (2015).

208. Fredrickson, J. K. *et al.* Towards environmental systems biology of Shewanella. *Nature Reviews Microbiology 2008 6:8* **6**, 592–603 (2008).

209. Shi, L. *et al.* Identification and Characterization of $Und_{AHRCR-6}$, an Outer Membrane Endecaheme c-Type Cytochrome of *Shewanella* sp. Strain HRCR-6. *Appl Environ Microbiol* **77**, 5521 (2011).

210. Shimizu, K., Hutcheson, R., Engelmann, M. D. & Francis Cheng, I. Cyclic voltammetric and aqueous equilibria model study of the pH dependant iron(II/III)ethylenediamminetetraacetate complex reduction potential. *Journal of Electroanalytical Chemistry* **603**, 44–50 (2007).

211. Wu, J., Kim, K. S., Sung, N. C., Kim, C. H. & Lee, Y. C. Isolation and characterization of *Shewanella oneidensis* WL-7 capable of decolorizing azo dye Reactive Black 5. *J Gen Appl Microbiol* **55**, 51–55 (2009).

212. Le Laz, S., Kpebe, A., Lorquin, J., Brugna, M. & Rousset, M. H2-dependent azoreduction by *Shewanella oneidensis* MR-1: Involvement of secreted flavins and both [Ni-Fe] and [Fe-Fe] hydrogenases. *Appl Microbiol Biotechnol* **98**, 2699–2707 (2014).

213. Cai, P. J. *et al.* Anaerobic biodecolorization mechanism of methyl orange by *Shewanella oneidensis* MR-1. *Appl Microbiol Biotechnol* **93**, 1769–1776 (2012).

214. Yang, Y. Y., Du, L. N., Wang, G., Jia, X. M. & Zhao, Y. H. The decolorisation capacity and mechanism of *Shewanella oneidensis* MR-1 for Methyl Orange and Acid Yellow 199 under microaerophilic conditions. *Water Science and Technology* **63**, 956–963 (2011).

215. Calogero, G., Bartolotta, A., Di Marco, G., Di Carlo, A. & Bonaccorso, F. Vegetable-based dye-sensitized solar cells. *Chem Soc Rev* **44**, 3244–3294 (2015).

216. Yin, X. *et al.* Physiological versatility of ANME-1 and Bathyarchaeotoa-8 archaea evidenced by inverse stable isotope labeling. *Microbiome* **12**, 1–11 (2024).

217. Miroshnichenko, M. L. *et al. Oceanithermus profundus* gen. nov., sp. nov., a thermophilic, microaerophilic, facultatively chemolithoheterotrophic bacterium from a deep-sea hydrothermal vent. *Int J Syst Evol Microbiol* **53**, 747–752 (2003).

218. Gassler, T. *et al.* The industrial yeast *Pichia pastoris* is converted from a heterotroph into an autotroph capable of growth on CO2. *Nature Biotechnology 2019 38:2* **38**, 210–216 (2019).

219. Bryant, D. A. Phototrophy and Phototrophs. in *Encyclopedia of Microbiology* 527–537 (Academic Press, 2019). doi:10.1016/B978-0-12-809633-8.20672-9.

220. Yafremava, L. S. *et al.* A general framework of persistence strategies for biological systems helps explain domains of life. *Front Genet* **4**, 36588 (2013).

221. Vera, M., Pagliai, F., Guiliani, N. & Jerez, C. A. The Chemolithoautotroph *Acidithiobacillus ferrooxidans* Can Survive under Phosphate-Limiting Conditions by Expressing a C-P Lyase Operon That Allows It To Grow on Phosphonates. *Appl Environ Microbiol* **74**, 1829 (2008).

222. Schrödinger LLC. The PyMOL Molecular Graphics System, Version 3.0.

223. McNicholas, S., Potterton, E., Wilson, K. S. & Noble, M. E. M. Presenting your structures: the *CCP* 4 *mg* molecular-graphics software. *Acta Crystallogr D Biol Crystallogr* **67**, 386–394 (2011).

224. Pitts, K. E. *et al.* Characterization of the *Shewanella oneidensis* MR-1 Decaheme Cytochrome MtrA: Expression in *Escherichia coli* confers the ability to reduce soluble Fe(III) chelates. *Journal of Biological Chemistry* **278**, 27758–27765 (2003).